ADVERTIMENT. La consulta d’aquesta tesi queda condicionada a l’acceptació de les següents condicions d'ús: La difusió d’aquesta tesi per mitjà del servei TDX (www.tesisenxarxa.net) ha estat autoritzada pels titulars dels drets de propietat intel·lectual únicament per a usos privats emmarcats en activitats d’investigació i docència. No s’autoritza la seva reproducció amb finalitats de lucre ni la seva difusió i posada a disposició des d’un lloc aliè al servei TDX. No s’autoritza la presentació del seu contingut en una finestra o marc aliè a TDX (framing). Aquesta reserva de drets afecta tant al resum de presentació de la tesi com als seus continguts. En la utilització o cita de parts de la tesi és obligat indicar el nom de la persona autora.

ADVERTENCIA. La consulta de esta tesis queda condicionada a la aceptación de las siguientes condiciones de uso: La difusión de esta tesis por medio del servicio TDR (www.tesisenred.net) ha sido autorizada por los titulares de los derechos de propiedad intelectual únicamente para usos privados enmarcados en actividades de investigación y docencia. No se autoriza su reproducción con finalidades de lucro ni su difusión y puesta a disposición desde un sitio ajeno al servicio TDR. No se autoriza la presentación de su contenido en una ventana o marco ajeno a TDR (framing). Esta reserva de derechos afecta tanto al resumen de presentación de la tesis como a sus contenidos. En la utilización o cita de partes de la tesis es obligado indicar el nombre de la persona autora.

WARNING. On having consulted this thesis you’re accepting the following use conditions: Spreading this thesis by the TDX (www.tesisenxarxa.net) service has been authorized by the titular of the intellectual property rights only for private uses placed in investigation and teaching activities. Reproduction with lucrative aims is not authorized neither its spreading and availability from a site foreign to the TDX service. Introducing its content in a window or frame foreign to the TDX service is not authorized (framing). This rights affect to the presentation summary of the thesis as well as to its contents. In the using or citation of parts of the thesis it’s obliged to indicate the name of the author

Investigation of continuous-wave range-resolved lidar systems for gas detection and concentration measurement

Ph.D. Thesis

Oscar Batet Torrell

Thesis Advisors:

Prof. Federico Dios Otín

Prof. Adolfo Comeron Tejero

Remote-Sensing Lab
Department of Signal Theory and Communications
Universitat Politècnica de Catalunya (UPC)

Abstract

he techniques for detection of the atmosphere constituents and their distribution in the space have evolved in the last years driven by needs in the environmental, meteorological and climate science fields and backed by technological developments. The study of the atmosphere behavior, the health risks provoked either by natural or man-made phenomena or the study of the climate change are examples of applications of optical remote sensing techniques that tend to increase as time goes by.

This thesis presents an innovative lidar system for gas detection with range resolution and moderate cost. We study a frequency-modulated continuous-wave lidar system (FMCW) for gas detection in the atmosphere. As a previous step a system for aerosol detection has been studied, which has led to the development of a phase switching technique in the modulating signal to make possible the retrieval of the low-spatial-frequency components of the atmosphere optical parameters. This technique has been tested with an experiment of discrimination of targets close each other. Then the system has been extended to gas detection either with topographical targets or with aerosols as backscattering medium and a preliminary experiment for the first case has been performed. An analysis of the uncertainty in the gas-concentration retrieval as a function of the signal-to-noise ratio (SNR) has been developed and the extension of the 'phase-hop' technique for gas-detection FMCW-lidar systems has been proposed.

Previous to this system, a wavelength modulation spectroscopy (WMS) system has been developed as an intermediate step to achieve some degree of expertise in gas detection by means of absorption spectroscopy techniques. Different experiments with gas cells and open-path environments have been carried out.

Finally an optical amplifier which can be used in WMS systems as well as in FMCW-lidar systems is studied, designed, developed and tested. The analysis of the fiber-amplifier behavior for conditions of temperature and pressure change has been performed with a certain dependence of the background with temperature.

Keywords: Lidar, gas detection, absorption spectroscopy, remote sensing, laser, atmospheric pollution.

Foreword

It all started a day of September when I was looking for an opportunity of doing a PhD in applied optics or photonics. I came to the University where I obtained the title of engineer and I started asking for the possibility of doing this PhD. I found professors Dios and Comeron in the stairs when they were about to go to have lunch. I asked them and they offered me different projects. After some days and some discussions I decided the project of developing a new type of lidar system could be really exciting and I accepted it. Some years later I'm very happy because of the work done and the possibilities opened with this project.

"Hay una fuerza motriz más poderosa que el vapor, la electricidad y la energía atómica: la voluntad"

Albert Einstein

"El conocimiento y el amor son iguales, porque son las dos únicas cosas que aumentan cuando se comparten",

Proverbio Africano

الصبر مفتاح الفرج
(La paciencia es la llave de la liberación)
Proverbio Árabe

Acknowledgements

The first ones this work is dedicated to are professors Adolfo Comeron and Federico Dios. Some 6 years ago we met in the stairs and decided to start a project which lasted until today and I hope it can go on. Thanks as well to professor Ravyl Agishev for the initial idea of the PhD thesis and to the people in Boulder: Dirk, Al, Petter, Scott, Lars and Martha… that so kindly received me at NCAR during the stay and, of course, to Paco López-Dekker which put me in touch with such fantastic people. And thanks again to the other guys in the group: Constan, Alejandro, Michäel, Sergio, … to help me in so many ways and to Josep Anton Morguí of the IC3 to give me the opportunity to test the system. A special memory I will retain of Professor Miguel González for the explanations of the chemistry topics of this work.

Obviamente nunca podré olvidar los ratos en el despacho y en el D3 con toda la gente que he visto pasar. Tanta gente, tantos nombres que a alguien me dejaré en el tintero: Emilio, Alex, Jaber, Raquel, Francesc, David, Isaac, Xavi, Pere, María, Sergi, Santi, Dani, Marta, René, Verónica, Marc, Roberto, Hugo, Mariví, Ricardo, Gemma, Juan Carlos (gracias especialmente por el desarrollo del generador de funciones), Txema, Jordi, Luca, Juanfer, Javi, Zabdiel, Benji, Sandra, Pablo, Gerard, Marco… Tampoco me puedo descuidar de dos personas con las que conviví compartiendo el piso: Pavel y Bea, gracias por vuestra paciencia. También para mis grandes amigos de Barcelona, Pedro y Carme, y la gente de árabe, que tanto me ayudaron a desconectar en los momentos difíciles. Puede que fueran demasiados años en la Universidad pero los momentos que me habéis dejado no los cambio por nada. Gracias.

També toca recordar-se de la gent del poble, del Xino, Iker, Samel, Ciscu, Edgar, Piti, Anton, Antonio, Antoniu, Jordi, Gallofa, Perro, Caparó, Nyenyo, Koixi, Estevet... també ells tenen una part de la culpa d'haver arribat aquí. I com no, la família, Ramon i Mª Lluïsa, sense els que segur que no estaria aquí, l'Olga, el Javi i, especialment, l'Helena, el nou terror de la casa que ens ha omplert de vida. Per ells i pel Josep, la Maria, el Rafael i la Rosita, que segueixen dins el meu cor.

Manca infine una persona speciale, una persona che non ha visto iniziare questa tesi dottorale ma che l'ha sofferta quasi quanto me. Ha un nome primaverile e una energia che ti spinge avanti fino che non arrivi alla fine delle cose più difficili come una tesi dottorale. Lei è Florence, una parte del mio cuore.

Index

1 Introduction

The main objective of this project, which serves as the framework for this PhD thesis, is to investigate a frequency-modulated continuous-wave (FMCW) lidar system to obtain gas-concentration profiles along the line of sight. The reference technique for this project was the differential-absorption lidar technique (DIAL) which achieves gas detection with range resolution at long distances using high-power pulsed lasers emitting at two different wavelengths.

The main anticipated advantages of a FMCW system over classic DIAL systems would be cost, maintenance and the fields where it can be applied, and that it poses fewer hazardous risks compared to a high-power pulsed system. Potential applications could be safety, control, surveillance and monitoring of the environment.

The ideas of Professor R. R. Agishev, set out in [1, 2], were the starting point for the study on which this thesis is based. These articles explain the basics of the FMCW-lidar technique for range-resolved gas detection and propose the use of a frequency-modulated signal to modulate the current input of a laser-diode in order to obtain a wavelength-modulated signal capable of interacting with the gas-absorbing peaks in such a way that the local concentration of the gas can be extracted from the echo signal.

One example of its application could be to detect the plume of a given gas located at a distant range and simultaneously measure the gas concentration and the plume location. One immediate application of this idea would be to detect gas leaks in chemical plants or chemical-product warehouses, or even along gas pipelines.

A possible and interesting development of this idea would be to obtain concentration profiles along the lidar line of sight. A system with these characteristics would have useful applications, for example, monitoring fire seats in wooded zones, parks or green zones in general. Used for this purpose, the system could periodically sweep the zone being monitored within a range of no more than a few hundred meters looking for anomalous concentrations of CO or CO_2. A classic DIAL system is out of the question here for safety reasons because of the excessive high density of energy required.

Another type of application would be continuous monitoring of concentrations of greenhouse-effect gases with the aim of performing scientific studies with a large statistical database.

The objective of this study is to set the bases for developing a range-resolved system to detect gases using aerosols as backscattering distributed medium. It began with a study of the FMCW technique to detect targets in close proximity at arbitrary ranges. In this study different interference phenomena were observed that masked the real magnitudes of the different target responses as well as their real positions. These effects were studied analytically and corroborated experimentally.

At the same time a careful study was also carried out on the well-known WMS technique for *in-situ* gas detection as a prior step to detecting gas using lidar measurements. Some experiments were performed to gain a certain degree of expertise and joint measurements were also carried along with the *Institut Català de Ciències Climàtiques* (IC3).

Based on the analysis of the FMCW lidar technique, different alternatives were studied to deal with the problem of interferences between targets close to each other. The resulting proposal is a method that we have called “phase hop”, which overcomes these effects and paves the way for the development of the FMCW lidar system for distributed media (aerosols).

Finally, an analytical study of the FMCW system for gas detection was performed analyzing the different parameters that determine its performance. This study includes an extended version of the phase-hop method to remove the harmful influence from higher order harmonics produced by the interaction of the optical signal with the gases under study. A point that required particular attention was the trade-off between sensitivity and measurement time, because of the continuous nature of our laser sources.

This thesis is organized as follows:

Chapter 2 sets out the theoretical fundamentals of WMS technique. The first part reviews the light spectrum theory via the study of energy transitions in molecules, radiative transfer and line shapes to explain the position of the absorption lines and their strength and width. The second part of the chapter describes some spectroscopy techniques, such as direct absorption measurement and the differential techniques such as WMS, and a parametric analysis of these techniques.

Chapter 3 explains the behavior of the output-signal wavelength of laser diodes with respect to the input current and temperature, followed by a discussion of the experimental setup used to perform direct-absorption-measurement and WMS-spectroscopy experiments. These two methods were implemented to test the content of three gas cells and the results. After this, WMS was used to obtain the CO_2 and H_2O concentration in an open air path. Finally, a test comparing WMS integrated concentration measurements with localized measurements was performed to test the validity of the implemented WMS technique.

Chapter 4 is the central chapter of this study. It begins with an introduction to the lidar technique with the most common variants prior to presenting a study of the FMCW technique for radar (its initial use) and lidar. Section 3 analytically develops the technique for distributed media, showing the signal-processing problems that arise and proposing a possible solution. Section 4 is devoted to the application of this technique to gas detection using topographical targets or distributed media (aerosols) as backscattering medium. The extension of the phase-hop method is proposed as a solution to overcome the interference of higher order harmonics.

Chapter 5 presents two different experiments as initial tests of the techniques previously developed. Before starting with the experiments, a baseband-chirp generator was developed as a laser modulating source for the measurements of distributed media. This is followed by an explanation of an experiment showing the behavior of the lidar FMCW technique with two targets approaching each other. The last section of the chapter is dedicated to gas detection using the FMCW technique with a topographical target (an initial experiment), employing the WMS technique with high frequencies (some tenths of MHz) as a first step.

The last chapter explains the design and development of an optical amplifier carried out at the NCAR premises at Boulder. The study of the amplifier’s behavior is explained at the beginning of the chapter followed by a number of simulations to find the best configuration for the amplifier. The development is then explained step by step with all the intermediate measurements leading to the final modulation test. The last section of the chapter is devoted to the study of the concentration variation with respect to temperature and pressure variations. This development is particularly important to achieve higher levels of output power in the FMCW lidar system described.

Finally, future lines of investigation suggested by the conclusions of this work are outlined.

2 WMS Spectroscopy Theory

The aim of this thesis is to study gases in the atmosphere, their concentration and the evolution of this concentration across time. For this purpose, techniques based in absorption spectroscopy are used, which means that we need to know the fundamentals of spectroscopy and the origin and characteristics of light absorption in gases to understand the detection techniques. The first part of this chapter begins with an analysis of the physical principles on which absorption spectroscopy is based and describes the vibrational and rotational transitions in diatomic molecules. This is followed by a simple radiative-transfer analysis to calculate the absorption line strength and an explanation of the absorption lineshape and the phenomena involving line broadening. Sections 2.1.5 and 2.1.6 introduce and explain the HiTran database with a description of the effect of the gas concentration in the shape of the absorption lines for two extreme cases.

Having explained the physical phenomena involved in the WMS spectroscopy, the second part of the chapter is devoted to analyzing the technique itself. This begins with and explanation of the direct absorption measurement technique as a simple method for gas concentration estimation, followed by an analysis of wavelength modulation spectroscopy and a definition of the parameters to be taken into account in this technique. Some graphics of the peak amplitude and the distance between extremes of the first and second harmonic curves are explained which prove to be very useful to obtain the gas concentration as will be seen in the following chapter.

2.1 Light Spectrum Theory

As regards important aspects of spectroscopy, this section begins by accepting some key theoretical results as set out below [3].

Quantum Mechanics states through Planck’s law that an atom or molecule may exist only in specific quantum states, with each quantum state having its own discrete values of energy. The internal energy is the sum of the energy stored in three modes: rotation, vibration and electronic:

$$E_{tot} = E_{rot} + E_{vib} + E_{elec} \tag{2.1}$$

Note that discreteness of internal energy states leads to discrete transitions in energy when molecules change quantum states. These energy differences correspond directly to the energy of emitted or absorbed photons in discrete spectra.

Emission results when a molecule or atom changes quantum states from higher to lower energy, and in the process releases a photon. Absorption occurs when a molecule or atom changes quantum states from lower to higher energy, and the process absorbs a photon.

For the sake of convenience we can think of spectroscopy as comprising three primary elements: i.e., the positions, strengths and shapes of lines. Line positions, which receive emphasis in classical spectroscopy and their strength, depend on molecular structure. The strength and shape of lines are particularly important in diagnostics applications. All three elements will be addressed in this chapter, especially the last two elements which are essential for the development of our techniques.

2.1.1 Beer-Lambert’s law of Absorption and Boltzmann Distribution

Before starting with the topics of spectroscopy in the strictest sense, two important results are particularly important as they will be used in this chapter [3].

On the one hand, the governing law for absorption spectroscopy is Beer’s Law, listed below:

$$T_\nu = \left.\frac{I}{I_0}\right|_\nu = \exp\left(-k_\nu L\right) \tag{2.2}$$

where T_ν is the fractional transmission at frequency ν, k_ν is the spectral absorption coefficient [cm^{-1}], and L is the absorption path length [cm]. The combined quantity $k_\nu L$ is known as the spectral absorbance. The spectral absorption coefficient is given by:

$$k_\nu = S_i \times \phi\left(\nu\right) \times P_i \tag{2.3}$$

where S_i is the strength of the transition, ϕ is the lineshape function, and P_i is the partial pressure of the absorbing species. Beer’s Law can also be expressed in terms of absorption:

$$A_\nu = 1 - T_\nu = \left.\frac{I_0 - I}{I_0}\right|_\nu = 1 - \exp\left(-k_\nu L\right) \tag{2.4}$$

On the other hand, Boltzmann’s equation for the fraction of molecules in energy level i is:

$$F_i = \frac{n_i}{n} = \frac{g_i \exp\left(-\frac{\varepsilon_i}{kT}\right)}{Q}, \tag{2.5}$$

where g_i is the degeneracy of level i (i.e., the number of individual states with a common energy, ε_i) and Q is given by:

$$Q = \sum_i g_i \exp\left(-\frac{\varepsilon_i}{kT}\right) = Q_{rot} Q_{vib} Q_{elec} \tag{2.6}$$

and it corresponds to the partition function of the specific molecule. Q_{rot}, Q_{vib} and Q_{elec} correspond, respectively, to the rotational, vibrational and electronic partition functions. The partition function is a tool used to calculate the probability of a certain state in a system at a given temperature and corresponds to the energy-weighted sum over all the possible energy levels. [3]. Note that the overall partition function Q may be written as a product of partition functions for the different types of internal energy, since these energies are taken to be additive. The Boltzmann distribution function describes the distribution of molecules (or atoms) of a single species over its allowed quantum states. The parameter T is the temperature, and the species may be said to be in local thermodynamic equilibrium (LTE) if the populations in all the quantum levels obey Boltzmann's equation. In essence, this equation defines temperature.

2.1.2 Energy transitions in molecules. Diatomic molecules

The position of the absorption lines is established by the molecular energy states and the different transitions that take place between all these possible states. This section analyses the different components of the inner energy in a molecule and its contribution to the position of the absorption lines in the case of diatomic molecules where the energy states are more easily explained. For the case of bigger molecules, an extension of these factors must be applied in order to obtain the positions of their absorption lines and other fundamental parameters.

An important factor to be taken into account is the selection rules, which indicate the permitted transitions. Thus, e.g., for a diatomic molecule like CO $\Delta J = \pm 1$ and $\Delta \nu = 0,1,2...$ where J and υ correspond to the rotational and vibrational quantum numbers ($J = 0,1,2...$ and $\upsilon = 0,1,2...$ respectively), which specify the vibrational state of the molecule [4]. This is explained in more detail below. When the models are improved, the probability of higher jumps between states is greater than zero, or even slight.

2.1.2.1 Rotational states and transitions

When heteronuclear diatomic molecules rotate, their dipole moments also rotate. Molecular motions at characteristic frequencies create opportunities for resonances with EM waves, leading to absorption or emission at these frequencies.
The electric dipole moment is specified by

$$\vec{p} = \sum_i q_i \vec{r}_i \,, \tag{2.7}$$

where i refers to atoms in a molecule or system, q_i is the particle charge and $\vec{r}_i$ is the vector specifying location. When $\nu_{rad}^{-1} = T_{rot}$, that is, when the inverse of the radiation frequency and molecular rotation period coincide, resonance occurs increasing the chances of energy exchange between the EM wave and molecule by absorption or stimulated emission. The frequency of molecular rotation is located in the microwave region. All molecules with a permanent electric dipole can interact with light as a result of their rotation, and hence are considered “microwave active”. Molecules with no permanent electric dipole are termed “microwave inactive”.

The analysis of the rotational spectra of a diatomic molecule works from the rigid rotor (RR) model approach, which is a blend of classical and quantum mechanics. For this model, the atoms are assumed as being point masses (m_1 and m_2) with an equilibrium separation distance r_e that is constant or *rigid*. Typical separation lengths are $r_e \approx 10^{-8} cm$. The first step is to define the molecular moment of inertia I and the reduced mass μ:

$$I = \sum q_i r_i^2 = \mu r_e^2 \qquad \mu = \frac{m_1 m_2}{m_1 + m_2} \tag{2.8}$$

So the two-body problem is equivalent to the motion of a single-point mass μ, rotating about the center of mass.

The angular momentum of a molecule is quantized. The quantum number that characterizes the total angular momentum J and the allowed values of angular momentum are given by:

$$I\omega = \sqrt{J\left(J+1\right)}\hbar \qquad J = 1, 2, 3... \tag{2.9}$$

where ω is the rotation frequency and $\hbar$ is the reduced Planck constant. Then, we can express the energy of a classical rotor in the quantum form in order to see how it is quantized:

$$E_{rot} = \frac{1}{2} I\omega^2 = \frac{\hbar^2}{2I} J\left(J+1\right) \qquad J\left(J+1\right) = 2, 6, 12, 20... \tag{2.10}$$

The rotational constant, known as B, is:

$$B = \frac{\hbar^2}{2I} \tag{2.11}$$

This is an important value because, as we can observe in Eq. (2.10), the energy difference between two consecutive bands is equal to $2B$ times the rotational quantum number of the lower state J. So these will indicate the distribution of the lines in the band.

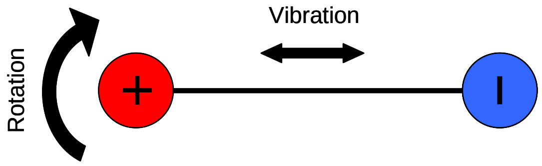

Figure 2.1. Representation of the rotational and vibrational movement of the CO molecule.

2.1.2.2 Vibrational states and transitions

At the IR region, the molecule vibration is what leads to the changes in electric dipole moment and the possibility to interact with light. The basic model for a diatomic vibration is the simple harmonic oscillator (SHO). This model assumes that two masses, m_1 and m_2, have an equilibrium separation distance r_e. The bond length, or separation distance between the masses, oscillates about the equilibrium distance as if the bond were a spring. Hooke's law describing linear spring forces can be applied for the SHO, with the force and the potential energy described as:

$$Force = -k_s\left(r - r_e\right) \qquad U = \frac{1}{2}k_s\left(r - r_e\right)^2 \tag{2.12}$$

where k_s is the spring constant. Such systems have a fundamental angular frequency of vibration, ω_e given by:

$$\omega_e = \sqrt{k_s / \mu} \tag{2.13}$$

As in the case of angular momentum, the vibrational state of a particle is quantized and, if we accept the results of quantum mechanics, the discrete values of the total energy for a vibrating diatomic are:

$$G(\upsilon) = \hbar\omega_e(\upsilon + 1/2) \tag{2.14}$$

which gives place to a constant value of energy between adjacent states of $\hbar\omega_e$.

2.1.2.3 Improved rotational and vibrational models: Non-Rigid Rotor and Anharmonic Oscillator

The models previously explained are simple models which may prove imprecise if excited rotational and vibrational states are taken into consideration. The non-rigid rotor and the anharmonic oscillator are better models for taking into account the interaction between both phenomena (rotation and vibration).

For the case of the non-rigid rotor, some modifications are applied to the previous rigid rotor analysis (Eq. (2.10)), in order to take into account the effects of the vibration phenomenon and the change in the mean distance to the center of mass of the molecules when changing the rotation state. Then the rotation-state energy formula becomes:

$$F_{\upsilon}(J)=B_{\upsilon}J(J+1)-D_{\upsilon}J^{2}(J+1)^{2} \tag{2.15}$$

where B_{υ} and D_{υ} are coefficients that depend on the vibrational state υ. So the energy difference between consecutive rotational states becomes:

$$\Delta F_{\upsilon,J\rightarrow J+1}(J)=2B_{\upsilon}(J+1)-4D_{\upsilon}(J+1)^{3} \tag{2.16}$$

In the case of the anharmonic oscillator, the potential model is very different from the harmonic oscillator as can be seen below; this is particularly important for excited vibrational states. Despite this change, the vibrational-state energy can be approximated with the energy of the harmonic oscillator plus some perturbations of higher order:

$$G(\upsilon)=\hbar\omega_{e}(\upsilon+1/2)-\hbar\omega_{e}x_{e}(\upsilon+1/2)^{2}+\ldots H.O.T. \tag{2.17}$$

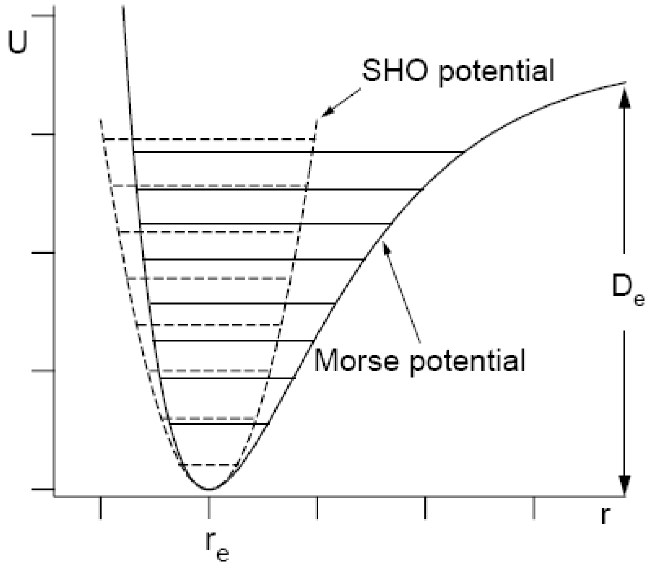

Figure 2.2. Morse potential model (solid line) compared to the simple harmonic oscillator model (SHO) (dashed line).

A much more realistic description of diatomic-molecule potential energy is given by the function known as Morse potential, which is shown in figure 2.2 and expressed as:

$$U=D_{e}\left(1-\exp\left(-\beta\left(r-r_{e}\right)\right)\right)^{2} \tag{2.18}$$

where D_{e} and β are coefficients that depend on the molecular structure. This means that the change of energy between consecutive vibrational states is no longer constant but a function of the vibrational state, in such a way that the energy increment between levels decreases as the energy approaches molecule dissociation energy, D_e:

$$\Delta G_{\upsilon \to \upsilon+1}(\upsilon) = \hbar\omega_e - 2\hbar\omega_e x_e(\upsilon+1) + \ldots H.O.T. \tag{2.19}$$

So finally, we will have some bands that will be determined by the vibrational state. On the one hand, there are the pure rotational bands where no vibrational state change takes place. However, these bands are located in the microwave zone and they are not of interest to us here. On the other hand, there are the vibrational-rotational bands where a change of both states takes place, normally with a unitary increase/decrease in both quantum numbers. In this case, the emission/absorption is produced in the infrared zone where they can be detected by using laser sources. Table 2.1 shows the values for the rotational and vibrational characteristic frequencies for some molecules [5].

Table 2.1. Characteristic vibrational energies for some diatomic species

Species	Rotational frequency [cm^{-1}]	Vibrational frequency [cm^{-1}]	Equilibrium distance [Å]
O_2	1.43768	1580.19	1.20753
N_2	1.99824	2358.57	1.09678
NO	1.67196	1904.20	1.15077
Cl_2	0.24392	559.717	1.98719

2.1.2.4 Electronic states and transitions

Electronic spectra involve transitions between different potential energy wells, each representing a different molecular electronic state, which have different electronic distributions. There are different potential energy wells for each different electronic state. All these wells illustrate the variation of electronic forces with internuclear spacing. As the electronic configurations change, the electronic forces change, and thus the shape of the potential wells changes.

Absorption and emission from one potential well to another is essentially instantaneous because the time involved to move or excite electrons is much shorter that the time required to move or excite nuclei during vibrations or rotations. The Franck-Condon principle sums up the relative characteristic time by approximating that the internuclear distance, r remains constant during an electronic transition. While the time to move/excite electrons is about 10^{-16} seconds, the typical time to change the nuclei vibrational state is about 10^{-13} seconds (higher times are needed in the case of rotations).

The absorption lines produced by electronic transitions are located in the ultraviolet zone, and so this study is not interested in this type of spectroscopy.

2.1.3 Radiative Transfer

The study of radiative transfer in the interaction between molecules and radiation can be used to obtain the absorption-lines strength [6], so this section analyses a generic two-state molecule in order to show how this and other values can be obtained.

Two states of the molecule which are radiatively coupled need to be considered, that is, the ground state 1 and the excited state 2. Between these states, there are basically three processes related to absorption, namely the spontaneous emission, the induced absorption and the induced emission. The transition rates due to each of these processes are:

$$\begin{aligned} \text{Spontaneous emission:} \quad & N_2 A_{21} \\ \text{Induced absorption:} \quad & N_1 B_{12} \rho(\nu) \\ \text{Induced emission:} \quad & N_2 B_{21} \rho(\nu) \end{aligned} \tag{2.20}$$

where N_i is the density of molecules in state i and $\rho(\nu)$ is the radiation spectral density. The coefficients A_{21}, B_{12} and B_{21} are known as the Einstein coefficients and they can be defined as:

B_{12}: Probability per second that a molecule in ground state exposed to radiation of spectral density $\rho(\nu)$ will absorb a quantum $h\nu$ and pass to the excited state.

B_{21}: Probability per second that a molecule in the excited state exposed to radiation of spectral density $\rho(\nu)$ will emit a quantum $h\nu$ and pass to the ground state.

A_{21}: Probability per second of spontaneous transfer from the excited state to the ground state with release of photon energy $h\nu$ (without regard to the presence of $\rho(\nu)$).

2.1.3.1 Equilibrium

When the system is at equilibrium, the rate of absorption transitions is equal to the rate of emission transitions. This fact can be expressed in some phenomenological relations that will help to calculate the Einstein coefficients. If we analyze the population change in the excited state, which is equal to zero in equilibrium, according to this kinetic strategy we have:

$$\dot{N}_2 = N_1 B_{12} \rho(\nu) - N_2 \left(A_{21} + B_{21} \rho(\nu) \right) = 0 \tag{2.21}$$

Another way to express the equilibrium condition is through the use of the Boltzmann fraction from statistical mechanics:

$$\frac{N_2}{N_1}=\frac{B_{12}\rho(\nu)_{eq}}{A_{21}+B_{21}\rho(\nu)_{eq}}=\frac{g_2}{g_1}\exp\left(-h\nu/kT\right) \tag{2.22}$$

Solving for $\rho(\nu)_{eq}$ in Eq. (2.22) and equating it to the known result of $\rho(\nu)_{eq}$ in the atmosphere, i.e. Planck's blackbody distribution,

$$\rho(\nu)_{eq}=\frac{8h\nu^3/c^3}{\exp\left(h\nu/kT\right)-1} \tag{2.23}$$

it gives:

$$\rho(\nu)_{eq}=\frac{A_{21}/B_{21}}{\frac{g_1}{g_2}\frac{B_{12}}{B_{21}}\exp\left(h\nu/kT\right)-1}=\frac{8h\nu^3/c^3}{\exp\left(h\nu/kT\right)-1} \tag{2.24}$$

Equation (2.23) must hold for all ν and T, producing the two following important conclusions:

$$g_1B_{12}=g_2B_{21} \qquad\qquad A_{21}=\frac{8h\nu^3}{c^3}B_{21} \tag{2.25}$$

A_{21} and hence B_{12} and B_{21} are calculable from quantum mechanics. However, in practice, A_{21} and B_{12} are measured.

2.1.3.2 Absorption and Emission in a strong-radiation submerged medium

As indicated before, the interaction between radiation and matter due to absorption is not produced between two "precise" energy states of the matter but between two bands that will define the shape of the absorption lines. This implies the analysis of matter-radiation interaction with respect to the frequency of this radiation.

From the general form for Beer-Lambert's Law (Eq. (2.2) and (2.3)), the line-absorption distribution can be defined along the frequency as the value of the absorbance in each frequency normalized by the integrated value of k_ν for all frequencies:

$$\phi(\nu)=\frac{k_\nu}{\int k_\nu d\nu} \tag{2.26}$$

So that:

$$\int_{line}\phi d\nu=1 \tag{2.27}$$

Then, we can apply this to the thermal equilibrium formula (2.21) and analyze the energy balance for an incremental gas slab dx, while dismissing the spontaneous emission factor due to the high level of radiation present in the medium. This gives us:

$$\frac{dI_\nu}{dx} = N_2\left[B_{21}\phi(\nu)I_\nu / c\right]h\nu - N_1\left[B_{12}\phi(\nu)I_\nu / c\right]h\nu \tag{2.28}$$

Therefore,

$$-\frac{dI_\nu}{I_\nu dx} = k_\nu = \frac{h\nu}{c}\left[N_1B_{12} - N_2B_{21}\right]\phi(\nu) \tag{2.29}$$

so we have an expression for absorbance as:

$$k_\nu = \frac{h\nu}{c}N_1B_{12}\left[1-\exp\left(-h\nu / kT\right)\right]\phi(\nu) \tag{2.30}$$

where k_ν is the spectral absorption coefficient from Beer-Lambert’s law. Integrating k_ν over the absorption line yields:

$$S_{12} = \int_{line} k_\nu d\nu = \frac{h\nu}{c}N_1B_{12}\left[1-\exp\left(-h\nu / kT\right)\right]\left[cm^{-1}s^{-1}\right] \tag{2.31}$$

where S_{12} is the integrated absorption for the absorption transition 1 → 2 or the line strength. Note that the quantity does not depend on lineshape and is simply a function of n_1, T and B_{12}. This quantity, like Einstein coefficients, is fundamental in nature. Another way to use it is by giving a version which is independent of the molecules concentration and would give us:

$$S_{12} = \frac{h\nu}{c}\frac{N_1}{N}B_{12}\left(1-\exp\left(-h\nu / kT\right)\right)[cm^{-1} / mol{\cdot}cm^{-2}] \tag{2.32}$$

where N is the total number of molecules in the incremental gas slab. It can be observed from this formula that temperature is the only variable in S_{12}. A correction of this aspect can be performed for the case of high-precision measurements taking into account the implicit dependence of n_1 on this variable.

2.1.4 Lineshapes

The lineshape reflects the relative variation of the absorption in a line along frequency:

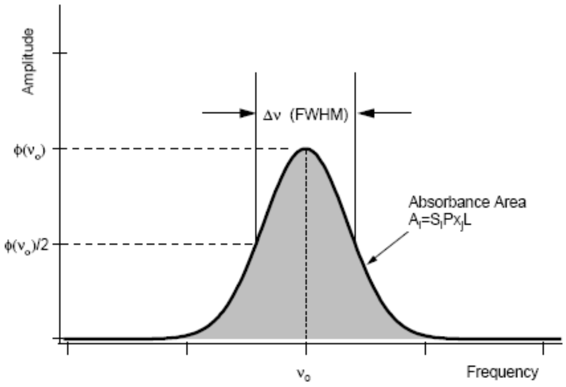

Figure 2.3. Spectral shape for a generic absorption line with different details

This can be defined as the quotient between the spectral absorption coefficient and the absorption line strength:

$$\phi(\nu) = \frac{k_\nu}{S_{12}} = [cm] \tag{2.33}$$

And its area is normalized to unity, so we have this expression:

$$\int_{-\infty}^{\infty} \phi(\nu)\, d\nu = 1 \tag{2.34}$$

Three different broadening mechanisms are present in the absorption lines due to three different causes, respectively, that perturb the transition energy levels: a) natural broadening; c) collisional broadening; c) Doppler broadening [7, 8].

2.1.4.1 Natural Broadening

The principle of uncertainty tells us that the uncertainty of the level energy times the electron lifetime cannot be smaller than the Planck constant.

$$\Delta E \tau \geq \frac{\hbar}{2\pi} \tag{2.35}$$

where τ is the lifetime of the level. Thus, in terms of frequency, we have:

$$\gamma \geq \frac{1}{4\pi}\left(\frac{1}{\tau'} + \frac{1}{\tau''}\right) \tag{2.36}$$

where γ corresponds to the absorption linewidth in the frequency domain. Then, the lineshape function can be derived by modeling the atomic system as a damped oscillator. It takes the form of a Lorentzian function:

$$\phi_N(\nu) = \frac{1}{\pi}\frac{\gamma_N}{(\nu - \nu_0)^2 + \gamma_N^2} \tag{2.37}$$

where γ_N is the so-called natural linewidth and the distribution has a maximum value at ν_0 of:

$$\phi_N(\nu_0) = \frac{1}{\pi\gamma_N} \tag{2.38}$$

2.1.4.2 Collisional Broadening

The lifetime of an energy level can be shortened due to perturbations that occur during collisions resulting from interactions between the species involved. According to Eq. (2.36), the shortening of a state lifetime leads to greater uncertainty, and thus a broader absorption lineshape. Thus the more likely collisions occur, the smaller the lifetimes and the broader the lineshapes.

If the diameters of molecules A and B are defined as σ_A and σ_B, the optical collision diameters are:

$$\sigma_{AB} = \frac{1}{2}(\sigma_A + \sigma_B) \tag{2.39}$$

Then the number of collisions per second of a single B for all A is given by:

$$Z_{AB} = N_A \pi \sigma_{AB}^2 \overline{c} \tag{2.40}$$

where N_A is the density of A molecules and $\overline{c}$ is the mean relative speed of the molecules. The total collision frequency is obtained by summing across the different species:

$$Z_B = \sum_A N_A \pi \sigma_{AB}^2 \overline{c} \tag{2.41}$$

Using Eq. (2.35) with $1/\tau' = 1/\tau'' = Z_B$, it follows that γ_C, the HWHM due to collisional broadening is given by:

$$\gamma_C = \frac{Z_B}{2\pi} \tag{2.42}$$

This gives us the pressure broadened line distribution with the next expression:

$$\phi_C(\nu) = \frac{1}{\pi}\frac{\gamma_C}{(\nu - \nu_0)^2 + \gamma_C^2} \tag{2.43}$$

An important factor to take into account is the linewidth dependence on temperature that is expressed in the next formula:

$$\gamma_C(T) = \gamma_C(T_0)\left(\frac{T}{T_0}\right)^n \tag{2.44}$$

where the n exponent is an empirical value.

2.1.4.3 Doppler Broadening

When a molecule has a velocity component with the same direction as the propagation of a beam of light, there will be a shift in the frequency at which it will absorb a photon. This effect is called the Doppler shift and appears both in the case of a net movement between the source and the gas under test, and in the case of the movement of the gas molecules themselves. The molecules of any gas are in constant movement and the distribution of random velocities can be explained by the Maxwellian distribution function. This Maxwellian distribution leads us directly to a lineshape function with a Gaussian form:

$$\phi_D(\nu) = \frac{1}{\gamma_D}\sqrt{\frac{\ln(2)}{\pi}}\exp\left[-\left(\frac{\nu-\nu_0}{\gamma_D}\right)^2\ln(2)\right] \tag{2.45}$$

where the Doppler function peak and HWHM, γ_D can be expressed as:

$$\phi_D(\nu_0) = \frac{1}{\gamma_D}\sqrt{\frac{\ln(2)}{\pi}}; \qquad \gamma_D = \nu_0\left[\frac{2\ln(2)kT}{mc^2}\right]^{1/2} \tag{2.46}$$

for which a more convenient form is:

$$\gamma_D = 3.581\times10^{-7}\nu_0\sqrt{\frac{T}{M}} \tag{2.47}$$

where T is given in Kelvin and M is the molecular weight expressed in grams/mole.

2.1.4.4 Voigt Profiles

When one of either broadening mechanisms is more intense than the other, that is, when the collisional-broadening halfwidth is much greater than Doppler-broadening or vice versa, an approximation can be applied where the smaller broadening factor is ignored and the lineshape is approximated by the greater broadening factor. Nevertheless there are many cases where both components are quantitatively similar and they need to be dealt with at the same time. In figure 2.4 we can observe the difference between a Gaussian and a Lorentzian function with the same halfwidth. The Gaussian function has a peak that is approximately 50% higher peak but, at the same time, drops off faster in the wings.

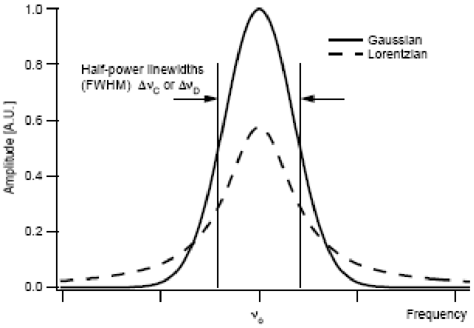

Figure 2.4. Comparative between Gaussian and Lorentzian lineshapes.

So, in this case when neither of the components can be neglected, the appropriate lineshape is a combination of the two. If we assume that the effects of Doppler and collisional broadening are decoupled, then each velocity class can be seen to be collisionally broadened. This leads to a lineshape which is a convolution of Doppler and collisional broadening:

$$\phi_V(\nu) = \int_{-\infty}^{+\infty} \phi_D(u)\,\phi_C(\nu - u)\,du \tag{2.48}$$

that can be expressed in a more convenient form as:

$$\phi_V(\nu) = \phi_D(\nu_0)\frac{y}{\pi}\int_{-\infty}^{+\infty} \frac{e^{-t^2}}{y^2 + (x-t)^2}\,dt \tag{2.49}$$

where:

$$x = \frac{\nu - \nu_0}{\gamma_D}\sqrt{\ln 2}\,; \qquad y = \frac{\gamma_L}{\gamma_D}\sqrt{\ln 2}\,; \qquad t = \frac{u}{\gamma_D}\sqrt{\ln 2} \tag{2.50}$$

There are a number of efficient polynomial expansion solutions [9, 10] to calculate this Voigt-function peak value and its HWHM.

Table 2.2. Parameter description for the calculation of absorption line strengths and widths

Parameter	Description
$\nu_{\eta\eta'}$	Spectral line transition frequency [cm^{-1}].
$S_{\eta\eta'}$	Spectral line intensity [cm^{-1}/(molecule·cm^{-2})] at $\mathrm{T_{ref}} = 296\,K$
γ_{air}	Air-broadened halfwidth at half maximum (HWHM) [cm^{-1}/atm] at $\mathrm{T_{ref}} = 296\,K$ and reference pressure $\mathrm{P_{ref}} = 1\,atm$
γ_{self}	Self-broadened halfwidth (HWHM) [cm^{-1}/atm] at $\mathrm{T_{ref}} = 296\,K$ and reference pressure $\mathrm{P_{ref}} = 1\,atm$

2.1.5 HiTran Database and formulas

For our experiments we have used data from the HITRAN database which is one of the most well known and used databases for atmospheric chemistry [11, 12]. The data used to calculate the line strengths and widths are given in table 2.2.

Other parameters can be used for a more precise estimation of these parameters and their dependence on temperature and pressure. However, the objective was not the precision of the technique but using it correctly so that it could be applied to a lidar system for gas detection. Moreover, the calculation of the parameters used was carried out with the help of the *HiTran Program*, where temperature corrections are automatically applied. The selected wavelengths and the parameters obtained fixing the temperatures at 296 ºK are as follows:

Table 2.3. CO, CO_2 and H_2O absorption lines parameters.

Gas Molecule	CO	CO_2	H_2O
$\nu\left[cm^{-1}\right]$	6334.430	6334.465	6647.218
$\lambda\left[cm\right]$	1578.674	1578.665	1504.389
$S_{\eta\eta'}\left[cm^{-1}/\left(molec\cdot cm^{-2}\right)\right]$	$1.392\cdot 10^{-23}$	$1.622\cdot 10^{-23}$	$1.662\cdot 10^{-23}$
$\gamma_{air}\left[cm^{-1}/atm\right]$	0.0667	0.0740	0.0965
$\gamma_{self}\left[cm^{-1}/atm\right]$	0.0748	0.1020	0.4850

An approximate representation of the lines which were studied is illustrated in the graphic below:

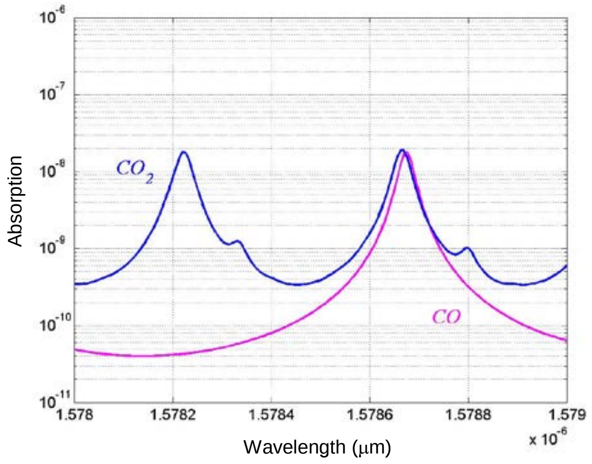

Figure 2.5. Absorption spectrum of CO and CO_2 around 1.5785 um.

Finally, the formulas for the line-parameters calculation indicated by HiTran are given below. They have been used to obtain the total absorption, the width and the shape of the absorption lines used in the experiments,

$$\gamma\left(p,T\right)=\left(\frac{T_{ref}}{T}\right)^{n}\cdot\left(\gamma_{air}\left(p_{ref},T_{ref}\right)\cdot\left(p-p_{s}\right)+\gamma_{self}\left(p_{ref},T_{ref}\right)\cdot p_{s}\right)\approx$$
$$\approx\gamma_{air}\left(p_{ref},T_{ref}\right)\cdot\left(p-p_{s}\right)+\gamma_{self}\left(p_{ref},T_{ref}\right)\cdot p_{s} \qquad (2.51)$$

$$f\left(\nu,\nu_{\eta\eta'},T,p\right)=\frac{1}{\pi}\cdot\frac{\gamma\left(p,T\right)}{\gamma\left(p,T\right)^{2}+\left[\nu-\left(\nu_{\eta\eta'}+\delta\left(p_{ref}\right)\cdot p\right)\right]^{2}}\approx\frac{1}{\pi}\cdot\frac{\gamma\left(p\right)}{\gamma\left(p\right)^{2}+\left(\nu-\nu_{\eta\eta'}\right)^{2}} \qquad (2.52)$$

$$\alpha=S_{\eta\eta'}\cdot f\left(\nu_{\eta\eta'}\right)\cdot L\cdot C_{g} \qquad (2.53)$$

where C_g corresponds to the gas concentration.

2.1.6 Gas-cell and open-path measurements

Once the characteristics of the absorption lines to be investigated were defined, they needed to be analyzed in terms of how they behave in two different cases with respect to the gas concentration to be measured. These cases are the measurement using a gas cell with 100% concentration of the gas under detection and the measurement in an open path environment.

If we assume we are trying to examine ideal gases, then the following formula is applied:

$$PV=nRT \qquad (2.54)$$

where P is the gas pressure, V is the volume containing the gas, n is the number of moles of gas and R is the universal gas constant. If we reorder the terms, we can define the concentration of the gas as the number of molecules per volume unit. This gives us:

$$C_{g}=\frac{nN_{A}}{V}=\frac{PN_{A}}{RT} \qquad (2.55)$$

being N_A the Avogadro constant. Then, applying Eq. (2.52) and (2.55) to Eq. (2.53), we obtain:

$$\alpha=\frac{S_{\eta\eta'}Lp_{s}N_{A}}{\pi RT}\frac{1}{\gamma_{\mathrm{air}}\left(p-p_{\mathrm{s}}\right)+\gamma_{\mathrm{self}}\ p_{\mathrm{s}}} \qquad (2.56)$$

Here we must distinguish between two cases:

Case 1 – Gas cell:

In this case, the pressure of the gas under measurement is essentially equal to the total pressure, so the expression for the linewidth and the absorption is:

$$\gamma\left(p=p_S\right)=\gamma_{\text{self}}\cdot p_S=\gamma_{\text{self}}\cdot\frac{C_g}{N_A}\cdot R\cdot T \qquad \alpha_{Max\_Cell}=\frac{S_{\eta\eta'}LN_A}{\pi RT\gamma_{\text{self}}} \tag{2.57}$$

Case 2 – Open Path:

In this case, the pressure of the gas under measurement is much smaller than the total pressure, so the expression for the linewidth and the absorption is:

$$\gamma\left(p=p_S\right)=\gamma_{\text{air}}\cdot p \qquad \alpha_{OP}=\frac{S_{\eta\eta'}LC_g}{\pi\gamma_{\text{air}}p} \tag{2.58}$$

In view of the previous results, we observe that for the gas cell measurement (Eq. (2.57)) the linewidth is proportional to the concentration while the absorption peak is invariant with this respect (Fig. 2.6.a). In contrast, for the open path measurement (Eq. (2.58)), the absorption peak is proportional to the concentration value while the linewidth is invariant (Fig. 2.6.b). So a different evolution of the absorption lines must be expected for each case.

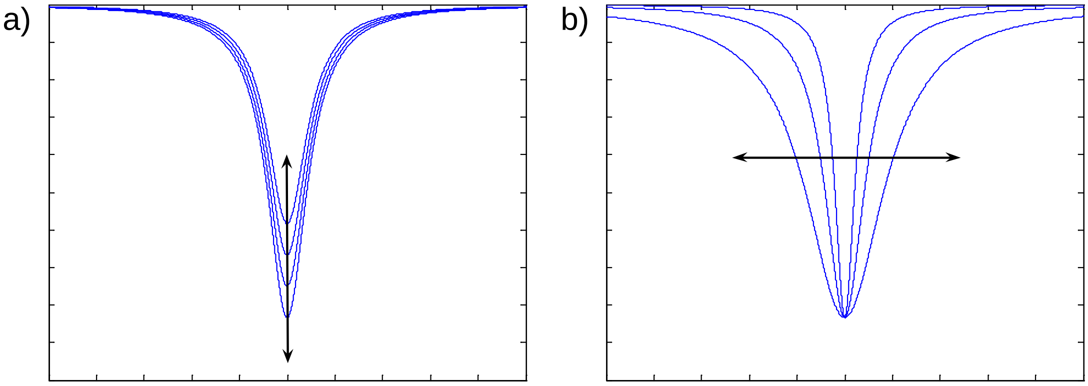

Figure 2.6. Variation of the absorption line depending on the value of gas concentration for open path (a) and for a gas cell (b).

2.2 Spectroscopy techniques for gas detection

Assuming that the absorption lines to be detected are approximately Lorentzian in atmospheric conditions and, in general, in the experiment conditions, there are two variables that will completely define the detected gas concentration, namely, the peak absorption and the linewidth. This section first discusses direct absorption measurement in order to obtain an approximated estimation of the concentration in the gas cells analyzed in the experiments. The wavelength modulation methods are then set out, and in particular wavelength modulation spectroscopy (WMS) is studied from a theoretical perspective and experimentally tested in the next chapter. This is one of the components of the gas-measurement frequency-modulated continuous-wave (FMCW) technique presented in this thesis.

2.2.1 Direct Absorption Measurement

As stated earlier, the first method which will be explained here is the direct absorption measurement. In this method, a laser beam is focused into the sample under study and then detected after it has passed through a path which is long enough in the gas sample. The laser frequency is linearly swept along a range of frequencies around the absorption line to be detected. The result of this sweep can be seen in figure 2.7, where the receiver power has been plotted as a function of the swept range. A linear function is represented with the Lorentzian function superimposed in the zone where the absorption line is located.

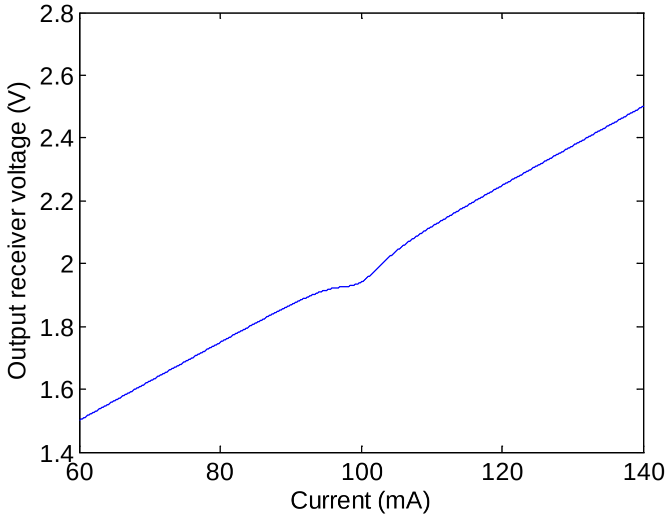

Figure 2.7. Sweep of current in a laser diode along a gas absorption line.

If we then divide the function obtained by the linear background function, we obtain the curve shown in figure 2.8 which is the Lorentzian function we are looking for. The analysis of its characteristics, that is, the peak value and the linewidth gives us the information we need to obtain the concentration measurement, as seen in the previous section.

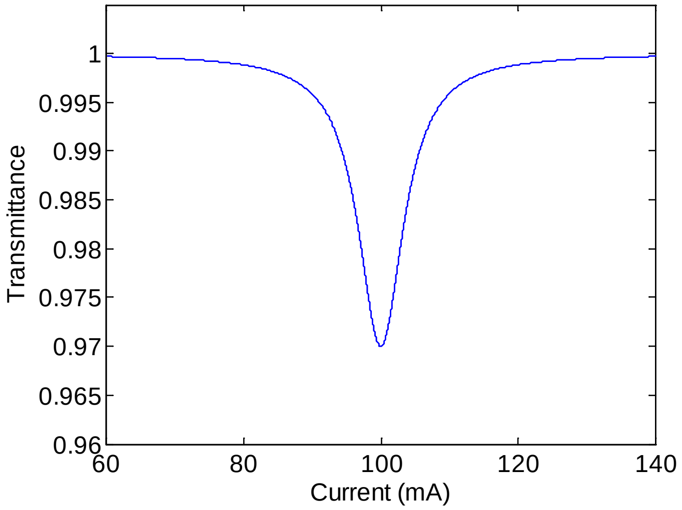

Figure 2.8. Resulting Lorentzian profile of a gas absorption line after extracting the power linear background profile.

2.2.2 Wavelength Modulation Techniques

Direct measurement of the absorption is the easiest method in cases in which a large gas concentration is available, but not for detecting and measuring gas traces in the atmosphere. The possibility of modulating the input current of the laser emerged as a method for the measurement of wavelength-related characteristics to overcome the problems of DC measuring that appear when performing direct detection, such as the presence of a background signal and the DC noise.

Frequency or wavelength modulation in laser spectroscopy is a commonly used technique for gas detection [13 - 18]. As this is a differential method it is not affected by baseband noises and drifts and so it has much better resolution than direct detection methods. These methods can be understood from two points of view: temporal and spectral. Frequency modulation methods produce an amplitude modulation through scanning the absorption line with a frequency modulated signal (Fig. 2.9). These techniques cause two (or more) side components to appear in the spectrum of the laser signal. The absorption of these components is a function of the position of the laser spectral main peak with respect to the position of the gas absorption line and, by using mathematical analysis it may be possible to show that this differential absorption can be used to determine sensitive measurements of gas concentrations.

The operation mode relies on the modulation of the bias current of the laser. Excepting a constant, the wavelength of a laser diode is actually proportional to the input current. This means that an amplitude modulation in the input current is converted into both amplitude and frequency modulation in the output laser-diode signal because the output power of the optical signal is also proportional to the laser input current. Temperature change also can be used to center the emission line with respect to the absorption line wavelength.

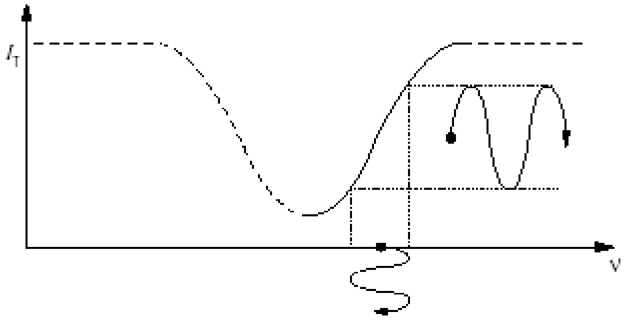

Figure 2.9. Amplitude modulation produced by frequency modulation in an absorption line [17].

Depending on the characteristics of this frequency modulation we can talk in terms of Wavelength Modulation Spectroscopy or Frequency Modulation Spectroscopy (FMS) (Fig. 2.10). Although the philosophy behind both techniques is basically the same, it is common to distinguish between them depending on the value of two parameters: the modulation frequency of the carrier and the modulation index. In order to obtain good performance, the product of modulation frequency and modulation index must be of the order of the linewidth. So the two extreme cases define the two frequency modulation methods.

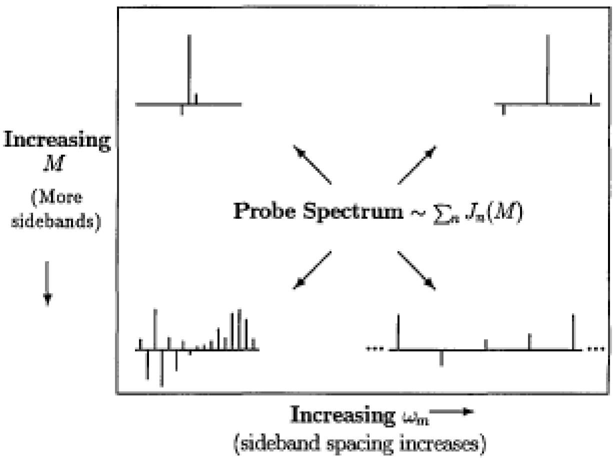

Figure 2.10. Spectrum of a frequency modulated signal with respect to modulation index and frequency [17].

We talk of FM spectroscopy when the modulation index is low and the modulation frequency is high [14]. In this case, the modulation frequency is so high that the side tones of the modulation frequency are separated by a frequency distance comparable to the width of the line under study. If we look at the figure 2.10 graphic, the FMS case would be the situation in the top right corner. In general, only one or few FM side tones interact with the absorption line at a time. This allows one to perform a theoretical analysis of the response from the point of view of the electric field of the wave that is being emitted [17].

This technique requires modulation frequencies of the optical carrier much higher (of the order of hundreds of MHz or even GHz) than those used in the WMS technique, which makes it somewhat more difficult to implement. By way of compensation, intensity noise and low-frequency noise are greatly reduced. The result for the first harmonic level evolution, in the case of a frequency sweep, is shown qualitatively in the top right in figure 2.10.

We talk of WMS spectroscopy when the modulation index is high and the modulation frequency is low. Because of this low modulation frequency, a high modulation index must be used for the frequency deviation to be similar to the absorption line width. The large number of side tones that interact with the absorption line makes the calculus from the point of view of electric field practically impossible. So the response of the absorption line is calculated theoretically working with optical intensity [13, 16 - 18]. This technique is less demanding technologically because the modulation at levels of kilohertz or even some megahertz of laser diodes is easy to achieve. Unfortunately, using this technique generates significant low-frequency noise levels. A qualitative representation of the first harmonic level evolution is shown in the bottom left in figure 2.11.

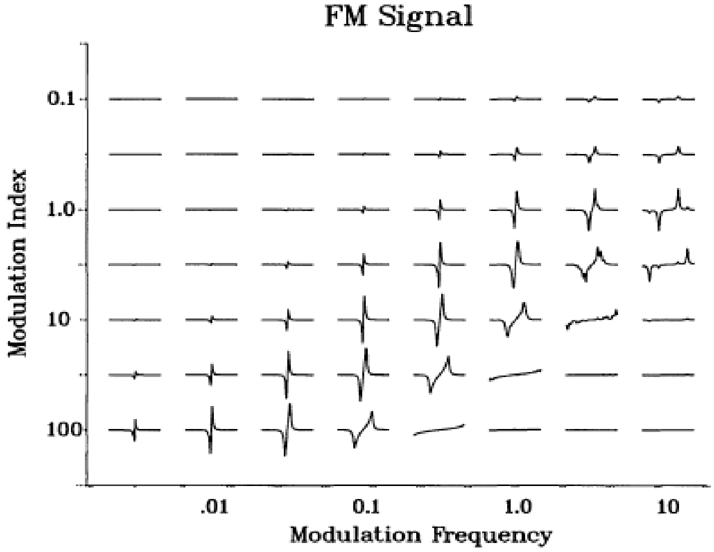

Figure 2.11. First harmonic level evolution with respect to the central wavelength [17].

2.2.3 WM Spectroscopy

As seen in section 2.2.2, in the WM Spectroscopy technique the incident-light spectrum is composed of a large number of harmonics that interact with the absorption line. The resulting signal is usually described by analyzing the fundamental tone and the 2nd harmonic of the output signal [13, 16].

The intensity $I(\nu)$ of an electromagnetic wave with a frequency ν that travels through a path L in the presence of a gas can be defined as:

$$I(\nu) = I_0(\nu)e^{-\alpha(\nu)L} \tag{2.59}$$

$I_0(\nu)$ being the incident intensity and $\alpha(\nu)$ the gas absorption coefficient at frequency ν. If we take into account that the total absorption is small $\alpha(\nu)L \leq 0.05I(\nu)$, we can make the following approximation:

$$I(\nu) = I_0(\nu)[1-\alpha(\nu)L] \tag{2.60}$$

In order to obtain the output signal and study the different harmonics, the laser current input is modulated with a sinusoidal signal that will give rise to a modulation in the laser frequency with an amplitude α and an angular frequency ω:

$$\nu(t) = \nu_L + a\cos\omega t \tag{2.61}$$

ν_L being the central frequency of the laser. Then, assuming the absorption line shape is Lorentzian, we have an absorption of:

$$\alpha(v) = \frac{1}{1+\left[\frac{v(t)-v_0}{\Delta v}\right]^2} \tag{2.62}$$

v_0 being the absorption-line central frequency and Δv the half width at half maximum (HWHM) of the absorption line. Then we can define two normalized parameters in order to simplify this expression:

$$x = \frac{v_L - v_0}{\Delta v} \qquad\qquad m = \frac{a}{\Delta v} \tag{2.63}$$

Applying Eq. (2.63) to Eq. (2.62), the expression of the absorption can be written as:

$$\alpha(x,m,t) = \frac{1}{1+(x+m\cos\omega t)^2} \tag{2.64}$$

this being equivalent to a function defined as $S(x,m,t) = G(x+m\cos wt)$ with $G(x)$, the Lorentzian function defined as $G(x) = 1/(1+x^2)$. By performing a Fourier series development, $S(x,m,t)$ can be expressed as:

$$S(x,m,t) = \sum_{n=0}^{\infty} S_n(x,m)\cos n\omega t \tag{2.65}$$

$S_n(x,m)$ being the coefficients of the Fourier series with the next expression:

$$S_n(x,m) = \frac{1}{2}\cdot\frac{1}{m^n} \in_n i^n \frac{\left\{\left[(1-ix)^2+m^2\right]^{\frac{1}{2}}-(1-ix)\right\}^n}{\left[(1-ix)^2+m^2\right]^{\frac{1}{2}}} + c.c \tag{2.66}$$

$$\in_0 = 1,\ \in_n = 2\ (n = 1...\infty)$$

By using Eq. (2.66) we can obtain the curves of the different harmonics needed to study the absorption lines. In this case, only the 1st and 2nd harmonic will be used.

2.2.3.1 Curves for the 1st harmonic

The curve for the 1st harmonic maximum-value evolution with respect to m [13, 16] is obtained using the expression (2.66) for $n = 1$:

$$S_1(x,m) = 2\cdot\mathrm{Re}\left\{\frac{1}{m}\cdot i\cdot\frac{\left[(1-ix)^2+m^2\right]^{\frac{1}{2}}-(1-ix)}{\left[(1-ix)^2+m^2\right]^{\frac{1}{2}}}\right\} \tag{2.67}$$

For each value of the modulation index m and for a range of values of x, the different figures of the first harmonic amplitude $S_1(x)$ were obtained as shown in Fig. 2.12.

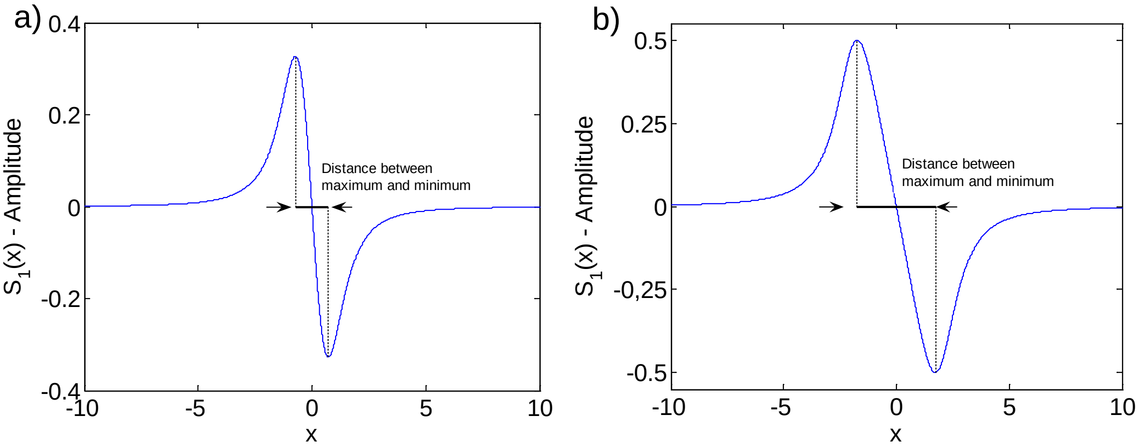

Figure 2.12. 1st harmonic amplitude, $S_1(x)$ along the normalized optical frequency position x for the case of $m = 0.6$ (a) and $m = 2$ (b). The m parameter corresponds to the normalized modulation index.

The maximum amplitude points (both negative and positive) of $S_1(x)$ are located at:

$$x_{\max} = \pm 3^{-\frac{1}{2}} \left[\left(4 + 3m^2\right)^{\frac{1}{2}} - 1 \right] \tag{2.68}$$

Allowing for this:

$$S_1(x_{\max}) = \frac{3^{\frac{1}{2}}}{2m} \cdot \frac{(4+3m^2)^{\frac{1}{2}} - 2}{\left[(4+3m^2)^{\frac{1}{2}} - 1 \right]^{\frac{1}{2}}} \tag{2.69}$$

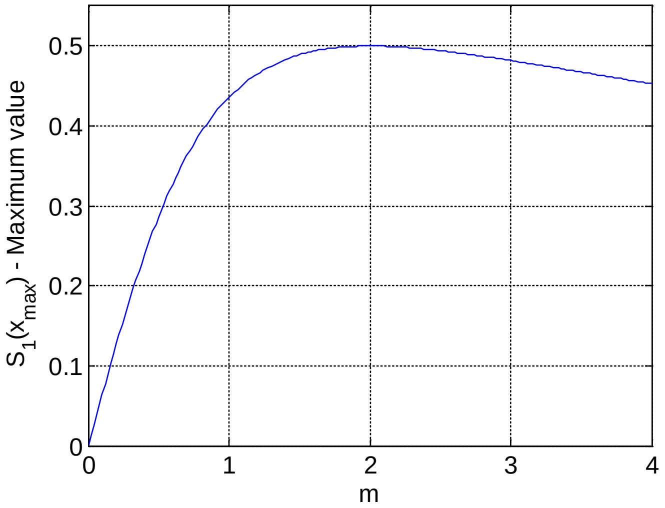

Figure 2.13. Theoretical curve of 1st harmonic maximum-value evolution with respect to m.

$S_1\left(x_{\max}\right)$ reaches the maximum for $m_{\max}=2$ with an amplitude value of $S_1\left(x_{\max}\right)_{\max}=\pm 0.5$. Then, if the maximum value of the 1st harmonic curve is depicted for each value of m, the curve of the 1st harmonic maxima is obtained (Fig. 2.13).

Another variable to analyze is the distance between the curve extremes depending on the modulation index m, as indicated in figure 2.12. If we plot this function, we obtain:

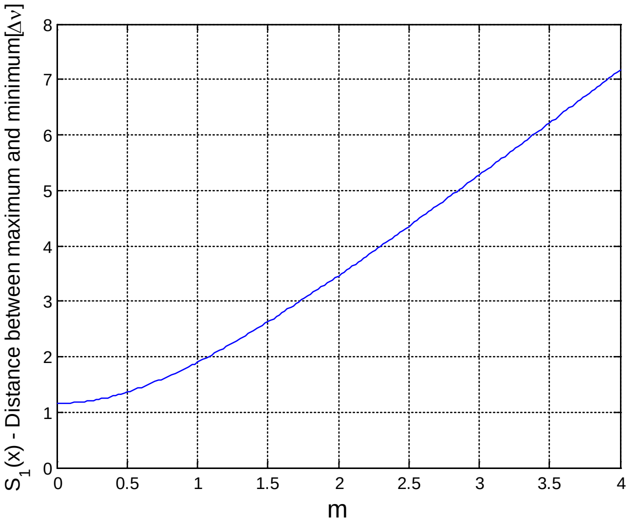

Figure 2.14. Curve of the distance between maximum and minimum of the 1st harmonic as a function of the modulation index

2.2.3.2 Curves for the 2nd harmonic

The 2nd harmonic data [13, 16] can be obtained using Eq. 2.66 with $n=2$:

$$S_2(x)=2\cdot\mathrm{Re}\left\{-\frac{1}{m^2}\cdot\frac{\left\{\left[(1-ix)^2+m^2\right]^{\frac{1}{2}}-(1-ix)\right\}^2}{\left[(1-ix)^2+m^2\right]^{\frac{1}{2}}}\right\} \tag{2.70}$$

The different curves of the 2nd harmonic $S_2\left(x\right)$ are obtained for a given modulation index m and for a range of values x as in the precedent $S_1\left(x\right)$ case (Fig. 2.15).

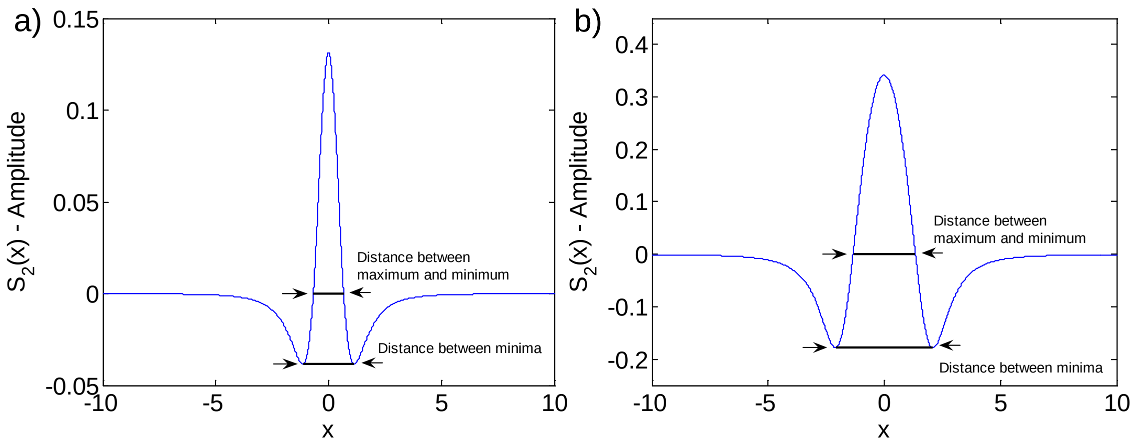

Figure 2.15. 2^{nd} harmonic amplitude, $S_2(x)$ along the normalized wavelength position x for the case of $m = 0.6$ (a) and $m = 2$ (b)

The maximum value of the 2^{nd} harmonic signal occurs at the center of the absorption line, that is, when $\nu_L = \nu_0$ (Fig. 2.15). Applying this value in Eq. (2.70), we obtain a function of maximum values in the 2^{nd} harmonic:

$$S_2(0) = \frac{2}{m^2}\cdot\left(2-\frac{2+m^2}{(1+m^2)^{\frac{1}{2}}}\right) \tag{2.71}$$

This equation reaches its maximum value at $m_{\max} = 2.197$ with an amplitude of $S_2(0)_{\max} = -0.343$. If for each value of m the 2^{nd} harmonic maximum value is plotted, the 2^{nd} harmonic maxima curve is obtained (Fig. 2.16).

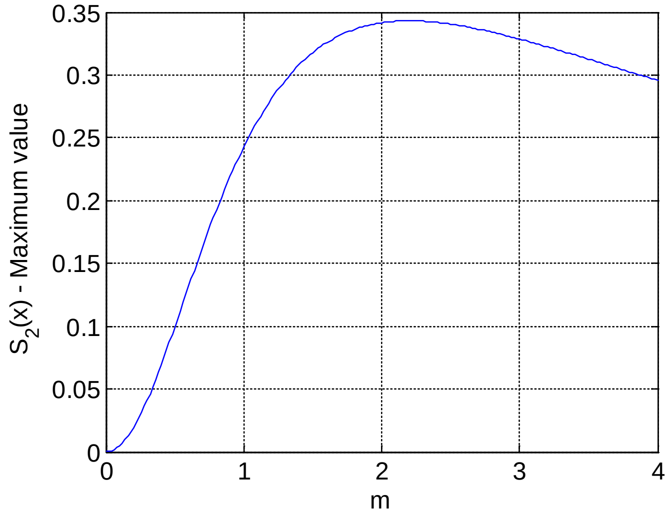

Figure 2.16. Theoretical curve for 2^{nd} harmonic maximum-value evolution as a function of m.

2^{nd} harmonic curves always show two zero crossings, and these crossings are always located between the minimum-maximum and maximum-minimum values. The difference of these values for each m gives the 2^{nd} harmonic distance-between-zeros curve (Fig. 2.17) as a result.

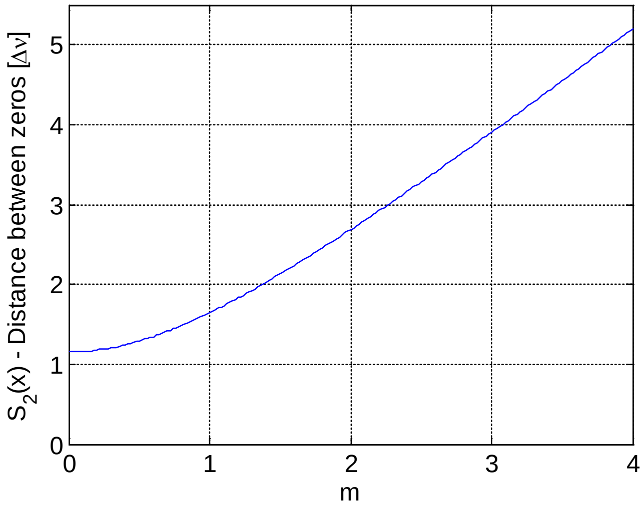

Figure 2.17. 2nd harmonic distance-between-zeros curve as a function of m.

Another useful function to better characterize the 2nd harmonic is the R-curve, which is defined as the quotient between the 2nd harmonic maximum-value and the minimum-value, for each concrete m value. This function is represented in figure 2.18.

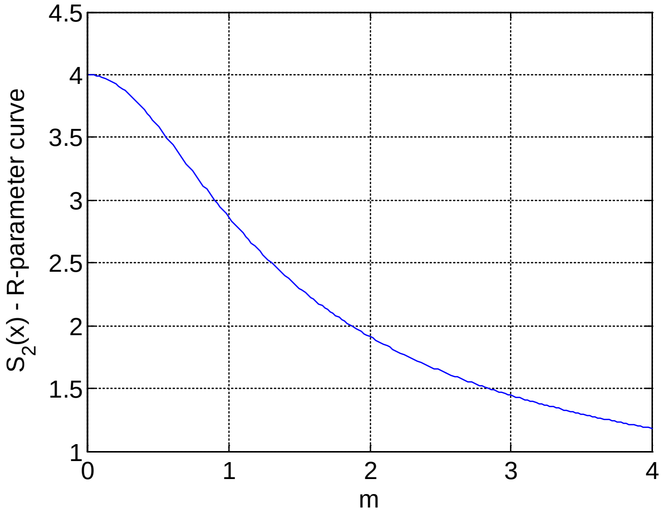

Figure 2.18. 2nd harmonic R-curve as a function of m.

One more function we are going to use in the measurement of gas concentration using the WMS technique is shown in figure 2.19. It is the 2nd harmonic curve peak-to-peak amplitude value along the different values of m.

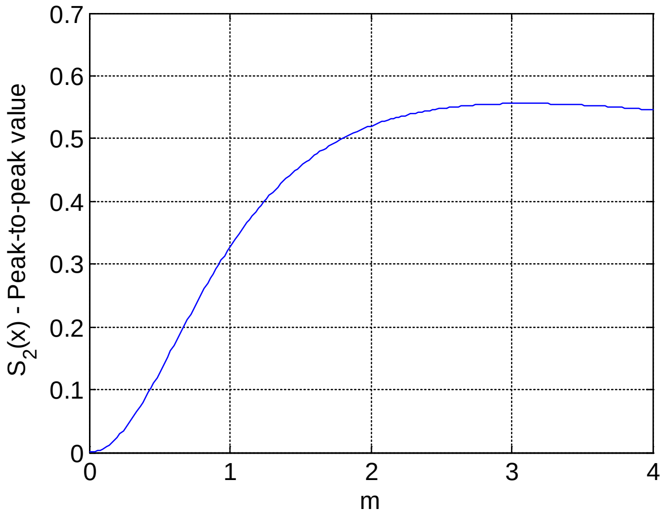

Figure 2.19. 2^{nd} harmonic peak-to-peak value as a function of m.

Finally, the last curve employed in these developments is the distance-between-minima curve, which is defined as the representation of the 2^{nd} harmonic distance between minima for all the different values of m and plotted as function of this last value, as shown in figure 2.20. This function as well as the previous one (Fig. 2.19) are independent of the position of the zero-amplitude level which is a very useful feature as we will see below.

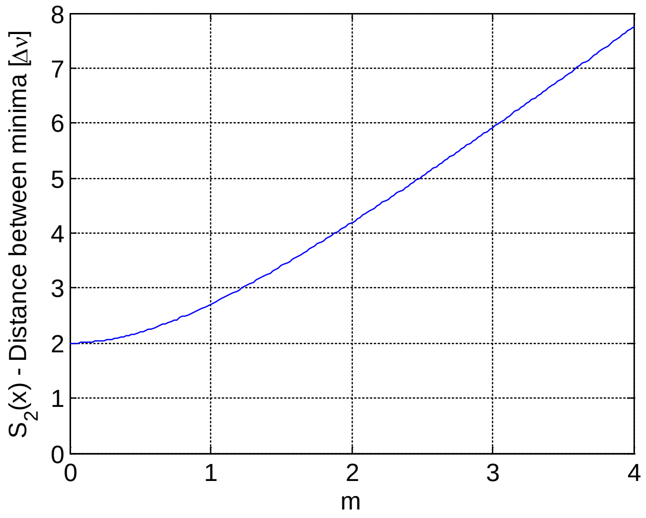

Figure 2.20. 2^{nd} harmonic distance-between-minima curve as a function of m.

List of variables of chapter 2	
E_{tot}	Total internal energy
E_{rot}	Rotational internal energy
E_{vib}	Vibrational internal energy
E_{elec}	Electronic internal energy
ν	Optical frequency
T_ν	Fractional transmission at frequency ν
I	Optical intensity
I_0	Initial optical intensity
k_ν	Spectral absorption coefficient
L	Absorption path length
S_i	Transition strength
ϕ	Lineshape function
P_i	Partial pressure of the absorption species
A_ν	Fractional absorption at frequency ν
F_i	Fraction of molecules in energy level i
n_i	Molecules in energy level i
n	Total molecules
g_i	Degeneracy level
ε_i	Number of individual states with a common energy
k	Boltzmann constant
T	Temperature
Q	Partition function
Q_{rot}	Rotational partition function
Q_{vib}	Vibrational partition function
Q_{elec}	Electronic partition function
J	Rotational quantum number
υ	Vibrational quantum number
$\vec{p}$	Electric dipole moment
q_i	Particle charge
$\vec{r}_i$	Location vector
T_{rot}	Rotational temperature
m_i	Mass of atom i
r_e	Equilibrium separation distance
I	Moment of inertia
μ	Reduced mass
ω	Rotation angular frequency
$\hbar$	Reduced planck constant
B	Rotational constant
U	Potential energy

k_s	Spring constant
ω_e	Angular frequency of vibration
r	Internuclear distance
ω_e	Fundamental angular frequency of vibration
$F_\upsilon(J)$	Rotation-state energy
B_υ, D_υ	Vibrational coefficients
$\Delta F_{\upsilon,J\rightarrow J+1}(J)$	Energy difference between consecutive rotational states
$G(\upsilon)$	Vibrational-state energy
x_e	Anharmonicity correction factor
$H.O.T.$	Higher order terms
D_e and β	Coefficients depending on the molecular structure
$\Delta G_{\upsilon\rightarrow\upsilon+1}(\upsilon)$	Energy difference between consecutive vibrational states
N_i	Density of molecules in state i
A_{21}	Spontaneous-emission Einstein coefficient
B_{12}	Induced-absorption Einstein coefficient
B_{21}	Induced-emission Einstein coefficient
$\rho(\nu)$	Radiation spectral density
$\dot{N}_i$	Population density change in state i
h	Planck constant
I_ν	Optical intensity at frequency ν
ΔE	Uncertainty of the level energy
τ	Electron lifetime
γ	Absorption linewidth
γ_N	Natural linewidth
ν_0	Absorption-line central optical frequency
σ_i	Diameter of molecule i
σ_{AB}	Optical collision diameter between molecules A and B
Z_{AB}	Number of collisions per second of a single B for all A
$\bar{c}$	Mean relative speed of molecules
Z_B	Total collision frequency
γ_C	HWHM due to collisional broadening
$\phi_C(\nu)$	Pressure-broadened line distribution
γ_D	HWHM due to doppler broadening
$\phi_D(\nu)$	Temperature-broadened line distribution
M	Molecular weight

$\phi_V(\nu)$	Voigt line distribution
$\gamma(p,T)$	Absorption-line width
$f(\nu,\nu_{\eta\eta'},T,p)$	Absorption line shape
α	Line peak absorption
C_g	Gas concentration
P	Pressure of gas
V	Volume containing the gas
R	Universal gas constant
N_A	Avogadro constant
v_L	Laser central frequency
x	Relative point of modulation
m	Modulation index
$S_n(x,m)$	Harmonics of the modulated optical signal after interacting with a Lorentzian absorption line

3 Experimental gas detection with WMS

The theoretical analysis performed in Chapter 2 on the gas absorption lines and the WMS technique has been tested in various experiments. The results show the capabilities of the WMS systems for measuring gas concentration in atmosphere-like environments and the possibilities this technique has for gas detection in a more complex system by combining it with the FMCW technique, as will be shown in chapter 4. This chapter explains the characteristics of the laser used for the measurements, introduces the direct-detection gas followed by the experiments performed using the WMS technique and compares both results.

3.1 Laser-diode characterization

Wavelength-modulation spectroscopy methods take advantage of wavelength tunability through the modulation of an injection current in laser diodes. In these experiments, some DFB laser diodes with the help of their modulation capabilities are used to extract the characteristics of an absorption-line for the gas under analysis.

The main characteristics that will be described here are the intensity modulation and the frequency/wavelength modulation features, both of which are produced by the current modulation of the laser diode. In figure 1, we can see the typical evolution of the intensity modulation, IM_{LD} along the injection-current modulation frequency. The device response is almost constant up to some gigahertz where a resonance peak appears and then the response falls dramatically.

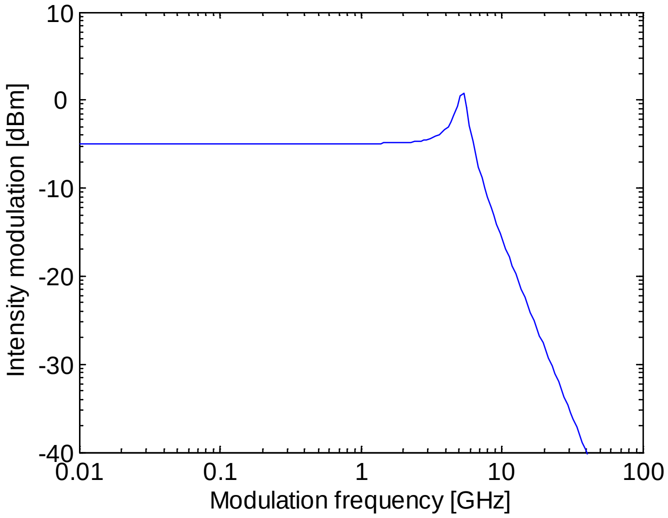

Figure 3.1. Intensity modulation as a function of modulation frequency for a DFB laser diode.

The frequency-modulation response, FM_{LD} of the laser diode due to changes in the input current, is directly related to the intensity-modulation response, IM_{LD} as shown in Eq. (3.1)

$$FM_{LD} = \alpha\left(j\omega + \omega_g\right) IM_{LD} / \left(2P_0\right) + C_{th} / \left(1 + j\omega / \omega_{th}\right) \tag{3.1}$$

where ω is the current modulation frequency, ω_g the adiabatic cutoff frequency, α the linewidth enhancement factor, IM_{LD} the intensity-modulation response plotted in the previous graphic, P_0 the input power, C_{th} the thermal FM coefficient and ω_{th} the thermal cutoff frequency. In this equation, two different terms appear to the right side of the equal sign. The first is the "carrier-induced tuning" that is directly related to intensity modulation. It shows frequency-independent behavior up to the adiabatic cutoff frequency (~1 GHz) and then starts rising until it reaches the resonance peak (~5 GHz) after which it drops off (Fig. 3.2 – red line). The second is the "temperature-induced tuning" which is a low-pass characteristic, smooth up to some hundreds of kilohertz where the pole starts acting and the response falls.

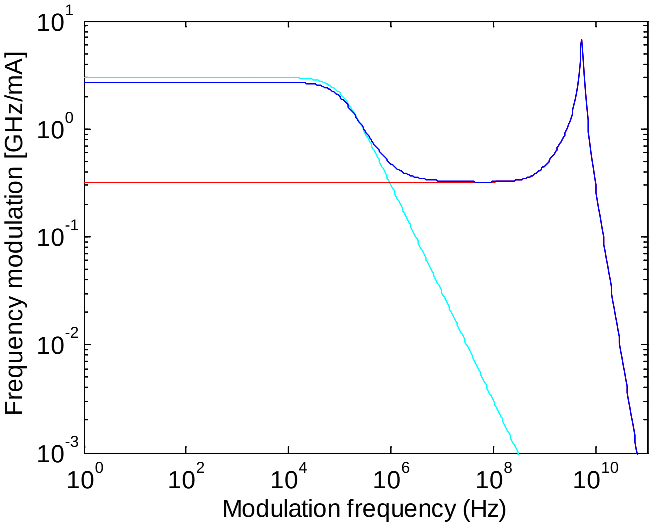

Figure 3.2. Frequency tuning as a function of modulation frequency for a DFB laser diode due to temperature effects (cyan), carrier effects (red) and joint effects (blue).

The combined action of both terms is shown in blue (Fig. 3.2). The initial zone up to some hundreds of kilohertz is quite significant for the WMS technique where low modulation frequencies are used. It is also important to pay attention to the behavior up to some tens of megahertz. The change in the response for this specific zone is important for the FMCW method explained in the following chapters where a constant response would be desirable. Moreover, a slight reduction of the joint response in the low frequencies can be observed, which is due to the opposed signs of both components.

Usually it is not easy to find the wavelength modulation characteristic for a commercial laser. In our case, we have decided to perform an analysis of this feature with respect to both current and temperature. The measurements where performed by selecting a number of points and then measuring the corresponding wavelength (Fig. 3.3). The results show a proportional dependence on wavelength with respect to both temperature and current.

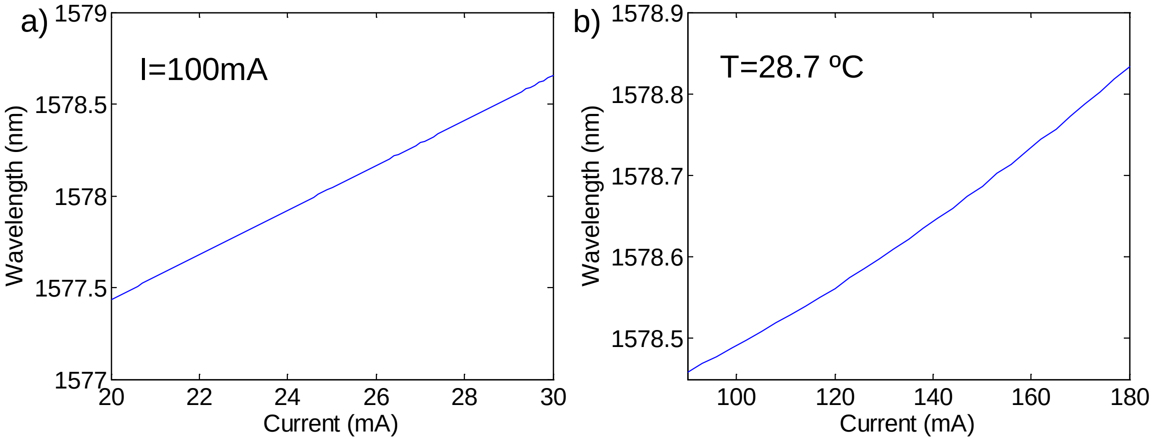

Figure 3.3. Wavelength evolution with temperature and current in a laser diode. The laser is a JDS-Uniphase DWDM-DFB laser diode at 1578 nm.

The most important variable to be extracted from these graphics is the Current/Wavelength derivative for each single current value. This indicates how much the laser output is modulated with respect to the input-current modulation and thus how broad the line under test is in terms of input current. Performing this analysis in DC mode indicates how this response will be up to some hundreds of kilohertz, as can be seen in figure 3.2. This is fundamental in order to establish the linearity of the system when measuring an absorption line and to understand some of the errors that appear in the detection process. Figure 3.4 shows this characteristic for two different lasers at 1578 nm (blue line) and 1504 nm (red line), respectively. Looking only at these graphics one can say that the linearity of the 1504-nm laser will be superior to the linearity of the 1578-nm laser for a wavelength motion of similar length. The characteristics of both lasers can be observed in table 3.1.

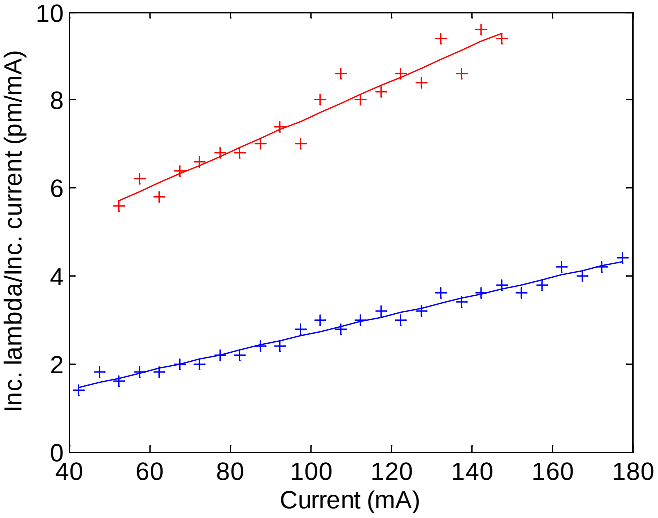

Figure 3.4. First derivative of the wavelength evolution with respect to the input current. The lasers under tests are (blue) a JDS-Uniphase DWDM-DFB laser diode at 1578 nm and (red) a NEL laser diode at 1504 nm designed for gas detection.

Table 3.1. Power and wavelength-shift characteristics of JDSU and NEL lasers

DFB Laser Type	Power @ 100 mA	dλ/dT (pm/ºC)	dλ/dI (pm/mA) @ 100 mA
JDS-Uniphase CQF975/208	21 mW	122	2.77
NEL NLK1556STG	23 mW	147	7.63

3.2 Experimental setup

The experimental setup used for the measurement of gas concentration using WMS technique is shown in figure 3.5.

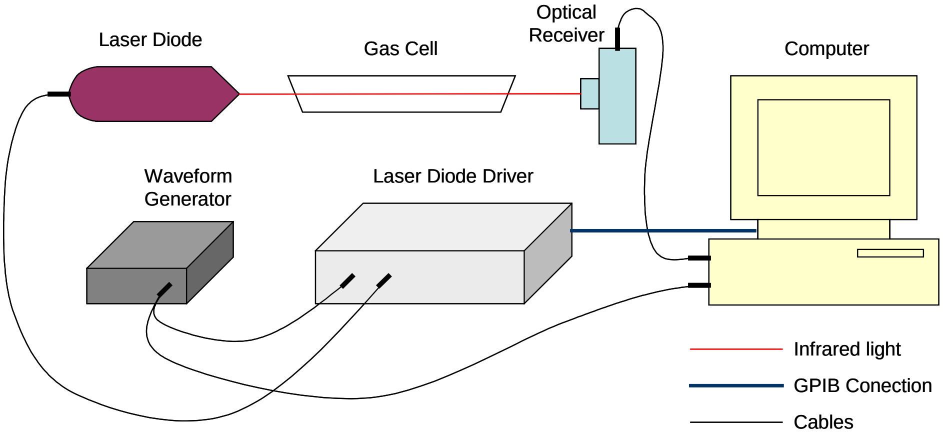

Figure 3.5. Experimental scheme of the WMS with a gas cell

The system is composed of a DFB laser diode plus its corresponding laser diode driver, the waveform generator that gives a sinusoidal signal for the laser modulation, the gas cell with the gas under study, the optical receiver and a computer that acquires and processes the signal.

The system operation consists of the emission of a wavelength-modulated beam across the gas cell in order to gauge its gas concentration. The waveform generator gives a sinusoidal signal to the driver which combines it with a bias current through a bias-T. This current is sent to the laser diode which emits a light signal modulated both in intensity and in frequency. This frequency modulation is responsible for the interaction with the gas absorption line that gives rise to different harmonics used to determine the gas concentration value. After this interaction, the light is detected in the optical receiver and acquired by the computer where it is processed. With the help of the original modulation signal and by means of a lock-in filtering process, the harmonics of the detected signal are measured and the absorption line characteristics, both amplitude and width, are extracted. Analyzing these data, the concentration of the gas under test is obtained. The characteristics of the cells under analysis are as follows:

Table 3.2. Characteristics of the gas cells under test.

Gas Cell	Gas type	Pressure	Purity	Length
Thorlabs	CO_2	200 Torr	99.75%	15 cm
Sacher-Laser 1	CO_2	600 Torr	99.75%	15 cm
Sacher-Laser 2	CO	600 Torr	99.75%	15 cm

3.3 Direct detection of gas

Before the WMS results were analyzed, another method was applied to offer an initial approximation of the concentration measurements. The Direct-detection method consists of applying a linear sweep to the laser input current which produces a linear frequency modulation as well as a parasite power sweep in the output light signal. By gauging the gas under test with this signal and detecting the power at the output of the gas cell, the absorption line appears superimposed on the laser output power as can be observed in figure 3.6.a. This figure also clearly shows the power sweep in the estimated reference background (red line) where the gas effect has been removed

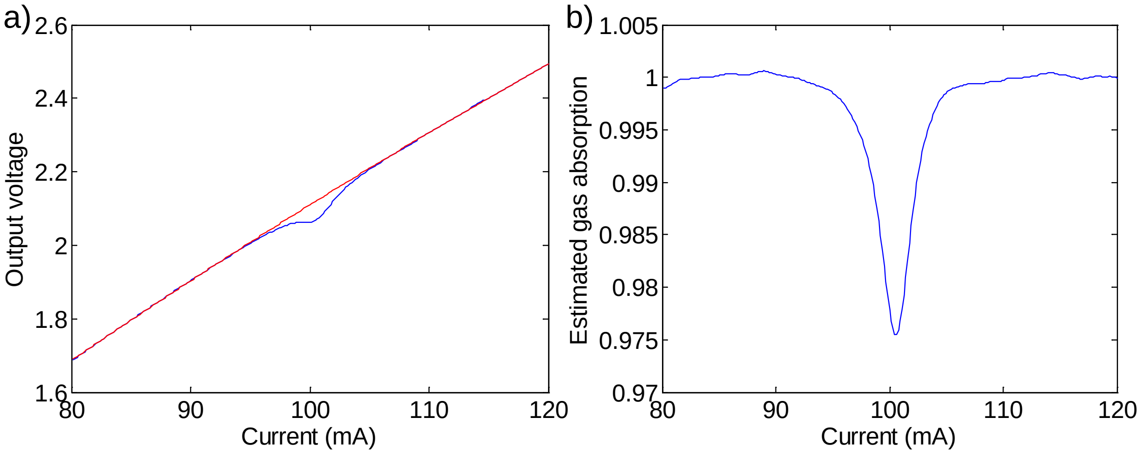

Figure 3.6. (a) Output-power voltage (blue) and reference background (red) after linear sweep and (b) output-power voltage divided by the reference background for the case of the Sacher gas cell with CO.

The gas concentration is calculated by finding the width and amplitude parameters of the absorption-line Lorentzian shape that minimize the total square error. This error is obtained by performing a 2nd order polynomial approximation of the resulting background after extracting the gas absorption effects. Then the Lorentzian-shape characteristics will be used to obtain the concentration of the gas present in the sample.

The steps for the error calculation in the minimization process would be as follows:

1. Choose certain values of amplitude and width for the Lorentzian-shaped absorption and divide the obtained data by this supposed absorption shape.
2. Perform a second order approximation of the remaining background
3. Calculate the distance (error) between the smoothed data and the background approximation, that is, the second-degree polynomial approximation for the background.

The aim of this method is to minimize this resulting error to give the best approximation of the Lorentzian shape. Then the characteristics of this Lorentzian function are used to extract the gas concentration value.

After performing this optimization process, we can compare the results obtained from the system with the optimized data. In figure 3.8 we can see (green) the measurement after extracting the 2nd order background, (red) the Lorentzian approximation and (blue) the residual background after extracting both the 2nd order background and the Lorentzian function for the case of the CO Sacher gas cell. The error in the amplitude and width values is less than 5% (Fig. 3.9).

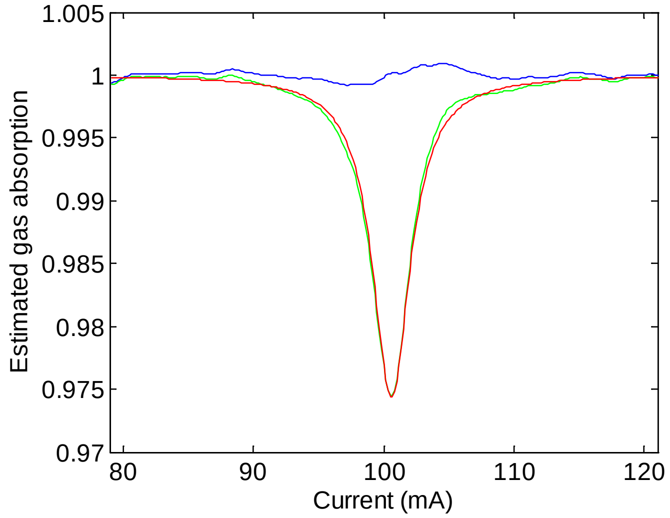

Figure 3.8. Comparison between simulated absorption line (red), output power after extracting the simulated background (green) and residual background (blue) for the case of the Sacher gas cell with CO.

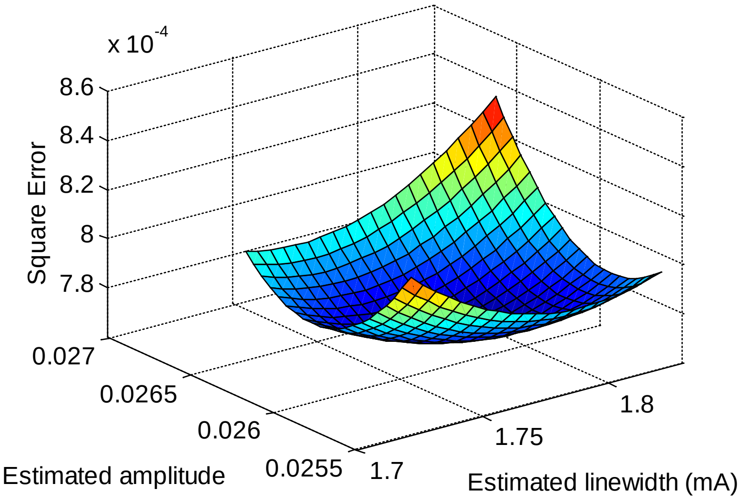

Figure 3.9. Error graphic with respect to Lorentzian-function amplitude and width, without fixing the peak absorption amplitude in the computer algorithm for the case of the Sacher CO cell.

Finally, the data corresponding to three different gas cells is shown in table 3.3.

Table 3.3. Direct-detection gas concentration analysis without fixing the peak absorption.

Gas Cell	Amplitude	Width (mA)	Width (cm^{-1})	Concentration (Torr)
Sacher CO	0.0261 ± 8E-4	1.675 ± 0.09	0.0496	516 ± 28
Sacher CO_2	0.01075 ± 5E-4	0.76 ± 0.035	0.0225	195 ± 9
Thorlabs	0.0102 ± 1.1E-3	1.735 ± 0.35	0.0514	447 ± 90

The theoretical values of width and concentration were obtained with Eq. (3.57) in the previous chapter, which can be rewritten in the next form in order to calculate the theoretical width and absorption for each cell correctly:

$$\gamma\left(p = p_S\right) = \gamma_{\text{self}} \cdot p_S = \gamma_{\text{self}} \cdot \frac{C_g}{N_A} \cdot R \cdot T \qquad \alpha_{Max\_Cell} = \frac{S_{\eta\eta'} L N_A}{\pi R T \gamma_{\text{self}}} \tag{3.57}$$

where γ_{self} is the absorption-line self broadening, p_S is the gas partial pressure in the cell, C_g is the gas concentration, N_A is the Avogadro number, R is the gases constant, T is the temperature, $S_{\eta\eta'}$ is the spectral line intensity and L is the gas cell length.

Moreover, in order to pass from width in mA (specific of this laser) to width in cm^{-1}, the following formula (Eq. (3.2)) needs to be applied, where the current-wavelength ratio in the central position of the absorption line dλ/dI and the frequency-wavelength ratio at the specific wavelength used by the system are taken into account.

$$\gamma_{CALC}\left(p = p_S\right) = \gamma_{\text{I}} \cdot \frac{\mathrm{d}\lambda}{dI} \cdot \frac{10^{10}\left[cm^{-1} pm\right]}{\lambda^2\left[pm^2\right]} \tag{3.2}$$

If we take a look at the amplitude values found in the data processing, we can observe that they do not have the theoretical value of 1.22% for the case of CO_2 and 2.92% for the case of CO. This is due to the error during the measurement process. Another way of analyzing data is by fixing these absorption theoretical values and finding the width value that minimizes the error. The obtained data are shown in table 3.4.

Table 3.4. Direct-detection gas concentration analysis fixing the peak absorption.

Gas Cell	Amplitude	Width (mA)	Width (cm^{-1})	Concentration (Torr)
Sacher CO	0.0292	1.535 ± 0.18	0.0454	473 ± 55
Sacher CO_2	0.0122	0.68 ± 0.08	0.0201	175 ± 21
Thorlabs	0.0122	1.49 ± 0.40	0.0441	383 ± 103

In this case, the amplitude of the absorption line was fixed at the nominal value but, as expected, the width values which are proportional to the gas concentration have changed by approximately 10%. This is one possible approximation to adjust the absorption lines characteristics, but some other sources of error such as the length of the tube or detector's linearity can affect this amplitude value and change it from the expected one.

A mismatch between nominal and real values is found in some cells particularly in the 2nd and 3rd cell. This might be due to an error in the gas cell manufacturing process, because the measurements indicate a quite small error compared to the manufacturer's values which differ significantly. Other errors may be present but the magnitude of the total error leads us to consider this possibility. Nevertheless, this hypothesis should be confirmed by measurements using an independent method. The observed values will be confirmed with the analysis using the WMS technique.

The background estimation could be the main source of error in these measurements, and some of the causes which could explain this are the interaction of light with the actual gas-cell cavity and the receiver behavior. In the case of the former, some rebounds in the interior of the cell and the non symmetry of the optical windows can cause certain interference in the output signal. In the case of the latter, the non-linearity of light conversion depending on the incident intensity can cause the output signal to vary.

3.4 WMS gas detection

After performing a detailed analysis of the WMS technique (chapter 3) and having obtained some results from the DC detection technique (previous section), the data obtained in the lab were analyzed and the capability of the WMS technique to perform gas measurements with high precision was confirmed.

3.4.1 Data acquisition and processing

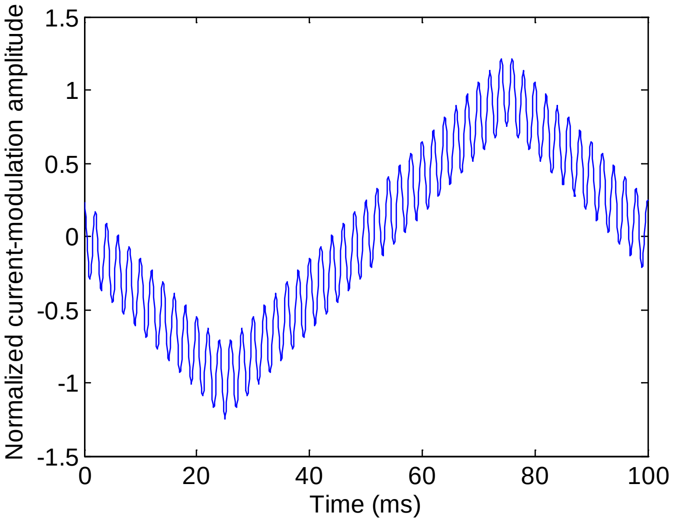

Figure 3.10. Representation of the sinusoidal modulation mounted on a linear sweep as the WMS sounding signal.

The measurements were carried out as indicated in section 3.2 and the data obtained after applying lock-in filtering were the 1st and 2nd harmonic curves as well as the DC sweep function. This last element was used to calibrate the measurements and obtain the amplitude data. The modulation signal is that given in figure 3.10, comprising the addition of a ramp function and a sinusoid.

After gauging the medium, this signal is acquired and lock-in filtered with a sinusoid of the corresponding fundamental and 2nd harmonic frequencies. A phase delay was applied in order to maximize both 1st and 2nd harmonic quadrature signals as shown in figure 3.11. The 1st and 2nd harmonic measurements were measured both in phase and quadrature. Figures 3.11.a and 3.11.b show the 1st harmonic measurement and figures 3.11.c and 3.11.d show the 2nd harmonic measurement. The presence of the absorption-line effects in the quadrature component is clear, while the in-phase component is almost smooth.

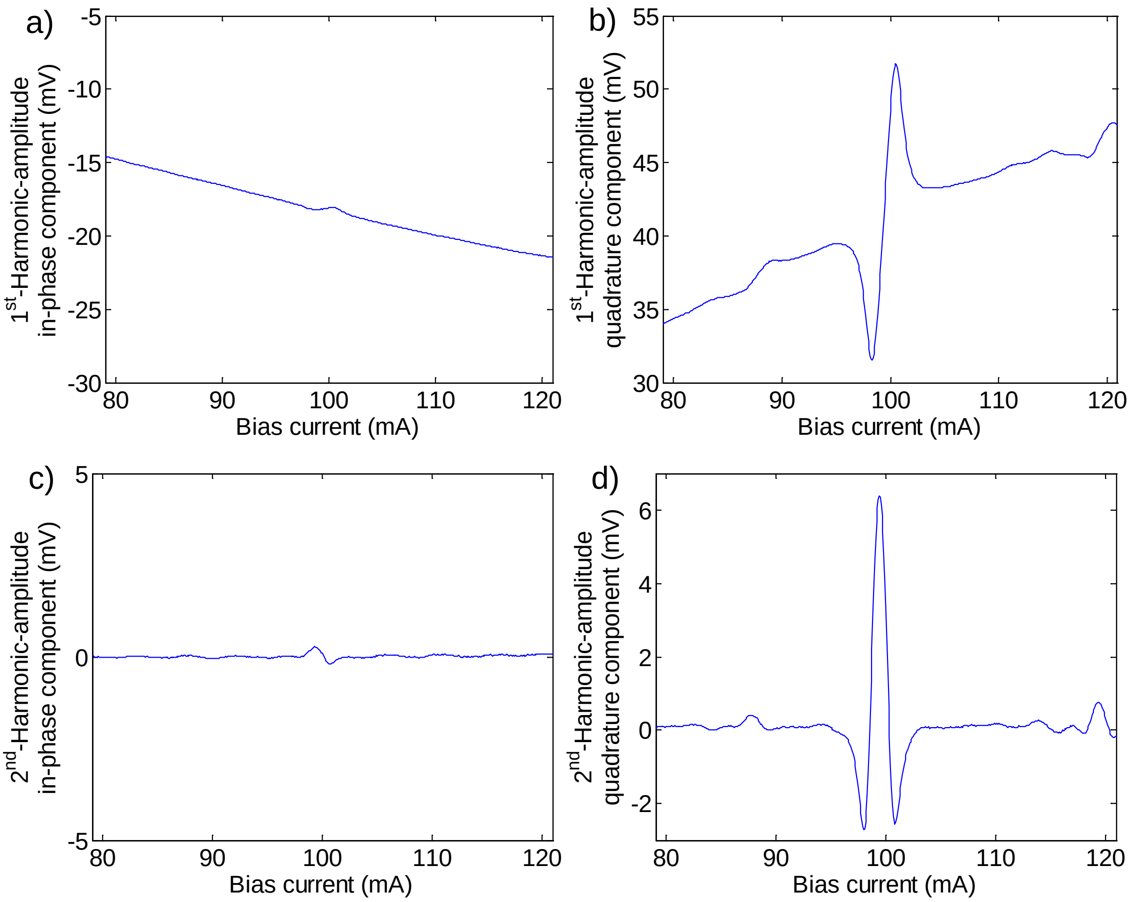

Figure 3.11. Results obtained from the in-phase (a) and quadrature (b) 1st harmonic amplitudes and the in-phase (c) and quadrature (d) 2nd harmonic amplitudes from the analysis of the CO_2 Sacher gas cell with a 3 mA-modulation current.

3.4.2 Results for the measurement of gas cells (CO and CO_2)

Once the harmonics curves were obtained, the results were analyzed and the different analyses explained in the last chapter were performed to test the validity of these results. First, the 1st and 2nd harmonic maxima are represented in two graphics as a function of the modulation voltage (Fig. 3.12) and the values co-adjusted in order to reduce the combined error (Fig. 3.13). The results show a high level of agreement with the theoretical curves.

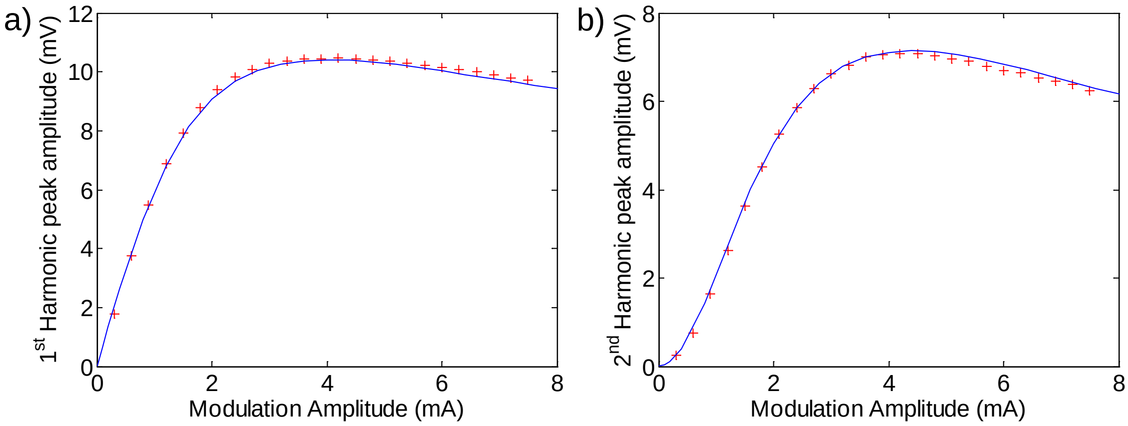

Figure 3.12. Maximum values of 1st harmonic (left) and 2nd harmonic (right) measurements for the Sacher CO_2 gas-cell case. The red points show the measurements while the solid blue line represents the adjusted curve.

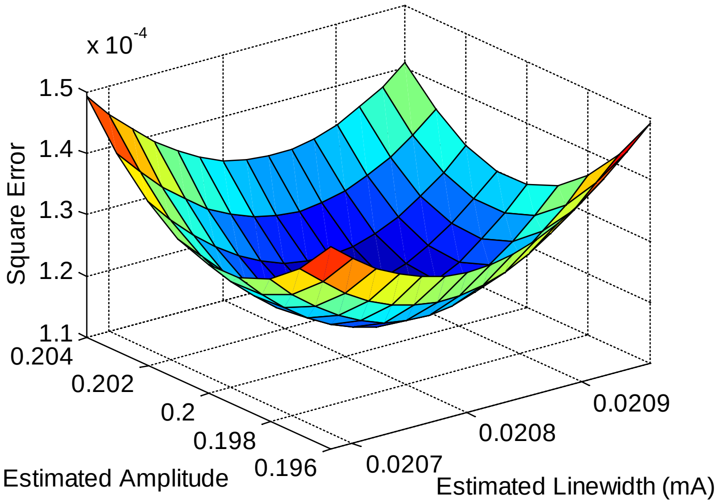

Figure 3.13. Error curve obtained while minimizing the distance between 1st and 2nd harmonic peak-values curves and the simulated ones with respect to linewidth and amplitude for the case of CO_2 in a gas cell.

Other graphics can be plotted which help us to confirm the measurements. In this case, the distance between extremes in the 1st harmonic and the zero-crossing-points distance for the 2nd harmonic are shown (Fig. 3.14). The graphics show a large degree of agreement between results and simulation. Some errors can be found in the left part of the curves due to the low signal levels in this zone especially in the 2nd harmonic data.

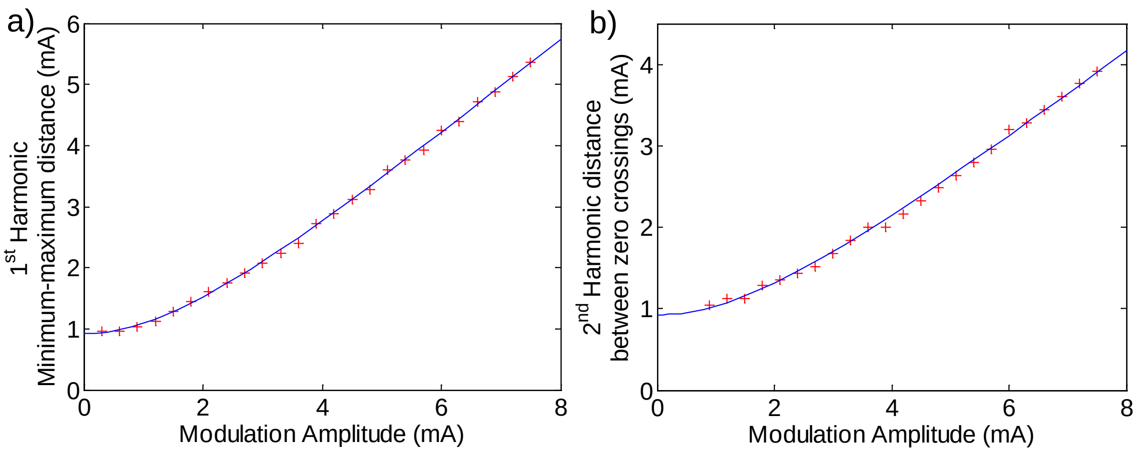

Figure 3.14. Evolution of the distance between extremes of the 1st harmonic (left) and the zero-crossing-points distance in the 2nd harmonic (right) for the Sacher CO_2 gas-cell case. The red points show the measurements while the solid blue line indicates the adjusted curve.

Two more graphics prove useful for this validation: first, the distance between minima of the 2nd harmonic, and second, the peak-to-peak value of the 2nd harmonic. Both help to test the previous 2nd harmonic curves because they are independent of the zero-crossing position. Errors in the location of the zero-crossing points can limit the effectiveness of the previous 2nd harmonics curves, both the peak value and the zero-crossing distance ones, but the following curves can overcome these problems (Fig. 3.15).

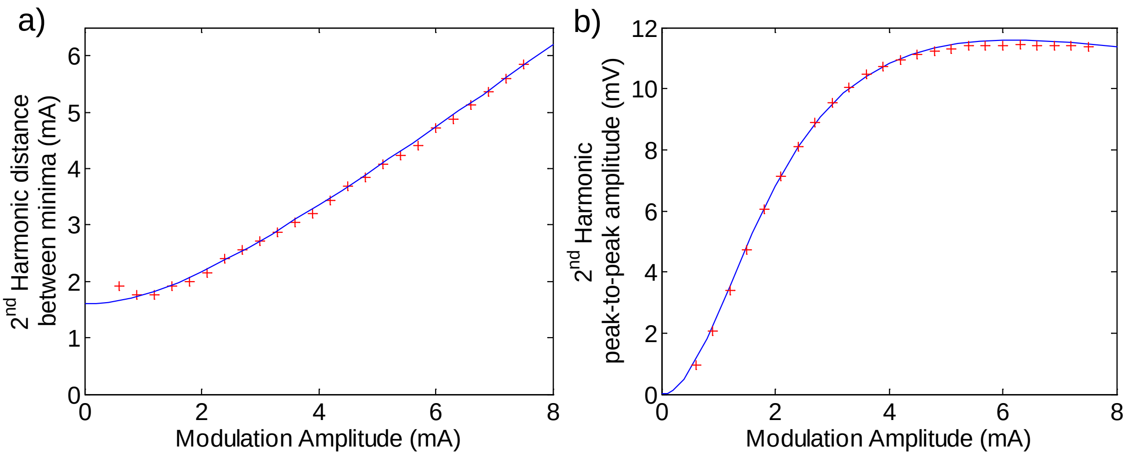

Figure 3.15. Evolution of the distance between minima (left) and peak-to-peak value (right) of the 2nd harmonic for the Sacher CO_2 gas-cell case. The red points show the measurements while the solid blue line indicates the adjusted curve.

A summary of the data adjusted to the physical values is shown in the following table:

Table 3.5. Results of the gas concentration measurements of the CO and CO_2 gas cells.

Gas Cell	Amplitude	Width (mA)	Width (cm^{-1})	Concentration (Torr)
Sacher CO	0.0280 ± 1.7E-4	1.775 ± 0.03	0.0525	544 ± 9
Sacher CO_2	0.0110 ± 7.5E-5	0.800 ± 0.016	0.0237	206 ± 4
Thorlabs	0.0113 ± 5E-5	1.808 ± 0.024	0.0535	464 ± 6

The amplitude data has been obtained by applying the condition that for $m = 2$, the 1st harmonic amplitude *WMS_1H* is equal to 0.5 times the absorption peak. So applying Eq. (3.3) we obtain the following value that confirms the validity of the method.

$$WMS\_peak\_value = \frac{2 \cdot WMS\_1H}{\overline{V\_out}} \tag{3.3}$$

In this equation, V_out corresponds to the detector output DC value at the center of the absorption line. The total error in these measurements is about 1% in width and 1.5% in amplitude.

Comparing the results obtained in the DC-detection case and the WMS case, a certain difference in amplitudes can be observed. Otherwise, the width differences between them are around 5%, except for the case of the Sacher CO_2 cell where a difference of some 15% appears between both cases. This shows that different sources of error are present in the measurements but the results are mutually coherent.

Nevertheless, there are two facts that appear to indicate that these measurements are correct: first, there is the correct matching between the theoretical curves and the results obtained with errors less than 2%; second, the high level of similitude between the theoretical width values and the experimental ones for the open path case with errors which are also less than 2%. This seems to indicate that the measurements were performed correctly and the width data are valid. Otherwise, problems can arise while calculating the amplitude value due to problems of scaling or other problems related to the equipment used to perform the measurements. These should be resolved in the future in order to obtain better results.

3.4.3 Results for the open path measurement (CO_2 and H_2O)

The WMS method was applied to detecting gases in open path with low levels of absorption, when it is much more sensitive than the direct detection method. The case of CO_2 and H_2O concentration in the air was studied, and an example of 1st and 2nd harmonic graphics can be seen in figure 3.16.

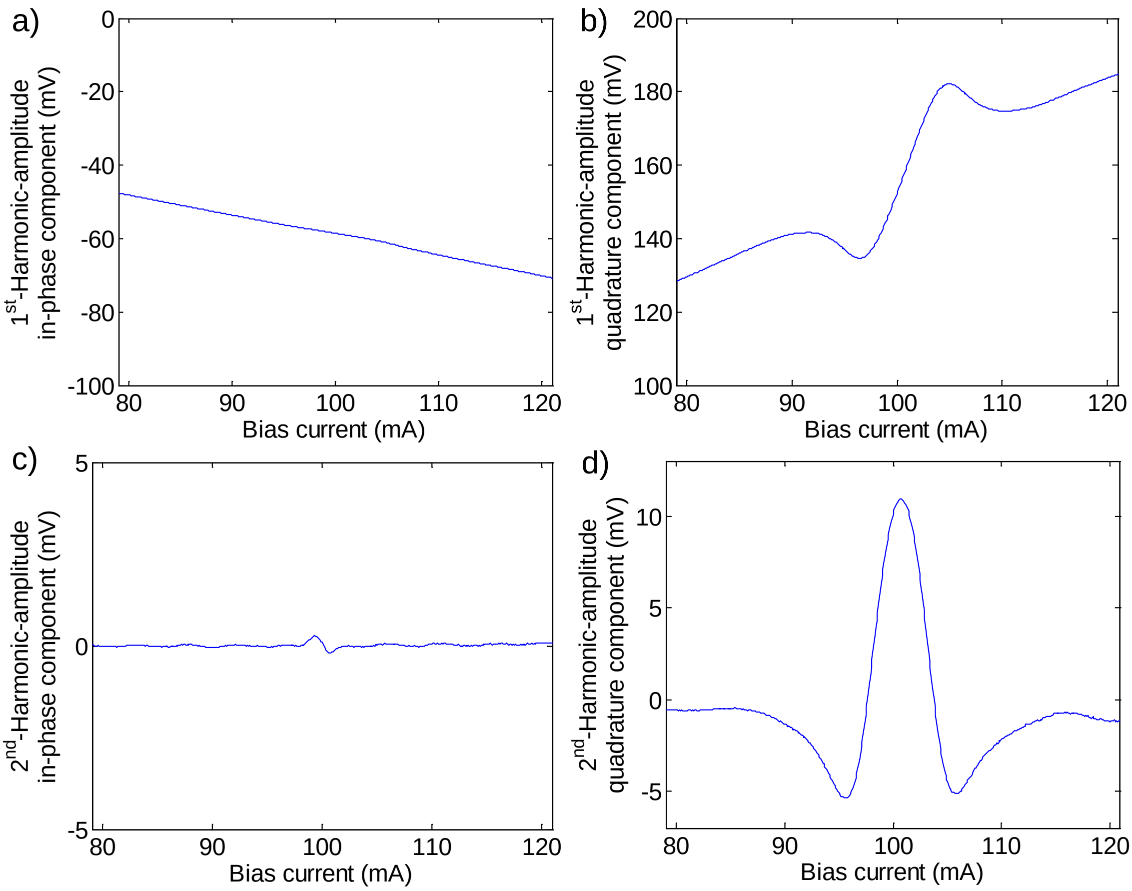

Figure 3.16. Results obtained from the in-phase (a) and quadrature (b) 1st harmonic functions and the in-phase (c) and quadrature (d) 2nd harmonic functions from the analysis of the H_2O Open-Path concentration with a 10 mA modulation.

Measurements similar to the gas cells case were performed to obtain the concentration of CO_2 and H_2O in the atmosphere. For the case of H_2O, the 1st and 2nd harmonic curves evolution graphics are shown below (Fig. 3.17).

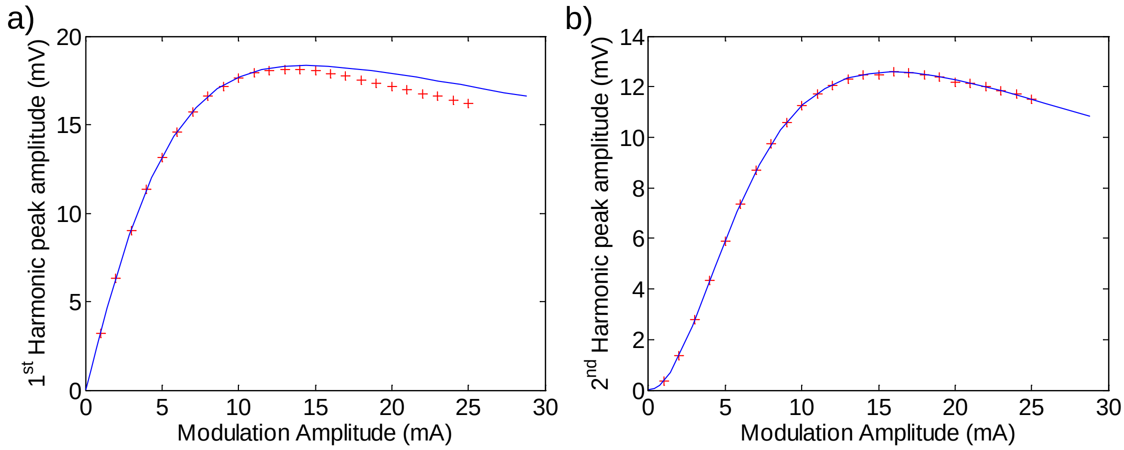

Figure 3.17. Maximum values for 1st harmonic (left) and 2nd harmonic (right) measurements for the H_2O open-path case. The red points show the measurements while the solid blue line indicates the adjusted curve.

In this case of measuring H_2O in the atmosphere, a certain fall in the 1st harmonic curve with respect to the ideal values appears, possibly due to the effects of background and the difference of wavelength modulation at different points, as explained in section 3.1. Moreover, the appearance of nonlinear behavior in the laser modulation due to the high linewidth in terms of current can also cause different problems with respect to detection.

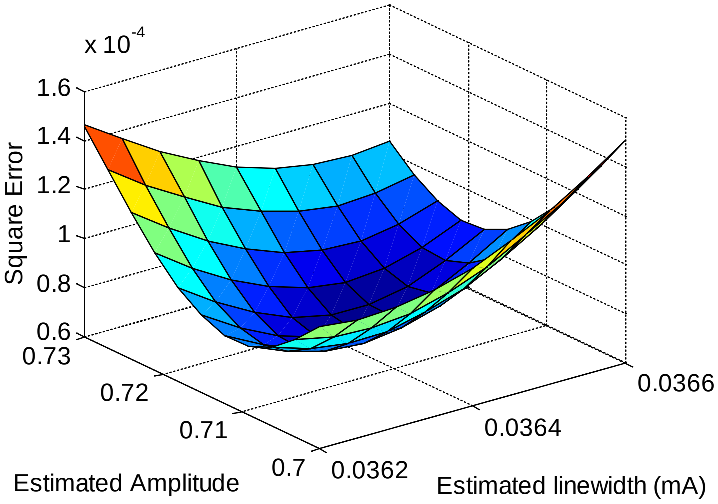

Figure 3.18. Error curve obtained while minimizing the distance between 1st and 2nd harmonic peak-values curves and the simulated curves with respect to linewidth and amplitude for the case of H_2O in the atmosphere.

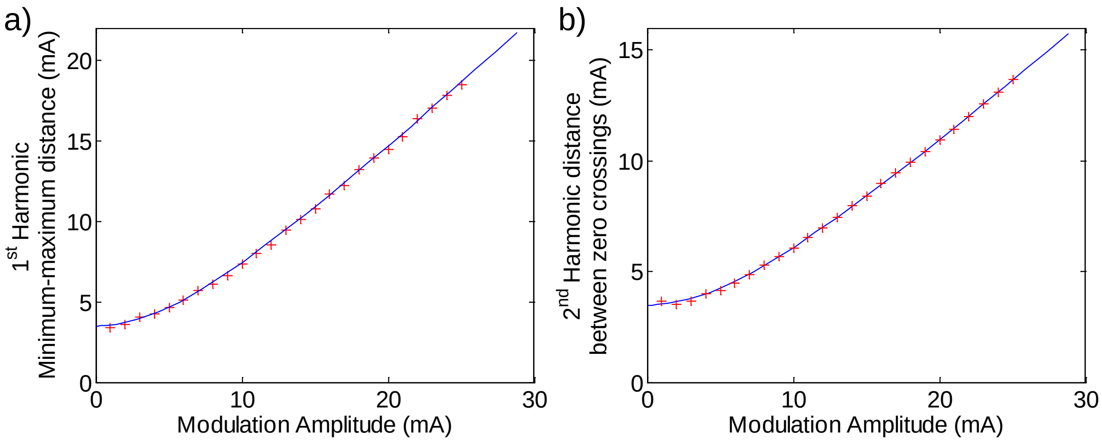

Figure 3.19. Evolution of the distance between extremes of the 1st harmonic (a) and the zero-crossing distance in the 2nd harmonic (b) for the H_2O open-path case. The red points show the measurements while the solid blue line indicates the adjusted curve.

The measurements of distance between extremes and zero-crossing distance indicate a reasonably good level of agreement with the theoretical curves, even in the lowest zone of amplitude where noise is high (Fig. 3.19).

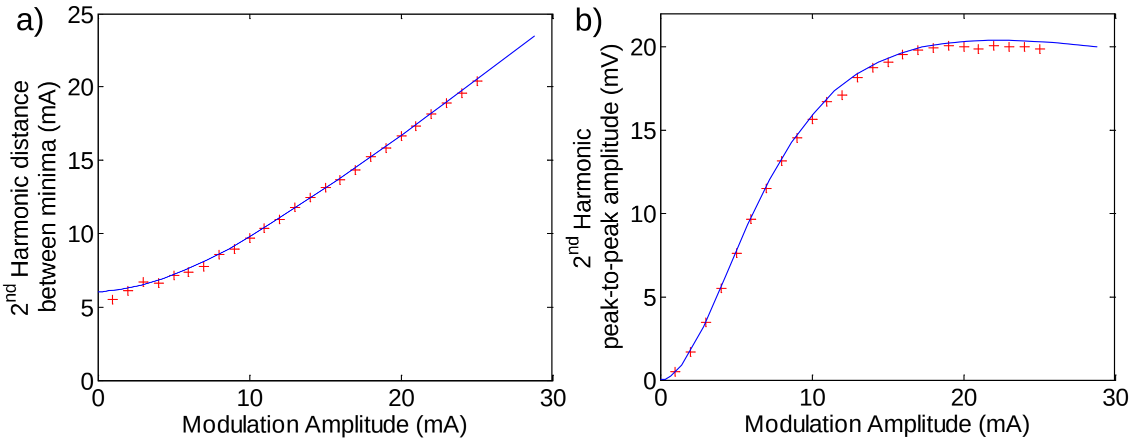

Figure 3.20. Evolution of the distance between minima (left) and peak-to-peak value (right) of the 2^{nd} harmonic for the H_2O open-path case. The red points show the measurements while the solid blue line indicates the adjusted curve.

Finally the measurements of both the distance between minima and the peak-to-peak value of the 2^{nd} harmonic curves (Fig. 3.20) show a high degree of agreement with the theoretical curves. In the distance-between-minima curve the presence of noise explains the behavior on the left of the graphic and, for the case of the peak-to-peak-value graphic, the separation of the points on the right of the graphic with respect to the theoretical curve could show some small error in amplitude but there is a reasonably good degree of agreement.

The calculus of the main values is performed applying the formulas at the end of the last chapter for the case of an open path:

$$\gamma(p=p_S)\approx\gamma_{\text{air}}\cdot p \qquad\qquad \alpha_{OP}=\frac{S_{\eta\eta'}LC_g}{\pi\gamma_{\text{air}}p} \tag{3.58}$$

where $\gamma(p=p_S)\approx\gamma_{\text{air}}\cdot p$ corresponds to the absorption-line air broadening. In this case, the concentration percentage (applying 3.58) must be obtained by comparing the number of molecules of gas per square centimeter obtained with the total concentration in the gas conditions of $T=23^{\circ}C$ and $P=1\,atm$. So we have:

$$C_g=\frac{\alpha_{OP}\pi\gamma_{\text{air}}p}{S_{\eta\eta'}L}\cdot\frac{100\%}{2.48\cdot10^{19}[molec\cdot cm^{-3}]} \tag{3.4}$$

The results are shown in table 3.6.

Table 3.6. Results of the open-path gas-concentration measurement of CO_2 and H_2O.

Open Path Gas	Amplitude	Width (mA) - γ_I	Width(cm^{-1}) - γ	Concentration
CO_2	0.00229 ± 2E-5	2.202 ± 0.060	0.0652 cm^{-1}	539 ± 5 ppm
H_2O	0.0175 ± 1E-4	3.00 ± 0.06	0.101 cm^{-1}	1.46 ± 1E-2 %

The first point to emphasize is the great level of coincidence of the width in both open path measurements and the one obtained theoretically. While the measured widths are 0.0652 cm^{-1} and 0.101 cm^{-1}, respectively, for the cases of CO_2 and H_2O, the theoretical widths are 0.0677 cm^{-1} and 0.102 cm^{-1}. These results suggest that the width measurements obtained using the WMS method are very good results and, at the same time, corroborate the correctness of the results for the gas-cell case.

Otherwise, the values of concentration of H_2O and CO_2 are compatible with the state of an underground lab that remains closed most of the time and with the measurement of H_2O on quite humid days.

3.5 Experimental problems

Different problems affect the measurements performed for gas detection. They can be divided into two types:

i) Background estimation (mainly for large linewidths): The measurement of the background is essential to be able to extract correct information from the data. Different phenomena affect this measurement, namely, possible interferences due to stationary waves formed between emitter and receiver, other absorption lines nearby the one under measurement, nonlinearities of the laser itself in the emission, etc. These problems must be carefully considered in order to obtain the best approximation for the background line. An example of this can be seen in figure 3.21 which shows the 2^{nd}-harmonic curve for an input modulation value of 18.4 mA. Looking at the graphic, the difficulties tracing the zero line are quite obvious. The amplitude measurement in this case is poor as shown in figure 3.22.a when we try to adjust it to a theoretical curve but if a peak-to-peak value analysis (Fig. 3.22.b) is performed, this provides better results with less error.

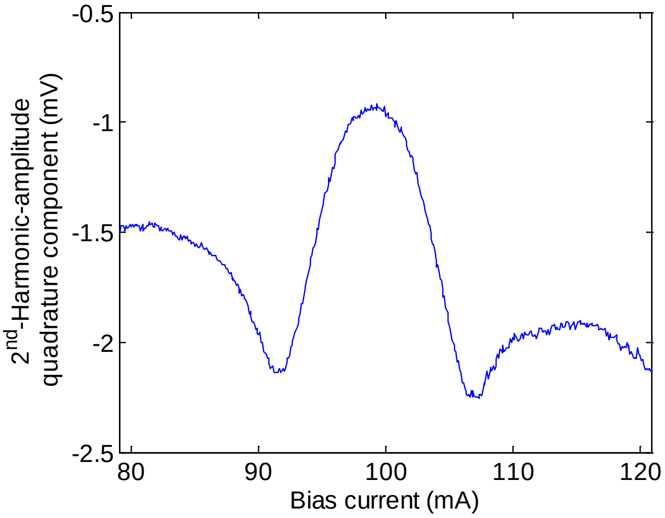

Figure 3.21. 2^{nd} harmonic curve along the modulation current for the case of an input modulation current of 18.4 mA in the CO_2 open-path measurement.

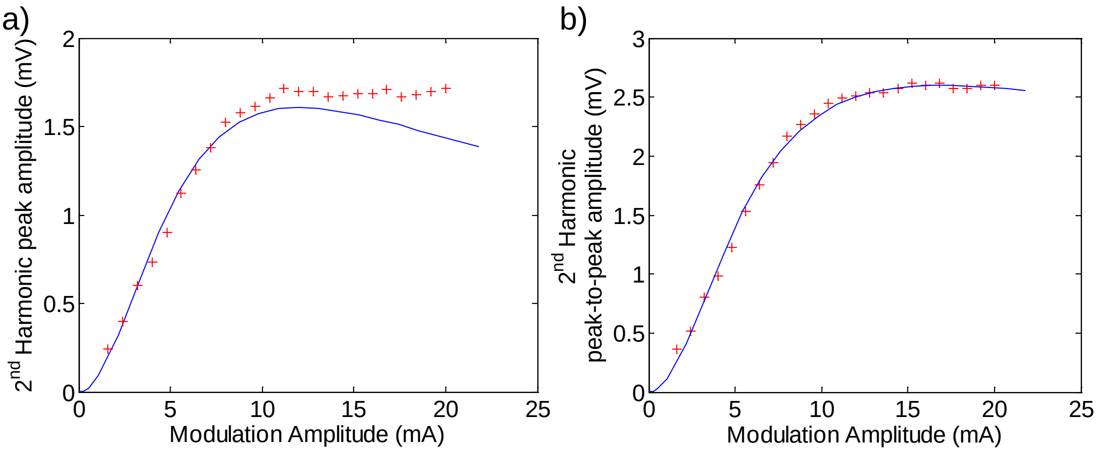

Figure 3.22. Evolution of the 2nd harmonic peak (a) and peak-to-peak (b) values along the input modulation current in the CO_2 open-path measurement.

ii) Current-lambda ratio: As shown in figure 3.4, the increase of lambda per unit of current changes along the actual current. This can result in harmonics shapes which are not exactly the same as in the simulations and some distortion in the measurements. The difference of amplitude between the maxima and the minima in the 1st harmonic curve and the different amplitudes of the minima in the 2nd harmonic function (Fig. 3.21) could be an example of these distortion effects. In this second case, the residual amplitude modulation (RAM) could be another element that causes this effect.

3.6 Comparison between integrated and localized CO_2 detection

To validate the WMS system for gas-concentration measurements in real conditions, an experimental campaign comparing in-situ CO_2 measurements to an integrated measurement (WMS) was performed in collaboration with a research group from the Institute of Climatic Sciences of Catalonia (IC3). A setup with different localized measurements along a path was designed, which was sensed with our WMS system. Different CO_2 meters where located along the path while the WMS system measured the integrated CO_2 concentration along this path. A comparison was made of the measurements and a calibration was performed using gas bottles in the center of the path which were analyzed using an FTIR system in the IC3 labs. The variability of the measurements and the analysis of an approximately 2-hour measurement in terms of variance will be discussed later on.

3.6.1 Experimental Setup

The IC3 group performed the in-situ measurements with the help of four Vaisala instruments of CO_2 concentration measurements and a number of gas bottles which were filled during the different measurements. The campaign was planned to perform two kinds of measurements: distributed measurements and calibration measurements. All the measurements where performed in a laboratory with two rooms which presented elevated levels of CO_2 concentration after some days without ventilation. Vaisala instruments were located along the WMS-system light path and the gas bottle inlet was located in the center of the light path. For the distributed measurements (Fig. 3.23) Vaisala instruments where located equidistant along the path to obtain a distributed measurement of CO_2 concentration while for the calibration measurements (Fig. 3.24) these Vaisala instruments were located together beside the gas bottle inlet to perform a calibration of their readings.

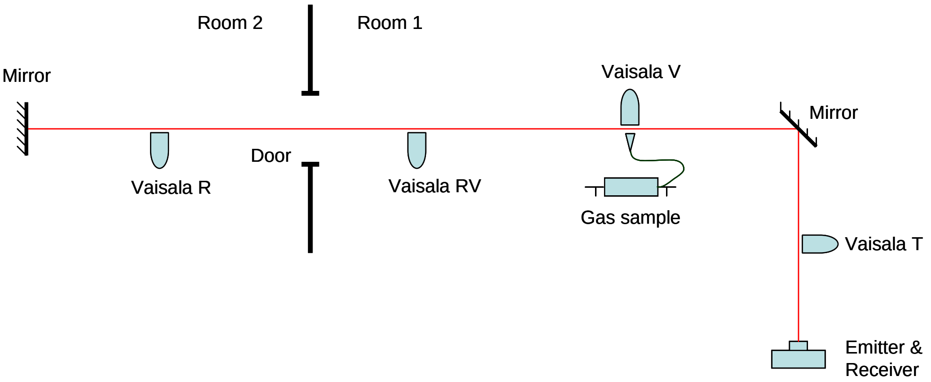

Figure 3.23. Distributed measurement of CO_2 gas concentration with WMS, Vaisala and gas sample systems.

The measurement sequence was carried out as follows. The experimental setup was performed on day 1 of the campaign and the first calibration measurement (Calib-1) was performed the same day as well. During day 2, six more measurements were performed. First, another calibration measurement (Calib-2) was performed before a distributed measurement (Meas-3) with all the doors and windows of the lab closed. Then the windows at both ends of the lab (one in room 1 and one in room 2) were opened and the measurement path was ventilated for a couple of hours. Another distributed measurement (Meas-4) was performed before carrying out a new calibration (Calib-5). The windows of the lab remained open for a further 3 hours before performing the last calibration measurement (Calib-6) and one more distributed measurement (Meas-7) to complete the campaign.

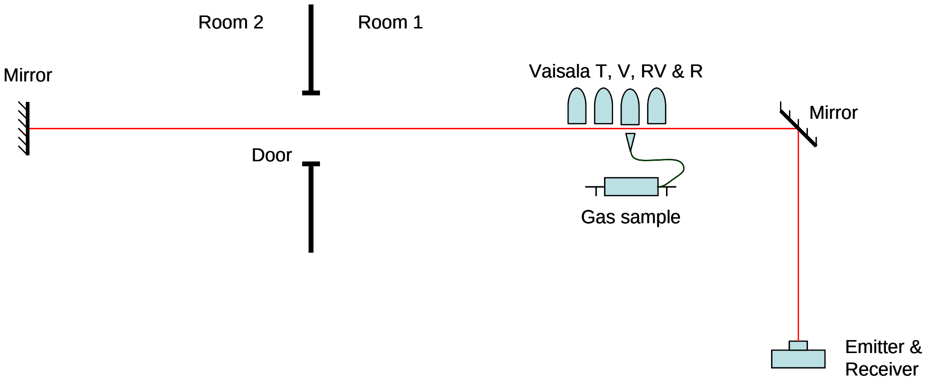

Figure 3.24. Calibration measurement of CO_2 gas concentration with WMS, Vaisala and gas sample systems.

3.6.2 Measurements and calibration

The WMS measurements performed during the campaign were approximately 2-3 minutes long so that they could be calibrated with the help of the previously cited CO_2 calibration bottles. Figure 3.25 shows the evolution of the measurements of the WMS system for two different cases before calibration (scaled by a factor 600 ppm/mV to compare the measurements) and the Vaisala instruments along time for the case of measurements (Calib-1) and (Calib-2). The grey star indicates the bottle sample which was used to calibrate both the WMS system and the Vaisala instruments. In both measurements (WMS and Vaisala) the trends are comparable.

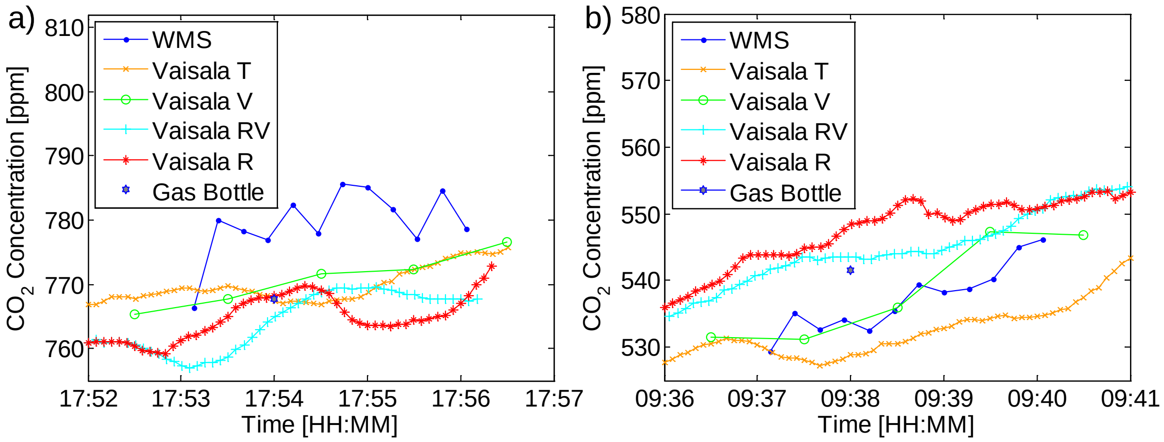

Figure 3.25. Calibration measurements Calib-1 (a) and Calib-2 (b) of CO_2. The WMS system without calibration (blue) as well as the Vaisala measurements are shown. The star corresponds to the gas bottle sample.

The WMS-system measurements were calibrated comparing the mean value of the WMS system measurement (some 3 minutes) with the 2-minute bottle measurement (some 0.05 ppm of resolution) and performing a linear regression between both measurements. The result is shown in figure 3.26 and the value of the correlation coefficient is of 0.9917, a high value taking into account the spatial averaging being performed by the WMS system.

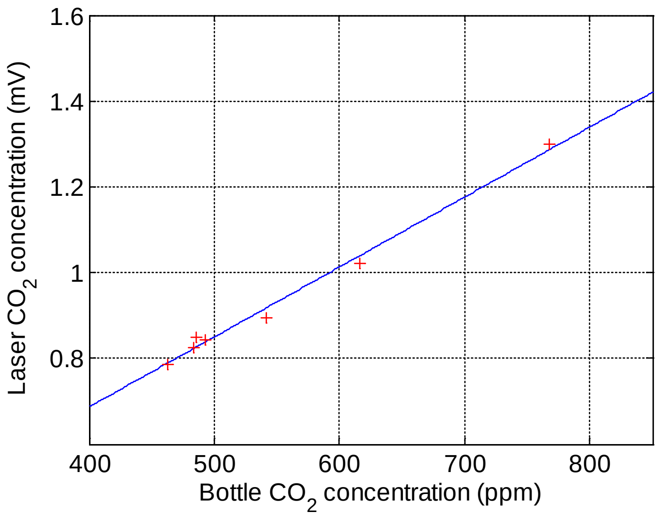

Figure 3.26. Calibration linear curve between the CO_2 bottle concentration and the WMS-system obtained CO_2 concentration. The points (red) correspond to the measured values.

Figure 3.27 shows the distributed measurements Meas-3 and Meas-7 with the calibrated version of the WMS-system data.

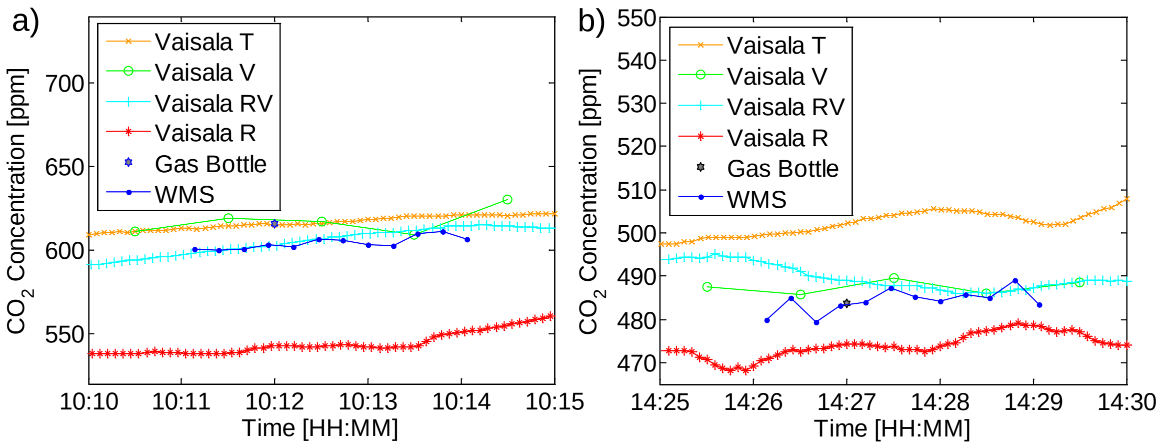

Figure 3.27. Distributed measurements Meas-3 and Meas-7 of CO_2. The calibrated WMS system (blue) as well as the Vaisala measurements is shown. The star corresponds to the gas bottle sample.

3.6.3 Variability of the measurement along the 20-meter path

Another perspective of the measurements taken can be seen in figure 3.28. The results of measurements Meas-3, Meas-4 and Meas-7 are represented superposed on the calibration line for the Vaisala instruments and the gas bottle. A noteworthy point is the shift from the mean value (blue line) of the red Vaisala instrument. This was due to the lack of ventilation in the room 2 (Fig. 3.23) which gave a lower concentration value. In the other measurements, the variation is small.

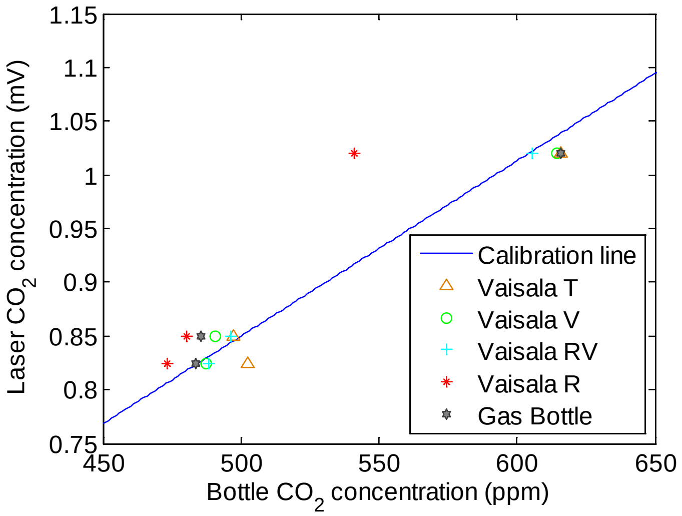

Figure 3.28. Time-averaged CO_2 concentration value for the different Vaisala instruments and the gas bottle for the distributed measurements Meas-3, Meas-4 and Meas-7.

3.6.4 Measurement of variance across time

This section explains an approximately 2-hour long measurement of CO_2 gas concentration along a very small path which implies a very small absorption (equivalent to some 20 ppm of concentration). Figure 3.29 shows the CO_2 concentration data, which indicates a variability that can be mainly attributed to the source noise and drift and to the detector noise. The mean value of the measurement is of some -16 ppm which indicates the drift produced by the background of the detected signal (some 35 ppm from the real ~20 ppm). Moreover, there is a clear high noise level which need to be eliminated by averaging measurements.

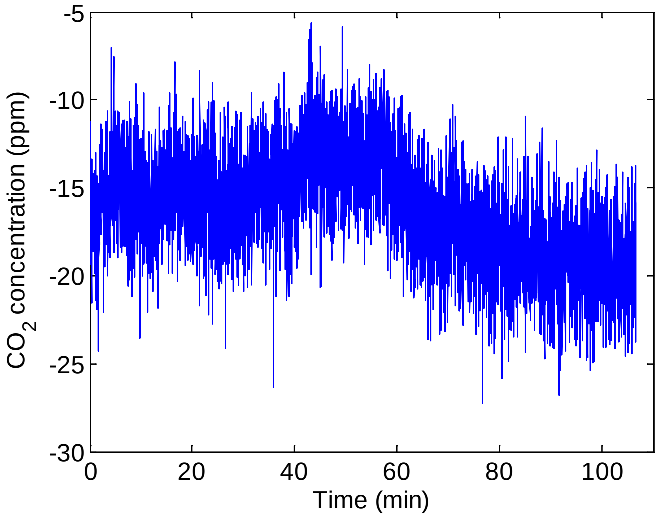

Figure 3.29. CO_2 concentration during a 2-hour measurement.

An interesting method to calculate the optimum average is the Allan Variance calculation [19] which also indicates the period between calibrations (Fig. 3.30). In this case, the optimum average should be approximately 200 or 300 averaged samples.

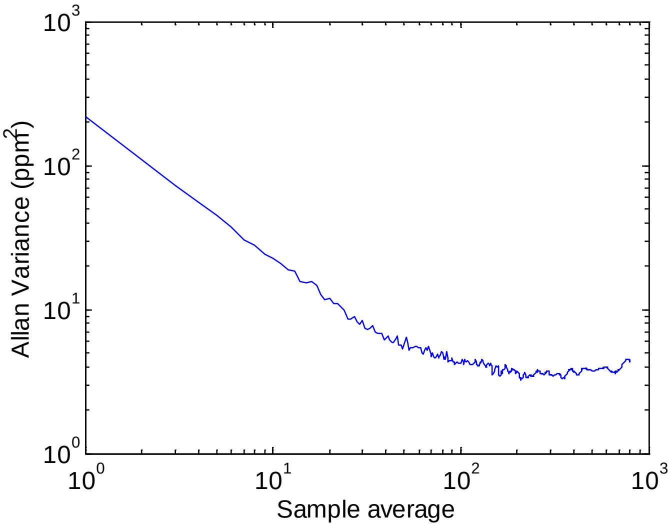

Figure 3.30. Allan-variance graphic of the CO_2 concentration measurement.

In the joint measurements previously described, an average of some 10 samples was applied to the acquired data. The same average was applied to the 2-hour measurement in order to see how the CO_2 concentration would appear (Fig. 3.31).

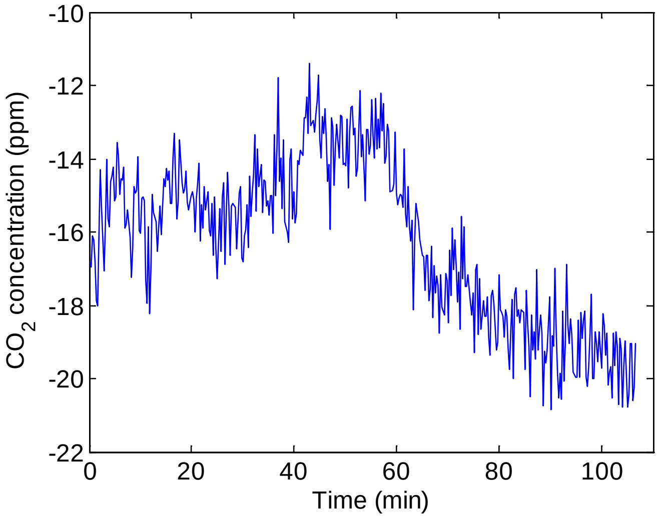

Figure 3.31. 10-second average CO_2 concentration graphic.

The 10-second averaged CO_2 concentration graphic shows a major decrease in the levels of noise from the original graphic (Fig. 3.29). The standard deviation value of the measurement calculated over 2 hours is 2.22 parts per million of CO_2 in the air which shows the quality of the measurements performed.

To summarize, it can be pointed out that with this system it is possible to obtain a series of measurements in agreement with the other classical in-situ measurement systems. This allows for the conclusion that this system has a precision in the order of ±3 parts per million in volume of CO_2. In contrast, the accuracy of the measurement has to be corrected (calibrated) because of the inner drift which could be as high as a few tens of ppmv.

4 FMCW Lidar Theory

Following on from the analysis of *in-situ* gas detection, this chapter is concerned with the study of the FMCW lidar. It is first studied from the perspective of a technique to detect aerosols and then its application to detecting gases, where the studies carried out and described in the previous chapters are applied.

Before embarking on an analysis of FMCW lidar, this chapter begins by setting out some of the basics of lidar and the common types of lidar and then goes on to discuss FMCW lidar. The FMCW technique is mainly used in radar systems, so the introduction to FMCW works from this perspective, followed by and overview of the evolution of this technique for lidar systems.

The use of FMCW lidar for sensing distributed media is studied in section 4.3. A bandpass filtering problem derived from the nature of the emitting signal is shown. In addition, a solution to overcome this problem is proposed using a novel technique called phase-hop, followed by a study of the signal-to-noise ratio (SNR).

Finally, the application of distributed-media FMCW lidar to gas detection is dealt with in section 4.4, first from an integrated-concentration approach and then as a range-resolved measurement. A special case is presented for the situation of a very low level of modulation, followed by a number of simulations that corroborate the method to be used and an SNR calculation to validate its use for small-range measurements. The last step of this section is the analysis of the phase-hop method for the gas-detection version of FMCW lidar. The original method is developed and a number of simulations are explained which prove the feasibility of the technique for gas detection.

4.1 Lidar Basics

Lidar systems are complex optoelectronic remote sensing systems. Advanced optics, high-speed electronics and signal processing must converge in order to obtain good measurements [20, 21]. A general lidar system setup is shown in figure 4.1, displaying the essential parts of the system, namely laser, telescope, optical receiver and equipment for data acquisition and signal monitoring.

The basic operation of a lidar system is as follows: a light pulse is emitted by a laser, then light is backscattered as the pulse propagates through the atmosphere (or encounters a hard target); the backscattered light is collected by a telescope and detected by an optical photoreceiver. Finally, the received signal is conditioned and acquired by an electronic system. These data are processed in order to obtain the desired information.

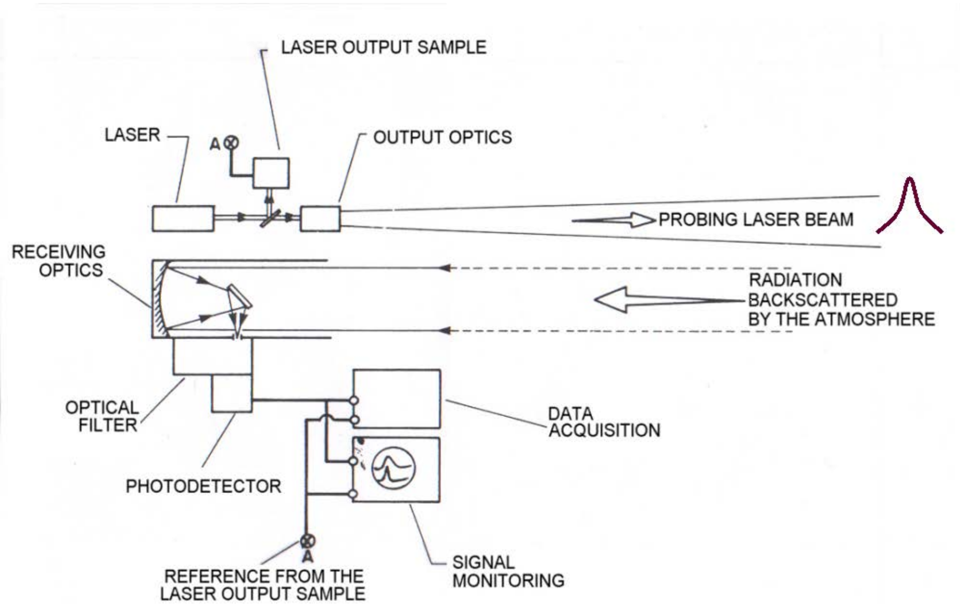

Figure 4.1. General lidar setup [20].

The power collected in a lidar system as a function of the range of the scattering volume is given by the lidar equation. A wave with a certain power time profile is emitted:

$$P = P(t) \tag{4.1}$$

The signal received after having interacted with the atmospheric medium has the following form [20]**:**

$$P_r(R) = \int_0^{R_{\max}/2c} dt P(t - 2R/c - \tau/2) \frac{A_R}{R^2} \beta(R) \exp\left(-2\int_0^R \alpha(x)\, dx\right) \tag{4.2}$$

where A_R is the area of the telescope, c is the speed of light, R is the spatial variable along the line of sight, $\alpha(R)$ is the extinction coefficient of the medium that generally includes scattering as well as absorption effects, and $\beta(R)$ is the backscattering coefficient of the medium giving rise to the radiation that will return to the instrument. The term A_R / R^2 represents the solid angle in reception and determines the amount of radiation collected by the telescope.

In the case of a pulsed lidar with an ideal rectangular pulse shape of duration τ, the equation will adopt the following form:

$$P_r(R) = \int_0^{R_{\max}/2c} dt P_0 \Pi\left(\frac{t - 2R/c - \tau/2}{\tau}\right) \frac{A_R}{R^2} \beta(R) \exp\left(-2\int_0^R \alpha(x)\, dx\right) \tag{4.3}$$

where $\Pi(t/T) = \{1\ for\, |t| < T/2; 0\ otherwise\}$. Assuming the integrand is almost constant in the interval $c\tau/2$, we would arrive at Eq. (4.4), where P_0 is the peak power and the pulse length is equal to $c\tau/2$.

$$P_r(R) = \frac{P_0 A_R c\tau}{2R^2}\beta(R)\exp\left(-2\int_0^R \alpha(x)\,dx\right) \tag{4.4}$$

In the case of a continuous wave lidar, range resolution is obtained by different techniques, such as, pseudo-random codes or frequency modulation, and this is described in the following section.

4.1.1 Types of lidar. Classification by interactive phenomenon

Lidar systems can be classified following different criteria in several ways, but maybe the most interesting ones for our case are the classification by light-matter interaction phenomenon (see table 4.1) and modulation technique as shown in section 4.1.2.

Elastic backscattering: In this case, the wavelength of the radiation scattered by the particles is the same as that of the incident wave, like in Mie scattering and Rayleigh scattering. Elastic backscatter lidars are usually employed to measure backscatter coefficients of aerosols or clouds.

DIAL: In this case the phenomenon of light absorption is used. Two wavelengths are emitted. Backscattering by aerosols occurs as in the previous case and data obtained from both wavelengths are compared because one wavelength is affected by an absorption line of the gas under measurement and the other is close to that line but detuned (Figure 4.2). So, by comparing them, one can obtain the concentration of the selected gas in the zone.

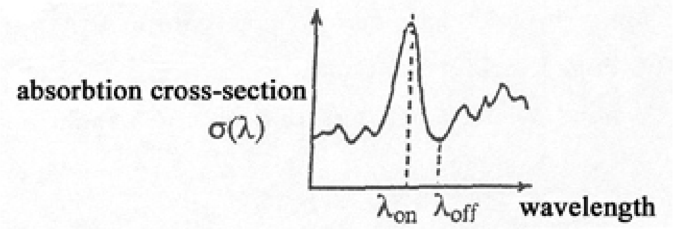

Figure 4.2. Transmitted wavelengths in a DIAL [22].

This technique is used for detecting water vapor or carbon dioxide with high spatial and temporal resolution.

Fluorescence: This is a technique using the homonymous phenomenon. The phenomenon consists of the spontaneous emission of a photon following a previous excitation by absorption of incident radiation at a optical frequency ν_0. The incident photon causes the leap of an electron to an excited level which, after that, relaxes to a lower level although not necessarily the initial. This is called resonant fluorescence in contrast with broad fluorescence, where prior to relaxing, the excited molecules can collide which redistributes their energy levels into other excited levels through non-radiative transitions. The re-emitted radiation is useful in identifying and monitoring the atomic or molecular species responsible for the fluorescence. Fluorescence is a two single-photon process (delayed response) with a given time uncertainty between the absorption of the incident photon and the emission of the new photon in contrast with Rayleigh or Raman backscattering which are two-photon processes (instantaneous response). This time uncertainty implies that fluorescence is not adequate for range-resolved measurements.

Raman backscattering: This is a phenomenon whereby the emitted signal, with a certain optical frequency, gives rise to a scattering spectrum with sidebands (inelastic Raman scattering) around the excitation wavelength (elastic Rayleigh scattering). This is produced because of metastable quantum states in molecules. Every molecule has a concrete Raman spectrum that can be used to identify it. The molecule concentration can be determined by applying filters to certain wavelengths where Raman lines are present.

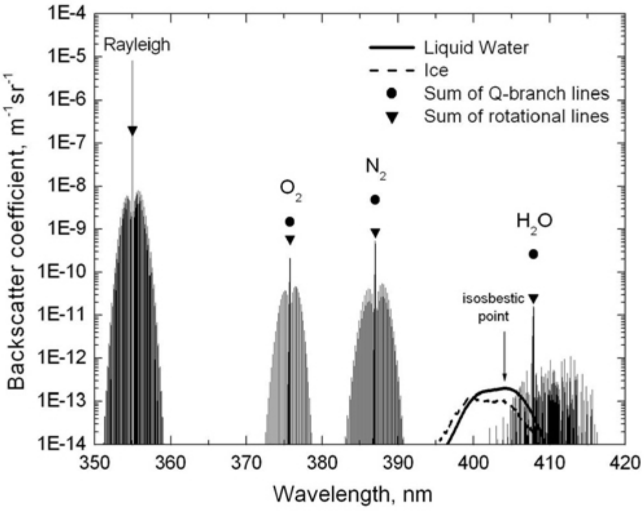

Figure 4.3. Simulation of Raman spectra under a 355nm wavelength excitation [23].

Figure 4.3 shows a simulation of the Raman spectra of different gases. Each Raman spectrum is composed of a number of bands with a central reemitting wavelength related to a certain vibrational energy level of the absorbing molecule surrounded by other wavelengths corresponding to the rotational levels of that molecule. The power received from Raman scattering is several orders of magnitude weaker than the one received from elastic backscattering; therefore a Raman lidar is usually built with a high-power pulsed lidar, relatively large telescopes and high-efficiency detectors.

Doppler lidar: This type of lidar corresponds to the elastic backscattering used to measure moving objects. The wavelength change produced by this effect is quite small (a change in the wavelength of some 10^{-8} times for speeds of some 1 m/s in the optical zone), therefore it is usually measured by means of heterodyne optical detection or using very narrow optical filters (for instance, Fabry-Perot etalons). This system is used in airports to measure air speed, predict meteorological changes and track turbulence produced by aircraft.

Table 4.1. Summary of lidar types and their applications

			Measurement type	
Type		Typical lasers used	Direct	Indirect
Elastic	Direct detection	Ruby (λ=694.3 nm, 347.2 nm) Nd:YAG (λ=1064 nm, 532 nm*, 355 nm**) XeF (excimer); λ=351 nm) * Frequency doubled; ** Frequency tripled	Dust, clouds, smoke	Transport phenomena, atmospheric stratification, temperature in the upper atmosphere, wind velocity fields
	Homodyne or heterodyne detection	CO_2 (λ=10.6 μm) Nd:YAG (λ=1064 nm) Tm,Ho:YAG (λ=2.1 μm)	Doppler shift of radiation backscattered by aerosols or air constituent molecules	Wind velocity fields
Differential absorption (DIAL)		Dye, CO_2, excimer, optical parametric oscillators (OPO)*, Ti:sapphire * Strictly speaking, not a laser source	Chemical species concentration (SO_2, O_3, C_2F_4, NH_3, CO, CO_2, HCl, ...	Temperature, pressure
Fluorescence		Dye, N_2 (λ=337 nm), Ne	Concentration of chemical species, especially in the upper atmosphere (OH, Na, K, Li, Ca Ca^+), detection of oil slicks on water, chlorophyll detection	
Raman		Ruby (λ=694.3 nm, 347.2 nm) N_2 (λ=337 nm) Nd:YAG (λ=532 nm*, 355 nm**) * Frequency doubled; ** Frequency tripled	Concentration of chemical species in the atmosphere (SO_2, NO, CO, H_2S, C_2H_4, CH_4, H_2CO, H_2O, N_2, O_2 ...)	Temperature

4.1.2 Classification by emitter type

Classification by modulation technique gives us the following types:

Pulsed lidar: The emitted signal is a train of very short pulses. Range resolution is achieved by time sampling the received signal. Figure 4.4 shows how the pulse travels through space and the cell from which backscattered power reaches the receiver at $t = t_0$.

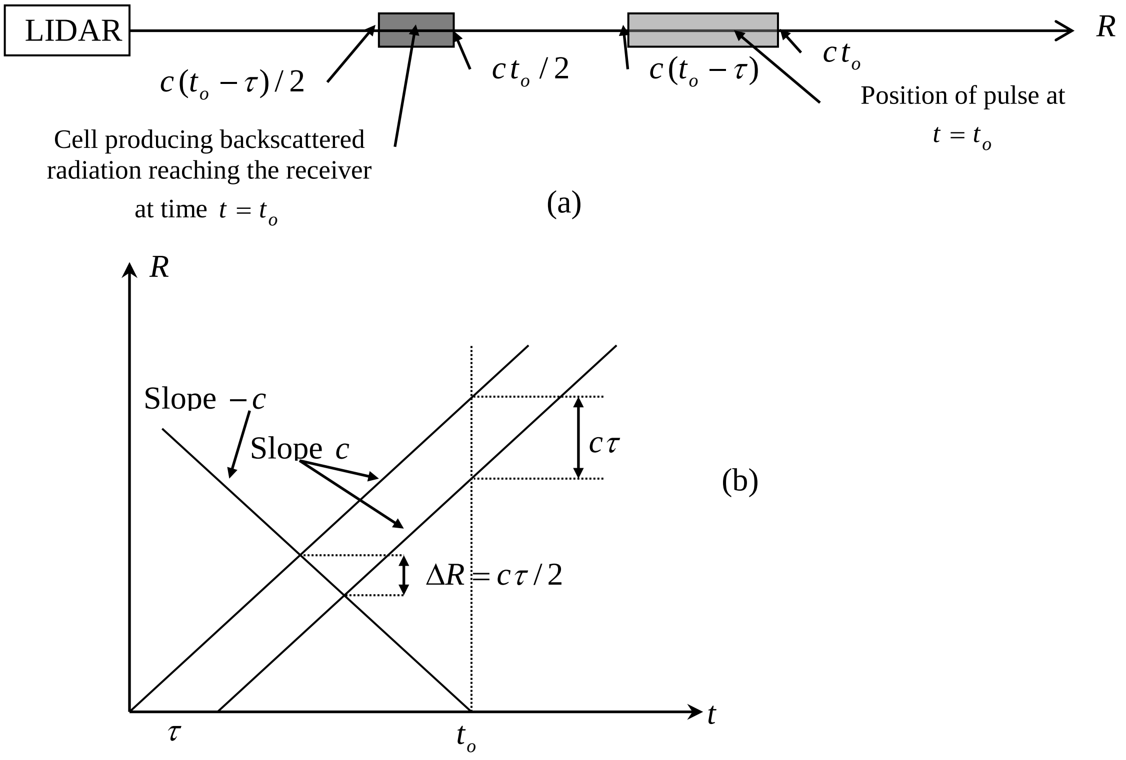

Figure 4.4. Propagation and backscattering of light pulse. (a) “Snapshot” t_o seconds after pulse transmission. (b) Space-time diagram for pulse propagation and backscattered radiation. [22].

Continuous wave lidar: The emitted signal is a continuous wave signal with certain characteristics that allow it to achieve range resolution. In the case of CW-FM (figure 4.5), range resolution is achieved using the evolution of the frequency in the emitted signal and relating this to target distance. After processing, the responses of targets at different ranges appear at different frequencies. In the case of pseudo-random codes (figure 4.5, right), range resolution is achieved through correlation between the received signal and the sequence modulating the transmitted signal [24 - 26]. The correlation is performed at different time shifts in order to obtain the response at each distance.

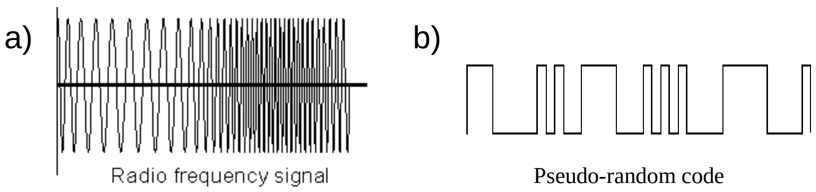

Figure 4.5. Frequency modulation (a) and pseudo-random codes (b).

4.2 FMCW Fundamentals

Despite the fact that the most commonly found techniques in lidar are based on pulsed systems, continuous–wave methods, given the technical difficulties in implementing them, have a number of advantages, such as low-power and eye-safe operation. FMCW (Frequency-Modulated Continuous Wave) is a technique commonly used in radar systems and is also used in lidar systems for hard-target detection. This is a continuous-wave technique where the emitted frequency is modulated by a tone that linearly increases its frequency across time. As a result of this modulation, one can measure the time the signal takes to travel to a certain target and back to the system by instantaneously comparing the frequencies of emission and reception (Fig. 4.6), and then estimating the distance to the target.

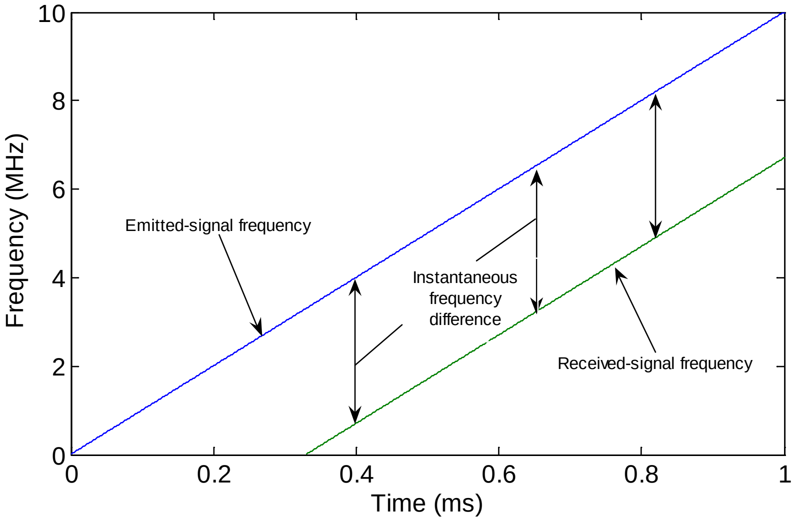

Figure 4.6. Instantaneous frequencies difference in FMCW.

The frequency difference between the emitted and the received signal remains constant while the probe beam impinges on a fixed target so by applying these signals to a mixer and low-pass filtering one can obtain a tone whose frequency is proportional to target distance. This signal coming from the receiver is spectrally analyzed in order to obtain the relevant information.

This method is not limited to detecting only one target, and can detect multiple targets at the same time. By analyzing the signal spectrum after filtering and rescaling the frequency axis to reflect the distance to the origin, the distribution of all the targets detected by the system can be obtained.

4.2.1 FMCW for Radar

Frequency-Modulated Continuous Wave (FMCW) was first designed to detect solid targets by microwave radar, and later to sound distributed media [27 - 32]. In this technique the transmitter produces a FMCW signal $s(t)$, that is, a sinusoidal signal (usually) with a constant rate of frequency change (Fig. 4.7).

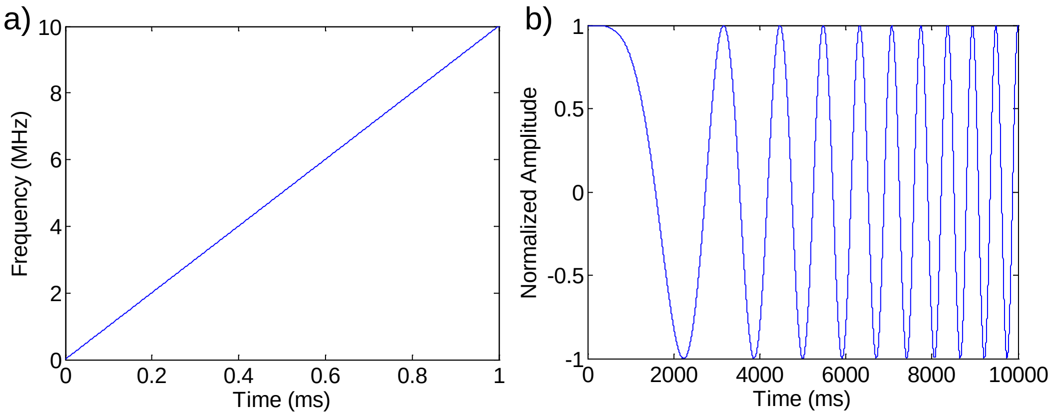

Figure 4.7. Emitted signal in FMCW with the evolution of the frequency (a) and the amplitude (b) along time.

$$s(t) = S_0 \cos\left[2\pi\left(f_0 t + \frac{K}{2}t^2\right)\right], \tag{4.5}$$

S_0 being the emitted amplitude, f_0 the initial RF frequency and K the rate of change in frequency [Hz/s]. This signal is backscattered by a target and goes back to the emitter with a shape that can be described as:

$$s_R(t) = A_t S_0 \cos\left\{2\pi\left[f_0\left(t-\tau\right) + \frac{K}{2}\left(t-\tau\right)^2\right] + \varphi_0\right\}, \tag{4.6}$$

with A_t a dimensionless factor that depends on the characteristics of the target and the distance, τ the (round trip) delay time and φ_0 a phase depending on the target characteristics. In the receiver, the detected signal is mixed with the emitted one. Representing the mixing process by a product, we obtain:

$$\begin{aligned} s_{RM}(t) = s(t)\cdot s_R(t) = S_0 \cos\left[2\pi\left(f_0 t + \frac{K}{2}t^2\right)\right] A_t S_0 \cos\left\{2\pi\left[f_0\left(t-\tau\right) + \frac{K}{2}\left(t-\tau\right)^2\right] + \varphi_0\right\} = \\ = \frac{A_t S_0^2}{2}\left[\cos\left(2\pi\left(f_0\tau - \frac{K}{2}\left(2t\tau - \tau^2\right)\right) + \varphi_0\right) + \cos\left(2\pi\left(f_0\left(2t-\tau\right) + \frac{K}{2}\left(2t^2 - 2t\tau + \tau^2\right)\right) + \varphi_0\right)\right] \end{aligned} \tag{4.7}$$

and the resulting signal is low-pass filtered in order to eliminate the sum-frequency components:

$$s_{RM}'(t) = \frac{A_t S_0^2}{2}\left[\cos\left(2\pi\left(f_0\tau - \frac{K}{2}\left(2t\tau - \tau^2\right)\right) + \varphi_0\right)\right], \tag{4.8}$$

The cosine of expression (4.8) has a constant frequency and the distance from the target to the system is proportional to this frequency:

$$f_\tau = K\tau = \frac{2K}{c}d_\tau, \tag{4.9}$$

This technique works in a similar way in a scenario of several targets or a distributed medium. The same FMCW signal is emitted and at reception it is mixed, low-pass filtered and Fourier transformed so the presence of each target is reflected in the signal spectrum, with the target position in the frequency axis proportional to its distance, and with an amplitude that corresponds to its backscattering coefficient.

4.2.2 FMCW for backscatter lidar

Although in general terms an FMCW lidar system behaves like an FMCW radar system, some differences in its implementation give rise to certain properties in the phases of the FMCW lidar signals.

In a lidar system, the laser-diode input current modulates (at the same time) the wavelength and the light-signal emitted power. For the particular case of aerosol-detection FMCW lidar, only the laser power modulation is taken into account, the wavelength modulation being superfluous. In this case the information used to obtain range resolution is the very amplitude modulation of the emitted signal and not the carrier wavelength modulation as in the FMCW radar case. Note that the modulation could be applied in the same way as in the case of radar, that is, directly to the carrier [33 - 35], but it is more appropriate to apply the envelope modulation to aerosol and gas remote sensing. In this last case, the information is obtained from the emitted chirp wavelength modulation [1, 2]. When the light interacts with gases, this wavelength modulation produces an amplitude modulation in the wave due to the absorption effects that will give us the information for both range and gas concentration as explained in section 4.4. The emitted amplitude modulation for the case of gas detection is a parasitic modulation that will have to be eliminated.

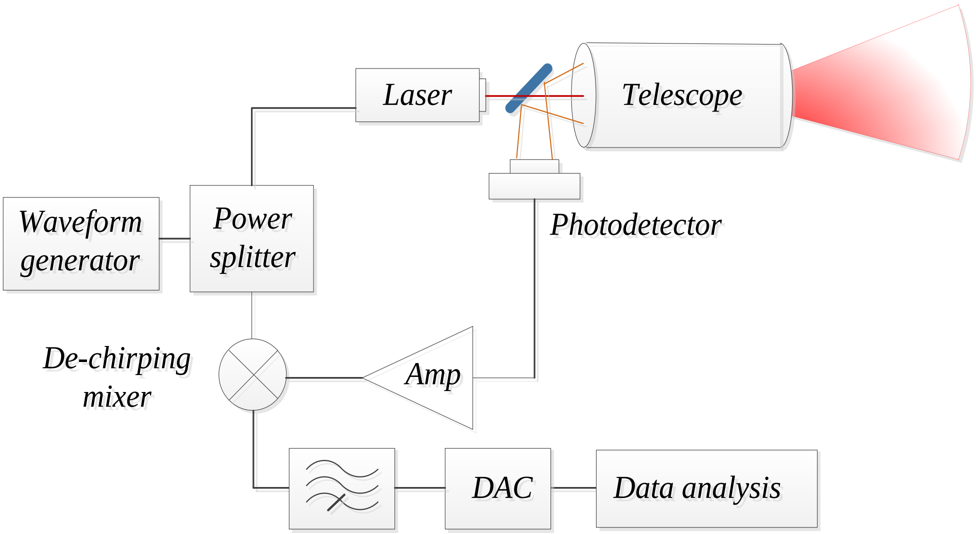

Figure 4.8. Scheme of detection of a FMCW lidar system.

The way to implement FMCW method in optical remote sensing is by applying a frequency modulation to an RF subcarrier which in turn modulates the optical carrier in intensity (Fig. 4.8) [36 - 38]. In this case, the frequency modulation that gives rise to the range resolution is applied to the bias current $i(t)$ of the laser diode, which takes the form:

$$i(t) = i_0 + \Delta i \cos\left[2\pi\left(f_0 t + Kt^2/2\right)\right], \tag{4.10}$$

i_0 being the dc bias current, Δi the current modulation amplitude, f_0 the initial frequency and K the rate of change in frequency. Then, the emitted power $P_T(t)$ is proportional to the modulation current except by an offset due to the threshold current of the laser diode:

$$P_T(t) = \gamma_{IP}\left(i(t) - i_{th}\right) = P_0\left\{1 + m_{AC}\cos\left[2\pi\left(f_0 t + \frac{Kt^2}{2}\right)\right]\right\}, \tag{4.11}$$

γ_{IP} being the slope efficiency, i_{th} the laser threshold current, P_0 the mean power emitted and m_{AC} the intensity modulation index. As pointed out previously, the wave field $u(t)$ of the laser output light is affected both in terms of amplitude (square root of power) and phase by the current modulation. The output light-signal frequency will vary almost linearly around the central wavelength as given in Eq. (4.12):

$$u(t) = \sqrt{P(t)}\cos\left(2\pi\nu_{LAS}(t) + 2\pi\delta_\nu\int_0^{t-t_0} i(t')dt'\right), \tag{4.12}$$

being ν_{LAS} the central wavelength and δ_ν the ratio between the increment of wavelength and the increment of current in the laser diode. This is important for the application to gas detection. The expression of the backscattered power by a certain target gives us the following form:

$$P_R(t) = \sigma_0 P_0\left(1 + m_{AC}\cos\left\{2\pi\left[f_0(t-\tau) + \frac{K}{2}(t-\tau)^2\right]\right\}\right), \tag{4.13}$$

where σ_0 is the target radar cross section.

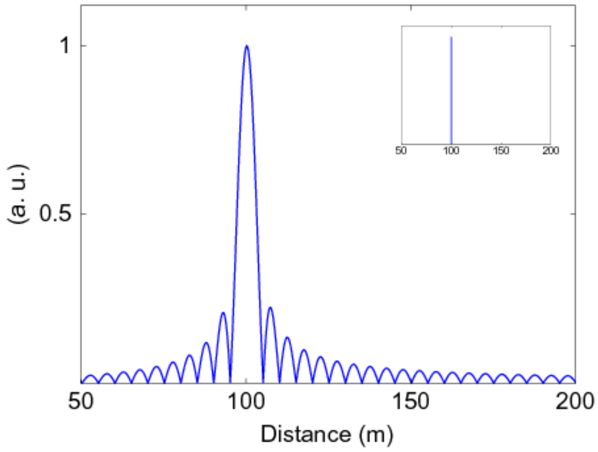

Figure 4.9. Simulation of the detection of a solid target using an FMCW radar system - 5 meters of resolution with the ideal retrieved signal in the inset.

The steps to extract the range and amplitude information from it are similar to those performed in the radar case. Figure 4.9 shows the result of the detection of a solid target at 100 meters with an FMCW lidar system, with the ideal detection result in the inset.

Note that the phase of the modulating received signal is the same as in the emitted signal (‘0’ in this case), unlike in the FMCW radar case where it also depends on the target phase response. This effect is a consequence of the fact that the range-resolution FMCW information travels on the signal envelope, hence it is not affected by the target-response phase which modifies the carrier phase.

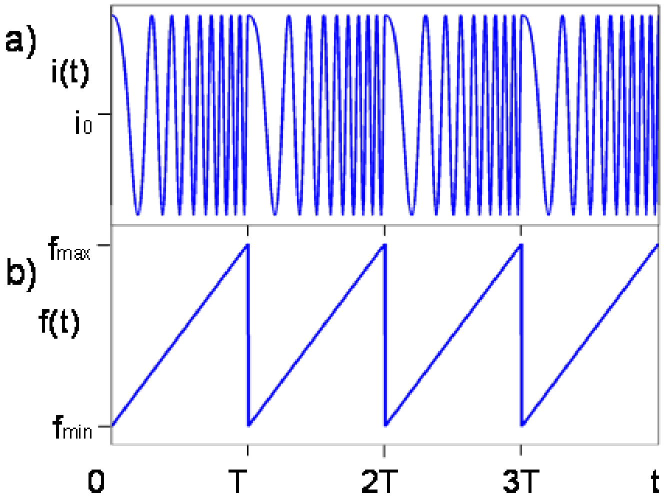

Figure 4.10. Evolution of current amplitude (a) and frequency (b) along time.

One unavoidable consideration to be made is the fact that frequency cannot increase indefinitely so it is necessary to use an implementable signal: the frequency saw tooth (Fig. 4.10). This signal can be seen as the windowing of signal s(t) by a pulse with duration T (signal period) and periodically structured by means of the convolution with a delta train (Fig. 4.10). This fact will ultimately limit the range resolution Δd of the system which in terms of frequency can be expressed as the inverse of the period T. The range resolution can be expressed as:

$$\Delta d = \frac{c}{2K}\frac{1}{T} = \frac{c}{2\Delta f_{dev}}. \tag{4.14}$$

A simulation of the reconstruction of two nearby targets shows the importance of this parameter and the way two targets separated by a smaller than resolution distance are mixed (Fig. 4.11). In this case, some errors in the position and the peak amplitude appear because of the sum of both target responses with different phases in the respective envelopes. This phenomenon will be increasingly harmful for the right location and the evaluation of the size of the targets as the number of targets grows. So, it seems there is a serious drawback to the use of this technique with continuous media. This point will be more carefully studied in the next section.

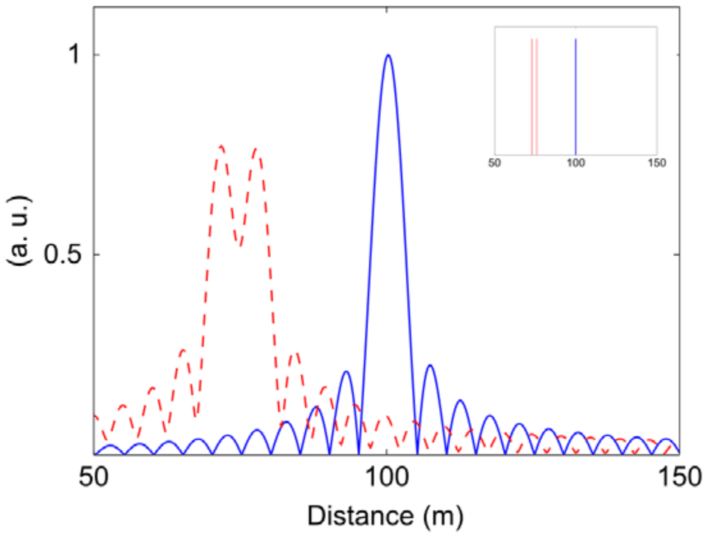

Figure 4.11: Results for the application of the FMCW technique to both a one-target (blue) and a two-target (red) media where amplitude and position changes. The ideal retrieved signal is shown in the inset.

4.3 Distributed–Media FMCW Lidar

The main goal of this thesis is to set the basis for the design of a CW lidar system for gas detection with range resolution. With this idea in mind, we will study how a lidar works with a continuous, distributed target, in order to be able to propose a design for the desired system. As discussed in the last section, some aspects of the traditional FMCW lidar technique are shown not to work properly for the sounding of distributed media. This section analyzes this classical technique and details critical and specific point which prove to be drawbacks for our purposes. As a result of this study a new modification of the technique is suggested.

4.3.1 Analysis of the classical method

One way of describing a distributed-media FMCW lidar system is starting from the original configuration for solid-target detection and extending the discrete medium to a distributed medium. Then, assuming the transmitted power defined in Eq. (4.11), we need to analyze the received power.

Because the atmosphere is composed of a great number of particles and gas molecules, it can be approximated by a continuous medium from the macroscopic point of view, while showing its microscopic discrete nature in producing scattering. The signal received by a lidar system $P_R(t)$ is partially absorbed and partially scattered by the atmosphere and can be described by Eq. (4.2). For convenience in the later analysis, this equation can be written as follows:

$$P_R(t) = \int P_T\left(t - \frac{2R}{c}\right) r(R) dR, \tag{4.15}$$

with $r(R) = A_R / R^2 \beta \exp\left(-2\int_0^R \alpha(x)dx\right)$. Expression (4.15) is the convolution of the emitted power with the function *r* just defined, which can be considered as the impulse response of the medium, using the variable change $\tau = 2R/c$ (Fig. 4.12); hence:

$$P_R(t) = P_T(t) * r(t), \tag{4.16}$$

where the symbol * denotes the convolution product. In the case of only one narrow target being probed, the response is the emitted signal delayed and multiplied by the target cross section. This is consistent with a delta-shaped power profile delayed by a time τ_0: $r(\tau) = \sigma_0 \delta(\tau - \tau_0)$, where σ_0 is proportional to the backscatter coefficient without taking into account extinction effects.

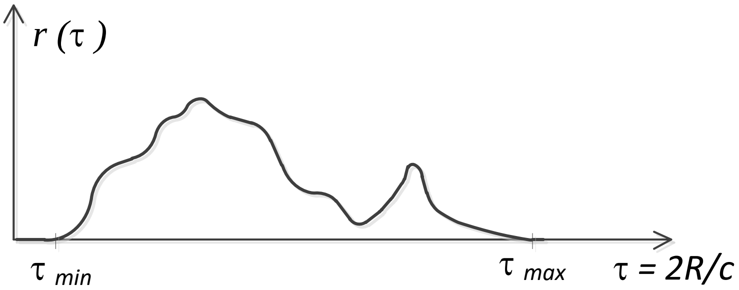

Figure 4.12. Lidar impulse response function *r*(τ) with respect to the delay *τ*.

Once the medium impulse response is defined, we can start analyzing an ideal and admittedly unrealistic case of an intensity-modulated FMCW laser radar where the frequency sweep spans from –∞ to +∞, to better explain some limitations of the technique when applied to realistic cases. In this ideal case, the expression of the received power after eliminating the DC component is:

$$P_R(t) = P_0 m_{AC} \int_0^{\tau_{MAX}} r(\tau) \cos\left\{2\pi\left[f_0(t-\tau) + \frac{K}{2}(t-\tau)^2\right]\right\} d\tau, \tag{4.17}$$

being τ_{MAX} the delay corresponding to the maximum scanned range R_{MAX} of the system ($R_{MAX} = c\tau_{MAX}/2$). Henceforth we assume the backscattered power coming from targets beyond R_{MAX} distance to be zero. Note that, unlike the case when the frequency modulation is applied to the carrier, represented by Eq. (4.8), Eq. (4.17) does not contain any target-produced phase because the use of optical direct detection does not preserve carrier characteristics such as the target-response phase. Once it has been detected by a photodetector, this signal must be mixed with the reference signal. We represent the mixing operation by a multiplication of the received signal by the local oscillator one $h(t)$:

$$h(t) = \cos\left[2\pi\left(f_0 t + \frac{K}{2}t^2\right)\right], \tag{4.18}$$

and we obtain a $g(t)$ signal:

$$g(t)=P_R(t)h(t)=\frac{P_0 m_{AC}}{2}\int_0^{\tau_{MAX}} r(\tau)\left[\cos\left\{2\pi\left[f_0\tau+\frac{K}{2}\left(2t\tau-\tau^2\right)\right]\right\}+\right.$$
$$\left.+\cos\left(2\pi\left\{f_0(2t-\tau)+\frac{K}{2}\left[t^2+(t-\tau)^2\right]\right\}\right)\right]d\tau. \tag{4.19}$$

If an appropriate low-pass filtering is applied, the sum-frequency components are eliminated and a $g_S(t)$ signal obtained:

$$g_S(t)=\frac{P_0 m_{AC}}{2}\int_0^{\tau_{MAX}} r(\tau)\cos\left\{2\pi\left[f_0\tau+\frac{K}{2}\left(2t\tau-\tau^2\right)\right]\right\}d\tau\,. \tag{4.20}$$

Eq. (4.20) shows that in this ideal case of an infinite-duration linear-FM function, we obtain an integration of sinusoids of different amplitudes and phases depending on the response of the medium to the probe signal. Hence the medium impulse response, the information we are looking for, can be obtained by means of a Fourier transform:

$$G_S(f)=\frac{P_0 m_{AC}}{4}r\left(\frac{|f|}{K}\right)\exp\left\{j\operatorname{sgn}(f)2\pi\left[f_0\frac{|f|}{K}-\frac{K}{2}\left(\frac{|f|}{K}\right)^2\right]\right\}, \tag{4.21}$$

where the fact that the Fourier transform of $\cos\left[2\pi(at+b)\right]$ is $\left[\delta(f-a)\exp(j2\pi b)+\delta(f+a)\exp(-j2\pi b)\right]/2$ has been applied. It can be observed that taking the modulus of Eq. (21) gives the information of r scaled in the frequency axis (Fig. 4.13).

This is an ideal case that helps to understand the operation principle. However the analysis needs to be extended to more realistic cases. To this end, the emitted signal is represented as a periodic sequence of chirp functions with a limited frequency deviation as shown in the previous section (Fig. 4.10):

$$P(t)=\sum_{n=-\infty}^{\infty}P_T(t-nT), \tag{4.22}$$

where

$$P_T(t)=P_0\left\{1+m_{AC}\cos\left[2\pi\left(f_0t+\frac{K}{2}t^2\right)\right]\right\}\Pi\left(\frac{t-T/2}{T}\right). \tag{4.23}$$

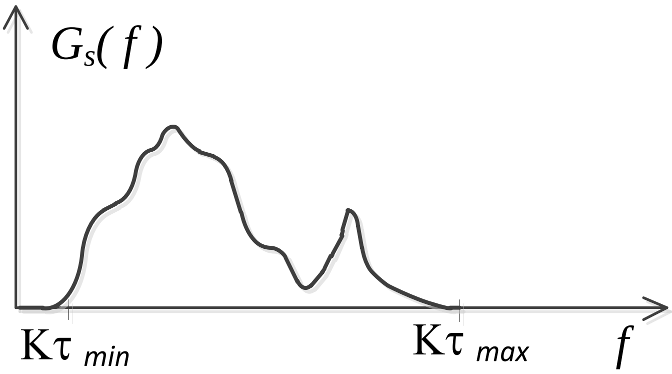

Figure 4.13. Final result for an ideal FMCW lidar system in a continuous medium.

In this case, the response of the medium to our signal after the mixing process and the low-pass filtering $g_P(t)$ would be a periodic function, counterpart to Eq. (4.20), in the following form:

$$g_p(t) = \left(\frac{P_0 m_{AC}}{2} \int_0^{\tau_{MAX}} r(\tau)\cos\left\{2\pi\left[f_0\tau + \frac{K}{2}\left(2t\tau - \tau^2\right)\right]\right\}\Pi\left(\frac{t - T/2}{T}\right)d\tau\right) * \sum_n \delta(t - nT), \quad (4.24)$$

being T the period duration. In this expression we assume $\tau_{MAX} << T$, so the received period approximately lasts from 0 to T. Moreover, it is assumed that for the data acquisition the signal is sampled respecting the Nyquist theorem limits, so the Fourier transform of the signal is:

$$\begin{aligned} G_p(f) = \frac{P_0 m_{AC}}{2T}\left[\int_{-\infty}^{\infty}\int_0^{\tau_{MAX}} r(\tau)\cos\left\{2\pi\left[f_0\tau + \frac{K}{2}\left(2t\tau - \tau^2\right)\right]\right\}d\tau \times \right. \\ \left. \times \Pi\left(\frac{t - T/2}{T}\right)\exp(-j2\pi f t)\,dt\right]\sum_m \delta\left(f - \frac{m}{T}\right). \end{aligned} \quad (4.25)$$

Eq. (4.25) can be rewritten as

$$G_p(f) = \frac{P_0 m_{AC}}{4}\left(\int_0^{\tau_{MAX}} r(\tau)\,\mathrm{sinc}\left[T(f - K\tau)\right]\exp\left\{j\left[\phi_1(\tau) + \phi_2(\tau)\right]\right\}d\tau + NP\right)\sum_m \delta\left(f - \frac{m}{T}\right), \quad (4.26)$$

with $\phi_1 = 2\pi\tau(f_0 + KT/2)$, $\phi_2 = -2\pi\left(K/2\tau^2 + fT/2\right)$ and $\mathrm{sinc}(x) = \sin(\pi x)/(\pi x)$. NP is the negative-frequency part of the function which behaves similarly to the positive-frequency, and will not be represented from now on for the sake of simplicity. As it will be seen ϕ_1 has an important impact on the target retrieval. We can instead obviate the ϕ_2 term because of its low influence (see appendix A). Assuming that in practice the time-domain signal is sampled at a sampling frequency F_s, its Fourier Transform will be periodical with all the retrieved information contained in the frequency range between 0 and $(N-1)/T$:

$$G_p\left(f\right)=\frac{P_0 m_{AC}}{4}\left\{\int_0^{\tau_{MAX}} r\left(\tau\right)\operatorname{sinc}\left[T\left(f-K\tau\right)\right]\exp\left(+j2\pi f_c\tau\right)d\tau\right\}\sum_{m=0}^{N-1}\delta\left(f-\frac{m}{T}\right), \tag{4.27}$$

with $N=F_sT$ and $f_c=f_0+KT/2$. Comparing this result with that of the ideal case with an infinite frequency deviation (Eq. (4.21)), we can see that the delta function has become a sinc function. This dramatically changes the result of the detection. Actually the effect of the sinc function combined with the exponential factor in the integrand becomes a filtering of the function r whose characteristics depend on the sweep central frequency f_c and the period frequency deviation KT. To assess the consequences of this filtering, we re-write $G_p\left(f\right)$ given by Eq. (4.27) in terms of the transform of $r\left(\tau\right)$, that is, $R\left(\nu\right)$ (see appendix B):

$$G_p\left(f\right)=\frac{P_0 m_{AC}}{4KT}\left[\int_{-\infty}^{+\infty} R\left(\nu-f_c\right)\Pi\left(\frac{\nu}{KT}\right)\exp\left(-j2\pi\nu\frac{f}{K}\right)d\nu\right]\sum_{m=0}^{N-1}\delta\left(f-\frac{m}{T}\right) \tag{4.28}$$

In this form, the filtering effect is clearly seen, as the factor $\Pi\left(\frac{\nu}{kT}\right)$ in the integral limits the probing of the medium by the system to the sweep frequency range $\left(f_c-KT/2, f_c+KT/2\right)$. The signals employed for the FMCW technique are usually bandpass with $f_0>\left(f_{\max}-f_{\min}\right)/2$ in order to allow filtering out the sum-frequency components. This means that the final resulting signal will be a bandpass filtered version of the medium response r and the low-frequency components will be lost in the process. Because aerosol concentration distributions are typically smooth and consequently r will be a baseband signal, the use of this technique as conventionally implemented for discrete targets means that it is practically impossible to recover the the r function accurately.

Some simulations have been performed in order to test these theoretical results. In Fig. 4.14 we show this band-pass effect for the case of a Gaussian-shaped impulse-response medium with a peak located at 100 meters from the lidar and with a half width at half maximum (HWHM) of 1.67 meters. The modulation applied to the emitter extends from 15 MHz to 45 MHz and the period is one millisecond. Fig. 4.14 (a) shows one period (upper axis) of the acquired return signal that corresponds to the spatial spectrum of the retrieved target shape; the bandpass filtering observed in that the lowest spatial frequency is 0.067 m^{-1}. Fig. 4.14 (b) shows the retrieved target shape. The upper right corner insets correspond to the target medium impulse response under retrieval. We can clearly observe this band-pass effect by comparing the original spectrum (inset plot in Fig. 4.14 (a)) with the one obtained by simulation.

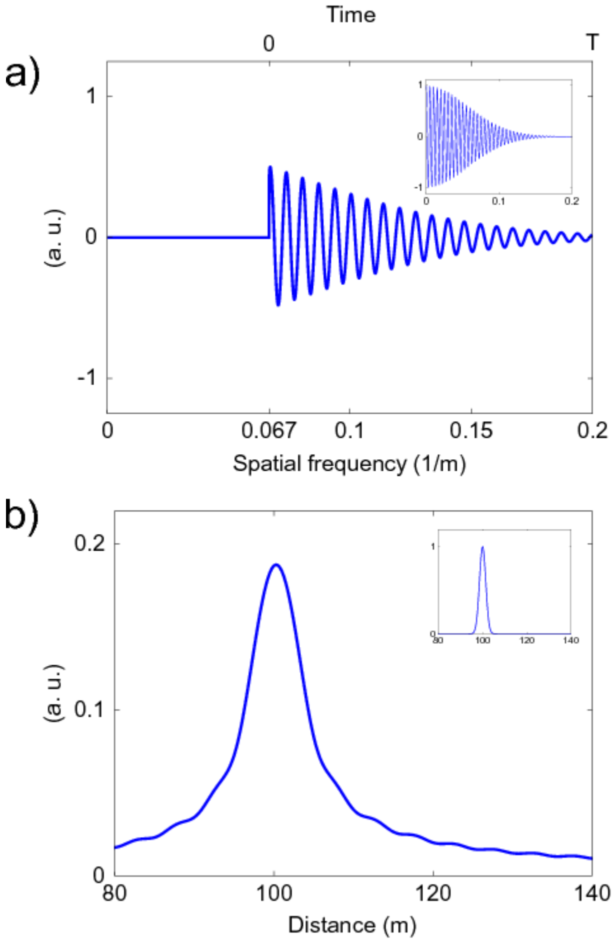

Figure 4.14. Retrieved data without sum-frequency components (a) and result after Fourier transforming (b) for a Gaussian-shaped impulse-response medium. The plot in (a) corresponds as well to real part of the recovered spatial-frequency spectrum of the target profile. Ideal retrieved signal in the insets.

Another case was simulated to show the problems of this technique in discriminating distributed targets. Fig. 4.15 shows the simulation of the retrieval of an impulse response corresponding to a rectangular pulse. The result consists of two peaks at the initial and final position of the pulse, being the information of its shape lost.

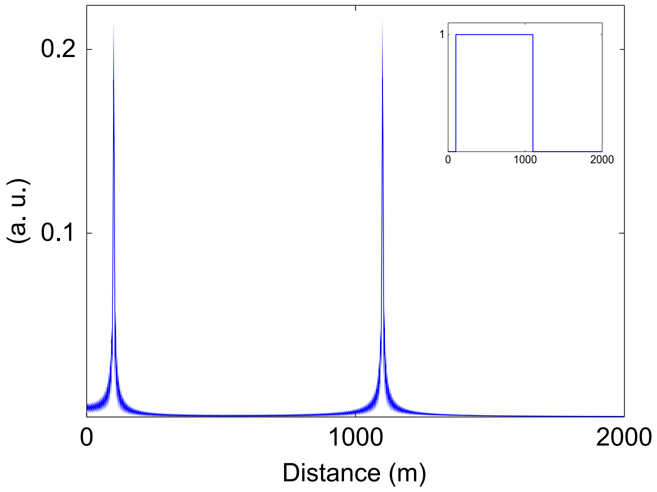

Figure 4.15. Results for the application of FMCW technique to continuous media for an idealistic rectangular impulse-response medium with the ideal retrieved signal in the inset.

From these graphics, the filtering effect pointed out is obvious. Clearly changes in the basic technique must be introduced to fully recover the response of the medium. This is dealt with in the following section.

4.3.2 Phase-Hop Solution

The loss of the low spatial-frequency content in the FMCW technique explained in the previous chapter can be traced back to the use of a bandpass frequency chirp which was applied due to need to filter out the sum-frequency components (Eq. (4.19) and (4.20)) in the receiving subsystem. To overcome this limitation the proposal put forward here is a periodic sequence of baseband chirps combined with a phase hop of the emitted signal between successive periods. This last step allows for compensating the sum-frequency components. This solution will allow the recovery of the low spatial-frequency content of the medium impulse response.

4.3.2.1 Baseband Shifting

The first step for this solution is the baseband shift of the modulating signal. If we examine the result at the end of our system in the pass-band case (Eq. (4.27)), we observe that the sinc function multiplied by a complex exponential performs a bandpass effect. This bandpass effect can be eliminated by working in a baseband environment, as per:

$$f_c = f_0 + K\frac{T}{2} = 0\,. \tag{4.29}$$

In this way we have the signal converted to baseband as is desired:

$$G_p\left(f\right) = \frac{P_0 m_{AC}}{4}\left\{\int_0^{\tau_{MAX}} r\left(\tau\right)\mathrm{sinc}\left[T\left(f - K\tau\right)\right]d\tau\right\}\sum_{m=0}^{N-1}\delta\left(f - \frac{m}{T}\right). \tag{4.30}$$

In practice, this is achieved by using a signal $P_{TB}\left(t\right)$:

$$P_{TB}\left(t\right) = \begin{cases} P_0\left(1 + m_{AC}\cos\left\{2\pi\left[f_0\left(t - \frac{T}{2}\right) + \frac{K}{2}\left(t - \frac{T}{2}\right)^2\right] + \phi_0\right\}\right); & 0 \le t < \frac{T}{2} \\ P_0\left(1 + m_{AC}\cos\left\{2\pi\left[f_0\left(t - \frac{T}{2}\right) + \frac{K}{2}\left(t - \frac{T}{2}\right)^2\right] - \phi_0\right\}\right); & \frac{T}{2} \le t < T \end{cases} \tag{4.31}$$

being ϕ_0 an arbitrary phase. Figure 4.16 shows the formal representation of this baseband-frequency version with its practical implementation as described in Eq. (4.31).

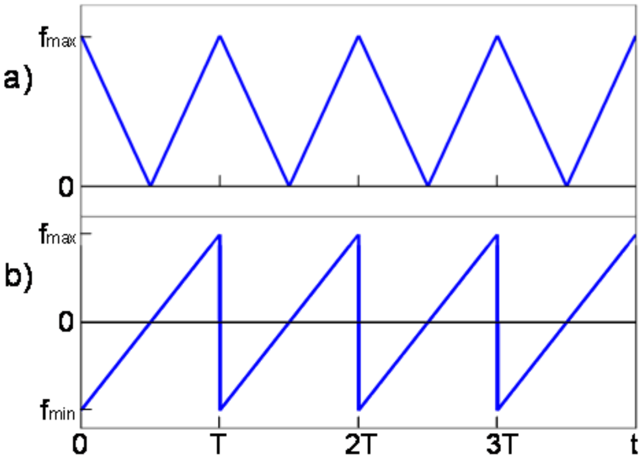

Figure 4.16. Frequency evolution in P_{TB} in real (a) and formal (b) representations

However, due to the baseband shift, the sum-frequency components are superimposed on the difference-frequency ones, if no further action is taken. Then, as shown in Fig. 4.17 for the case of an ideal rectangular impulse response, these components generate interferences which lead to a noisy-like signal. What follows is a more detailed analysis of the components of this sum-frequency.

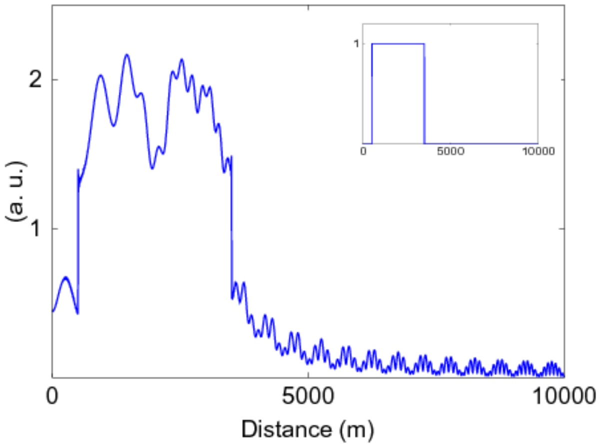

Figure 4.17. Simulation of a rectangular pulse in baseband FMCW with the ideal retrieved signal in the inset. Here, the interference from the sum-frequency components is clearly visible.

The sum-frequency components $g_{Sum\_F}(t)$ filtered out in the conventional implementation of FMCW technique (see Eq. (4.19)) are those which interfere with data signal and have the form:

$$g_{Sum\_F}(t)=\frac{P_0 m_{AC}}{2}\int_0^{\tau_{MAX}} r(\tau)\cos\left(2\pi\left\{f_0(2t-\tau)+\frac{K}{2}\left[t^2+(t-\tau)^2\right]\right\}\right)d\tau\,, \tag{4.32}$$

its Fourier transform (see appendix C) being:

$$G_{Sum\_F}(f)=\frac{C_I}{2}\exp\left[-j2\pi\frac{(f-f_0)^2+f_0^2}{2K}\right]\int_0^{\tau_{MAX}} r(\tau)\exp\left[j2\pi\frac{K}{4}\left(\tau-\frac{f}{K}\right)^2\right]d\tau\,, \tag{4.33}$$

with C_1 a constant factor. In Eq. (4.33), there is an exponential term (left) independent of τ -common for all targets-, and an integrated exponential term (right) that varies depending on the range (or its corresponding delay τ) of the targets. Figure 4.18 shows the real part of the sum-frequency components: the integral in Eq. (4.33), without the common phase factor and normalizing with respect to one-target case, has been plotted for three different cases, of a) one target (100 m), b) four equidistant targets (100…400 m), and c) twenty equidistant targets (100…2000 m). The relevant characteristic is the constructive addition of the different sum-frequency components. As the continuous medium target becomes more extended, the sum-frequency components energy becomes more concentrated in the zone where targets are located, leading to distortions in the final result that cannot be simply considered as random noise.

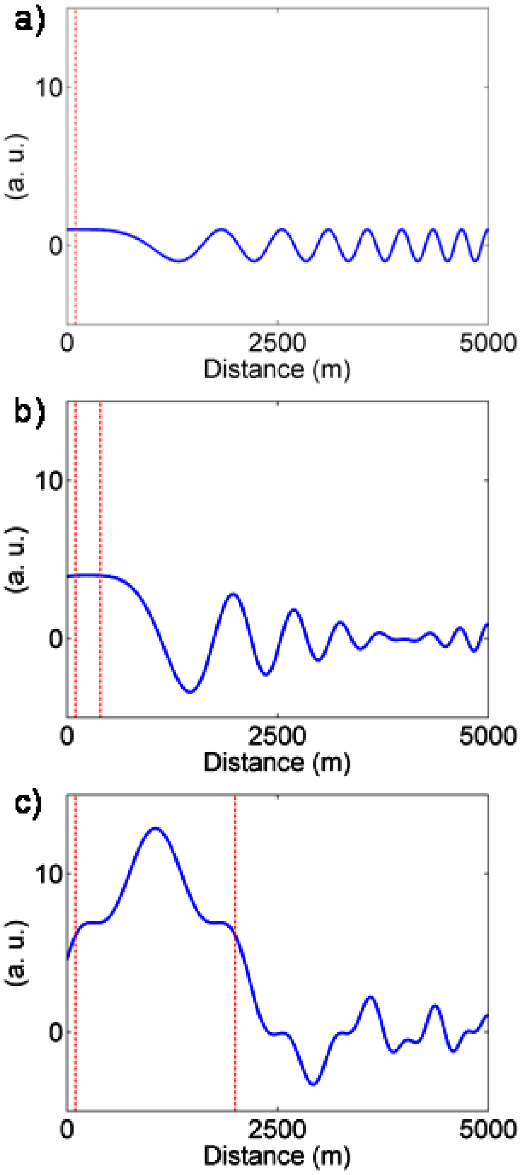

Figure 4.18. Real part of the sum-frequency components generated in three different cases: a) one point target (100 m), b) four equidistant point targets (100…400 m), and c) 20 equidistant point targets (100…2000 m). Dotted lines mark the zone where targets lie.

4.3.2.2 Sum-frequency Compensation

The sum-frequency components can be eliminated by changing the initial phase for successive periods (phase hop), so that one pulse will have phase ϕ_0 and the next one, $\phi_0 + \pi / 2$. This idea comes from the basic cosine product formula:

$$\cos(a)\cos(b) = \frac{1}{2}\left[\cos(a-b) + \cos(a+b)\right]. \tag{4.34}$$

Looking at the formula, if we add a $\pi / 2$ shift to both phases a and b, we will obtain a similar result to the previous one but with an added π phase in the second term on the right. If we add both versions, with and without this $\pi / 2$ phase, the first term will double and the second one will disappear because the phase is opposite in the first version with respect to the second version. Having in mind this scheme, we can design a signal $h(t)$ with two concatenated periods $\pi / 2$ out of phase:

$$h(t) = \left\{\cos\left[2\pi\phi_{FM}(t)\right]\Pi\left(\frac{t-T/2}{T}\right) + \cos\left[2\pi\phi_{FM}(t-T) + \frac{\pi}{2}\right]\Pi\left(\frac{t-3T/2}{T}\right)\right\} * \sum_n \delta(t-2nT), \tag{4.35}$$

where $\phi_{FM}(t) = f_0(t-T/2) + K/2(t-T/2)^2$. The received signal would then be:

$$P_R(t) = P_0 m_{AC}\left(\int_0^{\tau_{MAX}} r(\tau)\left\{\cos\left[2\pi\phi_{FM}(t-\tau)\right]\Pi\left(\frac{t-T/2}{T}\right) + \right.\right.$$
$$\left.\left. + \cos\left[2\pi\phi_{FM}(t-T-\tau) + \frac{\pi}{2}\right]\Pi\left(\frac{t-3T/2}{T}\right)\right\} d\tau\right) * \sum_n \delta(t-2nT), \tag{4.36}$$

and the mixed signal $g(t)$:

$$g(t) = P_R(t)h(t) = P_0 m_{AC}\left(\int_0^{\tau_{MAX}} r(\tau)\left\{\cos\left[2\pi\phi_{FM}(t)\right]\cos\left[2\pi\phi_{FM}(t-\tau)\right]\Pi\left(\frac{t-T/2}{T}\right) + \right.\right.$$
$$\left.\left. + \cos\left[2\pi\phi_{FM}(t-T) + \frac{\pi}{2}\right]\cos\left[2\pi\phi_{FM}(t-T-\tau) + \frac{\pi}{2}\right]\Pi\left(\frac{t-3T/2}{T}\right)\right\} d\tau\right) * \sum_n \delta(t-2nT). \tag{4.37}$$

If we reorder the terms of this mixed signal, we obtain:

$$g(t) = P_0 m_{AC}\left[\int_0^{\tau_{MAX}} r(\tau)\left(\left[\cos(\theta_-) + \cos(\theta_+)\right]\Pi\left(\frac{t-T/2}{T}\right) + \right.\right.$$
$$\left.\left. + \left\{\left[\cos(\theta_-) + \cos(\theta_+ + \pi)\right]\Pi\left(\frac{t-T/2}{T}\right)\right\} * \delta(t-T)\right) d\tau\right] * \sum_n \delta(t-2nT), \tag{4.38}$$

where

$$\begin{aligned}
\theta_- &= 2\pi\left[f_0\tau + \frac{K\tau}{2}\left(2t-\tau-T\right)\right] \\
\theta_+ &= 2\pi\left\{ f_0\left[2\left(t-\frac{T}{2}\right)-\tau\right]+\frac{K}{2}\left[\left(t-\frac{T}{2}\right)^2+\left(t-\frac{T}{2}-\tau\right)^2\right]\right\}.
\end{aligned} \tag{4.39}$$

Finally, we perform the Fourier transform and separate the difference-frequency components from the sum-frequency ones:

$$\begin{aligned}
G(f) = P_0 m_{AC}\Bigg(\int_0^{\tau_{MAX}} r(\tau)\Bigg\{ & FT\left[c\mathrm{os}(\theta_-)\Pi\left(\frac{t-T/2}{T}\right)\right]\left[1+\exp\left(-j2\pi fT\right)\right]+ \\
+FT\left[\cos(\theta_+)\Pi\left(\frac{t-T/2}{T}\right)\right]\left[1-\exp\left(-j2\pi fT\right)\right]\Bigg\} d\tau\Bigg) & \frac{1}{2T}\sum_m \delta\left(f-\frac{m}{2T}\right).
\end{aligned} \tag{4.40}$$

To better understand this result, we note that this function is sampled in the points indicated by the delta-function train. So the valid points will be the ones where $f = m/2T$. Hence separating both terms, we see how they behave in these points:

Diff. frequency: $FT\left[\cos(\theta_-)\Pi\left(\frac{t-T/2}{T}\right)\right]\left[1+\exp\left(-j2\pi fT\right)\right] \qquad f=\frac{m}{2T}$ (4.41)

Sum frequency: $FT\left[\cos(\theta_+)\Pi\left(\frac{t-T/2}{T}\right)\right]\left[1-\exp\left(-j2\pi fT\right)\right] \qquad f=\frac{m}{2T}$ (4.42)

The difference-frequency components appear in the even cases of m and become zero in the odd cases. Conversely, the sum-frequency components appear in the odd cases of m and are zero in the even cases. Since the objective here is to eliminate the sum-frequency components due their distortion effect, then we can simply sample this signal at the even m points, where we only have the difference-frequency components. This allows us to recover the original *r* signal.

4.3.2.3 Simulations

Different simulations were performed to validate the results reported above. First, the simulation of a point target allows one to observe the correspondence between the original signal (in the figure inset) and the final result (Fig. 4.19), except those effects of low-pass filtering that cause this change from a delta-shaped response to a sinc function response. Whether the phase-hop method is applied or not, the result is almost the same in the case of a narrow target because of the high dispersion of the sum-frequency components.

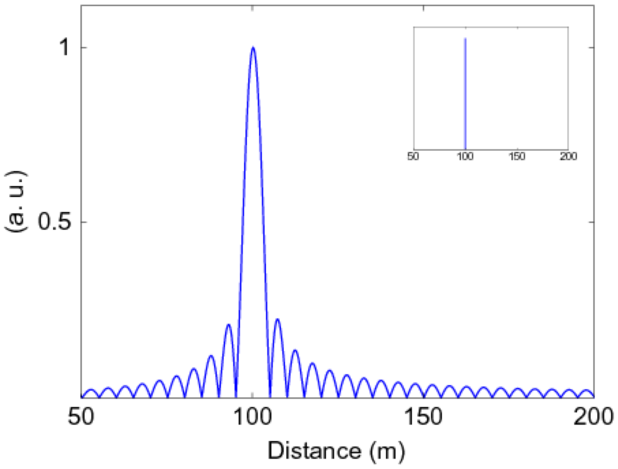

Figure 4.19. Simulation with the Phase-Hop method of a solid target with the ideal retrieved signal in the inset.

The signals retrieved from two distributed targets (or medium impulse responses) are plotted in Figure 4.20 with the original target shape depicted in the insets. In Figure 4.20 (a), the impulse response of the medium is constant between 100 and 1100 m; while in Fig. 4.20 (b), the medium impulse response has a Gaussian-like profile. The results show that for the case of extended continuous media, the effects of the sum-frequency components (dashed lines) produce unacceptable distortions in the retrieval and must be removed.

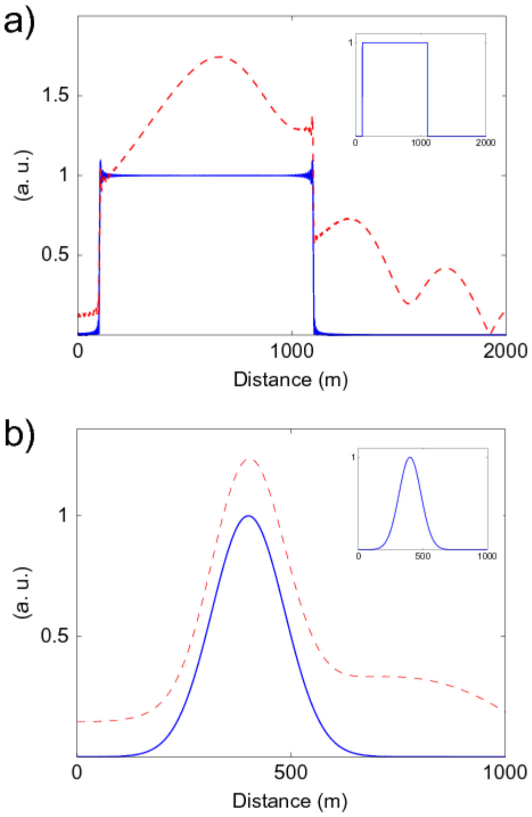

Figure 4.20. Simulations of a rectangular-pulse (a) and a Gaussian (b) shaped impulse-response medium with (solid) and without (dashed) Phase-Hop with the ideal retrieved signal in the insets.

Finally, we have the simulation of a lidar-like signal (Fig. 4.21) as an extended target with homogeneous backscatter coefficient, where both the effects of range and overlap function were considered. In this simulation, two inhomogeneities, with square and Gaussian shapes respectively, were located along the homogeneous media. Figure 4.21 (a) shows the retrieved raw signal, and Figure 4.21 (b) shows the retrieved range-corrected signal with (solid line) and without (dashed line) phase-hop method, whereas the dotted line corresponds to the ideally retrieved data. While the retrieved signal using the phase-hop method is almost equal to the ideal signal, excepting limited-bandwidth effects that will ultimately limit the resolution, the retrieved signal without applying this method is heavily distorted. As in the previous cases, because this signal is extended in range, the sum-frequency components have a significant effect and must be removed in order to obtain accurate results.

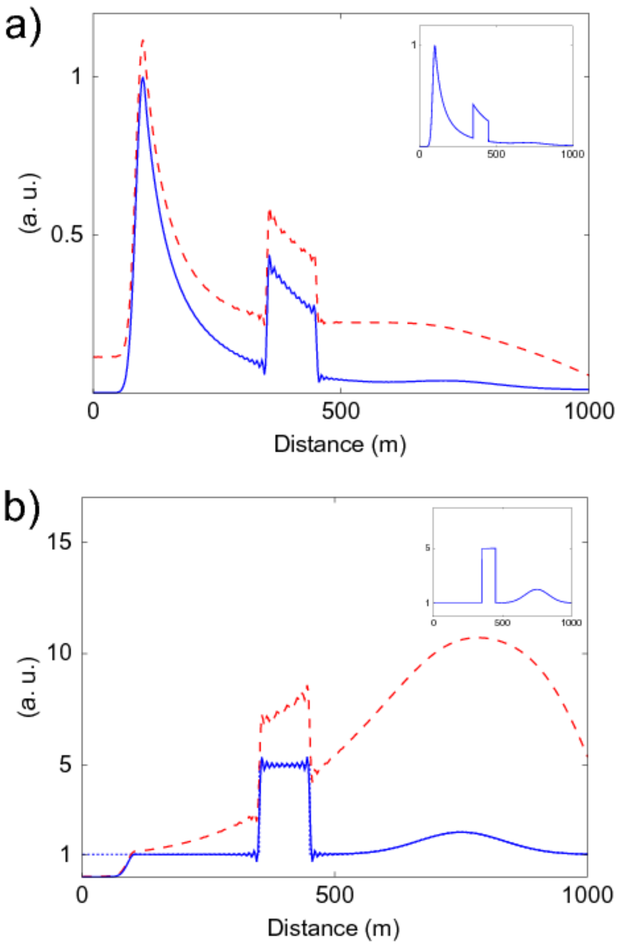

Figure 4.21. Simulation of the retrieved signal (a) and the corresponding processed data (b) of a lidar-like signal with both a rectangular and a Gaussian-shaped targets along the path while using (solid line) or not (dashed line) the Phase-hop method. The dotted line corresponds to the ideally retrieved data.

To provide a numerical value which shows the accuracy of the retrieved profile with respect to the real target shape, the normalized correlation coefficient for the range-corrected signals is calculated in both cases in the range between 100 m. and 1 km as expressed in Eq. (4.43):

$$\rho = \frac{\int x(z)\, y(z)\, dz}{\left[\int x^2(z)\, dz \int y^2(z)\, dz\right]^{1/2}} \,. \tag{4.43}$$

When the phase-hopping method is applied in the last example, a value of 0.998 is obtained for ρ as compared to 0.80 when the method is not applied.

4.3.3 FMCW lidar SNR

To complete the assessment of the FMCW technique as a candidate for remote sensing of distributed media requires an analysis of the signal-to-noise ratio (SNR). The method used for this calculation is based upon the conventional matched filter theory applied to range-resolved systems using long temporal signals which are compressed after detection [39]. This theory states that for a certain time t_M, the ideal SNR can be expressed as:

$$SNR_i = \frac{\left|s_0(t_M)\right|^2}{\overline{n_0^2(t_M)}} \,. \tag{4.44}$$

where s_0 is the received signal at t_M and n_0 the noise after detection. So if we write this SNR after the detection process we have the expression:

$$SNR_i = \frac{\left|\int_{-\infty}^{\infty} d\omega H(\omega) S(\omega) \exp(j\omega t_M)\right|^2}{\pi N_0 \int_{-\infty}^{\infty} d\omega \left|H(\omega)\right|^2} \tag{4.45}$$

where $S(\omega)$ is the Fourier transform of the signal before detection, $H(\omega)$ is the Fourier transform of $h(t)$, the matched filter function, and N_0 is the electrical noise power spectral density, which is assumed to be additive white noise (AWN). If we take into account the Schwartz inequality:

$$\left|\int_{-\infty}^{\infty} d\omega A(\omega) B(\omega)\right|^2 \le \int_{-\infty}^{\infty} d\omega \left|A(\omega)\right|^2 \int_{-\infty}^{\infty} d\omega \left|B(\omega)\right|^2 \tag{4.46}$$

where the equality holds when $A(\omega) = KB^*(\omega)$. Then we have:

$$SNR_i \le \frac{1}{\pi N_0} \int_{-\infty}^{\infty} d\omega \left|S(\omega)\right|^2 = \frac{E_{Period}}{N_0/2} \tag{4.47}$$

where E_{Period} is the energy of the detected period. For the FMCW technique, detection is not performed with the exact matched filter but by mixing the received signal with the emitted signal. In this way, the system complexity is reduced and the coherence between the local-oscillator and the received signals improves the final result substantially, however there is a drawback. In the mixing process, the product of two cosine signals gives a difference-frequency component (our final signal) and a sum-frequency component with its energy scattered over a broad bandwidth, which reduces the signal power level by a factor of 2. Meanwhile the noise undergoes the same process, but due to the presence of the image-frequency component its final power value remains the same. The outcome is the reduction of the SNR ratio by a factor 2, as seen in Eq. (4.48):

$$SNR = \frac{SNR_i}{2} = \frac{E_{Period}}{N_0} \tag{4.48}$$

From this point on the case of the backscattered power coming from the target at distance R will be analyzed. With respect to the variables in the SNR expression, in this case, s_0 corresponds to the electrical amplitude of the signal coming from this distance R just after detection, that is, $\Re P_{Rec}$, where $\Re$ is the optoelectronic conversion factor [Amperes/Watts] and P_{Rec} the AC optical signal amplitude. Moreover, N_0 corresponds to the electrical-noise power spectral density. So, E_{Period} can be expressed as:

$$E_{Period} = \int_0^T dt\, \Re^2 g_p(t)\Big|_R^2 = \int_0^T dt \Re^2 P_{Rec}^2 \cos^2\left[2\pi\left(f_0 t + \frac{K}{2}t^2\right)\right] = \frac{\Re^2 P_{Rec}^2 T}{2} \tag{4.49}$$

being $g_p(t)\big|_R$ the optical received signal coming from distance R, as shown in Eq. (4.20). Here it is assumed that the amplitude of the backscattered signal is approximately constant, so P_{Rec} is:

$$P_{\mathrm{Rec}} = P_0 m_{AC} r(R) = P_0 m_{AC} \beta(R) \Delta R \frac{A_R}{R^2} \xi T_0^2. \tag{4.50}$$

where ΔR is the resolution distance, ξ is the receiving optical-system transmittance and T_0 is the transmittance of medium between the lidar and the scattering volume, and P_0, A_R and m_{AC} have been defined previously. To account for all the noise sources, we need the expression of background power, P_B:

$$P_B = E \Delta\lambda_{filter} \pi \theta^2 A_R \tag{4.51}$$

where E is the background spectral irradiance, $\Delta\lambda_{filter}$ is the optical filter bandwidth and $\pi\theta^2$ is the solid angle of vision. Then, noise power, P_N is given by:

$$P_N = \sqrt{P_q \cdot \left(P_{Rec} + P_B\right) + NEP^2 \cdot \Delta f_D} \tag{4.52}$$

where Δf_D is the detector electrical bandwidth, NEP is the photoreceiver noise equivalent power and P_q is the equivalent quantum noise power given by:

$$P_q = \frac{2hc\Delta f_D F}{\eta\lambda} \tag{4.53}$$

where h is the Planck constant and F the photodetector excess noise factor [40]. Finally, we can write an expression for the electrical noise power spectral density:

$$N_0 = \frac{(\Re P_N)^2}{\Delta f_D} = \Re^2\left(\frac{P_q}{\Delta f_D}\left(P_{Rec}+P_B\right)+NEP^2\right) \tag{4.54}$$

Table 4.2. Values for the calculation of the SNR

Variable	Value
Incident DC power: P_0	150 [mW]
Modulation factor: m_{AC}	0.8
Backscatter coefficient: β	10^{-6} [$m^{-1}\cdot sr^{-1}$]
Resolution range: ΔR	5 [m]
Telescope area (20-cm diameter): A_R	$\pi\cdot 0.1^2$ [m^2]
Target range: R	10^3 [m]
Receiving optical-system transmittance: ξ	0.7
Quantum efficiency: η	0.7
Medium transmittance: T_0	~1
Noise equivalent power: NEP	10^{-13} [$W\cdot Hz^{-1/2}$]
Electrical bandwidth: Δf_D	$30\cdot 10^6$ [Hz]
Receiver noise: $P_{N\_Rec} = NEP\sqrt{\Delta f_D}$	5.5 10^{-10} [W]
Background spectral radiance: E	7 [$Wm^{-2}sr^{-1}\mu m^{-1}$]
Optical filter bandwidth: $\Delta\lambda_{filter}$	0.010 [μm]
Solid angle: $\pi\theta^2$	$0.78\cdot 10^{-6}$ [sr]
Photodetector excess noise factor: F	5
Wavelength: λ	1 [μm]
Background power: P_B	$1.7\cdot 10^{-9}$ [W]
Equivalent quantum noise power: P_q	$8.5\cdot 10^{-11}$ [W]
Time period: T	10^{-3} [s]

So we have an SNR equal to:

$$SNR = \frac{E_{Period}}{N_0} = \frac{P_{\mathrm{Rec}}^2}{P_N^2}\frac{T}{2}\Delta f_D \tag{4.55}$$

Finally, if we take into account the coherent averaging of signal periods we have:

$$SNR = M\,\frac{P_{\mathrm{Rec}}^2}{P_N^2}\frac{T}{2}\Delta f_D \tag{4.56}$$

where M corresponds to the number of averaged periods. At this point, we can perform the calculation of the SNR for a certain realistic case with typical values for the components of the system. Table 4.2 shows the values for the different variables to be taken into account.

The backscatter coefficient in table 4.2 has been taken for a clear atmosphere at around 1 micrometer wavelength [22]. The background spectral radiance is a common value for a sunlit clear sky [41]. In practical situations higher backscatter coefficient and lower background spectral radiance are likely to be encountered. The NEP is a conservative value for commercial APD-amplifier modules [see, for instance, Perkin Elmer Optoelectronics C30659 series], the excess noise factor is typical for APD photodiodes and the solid angle has been calculated for a detector with 2-mm diameter and a telescope with 2 m. of focal length. Using these values, we have a value of received signal power equal to:

$$P_{Rec} = 0.150\cdot 0.8\cdot 10^{-6}\cdot 5\cdot\frac{\pi\cdot 0.1^2}{\left(10^3\right)^2}\cdot 0.7\cdot 1 \approx 1.32\cdot 10^{-14}\left[W\right] = -108.8\left[dBm\right] \tag{4.57}$$

And a noise power of:

$$P_N = \sqrt{8.5\cdot 10^{-11}\cdot\left(1.32\cdot 10^{-14} + 1.7\cdot 10^{-9}\right) + 10^{-26}\cdot 3\cdot 10^{7}} = 6.67\cdot 10^{-10} \approx -61.8\left[dBm\right] \tag{4.58}$$

The signal-to-noise ratio then becomes:

$$\boxed{SNR = \frac{E_{Period}}{N_0} = \frac{\left(\Re P_{Rec}\right)^2 T/2}{\left(\Re P_N\right)^2/\Delta f_D} = \frac{P_S^2}{P_N^2}\frac{T}{2}\Delta f_D = -52dB} \tag{4.59}$$

This is the case of the electrical single-period (no averaging) SNR for a diffuse target at a distance of 1 km and a signal with a period length of 1-millisecond. The next graphic shows the evolution of the SNR along the range R for different values of period averaging M, equivalent to time periods of length equal to MT.

The evolution of the SNR shows a negative quadratic slope with range because of the dependence of P_{Rec} with the range R while the noise power is almost constant with R. It can be seen that for an integration time of 1 second ($M = 10^3$) the lidar system obtains an SNR of some 15 dB around 10 meters. This level is achieved at an approximate distance of 100 meters in the case $M = 6\cdot 10^4$ (equivalent to 1 minute integration), and at some 1000 meters in the case of $M = 3.6\cdot 10^6$, equivalent to 1 hour integration.

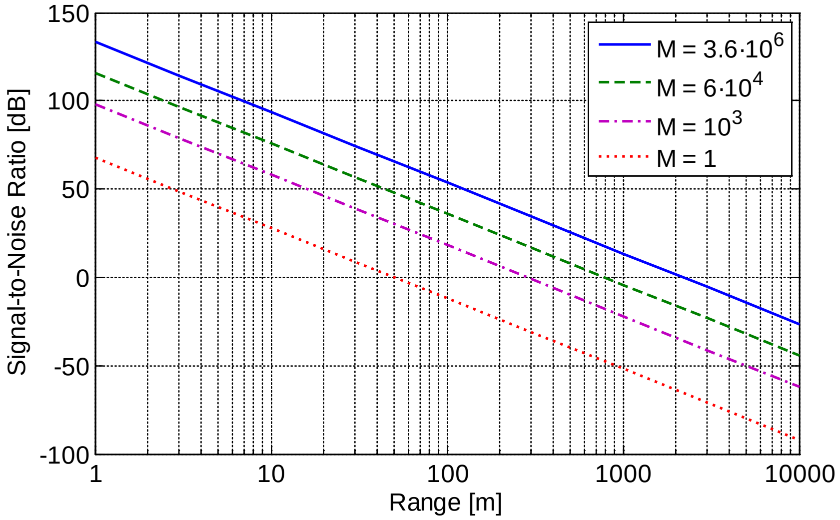

Figure 4.22. Evolution of the signal-to-noise ratio (SNR) with the distance to the target R for different number of averaged periods M

4.4 *FMCW for gas detection*

As stated in the introduction, a principal goal of this thesis is to investigate the feasibility of range-resolved FMCW systems for gas remote sensing. These references [1,2] constitute the basis upon which the contributions of this thesis to the FMCW technique for the detection of spatial distributions are developed. The previous section outlines the analysis and development of a range-resolved aerosol detection system, which was required prior to conducting such a feasibility study. This section details the next step in the investigation, that of the study of the proposed gas-sensing system model, which was developed from the aerosol-detection model. Figure 4.23 shows an example of interaction between the radiation and the absorption line and the by-product of the components of multiples of the fundamental-frequency.

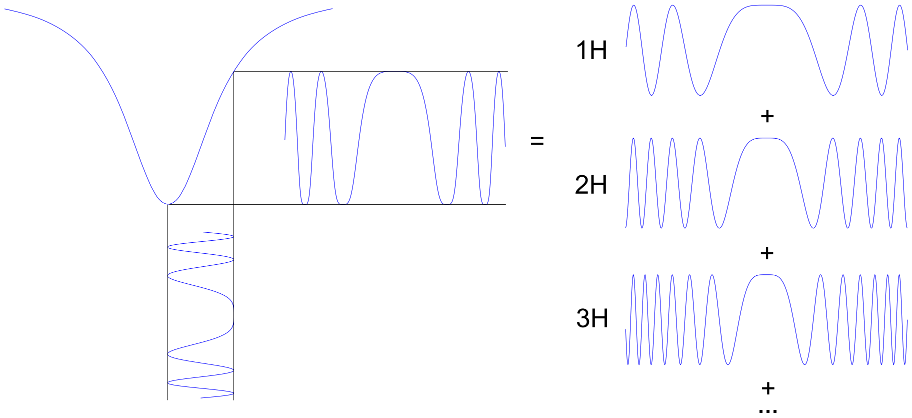

Figure 4.23. Interaction between the emitted wavelength-modulated signal and the gas absorption line producing the different harmonics (1H, 2H, 3H, etc).

Firstly, the application of the reflector-aided integrated gas detection technique is described. This is followed by a description of how this technique is extended to distributed media, parallel to the aerosol case. In the second section a general case is developed, followed by the presentation of a special case with low-level wavelength modulation. A series of simulations and an SNR analysis were carried out in order to test the viability of the technique. Finally, the phase-hop method was applied to resolve the problem of distortion due to the presence of higher harmonics, and a series of simulations were performed during which gas concentrations in a certain medium were retrieved.

4.4.1 FMCW integrated gas detection

Prior to the study of the range-resolved system for gas detection, a detailed analysis of the system for integrated (column) gas concentration measurement was performed, with the help of a topographical target to generate the echo signal. Thus helping to facilitate understanding of the fundamentals of the technique to be applied later to a more complex, range-resolved system.

I shall begin in reference to Eq. (4.10) and (4.12). Eq. (4.10) gives the expression of the current applied to the laser diode in the FMCW system for aerosol detection:

$$i\left(t\right)=i_0+\Delta i\cos\left[2\pi\left(f_0t+Kt^2/2\right)\right]. \tag{4.10}$$

Eq. (4.12) gives the laser-diode output optical field for that applied current:

$$u(t)=\sqrt{P\left(t\right)}\cos\left(2\pi\nu_{LAS}\left(t\right)+2\pi\delta_\nu\int_0^{t-t_0}i(t')dt'\right). \tag{4.12}$$

For the purposes of this study, it is crucial to take into account two important elements in equation (4.12). Firstly, as previously seen in section 4.2.2., the power emitted by the laser diode $P\left(t\right)$ is proportional to the injection current. Secondly, the output-light wavelength is dependent on the injection current through the coefficient δ_ν. This coefficient can be considered to remain constant over small variations of input current. Where this is the case (as described in Chapter 3 - WMS theory) wavelength dependence on current is practically linear. This brings us to the possibility of modulating the FMCW-system emitted light around a wavelength where a particular absorption line of a gas under measurement is located, as explained below.

Assuming that the laser source is wavelength-modulated, we have an output radiation field of:

$$u\left(t\right)=U\left(t\right)\cos\left\{2\pi\left[\nu_0+\Delta\nu(t)\right]t+\varphi\right\}. \tag{4.59}$$

where $U\left(t\right)$ is the field amplitude, ν_0 the radiation carrier optical frequency, $\Delta\nu(t)$ frequency modulation, and φ represents the random phase term.

Also assuming an atmospheric extinction coefficient of $\alpha=\alpha(R,\nu)$, where the presence of a gas introduces a marked dependence on the optical frequency of radiation ν. In turn, the extinction coefficient can be split into two parts: the first corresponds to aerosol-induced extinction, $\alpha_a(R)$, with negligible wavelength dependence where small range wavelength deviations occur, and the second to the marked frequency dependence contributed by the gas, $\alpha_g(R,\nu)$:

$$\alpha(R,\nu) = \alpha_a(R) + \alpha_g(R,\nu)\,. \tag{4.60}$$

The above expression does not take into account the extinction effect of molecular (Rayleigh) scattering. In turn $\alpha_g(x,\nu)$ can be written as

$$\alpha_g(x,\nu) = N(x)\sigma\, g(\nu) \tag{4.61}$$

where $N(x)$ is the gas concentration $\left[m^{-3}\right]$, σ the gas absorption cross-section at the optical frequency for which maximum absorption occurs, and $g(\nu)$ the normalized absorption-line shape.

If we allow for both power and wavelength variations in the transmitted radiation, the lidar return at time t from a topographic target at range R will be

$$P_R(t) = P_T^t\left(t - \frac{2R}{c}\right)\frac{A_R}{R^2}\rho_{top} e^{-2\int_0^R \alpha[x,\nu(t-2R/c)]dx} \tag{4.62}$$

where $P_T^t(t)$ is the time-dependent transmitted power, ρ_{top} [sr^{-1}] the target surface reflectivity, and $\nu(t)$ the optical frequency of the radiation leaving the transmitter. For the purpose of this study, partial overlap effects between the transmitted beam and the receiver field of view are considered irrelevant.

In turn we can split the integral in the argument of the exponential according to Eq. (4.60):

$$\begin{aligned} &\int_0^R \alpha\left[x,\nu(t-2R/c)\right]dx = \int_0^R \alpha_a(x)\,dx + \int_0^R \alpha_g\left[x,\nu(t-2R/c)\right]dx = \\ &\tau_a(R) + \int_0^R \alpha_g\left[x,\nu(t-2R/c)\right]dx \end{aligned} \tag{4.63}$$

where $\tau_a(R)$ gives the aerosol contribution to optical thickness between the lidar system and the range R. Using Eq. (4.61), the last integral in the above expression can be expressed:

$$\int_0^R \alpha_g\left[x,\nu(t-2R/c)\right]dx = \sigma g\left[\nu(t-2R/c)\right]\int_0^R N(x)\,dx \tag{4.64}$$

Using Eq. (4.63) and (4.64), the exponential in Eq. (4.62) can be written as

$$e^{-2\int_0^R \alpha[x,\nu(t-2R/c)]dx} = e^{-2\tau_a(R)} e^{-2\sigma g[\nu(t-2R/c)]\int_0^R N(x)dx} \tag{4.65}$$

or, by defining the aerosol transmittance back and forth between *0* and R as $T_a(R) = e^{-2\tau_a(R)}$

$$e^{-2\int_0^R \alpha[x,\nu(t-2R/c)]dx} = T_a(R)\, e^{-2\sigma g[\nu(t-2R/c)]\int_0^R N(x)dx} \tag{4.66}$$

so that the lidar Eq. (4.62) can be written as

$$P_R(t) = A_R P_T \left(t - \frac{2R}{c} \right) \frac{\rho_{top}}{R^2} T_a(R)\, e^{-2\sigma g[\nu(t-2R/c)]\int_0^R N(x)dx} \tag{4.67}$$

Focusing on the behavior over time of the factor $e^{-2\sigma g[\nu(t-2R/c)]\int_0^R N(x)dx}$ in the above integral, the notation is simplified by defining the optical depth of the gas $\tau_g(R)$ as:

$$\tau_g(R) = \sigma \int_0^R N(x)\, dx \tag{4.68}$$

so that

$$e^{-2\sigma g[\nu(t-2R/c)]\int_0^R N(x)dx} = e^{-2\tau_g(R) g[\nu(t-2R/c)]} \tag{4.69}$$

Note that information for gas concentration is contained in the optical depth of the gas $\tau_g(R)$. Expression (4.69) represents the transmittance back and forth between 0 and R due to the gas:

$$T_g(\tau_g(R), \nu(t,R)) = e^{-2\tau_g(R) g[\nu(t-2R/c)]} \tag{4.70}$$

chirp Referring back to the initial assumption in which the optical frequency is given in Eq. (4.59) and assuming a sinusoidal dependence of the time-dependent term:

$$\nu(t) = \nu_0 + \Delta\nu(t) = \nu_0 + \Delta\nu_{\max} \cos\left[2\pi(f_0 t + K t^2 / 2) \right] \tag{4.71}$$

with $\Delta\nu_{\max}$ giving the maximum optical frequency deviation of the carrier. The gas transmittance (Eq. (4.70)) can be written thus:

$$T_g\left(\tau_g, \nu\right) = e^{-2\tau_g(R) g\left\{\nu_0 + \Delta\nu_{\max} \cos\left[2\pi(f_0(t-2R/c) + K(t-2R/c)^2/2)\right]\right\}} \tag{4.72}$$

We can then perform a cosine series development of Eq. (4.72) obtaining:

$$T_g\left(\tau_g, \nu, t\right) = \sum_{n=0}^{\infty} T_{g,n}\left(\tau_g, \nu\right) \cos\left[2\pi n \left(f_0\left(t - 2R/c\right) + K\left(t - 2R/c\right)^2 / 2 \right) \right] \tag{4.73}$$

In chapter 2 the cosine-series coefficients were calculated for the case of low values of $\tau_g(R)$ in [13] and [18] (WMS Theory), however a general development for the case in Eq. 4.72 has yet to be carried out since this does not fall within the scope of this study. Nevertheless a number of simulations have been performed to demonstrate the viability of this approach and to assess what sounding signal would be required according to the characteristics of the probed medium.

These simulations are outlined in section 4.4.2.

Following these developments the lidar Eq. (4.67) is then expressed as

$$\begin{aligned} P_R(t) = A_R P_T\left(t-\frac{2R}{c}\right)\frac{\rho_{top}}{R^2}T_a(R)\times \\ \sum_{n=0}^{\infty}T_{g,n}\left(\tau_g,\nu\right)\cos\left[2\pi n\left(f_0\left(t-2R/c\right)+K\left(t-2R/c\right)^2/2\right)\right] \end{aligned} \tag{4.74}$$

At this point, we can apply formula (4.11) to Eq. (4.74):

$$P_T(t) = \gamma_{IP}\left(i\left(t\right)-i_{th}\right) = P_0\left\{1+m_{AC}\cos\left[2\pi\left(f_0 t+\frac{Kt^2}{2}\right)\right]\right\} \tag{4.11}$$

to obtain:

$$\begin{aligned} P_R(t) \approx P_0^{'}\left(R\right)\left\{1+m_{AC}\cos\left[2\pi\left(f_0\left(t-2R/c\right)+\frac{K\left(t-2R/c\right)^2}{2}\right)\right]\right\}\times \\ \sum_{n=0}^{\infty}T_{g,n}\left(\tau_g,\nu\right)\cos\left[2\pi n\left(f_0\left(t-2R/c\right)+K\left(t-2R/c\right)^2/2\right)\right], \end{aligned} \tag{4.75}$$

where all the constant terms affecting power have been grouped in $P_0^{'}\left(R\right)$:

$$P_0^{'}\left(R\right) = P_0 A_R\frac{\rho_{top}}{R^2}T_a(R)\,. \tag{4.76}$$

At this point, we can separate the different components of $P_R(t)$ in order to see the structure of the received signal. The DC component and the amplitude of the first two non-zero-frequency terms in Eq. (4.75) are given by:

$$\begin{aligned} P_R^{(0)} &= P_0^{'}\left(R\right)\cdot\left(T_{g,0}\left(\tau_g,\nu\right)+\frac{m_{AC}}{2}T_{g,1}\left(\tau_g,\nu\right)\right), \\ P_R^{(1)} &= P_0^{'}\left(R\right)\cdot\left[T_{g,1}\left(\tau_g,\nu\right)+\frac{m_{AC}}{2}\left(T_{g,0}\left(\tau_g,\nu\right)+T_{g,2}\left(\tau_g,\nu\right)\right)\right], \\ P_R^{(2)} &= P_0^{'}\left(R\right)\cdot\left[T_{g,2}\left(\tau_g,\nu\right)+\frac{m_{AC}}{2}\left(T_{g,1}\left(\tau_g,\nu\right)+T_{g,3}\left(\tau_g,\nu\right)\right)\right]. \end{aligned} \tag{4.77}$$

On mixing the received signal with the emitted-chirp signal and, assuming a sufficiently high initial chirp frequency f_0 to filter out the other terms, we obtain a signal of frequency proportional to the topographical target range and amplitude equal to $P_R^{(1)}$.

This amplitude is comprised of the following two components. The first component is proportional to $T_{g,1}(\tau_g, \nu)$, which contains the information about the gas concentration sought. The second component is proportional to $\frac{m_{AC}}{2}\left(T_{g,0}\left(\tau_g, \nu\right) + T_{g,2}\left(\tau_g, \nu\right)\right)$. Both terms $\frac{m_{AC}}{2}T_{g,0}\left(\tau_g, \nu\right)$ and $\frac{m_{AC}}{2}T_{g,2}\left(\tau_g, \nu\right)$ show a dependence on the gas concentration, but if m_{AC} is small, their values are negligible compared to the $T_{g,1}\left(\tau_g, \nu\right)$ component except by a constant contribution in the term $\frac{m_{AC}}{2}T_{g,0}\left(\tau_g, \nu\right)$ which can be eliminated. So by subtracting this component from the final result we obtain the quantity $P_0^{'}\left(R\right)T_{g,1}\left(\tau_g, \nu\right)$ which is a function of the integrated gas concentration. Finally, the gas concentration can be extracted using a calibration function.

4.4.2 FMCW gas detection for distributed media

In this section, a similar technique to that employed for aerosol measurement (section 4.3) is extended to distributed media. However, to understand this new proposal it is important to clarify that in order to ensure the emitting signal is entirely wavelength-modulated, spurious power modulation in the laser source should be avoided. To avoid the problems encountered in the previous section in the detection process associated with spurious power modulation, the use of an external FM modulator is preferable to conducting FM modulation through the laser-diode injection current. Therefore, in the following development it is assumed that the chirp modulating signal affects the optical frequency, but not the amplitude of the signal.

This section outlines an investigation of two different cases. The first case consists of developing the general equations and the second case is an approximation for a very small frequency sweep, where an analytical approach can be determined. In both cases, the proposed method obtains information about gas concentration by comparing the retrieved data of the first and second frequency coefficients.

Section 4.4.2.3 outlines a number of simulations that were performed to evaluate the viability of the general case. In this section the parameters appearing in this general case are analyzed under different conditions in order to understand the criteria to select their best values. In addition, a complete simulation of a lidar medium with gas was performed. The results indicate the existence of a high level of distortion which is explored in section 4.4.4.

4.4.2.1 Developing the general case

Taking Eq. (4.74) as a starting point and replacing the topographical target with an aerosol distribution as backscattering medium, the received power from a differential atmospheric section of thickness dR' at range R' can then be given as:

$$dP_R(t) = A_R P_T\left(t-\frac{2R}{c}\right)\frac{\beta(R)}{R^2}T_a(R)\times \\ \times\sum_{n=0}^{\infty}T_{g,n}\left(\tau_g,\nu\right)\cos\left[2\pi n\left(f_0\left(t-2R/c\right)+K\left(t-2R/c\right)^2/2\right)\right]dR, \tag{4.78}$$

Integrating for the whole range we have

$$P_R(t) = A_R\int_0^{\infty}P_T\left(t-\frac{2R}{c}\right)\frac{\beta(R)}{R^2}T_a(R)\times \\ \times\sum_{n=0}^{\infty}T_{g,n}\left(\tau_g,\nu\right)\cos\left[2\pi n\left(f_0\left(t-2R/c\right)+K\left(t-2R/c\right)^2/2\right)\right]dR. \tag{4.79}$$

Then, assuming:

$$P_T(t) = P_0\,\Pi\left(\frac{t-T/2}{T}\right), \tag{4.80}$$

and defining P_0'' as the product of the gas-independent constant terms,

$$P_0''\left(R\right) = P_0 A_R\frac{\beta(R)}{R^2}T_a(R)\ , \tag{4.81}$$

we have:

$$P_R(t) = \int_0^{\infty}P_0''\left(R\right)\Pi\left(\frac{t-2R/c-T/2}{T}\right)\times \\ \times\sum_{n=0}^{\infty}T_{g,n}\left(\tau_g,\nu\right)\cos\left[2\pi n\left(f_0\left(t-2R/c\right)+K\left(t-2R/c\right)^2/2\right)\right]dR. \tag{4.82}$$

A photo detector is used to detect the optical signal, which gives a current proportional to the detected power:

$$i_R(t) = \Re P_R(t) = \Re\int_0^{\infty}P_0''\left(R\right)\Pi\left(\frac{t-2R/c-T/2}{T}\right)\times \\ \times\sum_{n=0}^{\infty}T_{g,n}\left(\tau_g,\nu\right)\cos\left[2\pi n\left(f_0\left(t-2R/c\right)+K\left(t-2R/c\right)^2/2\right)\right]dR. \tag{4.83}$$

This current is then sent to a mixer, where it is multiplied by $\Pi\left(\frac{t-T/2}{T}\right)\cos\left[2\pi\left(f_0 t+K t^2/2\right)\right]$, so that the mixer output current signal is

$$i_1(t) = \Re P_R(t)\Pi\left(\frac{t-T/2}{T}\right)\cos\left[2\pi\left(f_0 t+Kt^2/2\right)\right]. \tag{4.84}$$

Using the explicit expression (4.82) for $P_R(t)$, one obtains

$$\begin{aligned} i_1(t) &= \Re\Pi\left(\frac{t-T/2}{T}\right)\int_0^\infty P_0''\left(R\right)\cos\left[2\pi(f_0 t+Kt^2/2)\right]\times \\ &\times\sum_{n=0}^{\infty}T_{g,n}\left(\tau_g,\nu\right)\cos\left[2\pi\left(f_0\left(t-2R/c\right)+K\left(t-2R/c\right)^2/2\right)\right]dR. \end{aligned} \tag{4.85}$$

where the approximation $2R/c \ll T$ has been applied to simplify the expression of the resulting period $\Pi\left(\frac{t-T/2}{T}\right)$. As can be seen below, this approximation has no influence on the final result. Otherwise, the lowest non-DC frequency term will derive from the difference between the arguments of $\cos\left[2\pi\left(f_0\left(t-2R/c\right)+K(t-2R/c)^2/2\right)\right]$ and $\cos 2\pi(f_0 t+Kt^2/2)$. Assuming that the other terms can be filtered out, the resulting current component will be

$$\begin{aligned} i_{1LF}(t) &= \frac{1}{2}\Re\Pi\left(\frac{t-T/2}{T}\right)\int_0^\infty P_0''\left(R\right)T_{g,1}\left(\tau_g,\nu\right)\times \\ &\cos\left[2\pi\left(f_0\left(t-2R/c\right)+K\left(t-2R/c\right)^2/2\right)-2\pi\left(f_0 t+Kt^2/2\right)\right]dR. \end{aligned} \tag{4.86}$$

By developing the argument of the cosine one finds

$$i_{1LF}(t) = \frac{1}{2}\Re\Pi\left(\frac{t-T/2}{T}\right)\int_0^\infty P_0''\left(R\right)T_{g,1}\left(\tau_g,\nu\right)\cos\left[4\pi K\frac{R}{c}t+\frac{4\pi Rf_0}{c}-\pi K\left(\frac{2R}{c}\right)^2\right]dR, \tag{4.87}$$

calculating the Fourier transform of this current, gives us:

$$\begin{aligned} I_{1LF}(f) &= \frac{1}{2}\Re\int_0^\infty P_0''\left(R\right)T_{g,1}\left(\tau_g,\nu\right)\times \\ &\int_{-\infty}^{\infty}\Pi\left(\frac{t-T/2}{T}\right)\cos\left[2\pi\left(f_0\frac{2R}{c}-\frac{K}{2}\left(2t\frac{2R}{c}-\left(\frac{2R}{c}\right)^2\right)\right)\right]\exp\left(-j2\pi ft\right)dt\,dR= \\ &= \frac{T}{4}\Re\int_0^\infty P_0''\left(R\right)T_{g,1}\left(\tau_g,\nu\right)\left[\operatorname{sinc}\left(T\left(f-K\frac{2R}{c}\right)\right)\exp\left\{j\left[\phi_1\left(R\right)+\phi_2\left(R\right)\right]\right\}+N.P.\right]dR. \end{aligned} \tag{4.88}$$

where $\phi_1\left(R\right)$ and $\phi_2\left(R\right)$ are defined in the same way as in Eq. (4.26) with $\tau = 2R/c$. As in the aerosol case, the presence of the phase terms ($\phi_1\left(\tau\right)$ and $\phi_2\left(\tau\right)$) will produce a bandpass filtering effect if the sweep band is not accurately selected. This will be explored below in section 4.4.4. From Eq. (4.88) an amplitude around the frequency $f_R = 2KR/c$ is obtained:

$$I_{1LF}(f_R) = \frac{T}{4}\Re P_0''\left(R\right)T_{g,1}\left(\tau_g,\nu\right)\Delta R\ , \tag{4.89}$$

where the spatial resolution of the system is defined as $\Delta R = \frac{c}{2\Delta f} = \frac{c}{2KT}$. The following equation was applied to calculate Eq. (4.89):

$$\int_{-\infty}^{\infty} \mathrm{sinc}\left(T\left(f - K\frac{2R}{c} \right) \right) dR = \frac{c}{2KT}, \tag{4.90}$$

in addition to the consideration that most of the energy of the *sinc* function is concentrated around the point where the sinc-function argument equals zero, that is, $R = f_R \frac{c}{2K}$, and assuming a slow variation of the component $P_0''\left(R\right)T_{g,1}\left(\tau_g,\nu\right)$ in the zone of the range R.

Now assuming that the received signal (Eq. (4.82)) is multiplied in another mixer by a local oscillator with twice the frequency of the subcarrier, that is, $\Pi\left(\frac{t-T/2}{T}\right)\cos\left[4\pi(f_0 t + K t^2/2)\right]$, so that the output signal current of the mixer is

$$i_2(t) = \Re P_R(t)\Pi\left(\frac{t-T/2}{T}\right)\cos\left[4\pi(f_0 t + Kt^2/2)\right] \tag{4.91}$$

or, more explicitly by substituting Eq. (4.83) in Eq. (4.90),

$$\begin{aligned} i_2(t) &= \Re\Pi\left(\frac{t-T/2}{T}\right)\int_0^{\infty} P_0''\left(R\right)\cos\left[4\pi(f_i t + Kt^2/2)\right]\times \\ &\times\sum_{n=0}^{\infty} T_{g,n}\left(\tau_g,\nu\right)\cos\left[2\pi n\left(f_0\left(t-2R/c\right) + K\left(t-2R/c\right)^2/2\right)\right]dR. \end{aligned} \tag{4.92}$$

the lowest frequency terms will now arise from the difference between the arguments of $\cos\left[4\pi\left(f_0\left(t-2R/c\right)+K\left(t-2R/c\right)^2/2\right)\right]$ and $\cos\left[4\pi\left(f_0 t + Kt^2/2\right)\right]$.

Again, assuming that the other terms are being filtered out we obtain

$$\begin{aligned} i_2(t) &= \frac{1}{2}\Re\Pi\left(\frac{t-T/2}{T}\right)\int_0^{\infty} P_0''\left(R\right)T_{g,2}\left(\tau_g,\nu\right)\times \\ &\cos\left[4\pi\left(f_0\left(t-2R/c\right)+K\left(t-2R/c\right)^2/2\right) - 4\pi\left(f_0 t + Kt^2/2\right)\right]dR. \end{aligned} \tag{4.93}$$

By developing the argument of the cosine one finds

$$i_{2LF}(t) = \frac{1}{2}\Re\,\Pi\left(\frac{t-T/2}{T}\right)\int_0^{\infty} P_0''\left(R\right)T_{g,2}\left(\tau_g,\nu\right)\cos\left[8\pi K\frac{R}{c}t + \frac{8\pi R f_0}{c} - 2\pi K\left(\frac{2R}{c}\right)^2\right]dR. \tag{4.94}$$

Performing a Fourier-transform on this current then gives us:

$$
\begin{aligned}
&I_{2LF}(f)=\frac{1}{2}\Re\int_{0}^{\infty}P_0''(R)T_{g,2}\left(\tau_g,\nu\right)\times\\
&\int_{-\infty}^{\infty}\Pi\left(\frac{t-T/2}{T}\right)\cos\left[4\pi\left(f_0\frac{2R}{c}-\frac{K}{2}\left(2t\frac{2R}{c}-\left(\frac{2R}{c}\right)^2\right)\right)\right]\exp\left(-j2\pi ft\right)dt\,dR=\\
&=\frac{T}{4}\Re\int_{0}^{\infty}P_0''(R)T_{g,2}\left(\tau_g,\nu\right)\left[\operatorname{sinc}\left(T\left(f-K\frac{4R}{c}\right)\right)\exp\left\{j2\left[\phi_1(R)+\phi_2(R)\right]\right\}+N.P.\right]dR.
\end{aligned}
\tag{4.95}
$$

Assuming a slow variation of the component $P_0''(R)T_{g,2}(R,\nu)$ around R as in Eq. (4.89), we can obtain from Eq. (4.95) an amplitude around the frequency $2f_R=4KR/c$ of:

$$
I_{2LF}(2f_R)=\frac{T}{4}\Re P_0''(R)T_{g,2}\left(\tau_g,\nu\right)\frac{\Delta R}{2}\ .
\tag{4.96}
$$

By dividing Eq. (4.96) by Eq. (4.89) and multiplying by 2, we construct the ratio

$$
r_{21}(R)=\frac{2I_{2LF}\left(f_R\right)}{I_{1LF}\left(f_R\right)}=\frac{T_{g,2}\left(\tau_g,\nu\right)}{T_{g,1}\left(\tau_g,\nu\right)},
\tag{4.97}
$$

which basically represents the division of the double frequency coefficient by the single frequency coefficient.

4.4.2.2 Development of the special case with very small wavelength sweep

Due to the analytical difficulties in calculating the coefficients in the expansion of Eq. (4.72) shown in Eq. (4.73), a computer-simulation approach was chosen. Consequently, no closed expression for the value of the detected concentration or for the calculation of the SNR will be obtained. In this section, an approximation for the case of very small wavelength sweep together with the application of the modulation at a certain point along the absorption line will enable us to obtain a closed expression for the concentration value with respect to distance. The drawback to this is the reduction in the SNR value as a result of a reduction in received power, as shown in section 4.4.3.

Starting from Eq. (4.70) and applying a Taylor's expansion of this expression around ν_0.By calling $h(x)=e^{-2\tau_g(R)g(x)}$, we have the first and second derivatives of $h(x)$:

$$
\begin{aligned}
h'(x)&=-2\tau_g(R)g'(x)e^{-2\tau_g(R)g(x)}\\
h''(x)&=-2\tau_g(R)\left[g''(x)-2\tau_g(R)g'^2(x)\right]e^{-2\tau_g(R)g(x)}
\end{aligned}
\tag{4.98}
$$

and the expansion of Eq. (4.72) up to the second order yields

$$\begin{aligned} T_g(R,\nu) \approx \Big\{ & 1-2\tau_g(R)\,g'(\nu_0)\Delta\nu(t-2R/c)+ \\ & \frac{1}{2}\Big[-2\tau_g(R)\,g''(\nu_0)+4\tau_g^2(R)\,g'^2(\nu_0)\Big]\Delta^2\nu(t-2R/c)\Big\}e^{-2\tau_g(R)g(x)} \end{aligned} \tag{4.99}$$

Taking into account the definition (Eq. (4.70)), it can be seen that $e^{-2\tau_g(R)g(\nu_0)} = T_g(R,\nu_0)$. With the above assumptions and approximations the lidar Eq. (4.67) becomes

$$\begin{aligned} P_R(t) \approx A_R P_T\left(t-\frac{2R}{c}\right)\frac{\rho_{top}}{R^2}T_a(R)T_g\left(\tau_g,\nu\right)\Big\{ & 1+-2\tau_g(R)\,g'(\nu_0)\Delta\nu(t-2R/c)+ \\ & \frac{1}{2}\Big[-2\tau_g(R)\,g''(\nu_0)+4\tau_g^2(R)\,g'^2(\nu_0)\Big]\Delta^2\nu(t-2R/c)\Big\}. \end{aligned} \tag{4.100}$$

In the case of a distributed medium such as an aerosol, after replacing the topographic backscattering factor with that of the aerosol and integrating for all ranges, we have:

$$\begin{aligned} P_R(t) \approx A_R\int_0^\infty P_T\left(t-\frac{2R}{c}\right)\frac{\beta(R)}{R^2}T_a(R)T_g\left(\tau_g,\nu\right)\Big\{ & 1-2\tau_g(R)\,g'(\nu_0)\Delta\nu(t-2R/c)+ \\ & \frac{1}{2}\Big[-2\tau_g(R)\,g''(\nu_0)+4\tau_g^2(R)\,g'^2(\nu_0)\Big]\Delta^2\nu(t-2R/c)\Big\}dR \end{aligned} \tag{4.101}$$

Assuming the frequency dependence:

$$\Delta\nu(t) = \Delta\nu_{\max}\cos 2\pi(f_i t + Kt^2/2)\,, \tag{4.102}$$

the emitted power shape (Eq. (4.80)) and defining $P_0''(R)$ as Eq. (4.81), we have:

$$\begin{aligned} & P_R(t) \approx \int_0^\infty P_0''(R)\,\Pi\left(\frac{t-2R/c-T/2}{T}\right)T_g\left(\tau_g,\nu\right)\times \\ & \Big\{1-2\tau_g(R)\,g'(\nu_0)\,\Delta\nu_{\max}\cos\Big[2\pi(f_i(t-2R/c)+K(t-2R/c)^2/2)\Big]+ \\ & \frac{1}{2}\Big[-2\tau_g(R)g''(\nu_0)+4\tau_g^2(R)\,g'^2(\nu_0)\Big]\Delta^2\nu_{\max}\cos^2\Big[2\pi(f_i(t-2R/c)+K(t-2R/c)^2/2)\Big]\Big\}dR \end{aligned} \tag{4.103}$$

Moreover, if the laser carrier wavelength ν_0 is kept at a value making $g''(\nu_0)=0$ (i.e., ν_0 is fixed at the point of maximum slope of $g(\nu_0)$), the expression of Eq. (4.103) can be simplified to

$$\begin{aligned} & P_R(t) \approx \int_0^\infty P_0''(R)\,\Pi\left(\frac{t-2R/c-T/2}{T}\right)T_g\left(\tau_g,\nu\right)\times \\ & \Big\{1-2\tau_g(R)g'(\nu_0)\,\Delta\nu_{\max}\cos\Big[2\pi(f_i(t-2R/c)+K(t-2R/c)^2/2)\Big]+ \\ & 2\tau_g^2(R)\,g'^2(\nu_0)\Delta^2\nu_{\max}\cos^2\Big[2\pi(f_i(t-2R/c)+K(t-2R/c)^2/2)\Big]\Big\}\,dR \end{aligned} \tag{4.104}$$

Comparing this last expression with Eq. (4.82), we can identify the fundamental and double frequency coefficients of expression (4.73):

$$\begin{aligned} T_{g,1}\left(\tau_g,\nu\right) &= -2\tau_g(R)\,g'(\nu_0)\,\Delta\nu_{\max} \\ T_{g,2}\left(\tau_g,\nu\right) &= \tau_g^2(R)g'^2(\nu_0)\Delta^2\nu_{\max} \end{aligned} \tag{4.105}$$

where $T_{g,2}(R,\nu)$ has been obtained taking into account that $\cos^2\left(x\right) = \dfrac{1+\cos\left(2x\right)}{2}$. Henceforth, for the sake of simplicity we will refer to these frequency coefficients as the 1st and 2nd harmonic even though the functions they multiply are not strictly periodic. Then, if we apply this information to Eq. (4.97), we have:

$$r_{21}(R) = \frac{1}{2}\frac{T_{g,2}\left(\tau_g,\nu\right)}{T_{g,1}\left(\tau_g,\nu\right)} = -\frac{1}{4}\tau_g(R)\,g'(\nu_0)\Delta\nu_{\max} \tag{4.106}$$

Naming the multiplicative constant on the right side of Eq. (4.106) k, we have

$$r_{21}(R) = k\,\tau_g(R) \tag{4.107}$$

from which

$$\tau_g(R) = \frac{r_{21}(R)}{k} \tag{4.108}$$

Substituting Eq. (4.68) into Eq. (4.109) we have

$$\sigma\int_0^R N(x)\,dx = \frac{r_{21}(R)}{k} \tag{4.109}$$

which gives us

$$N(R) = \frac{1}{k\sigma}\frac{d\left[r_{21}(R)\right]}{dR} \tag{4.110}$$

So in Eq. (4.110) an expression for the gas concentration is finally obtained after constructing a ratio between the first and second harmonics at the output of the photodetector.

4.4.2.3 Simulations

On completing the theoretical analysis of the FMCW lidar signal, some simulations were performed to demonstrate the behavior of the 1st and 2nd harmonic signals at the output of the detector after interacting with the gas absorption line.

The value of the 1st and 2nd harmonic depends on the gas optical depth τ_g, the relative level of modulation with respect to the linewidth m and the relative point of modulation $\overline{\nu}$ (equivalently defined in chapter 2) as:

$$m = \frac{\Delta \nu_{\max}}{\Delta \nu} \qquad \overline{\nu} = \frac{\nu - \nu_0}{\Delta \nu} \tag{4.111}$$

Figure 4.24 gives the shape of the exponential in Eq. (4.70) as a function of the optical frequency ν for different values of τ_g used as a parameter in that family of curves.

As we can see, the absorption value increases with τ_g and the curve changes from a smoother to sharper shape, whilst tending towards saturation for high values of τ_g. The values of the 1st and 2nd -harmonic of modulation evolve according to the values of τ_g.

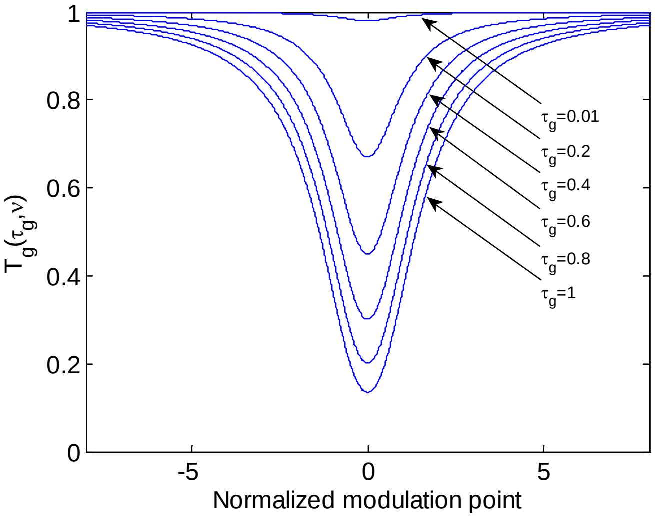

Figure 4.24. Evolution of the absorption line shape in Eq. (4.70) with respect to ν for τ_g values between 0.01 and 1

Taking into account the shape of these curves, another simulation (Fig. 4.25, 4.26) was performed to determine the evolution of the received-signal 1st- and 2nd-harmonics arising from the interaction between the emitted signal and the gas under measurement for the same values of τ_g considered in figure 4.24. We can see in this evolution that these 1st- and 2nd- harmonic amplitudes $\left(T_{g,1}\left(\tau_g,\nu\right) \text{and } T_{g,2}\left(\tau_g,\nu\right)\right)$ increase with τ_g but they tend to saturate and even decrease for high values of τ_g.

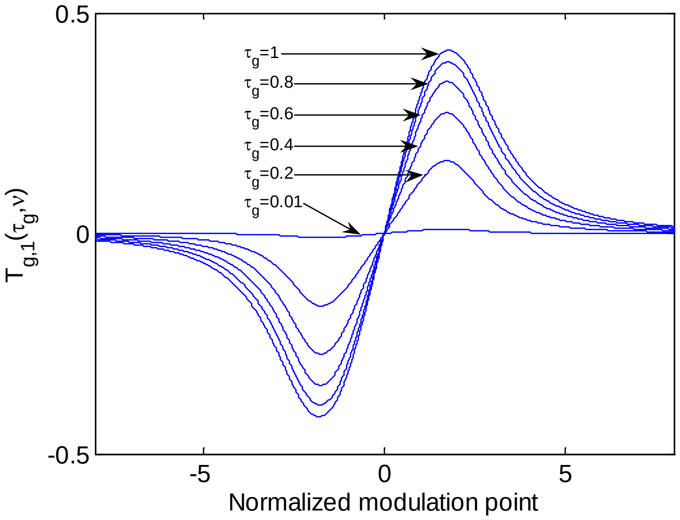

Figure 4.25. Evolution of the 1st harmonic $T_{g,1}\left(\tau_g,\nu\right)$ profiles as a function of τ_g value varying between 0.01 and 1 and with $m = 2$

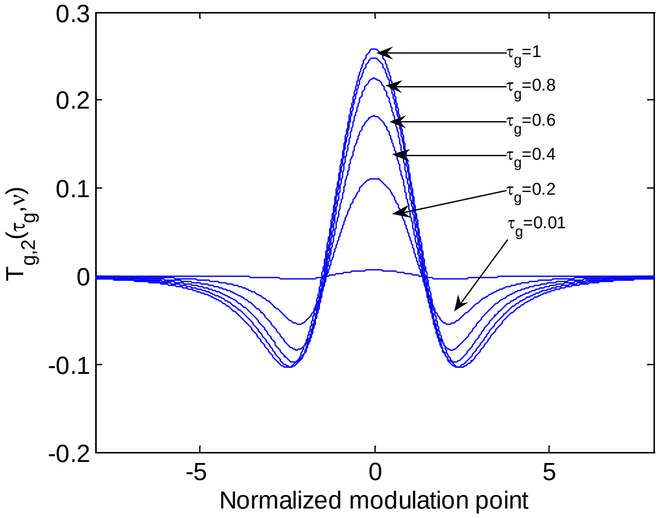

Figure 4.26. Evolution of the 2nd harmonic $T_{g,2}\left(\tau_g,\nu\right)$ profiles for τ_g values varying between 0.01 and 1 and with $m = 2$

The evolution of $T_{g,1}\left(\tau_g,\nu\right)$ and $T_{g,2}\left(\tau_g,\nu\right)$ at points $\bar{\nu} = 0.8$ (Fig. 4.27) and $\bar{\nu} = 2$ (Fig. 4.28) can be seen as a function of τ_g for $m = 2$. As clearly demonstrated in figures 4.27 and 4.28, the value of the harmonics starts to increase (decrease in the case of the 2nd harmonic at $\bar{\nu} = 2$). However, as the value of τ_g increases, the curve becomes smoother and the value even decreases (increases in the case of the 2nd harmonic at $\bar{\nu} = 2$).

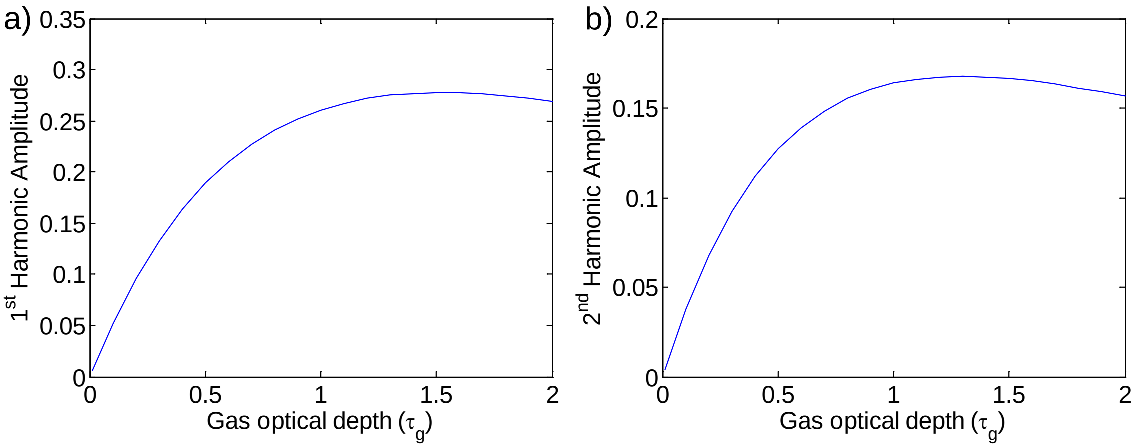

Figure 4.27. Evolution of $T_{g,1}\left(\tau_g,\nu\right)$ and $T_{g,2}\left(\tau_g,\nu\right)$ at $\overline{\nu}=0.8$ as a function of τ_g value with $m=2$

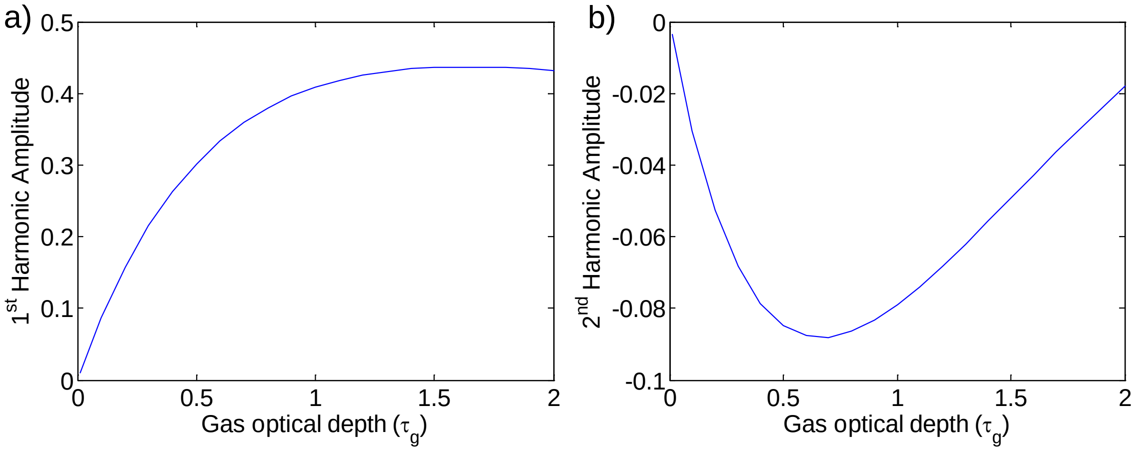

Figure 4.28. Evolution of $T_{g,1}\left(\tau_g,\nu\right)$ and at $\overline{\nu}=2$ as a function of τ_g value with $m=2$

As the value of τ_g in figure 4.29 is determined by means of a comparison between $T_{g,1}\left(\tau_g,\nu\right)$ and $T_{g,2}\left(\tau_g,\nu\right)$ (Eq. 4.97), we have graphically represented the $\left|r_{21}\right|$ ratio (the absolute value of the 2nd harmonic to 1st harmonic ratio) for both cases, as shown in figures 4.27 and 4.28 in order to show its evolution with τ_g. For the purposes of simplicity, the absolute value of r_{21} is used instead of r_{21} in both simulations and experiments. As demonstrated below in the SNR analysis section, obtaining a high SNR value is dependent on the ration being monotonous and the sharpest possible evolution of this ratio (r_{21}), to ensure the values of τ_g are easily calculated with the minimum effect of noise. It is clear that the $\overline{\nu}=2$ case is better in this aspect.

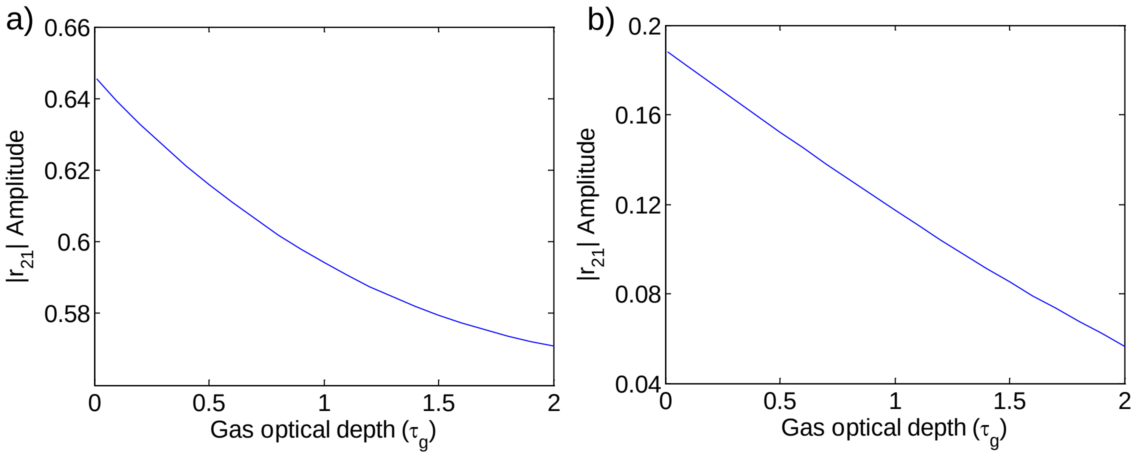

Figure 4.29. Evolution of the $|r_{21}|$ ratio at $\bar{\nu} = 0.8$ and $\bar{\nu} = 2$ as a function of τ_g value with $m = 2$

Section 4.4.2.2 demonstrated that for the case of a very small wavelength sweep, one with a very low value of m and a point of modulation where the second derivative of $g(\nu)$ vanishes ($g''(\nu)=0 \Rightarrow \bar{\nu}=1/\sqrt{3}$), it proved possible to obtain a closed expression for r_{21}. A comparison is now made between a case with a very low modulation value ($m=0.1$) and a case with a higher modulation value ($m=2$), while maintaining a modulation point of $\bar{\nu}=1/\sqrt{3}$ $\bar{\nu}=3^{-1/2}$. Figs. 4.30 and 4.31 give the values of the 1st and 2nd harmonic for the case of $m=0.1$ and that of $m=2$ around the point of modulation $\bar{\nu}=1/\sqrt{3}$.

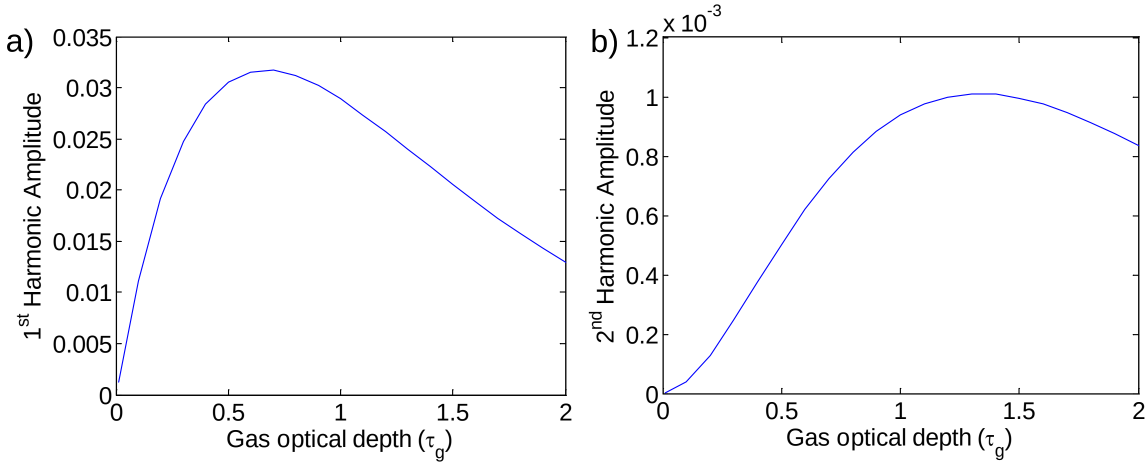

Figure 4.30. Evolution of $T_{g,1}(\tau_g,\nu)$ and $T_{g,2}(\tau_g,\nu)$ at $\bar{\nu}=1/\sqrt{3}$ as a function of τ_g value with $m = 0.1$

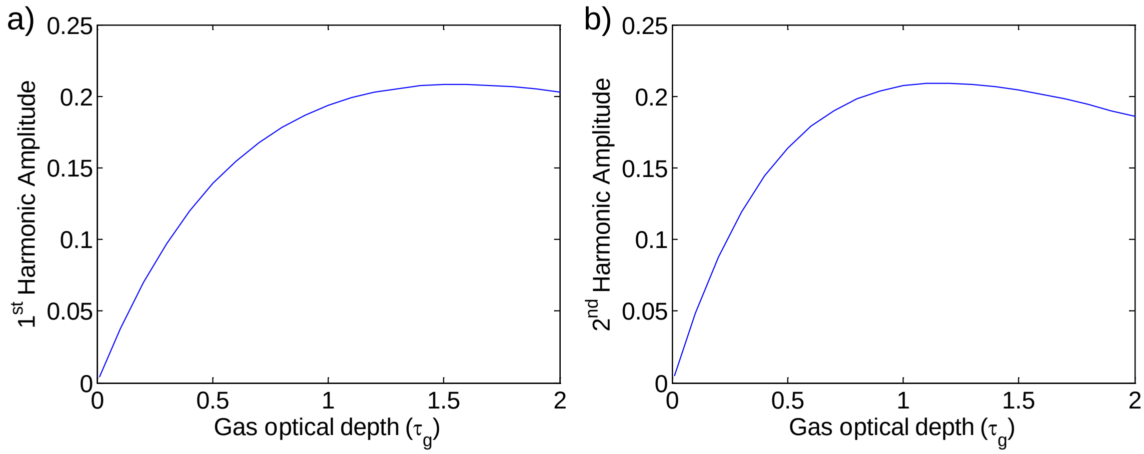

Figure 4.31. Evolution of $T_{g,1}\left(\tau_g,\nu\right)$ and $T_{g,2}\left(\tau_g,\nu\right)$ at $\overline{\nu}=1/\sqrt{3}$ as a function of τ_g value with $m=2$

In figure 4.32, the $|r_{21}|$ ratio is shown for the cases represented in figures 4.30 and 4.31. As stated in section 4.4.2.2, the evolution of this ratio is practically linear in cases of really low modulation values, while for high modulation values it becomes inversely proportional to the value of τ_g. Although the linearity of the first case is a desired feature, the change of the ratio with τ_g is very small (0.065 for values of τ_g from 0 to 2), while in the case of $m=2$ the change of the ratio with τ_g is much larger (0.4 for values of τ_g from 0 to 2). Therefore, in the case of the latter immunity to noise is better.

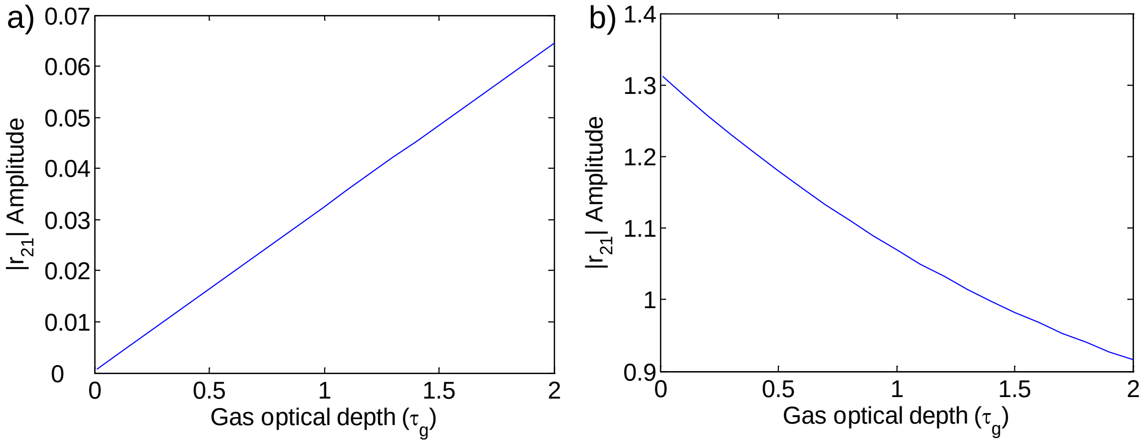

Figure 4.32. Evolution of the $|r_{21}|$ ratio at $\overline{\nu}=1/\sqrt{3}$ as a function of τ_g value for $m=0.1$ and $m=2$

Figure 4.33 shows the evolution of the $|r_{21}|$ ratio with respect to τ_g for different values of m. While for small values of m the ratio is almost linear and proportional to τ_g, this proportionality is lost as m increases and, above a certain value of τ_g, the change in the ratio with τ_g becomes greater. As previously stated and demonstrated below, this aspect is essential in obtaining improved behavior with respect to noise.

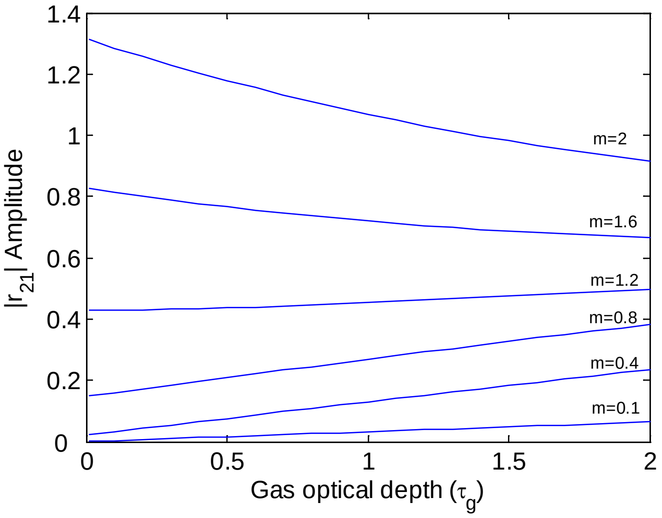

Figure 4.33. Evolution of the $|r_{21}|$ ratio at $\overline{\nu}=1/\sqrt{3}$ with respect to the value of τ_g for different values of m (0.1,…,2)

What follows is a discussion of the lidar signal under certain modulation conditions. As in the case of aerosol measurements the emitted signal is backscattered by aerosols. This means that in a distributed medium, a good response (one that permits the retrieval of a 0-spatial-frequency component of the gas distribution) is only obtained when the emitted signal is baseband modulated, resulting in a repetition of the problem of superposition between different harmonics and an inability to filter them easily, in the case of gas measurements.

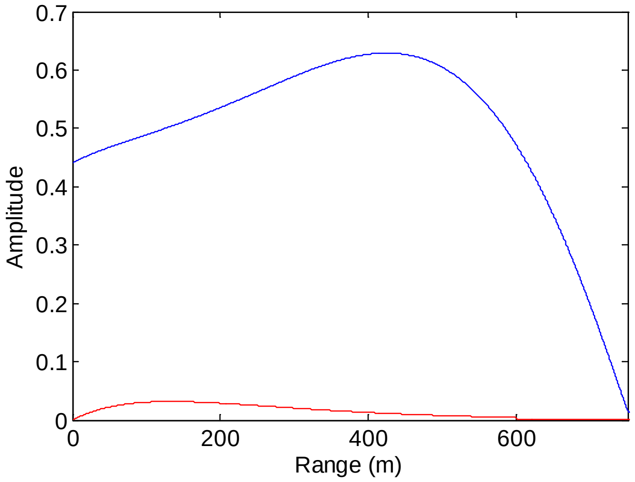

Figure 4.34. Expected (red) and realistic (blue) responses of $T_{g,1}(\tau_g,\nu)$ for a medium with both constant aerosol and gas concentrations with $m=0.1$ and at a modulation point of $\overline{\nu}=1/\sqrt{3}$

Figure 4.34 presents the expected $T_{g,1}(\tau_g,\nu)$ values obtained from an ideal medium with a constant signal return (i.e. referring to Eq. (4.78), a medium in which $\beta(R)T_a(R)\propto R^2$) up to 600 meters, a constant gas-concentration value with $\tau_g=3$ at 600 meters, and a modulation point of $\overline{\nu}=1/\sqrt{3}$ and $m=0.1$ (red). If it had proved possible to conduct a problem-free realistic simulation, this would represent an ideal, distortion-free case (Fig. 4.34 - red). However, interference from the other harmonics was translated into a distortion in the response, which made it impossible to retrieve the gas concentration value. All harmonics contribute to the final signal and the resulting shape departs greatly from that expected (Fig. 4.34 - blue). A possible solution for this problem is developed in the application of the previously developed phase-hop method for the case of gas-concentration measurements, and presented in section 4.4.4.

4.4.3 SNR impact on FMCW gas detection

Developments to this point demonstrate the possibility of extracting the gas concentration information from the retrieved data. In order to fully assess feasibility in terms of power, it is necessary to calculate the impact of the SNR on the retrieved data, or more specifically, to calculate its impact on the uncertainty of the retrieved gas concentration. For this purpose, a calculation of the gas concentration uncertainty in terms of the SNR ratio is performed, taking advantage of the previous calculations of the SNR ratio for the case of aerosols.

In both cases of aerosol and gas detection the noise level can be considered the same. However the signal power received by each of them differs significantly. If a comparison of the level of modulation in the signal received from a resolution cell in both cases is carried out, it is evident in the case of aerosols that the modulation is constant and its level is that of the emitter. In the case of the measurement of a gas, the gas-concentration information is contained in the increase of the gas optical depth $\tau_g(R)$ with distance, but the response of the signal to this increase in depth becomes smaller as $\tau_g(R)$ increases. There is a trade-off when selecting the absorption line with respect to the gas optical depth. If a strong absorption line is selected, and the gas optical depth $\tau_g(R)$ is appreciable, a higher interaction is achieved at shorter ranges, with the drawback of receiving less useful signal power at longer ranges due to the decrease in $T_g\left(\tau_g,\nu\right)$ (Eq. (4.70)). Conversely, with a smaller $\tau_g(R)$ value, less modulated power is achieved over shorter distances, but higher modulated power achieved over longer ranges.

An analytical calculation of the gas concentration uncertainty is given below. A number of equations that have been previously presented have been rewritten with their original numeration to simplify the development. Starting with the expression of the gas concentration calculation, without taking into account the effect of noise, Eq. (4.83) gives us the expression of the ideal detected current:

$$\begin{aligned} i_R(t) = \Re P_R(t) = \Re\int_0^\infty P_0''(R)\,\Pi\left(\frac{t-2R/c-T/2}{T}\right)\times \\ \times\sum_{n=0}^{\infty} T_{g,n}\left(\tau_g,\nu\right)\cos\left[2\pi n\left(f_0\left(t-2R/c\right)+K\left(t-2R/c\right)^2/2\right)\right]dR \end{aligned} \tag{4.83}$$

Then, the first and second harmonic contents are obtained by mixing the previous current with the emitted signal and its second harmonic, respectively:

$$i_1(t) = i_R(t)\Pi\left(\frac{t-T/2}{T}\right)\cos\left[2\pi\left(f_0 t + Kt^2/2\right)\right], \tag{4.84}$$

$$i_2(t) = i_R(t)\Pi\left(\frac{t-T/2}{T}\right)\cos\left[4\pi(f_0 t + Kt^2/2)\right]. \tag{4.90}$$

Performing a Fourier transform and assuming a slow variation of the terms depending on R, gives us an FT amplitude of:

$$I_{1LF}(f_R) = \frac{T}{4}\Re P_0''(R)T_{g,1}\left(\tau_g,\nu\right)\Delta R\ , \tag{4.89}$$

$$I_{2LF}\left(f_R\right) = \frac{T}{4}\Re P_0''(R)T_{g,2}\left(\tau_g,\nu\right)\frac{\Delta R}{2}\ . \tag{4.96}$$

Combining expressions (4.89) and (4.96), gives us the ratio:

$$r_{21}(R) = \frac{2I_{2LF}\left(f_R\right)}{I_{1LF}\left(f_R\right)} = \frac{T_{g,2}\left(\tau_g,\nu\right)}{T_{g,1}\left(\tau_g,\nu\right)} \tag{4.97}$$

which is solely dependent on gas-absorption parameters. Then the ratio r_{21} is related to the gas optical depth τ_g through:

$$\tau_g = \Im^{-1}\left(r_{21}\left(R\right)\right) = \Im^{-1}\left(\frac{T_{g,2}\left(\tau_g,\nu\right)}{T_{g,1}\left(\tau_g,\nu\right)}\right) \tag{4.112}$$

where $\Im(x)$ is the function that transforms the gas optical depth τ_g into the ratio r_{12}. This function has the closed expression (4.106) for small wavelength sweeps and must be computed numerically for large sweeps. Applying Eq. (4.68) to (4.112), gives us an expression of the gas concentration:

$$\square\,(R) = \frac{1}{\sigma}\frac{d\tau_g}{dR} = \frac{1}{\sigma}\frac{d\Im^{-1}(r_{21})}{dR} = \frac{1}{\sigma}\frac{d}{dR}\Im^{-1}\left(\frac{T_{g,2}\left(\tau_g,\nu\right)}{T_{g,1}\left(\tau_g,\nu\right)}\right) \tag{4.113}$$

This would be the case for an ideal situation without noise, but noise effects exist in all real systems. Assuming additive noise, the noise-corrupted detected current will be:

$$\begin{aligned}\hat{i}_R(t) = \Re P_R(t) = \Re\int_0^\infty P_0''(R)\Pi\left(\frac{t-2R/c-T/2}{T}\right)\times\\ \times\sum_{n=0}^{\infty}T_{g,n}\left(\tau_g,\nu\right)\cos\left[2\pi n\left(f_0\left(t-2R/c\right)+K\left(t-2R/c\right)^2/2\right)\right]dR + n\left(t\right)\end{aligned} \tag{4.114}$$

Then, the expression of the 1st and 2nd harmonic currents would be:

$$\hat{i}_1(t) = \Re P_R(t)\Pi\left(\frac{t-T/2}{T}\right)\cos\left[2\pi\left(f_0 t + Kt^2/2\right)\right] + n_1(t), \tag{4.115}$$

$$\hat{i}_2(t) = \Re P_R(t)\Pi\left(\frac{t-T/2}{T}\right)\cos\left[4\pi(f_0 t + Kt^2/2)\right] + n_2(t) \tag{4.116}$$

where $n_1(t) = n(t)\Pi\left(\frac{t-T/2}{T}\right)\cos\left[2\pi\left(f_0 t + Kt^2/2\right)\right]$ and, in contrast to $n_1(t)$, $n_2(t) = n(t)\Pi\left(\frac{t-T/2}{T}\right)\cos\left[4\pi\left(f_0 t + Kt^2/2\right)\right]$.

The Fourier transform of the 1st and 2nd harmonics would have the following form:

$$\hat{I}_{1LF}(f_R) = \frac{T}{4}\Re P_0''(R)T_{g,1}(\tau_g,\nu)\Delta R + N_1(f_R), \tag{4.117}$$

$$\hat{I}_{2LF}(2f_R) = \frac{T}{4}\Re P_0''(R)T_{g,2}(\tau_g,\nu)\frac{\Delta R}{2} + N_2(2f_R). \tag{4.118}$$

Combining expressions (4.117) and (4.118) gives us the ratio:

$$\hat{r}_{21}(R) = \frac{2\hat{I}_{2LF}}{\hat{I}_{1LF}} = \frac{C_1 T_{g,2}(\tau_g,\nu) + 2N_2(2f_R)}{C_1 T_{g,1}(\tau_g,\nu) + N_1(f_R)} \tag{4.119}$$

where $C_1 = \frac{T}{4}\Re P_0''(R)\Delta R$ includes all the factors with no dependence on wavelength at reception (P_0'', T, etc.). The noise-corrupted estimate of gas concentration would be obtained by substituting $\hat{r}_{21}(R)$ given by Eq. (4.120) for $r_{21}(R)$ into Eq. (4.113):

$$\hat{\square}(R) = \frac{1}{\sigma}\frac{d}{dR}\Im^{-1}\left(\frac{C_1 T_{g,2}(\tau_g,\nu) + 2N_2(2f_R)}{C_1 T_{g,1}(\tau_g,\nu) + N_1(f_R)}\right) \tag{4.120}$$

If the values of $N_1(f_R)$ and $N_2(2f_R)$ are considered to be much smaller respectively than $C_1 T_{g,1}(\tau_g,\nu)$ and $C_1 T_{g,2}(\tau_g,\nu)$, it is possible to limit the Taylor series expansion around the quotient $T_{g,2}(\tau_g,\nu)/T_{g,1}(\tau_g,\nu) = r_{21}$ to the first order with the result:

$$\hat{\square}(R) = \frac{1}{\sigma}\frac{d}{dR}\Im^{-1}\left(\frac{T_{g,2}(\tau_g,\nu)}{T_{g,1}(\tau_g,\nu)} + \frac{T_{g,2}(\tau_g,\nu)}{C_1 T_{g,1}(\tau_g,\nu)}\left(\frac{2N_2(2f_R)}{T_{g,2}(\tau_g,\nu)} - \frac{N_1(f_R)}{T_{g,1}(\tau_g,\nu)}\right)\right) \tag{4.121}$$

If dependence of $\Im^{-1}(x)$ on its argument is assumed to be a function with minor variations, it can be approximated by its Taylor expansion to the 1st-order term around the point r_{21}, giving us:

$$\hat{\square}(R) \approx \frac{1}{\sigma}\frac{d}{dR}\left[\Im^{-1}(r_{21}) + \left.\frac{d\Im^{-1}(x)}{dx}\right|_{r_{21}} \frac{r_{21}}{C_1}\left(\frac{2N_2(2f_R)}{T_{g,2}(\tau_g,\nu)} - \frac{N_1(f_R)}{T_{g,1}(\tau_g,\nu)}\right)\right] \tag{4.122}$$

At this point, we can consider the relative variation of noise realizations in a range resolution cell ΔR (or its respective frequency) to be much higher than that of the other components.

$$\begin{gathered}\frac{1}{N_1(f_R)}\frac{2K}{c}\frac{d}{df}N_1(f_R),\frac{1}{N_2(2f_R)}\frac{2K}{c}\frac{d}{df}N_2(2f_R)\square \\ \frac{1}{T_{g,1}(\tau_g,\nu)}\frac{d}{dR}T_{g,1}(\tau_g,\nu),\frac{1}{T_{g,2}(\tau_g,\nu)}\frac{d}{dR}T_{g,2}(\tau_g,\nu),\frac{1}{\left.\frac{d\Im^{-1}(x)}{dx}\right|_{r_{21}}}\frac{d}{dR}\left.\frac{d\Im^{-1}(x)}{dx}\right|_{r_{21}}\end{gathered} \tag{4.123}$$

Taking into account the previous consideration and developing the argument derived we have:

$$\hat{\square}(R) = \frac{1}{\sigma}\frac{d\Im^{-1}(r_{21})}{dR} + \frac{1}{\sigma}\left.\frac{d\Im^{-1}(x)}{dx}\right|_{r_{21}} \frac{r_{21}}{C_1}\frac{d}{dR}\left(\frac{2N_2(2f_R)}{T_{g,2}(\tau_g,\nu)} - \frac{N_1(f_R)}{T_{g,1}(\tau_g,\nu)}\right) \tag{4.124}$$

Or, in terms of frequency:

$$\hat{\square}(R) = \frac{1}{\sigma}\frac{c}{2K}\frac{d\Im^{-1}(r_{21})}{dR} + \frac{1}{\sigma}\left.\frac{d\Im^{-1}(x)}{dx}\right|_{r_{21}} \frac{r_{21}}{C_1}\frac{2K}{c}\frac{d}{df}\left(\frac{2N_2(2f_R)}{T_{g,2}(\tau_g,\nu)} - \frac{N_1(f_R)}{T_{g,1}(\tau_g,\nu)}\right) \tag{4.125}$$

Where we can identify the first term as the *true* gas concentration, we have:

$$\hat{\square}(R) = \square(R) + \frac{1}{\sigma}\left.\frac{d\Im^{-1}(x)}{dx}\right|_{r_{21}} \frac{r_{21}}{C_1}\frac{2K}{c}\frac{d}{df}\left(\frac{2N_2(2f_R)}{T_{g,2}(\tau_g,\nu)} - \frac{N_1(f_R)}{T_{g,1}(\tau_g,\nu)}\right) \tag{4.126}$$

To obtain a final expression of the uncertainty of the gas concentration, the standard deviation of expression (4.126) is calculated. The values derived from the difference equation of $N_1(f)$ and $N_2(f)$ calculated in appendix D are used instead of the derivative itself, as this is more suitable in a case such as ours, with a system of time resolution $\Delta f = 1/T$.

So the value used for the calculation is $\Delta f = 1/T$ and the result given as:

$$\mathrm{E}\left[\left|\frac{N_1(f+\Delta f)-N_1(f)}{\Delta f}\right|^2\right] = \eta_n T^3 \qquad \mathrm{E}\left[\left|\frac{N_2(2f+2\Delta f)-N_1(2f)}{\Delta f}\right|^2\right] = \frac{\eta_n T^3}{2} \tag{4.127}$$

where η_n is the spectral density of current fluctuations $\left[A^2/Hz\right]$, and taking into account that the derivatives of $N_1(f)$ and $N_2(f)$ with respect to frequency are practically uncorrelated (Appendix E), we have:

$$\left\{E\left[\left(\hat{\square}(R)-\square(R)\right)^2\right]\right\}^{1/2}=\frac{1}{\sigma}\frac{d\Im^{-1}(x)}{dx}\bigg|_{r_{21}}\frac{r_{21}}{C_1}\frac{2K}{c}\sqrt{\frac{2T^3\eta_n}{T_{g,2}^2\left(\tau_g,\nu\right)}+\frac{T^3\eta_n}{T_{g,1}^2\left(\tau_g,\nu\right)}} \tag{4.128}$$

Or, grouping terms, we have:

$$\left\{E\left[\left(\hat{\square}(R)-\square(R)\right)^2\right]\right\}^{1/2}=\frac{1}{\sigma}\frac{\sqrt{2}}{C_1}\frac{2K}{c}T^{3/2}\eta_n^{1/2}\frac{d\Im^{-1}(x)}{dx}\bigg|_{r_{21}}\frac{1}{T_{g,1}\left(\tau_g,\nu\right)}\sqrt{1+\frac{r_{21}^2}{2}} \tag{4.129}$$

If we apply $\eta_n^{1/2}=\frac{\Re P_N}{\sqrt{\Delta f_D}}\left[A/\sqrt{Hz}\right]$ and develop the term C_1 and the term $P_0''(R)$ inside C_1 (Eq. (4.81)), on reordering the terms we have a final estimation of the gas concentration uncertainty as:

$$\left\{E\left[\left(\hat{\square}(R)-\square(R)\right)^2\right]\right\}^{1/2}=\frac{16\sqrt{2}}{\sigma}\frac{R^2P_N}{P_0A_R\beta(R)T_a(R)}\frac{\Delta f_D{}^{3/2}}{c^2T^{1/2}}\frac{d\Im^{-1}(x)}{dx}\bigg|_{r_{21}}\frac{1}{T_{g,1}\left(\tau_g,\nu\right)}\sqrt{1+\frac{r_{21}^2}{2}} \tag{4.130}$$

Table 4.3. Values for the calculation of the gas-detection lidar-system SNR

Variable	Value
Incident DC power: P_0	150 [mW]
Backscatter coefficient: β	10^{-6} [$m^{-1}\cdot sr^{-1}$]
Resolution range: ΔR	5 [m]
Telescope area (20-cm diameter): A_R	$\pi\cdot 0.1^2$ [m^2]
Target range: R	10^2 [m]
Aerosol transmittance: T_a	~1
Electrical bandwidth: Δf_D	$30\cdot 10^6$ [Hz]
Total optical noise equivalent power: P_N	$6.67\cdot 10^{-10}$ [W]
Wavelength: λ	1 [μm]
Time period: T	10^{-3} [s]
Gas absorption coefficient: $d\tau/dR=N(R)\sigma$	0.005 [m^{-1}]

Due to the linearity of all the operations (the Fourier transform, the 1st-order Taylor series development, derivative…), the uncertainty in the measurement decreases when averaging multiple periods by a factor of $\sqrt{M}$, where M is the number of periods being averaged. This is due to the fact that as the signal power increases as the square of the number of accumulations, the noise power increases linearly due to its incoherence.

An increase in period length while maintaining range resolution ΔR constant has a similar effect.

As an example of an uncertainty calculation, a medium with a constant backscatter coefficient and gas concentration of the values shown above in table 4.3. is considered. The parameter values are similar to those used in the case of aerosol detection. The total noise equivalent power remains the same because the same conditions have been assumed. With the values selected in table 4.3, $\tau_g(R)$ shows a value of 1 at a distance of 200 meters with a linear behavior with respect to distance. The modulation conditions selected are $m = 0.8$ for the modulation index and $\overline{\nu} = 3^{-1/2}$ for the modulation point. The values of $\left.\frac{d\Im^{-1}(x)}{dx}\right|_{r_{21}}$, $T_{g,1}\left(\tau_g, \nu\right)$ and r_{21} are calculated numerically for the sounding range under these selected modulation conditions. Figure 4.35 gives the values of the first (a) and second (b) harmonics for the modulation conditions indicated up to a value of $\tau_g = 3$.

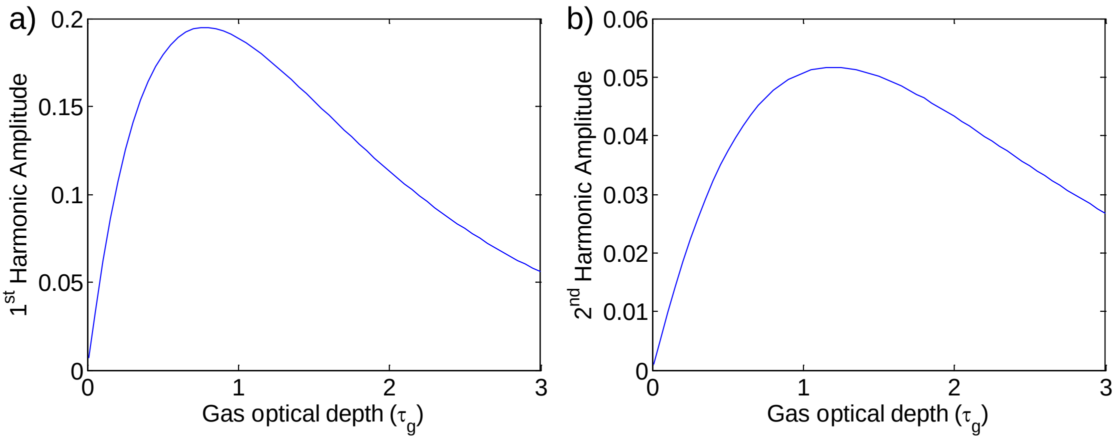

Figure 4.35. Evolution of the first (a) and second (b) harmonics with respect to τ_g for a modulation index of $m = 0.8$ and a modulation point of $\overline{\nu} = 3^{-1/2}$

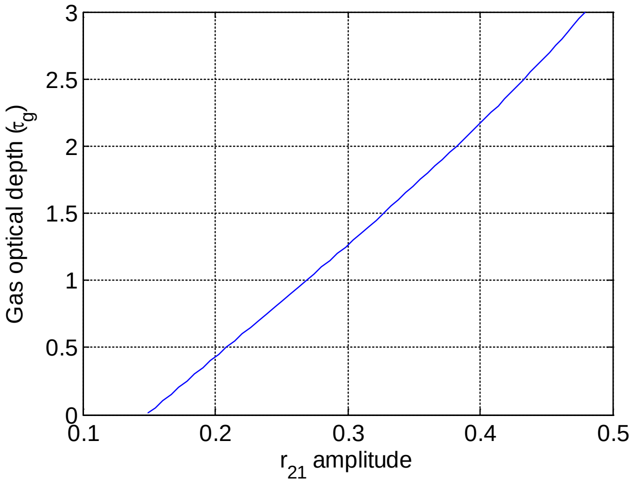

Figure 4.36. Evolution of second-to-first harmonic ratio r_{21} (a) with respect to τ_g for a modulation index of $m = 0.8$ and a modulation point of $\overline{\nu} = 3^{-1/2}$ and its inverse function (b)

In figure 4.36 the value of τ_g is shown as a function of the 2nd to 1st harmonic ratio. Using the values in figure 4.36 that correspond to function $\Im^{-1}(x)$, its derivative was numerically calculated (Fig. 4.37) and, by performing a 6th degree polynomial fit, we obtain the function $\frac{d\Im^{-1}(x)}{dx}$, which is required to calculate the evolution of the gas uncertainty along R.

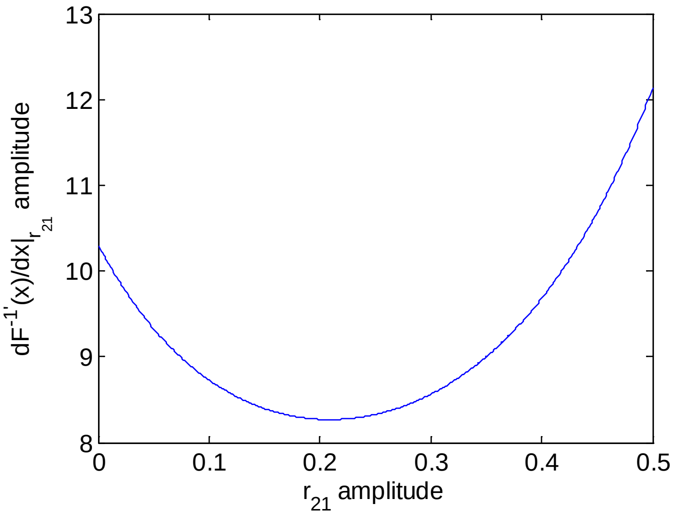

Figure 4.37. Evolution of the derivative of τ_g with respect to the second-to-first harmonic ratio r_{21} (Fig. 4.36) for a modulation index of $m = 0.8$ and a modulation point of $\overline{\nu} = 3^{-1/2}$

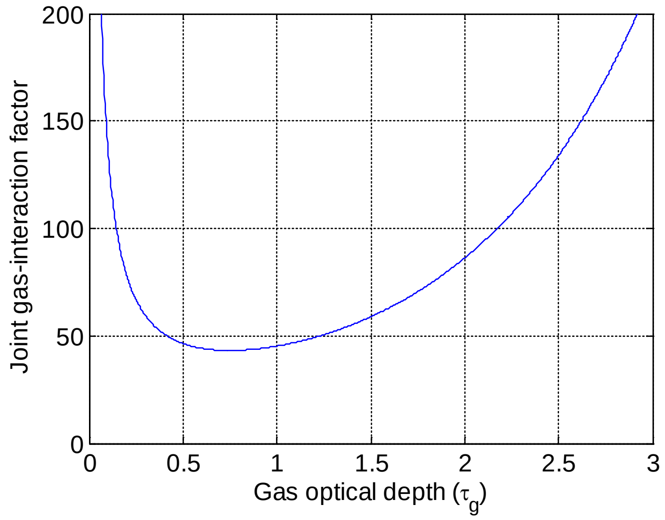

Figure 4.38. Evolution of the total gas-interaction factor $\left.\frac{d\Im^{-1}(x)}{dx}\right|_{r_{21}} \frac{1}{T_{g,1}\left(\tau_g,\nu\right)}\sqrt{1+\frac{r_{21}^2}{2}}$ with respect to τ_g for a modulation index of $m = 0.8$ and a modulation point of $\overline{\nu} = 3^{-1/2}$

The evolution of the total gas-interaction factor of the uncertainty expression (4.130), that is, $\left.\frac{d\Im^{-1}(x)}{dx}\right|_{r_{21}} \frac{1}{T_{g,1}\left(\tau_g,\nu\right)}\sqrt{1+\frac{r_{21}^2}{2}}$ is depicted in figure 4.38. We can see the zone around $\tau_g = 1$ where this value remains low.

Taking into account previous simulations we can calculate the value of the uncertainty for the case of a 100-meter range. To keep the analysis as general as possible a specific gas-absorption cross section σ is not defined, but rather the value $\hat{\square}(R)\sigma$ is used, which represents the noise-affected measurement of the absorption coefficient.

As stated in table 4.3:

$$\mathrm{E}\left[\hat{\square}(R)\sigma\right] = 0.005\,m^{-1} \tag{4.131}$$

The typical deviation of this value for the 100-meter-range case gives a value of:

$$\left\{E\left[\left(\hat{\square}(R)\sigma - \square(R)\sigma\right)^2\right]\right\}^{1/2} = 86.20m^{-1} \tag{4.132}$$

Figure 4.38 shows the evolution of both the real gas concentration and its typical deviation value check along the range up to 600 meters.

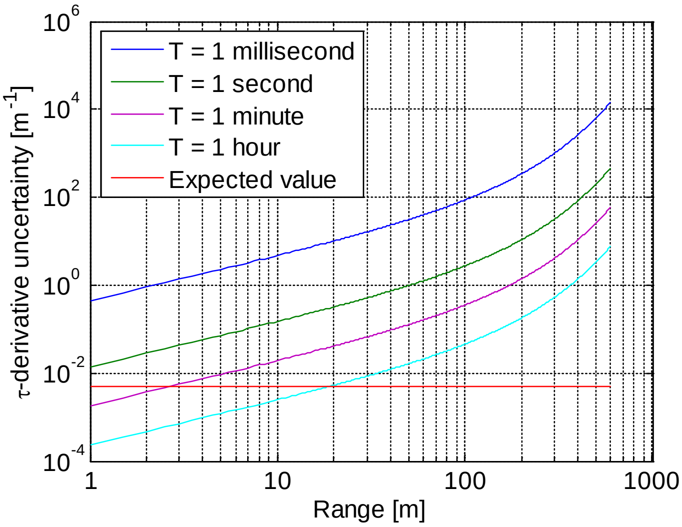

Figure 4.39. Evolution of the tau-derivative uncertainty along range for the values in table 4.3 with different integration times (blue lines) and expected tau-derivative value.

Once the uncertainty analysis is performed and its value calculated for a typical situation (table 4.3), the uncertainty values can then be analyzed. Obviously it is difficult to obtain good uncertainty values for the explained conditions using the values selected for the variables, even given long integration times. Nevertheless, there are a number of factors that can contribute to improving the uncertainty values. The output power of the P_0 system can be increased to values of about 1 Watt by using more powerful sources or even optical amplifiers, decreasing uncertainty to a factor of approximately 7. The noise power value P_N basically depends on the background radiation and the receiver NEP factor. The background radiation corresponds to a far from ideal situation in which the photoreceiver is directed at a sunlit sky. Pointing the system at darker background zones and the use of cooled photoreceivers (either APD or PMT based) would reduce this value.

Another point to be taken into account is the total gas-interaction factor in the uncertainty expression (Eq. 4.130). The value obtained for the conditions cited is 40, but values up to 3 times smaller can be achieved with other modulation conditions. This would be an interesting starting point for developing further research. Higher values of $\beta(R)$ might also be found in industrial environments, contributing to a decrease in uncertainty values. The system's range resolution, which is inversely proportional to the electrical bandwidth, can be also reduced in order to obtain better uncertainty values.

A final relevant point is the value of the expected gas-absorption coefficient. For this study a value of $N(R)\sigma = 0.005[m^{-1}]$ was selected, but in figure 4.40 we can see the evolution of the uncertainty along the range for two different values of the expected gas-absorption coefficient, 0.0025 (represented by the blue line) and 0.01 (represented by the green line). While in the first case the uncertainty is greater in the low ranges, it behaves much better over longer distances, in this case, beyond 140 meters. This is an interesting feature that requires analysis when selecting the gas absorption line to be tested.

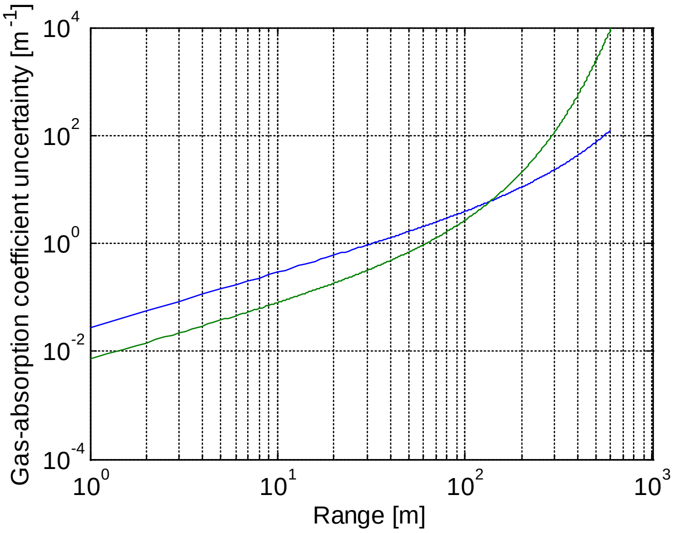

Figure 4.40. The evolution of system uncertainty with respect to range for expected gas-absorption coefficients of 0.0025 m^{-1} (blue line) and 0.01 m^{-1} (green line) and an integration time of 1 second.

4.4.4 The application of the baseband shift and phase-hop method

As happens with aerosol detection, applying the classical lidar FMCW method to gas detection poses the problem of bandpass filtering, not allowing the retrieval of accurate information about gas concentrations. Similarly, the only option that makes it possible to extract this information is to shift the modulation of the emitted signal to baseband and eliminate the presence of other harmonics in the received signal.

The use of phase-hop methodology in aerosol detection has made it possible to extract the 1st harmonic correctly by eliminating the distortion present in the received signal. Due to the characteristics of the gas detection signal, which presents multiple harmonics on reception, it is essential to use an extension of the phase-hop method in the extraction of relevant data from any undesired additional components. The data acquired from the distributed target can be described as a sum of harmonics with a certain amplitude and phase depending on both the emitted signal characteristics and the target interaction.

Therefore, the extraction of data from the harmonic m is carried out by mixing the received signal (Eq. (4.82)) with the corresponding harmonic of the emitted signal, obtaining the output current as follows:

$$\begin{aligned} i_m(t) \approx \Re\int_0^{\infty} P_0'(R)\cos\left[2\pi m(f_0 t + Kt^2/2) + m\phi_p\right]\times \\ \sum_{n=0} T_{g,n}\left(\tau_g,\nu\right)\cos\left[2\pi n(f_0(t-2R/c) + K(t-2R/c)^2/2) + n\phi_p\right]dR \end{aligned} \tag{4.133}$$

where $f_0 = -KT/2$.

This expression shows that it is not possible to eliminate all those harmonics with a degree different of m, including the harmonic produced by the received DC component, by a simple mixing process due to its superposition in the baseband zone. In order to eliminate such harmonics and avoid distortions in the measurements, the proposed solution is to employ an emitted signal comprising a train of periods of the single-period emitted signal with a different phase in each case similar to that of the original phase-hop method. So the phase of the emitted signal will have a value $\phi_p = \dfrac{2\pi p}{N_p}$ for each period p, N_p being the number of phase-shifted single periods.
The received signal will take the form of:

$$\begin{aligned} P_R(t) \approx \sum_{p=0}^{N_p-1}\int_0^{\infty} P_0'(R)\,\Pi\left(\frac{t-\left(p+1/2\right)T-2R/c}{T}\right)\times \\ \sum_{n=0} T_{g,n}\left(\tau_g,\nu\right)\cos\left[2\pi n\left(f_0\left(t-pT-2R/c\right)+K\left(t-pT-2R/c\right)^2/2\right)+n\phi_p\right]dR \end{aligned} \tag{4.134}$$

With this signal we can obtain the different harmonic responses by mixing the received signal with the corresponding harmonic of the emitted signal, as expressed in Eq. (4.135).

$$\begin{aligned} i_m(t) \approx \Re\sum_{p=0}^{N_p-1}\int_0^{\infty} P_0'(R)\cos\left[2\pi m\left(f_0\left(t-pT\right)+K\left(t-pT\right)^2/2\right)+m\phi_p\right]\times \\ \sum_{n=0} T_{g,n}\left(\tau_g,\nu\right)\cos\left[2\pi n\left(f_0\left(t-pT-2R/c\right)+K\left(t-pT-2R/c\right)^2/2\right)+n\phi_p\right]dR \end{aligned} \tag{4.135}$$

In order to obtain a final response from which the distorting harmonics have been eliminated, we must average all the responses obtained for the different periods so the final mth harmonic signal will take the form:

$$\begin{aligned}\bar{i}_m(t) \approx \Re \sum_{p=0}^{N_p-1} \Bigg[\Bigg\{ \int_0^{\infty} P_0'(R) \cos\left[2\pi m\left(f_0\left(t-pT\right)+K\left(t-pT\right)^2/2\right)+m\phi_p\right] \times \\ \sum_{n=0} T_{g,n}\left(\tau_g,\nu\right)\cos\left[2\pi n\left(f_0\left(t-pT-2R/c\right)+K\left(t-pT-2R/c\right)^2/2\right)+n\phi_p\right]dR\Bigg\} * \\ *\delta\left(t-\left(N_p-p\right)T\right)\Bigg]\end{aligned} \quad (4.136)$$

or, grouping the terms:

$$\begin{aligned}\bar{i}_m(t) \approx \Re \sum_{p=0}^{N_p-1} \int_0^{\infty} P_0'(R) \cos\left[2\pi m\left(f_0\left(t-N_pT\right)+K\left(t-N_pT\right)^2/2\right)+m\phi_p\right] \times \\ \sum_{n=0} T_{g,n}\left(\tau_g,\nu\right)\cos\left[2\pi n\left(f_0\left(t-N_pT-2R/c\right)+K\left(t-N_pT-2R/c\right)^2/2\right)+n\phi_p\right]dR\end{aligned} \quad (4.137)$$

So for each detected harmonic m, the distorting harmonics of order n will be eliminated when the condition (Eq. (4.138)) is satisfied. This can be tested for any harmonic.

$$\sum_{p=0}^{N_p} \exp\left(j2\pi \frac{p}{N_p}\left(n \pm m\right)\right) = 0 \quad (4.138)$$

To understand the principle behind the technique, an example for the detection of the 2nd harmonic in a case where $N_p = 4$ was developed. Table 4.4 gives the shape of each of the harmonics after being mixed with the 2nd harmonic signal (both sum-frequency and difference-frequency components) during a timeframe of 1 fundamental period at the beginning of the period and up to the 4th harmonic of the received signal. Each column represents the result for an initial signal phase of $\phi_p = 0, \pi/2, \pi, 3\pi/2$, and the final column shows the average of all 4 periods.

It is clear from table 4.4, that most of the resulting components (both sum-frequency and difference-frequency components) are suppressed when averaging the 4 periods, with the exception of the difference frequency for $n = 2$, where the desired 2nd harmonic value is retrieved.

As indicated by Eq. (4.138), the selection of N_p imposes a limitation that makes it impossible to suppress the resulting components multiple of N_p using this method, that is $n \pm m = kN_p$, where k is an integer. This is demonstrated in table 4.4 which gives the sum-frequency component average of $n = 2$. This is an unavoidable limit that will determine the selection of N_p. The effects of more harmonics are eliminated by the use of higher values of N_p.

Table 4.4. Results of the phase-hop method application for sum-frequency and difference-frequency components of different harmonics of the received signal. In this case, the detected/mixing harmonic is $m = 2$ and the analyzed harmonics are $n = 0..4$. The number of phase-shifted single periods N_p is 4.

2nd Harm. $m=2$	$\phi_p=0$	$\phi_p=\frac{\pi}{2}$	$\phi_p=\pi$	$\phi_p=\frac{3\pi}{2}$	Average
$n=0$ Diff. Freq.	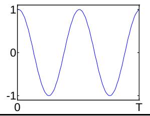	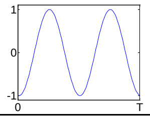	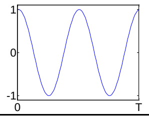	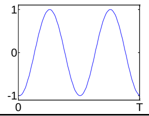	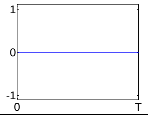
$n=0$ Sum Freq.	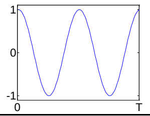	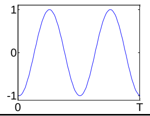	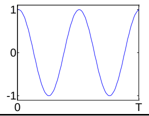	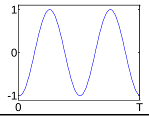	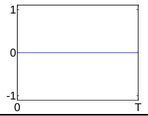
$n=1$ Diff. Freq.	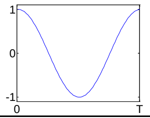	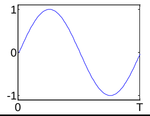	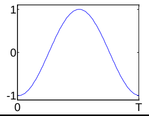	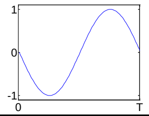	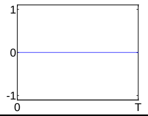
$n=1$ Sum Freq.	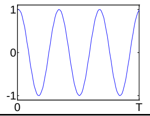	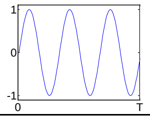	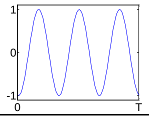	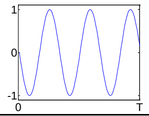	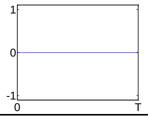
$n=2$ Diff. Freq.	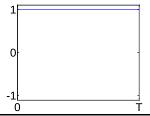	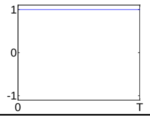	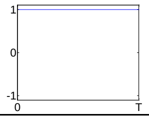	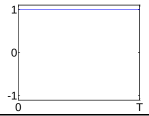	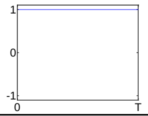
$n=2$ Sum Freq.	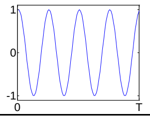	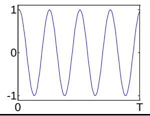	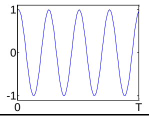	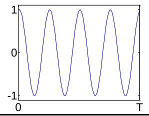	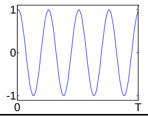
$n=3$ Diff. Freq.	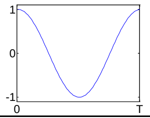	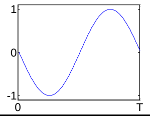	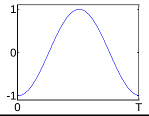	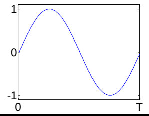	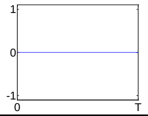
$n=3$ Sum Freq.	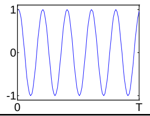	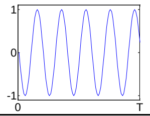	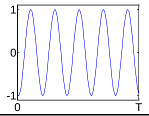	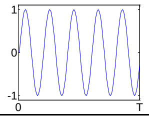	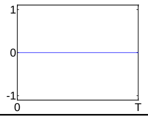
$n=4$ Diff. Freq.	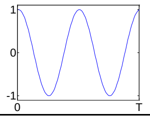	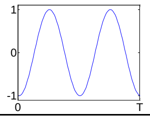	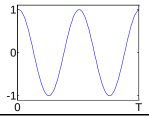	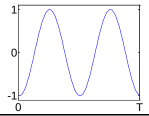	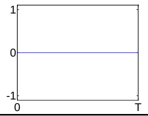
$n=4$ Sum Freq.	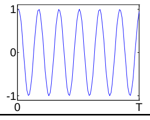	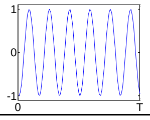	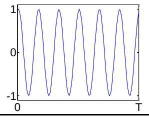	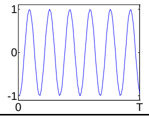	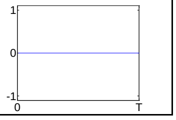

4.4.4.1 Applying the phase-hop method to an ideal medium of constant power return and constant gas concentration

Here, an analysis of the phase-hop method is applied to gas detection, followed by a series of simulations that corroborate the results obtained. This section described the simulation of an ideal medium with a constant power return up to 600 meters, independent of R, and where gas concentration is assumed to remain constant (Fig. 4.41). The simulations comprise testing and validating the extended phase-hop method when applied to gas-measurement systems up to obtaining the $|r_{21}|$ ratio.

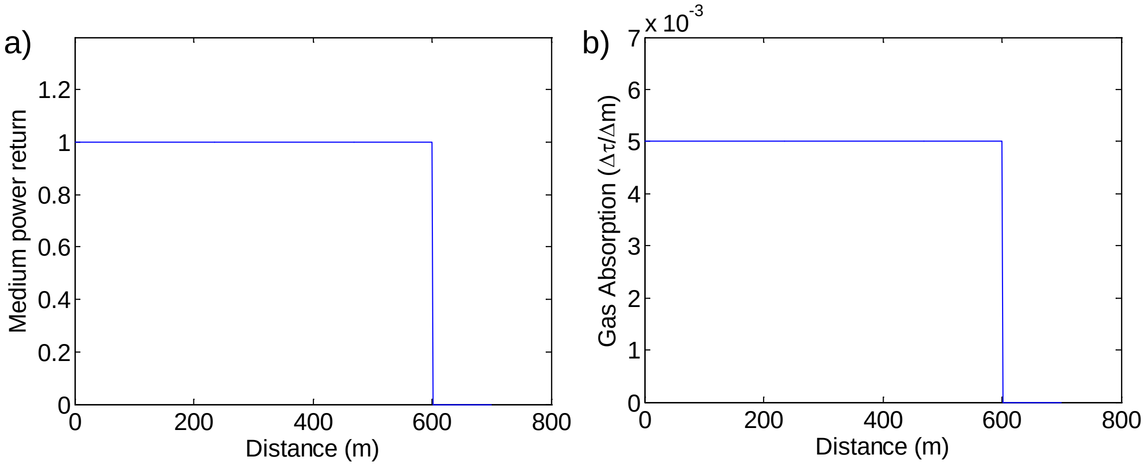

Figure 4.41. Ideal distributed-medium characteristics of aerosol backscattering (a) and gas absorption (b) along distance

The first example given is the case of a modulating signal with a modulation index of $m = 2$ (a high level of modulation) and centered at the modulation point $\bar{\nu} = 1/\sqrt{3}$ $\left(g''(\nu_0) = 0\right)$.

Figures 4.42 and 4.43 represent the 1st-harmonic medium response for different cases of N_p. The represented values of N_p are 1, 2, 4, 8, 16 and 32. The choice of powers of 2 for these values simply enables the changes produced as the value increases to be demonstrated more rapidly. In practice any natural number can be used as N_p.

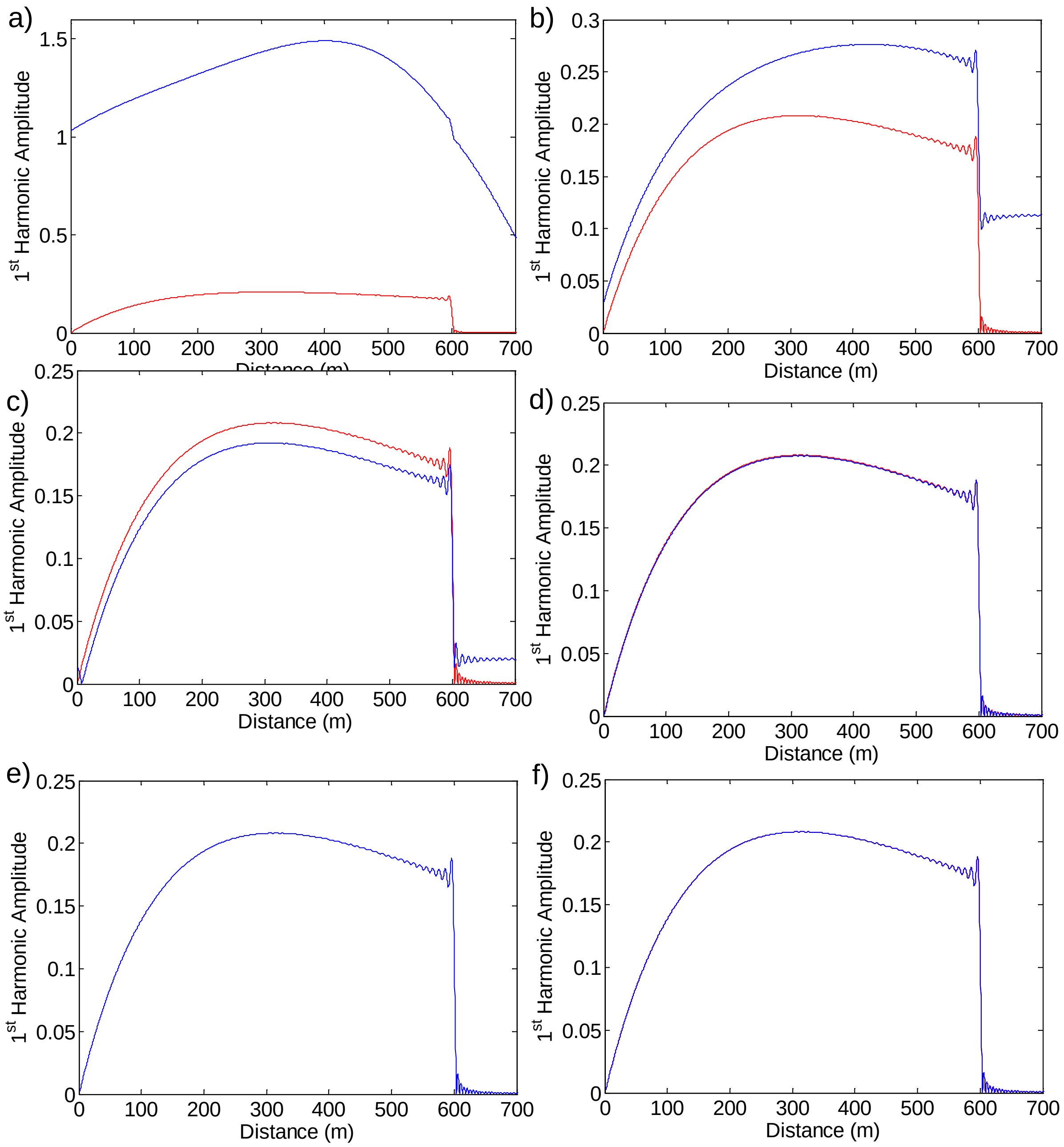

Figure 4.42. 1st harmonic retrieved data of a medium with gas for $N_p = 1\,(a), 2\,(b), 4\,(c), 8\,(d), 16\,(e)$ *and* $32\,(f)$ with (blue) and without (red) distortion coming from other harmonics for a modulation index of $m = 2$ and at a modulation point of $\overline{\nu} = 1/\sqrt{3}$ (Note that the vertical scale in panels (a) and (b) has been given a larger span than others to encompass the (blue) curves with distortion).

If we examine the results, it is clear that for $N_p = 1$ (Fig. 4.42.a) the retrieved data is totally distorted due to the effects of DC power. This effect disappears for $N_p = 2$ (Fig. 4.42.b) but the powerful effect of the 1st harmonic sum-frequency component remains. It is possible to eliminate DC power when the signal is detected but this can produce a level of distortion due to the bandpass filtering effects in the signal.

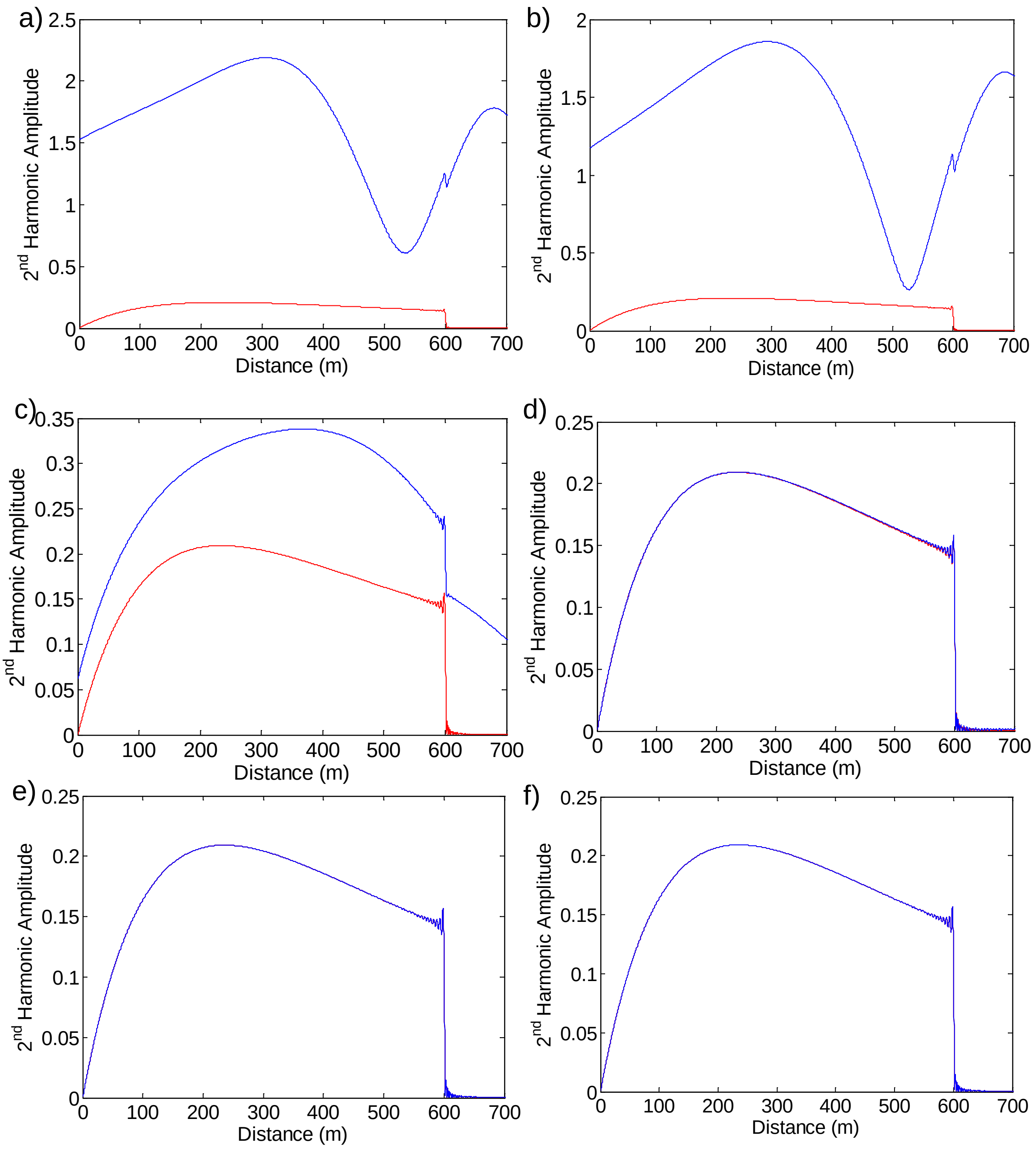

Figure 4.43. 2^{nd} harmonic data retrieval from a medium with gas for $N_p = 1\,(a), 2\,(b), 4\,(c), 8\,(d), 16\,(e)$ *and* 32 (f) with (blue) and without (red) distortion coming from other harmonics for a modulation index of $m = 2$ and at a modulation point of $\overline{\nu} = 1/\sqrt{3}$ (Note that the vertical scale in panels (a), (b) and (c) has been given a larger span than others to encompass the (blue) curves with distortion).

The proposal here is to eliminate DC power through software processing without any resulting distortion. For $N_p = 4$ (Fig. 4.42.c), the signal is quite similar to that of the ideal one (shown in red) but some effects of third-harmonic distortion remain. For the cases $N_p = 8$, 16, and 32 (Fig. 4.42.d, 4.42.e and 4.42.f), the retrieved data almost coincides with that of the ideal signal, with the distortion due to higher harmonics decreasing as N_p increases.

Figure 4.43 gives the 2nd harmonic, which behaves in a similar way to the case for the 1st harmonic. In the first two cases of $N_p = 1$ and 2 (Fig. 4.43.a and 4.43.b), the presence of the DC component produces a higher level of distortion. For $N_p = 4$ (Fig. 4.43.c), this distortion is suppressed but the effect of the 2nd harmonic sum-frequency component remains.

As with the 1st harmonic case, the retrieved data for cases $N_p = 8, 16 \textit{ and } 32$ (Fig. 4.43.d, 4.43.e and 4.43.f) almost coincides with that of the ideal case, with the distortion caused by higher harmonics decreasing as N_p increases.

Data from the last two figures indicates that it is possible to obtain good results for an $N_p = 8$ or higher and that the level of distortion is very slight. However, this research focuses on the case where the modulation index is $m = 2$. Different values can be selected for this variable to give the different results shown in figure 4.44, where the ideal representation of the 1st harmonic response for $m = 0.1$ (red line) and two different retrievals for different values of N_p (blue line) are shown.

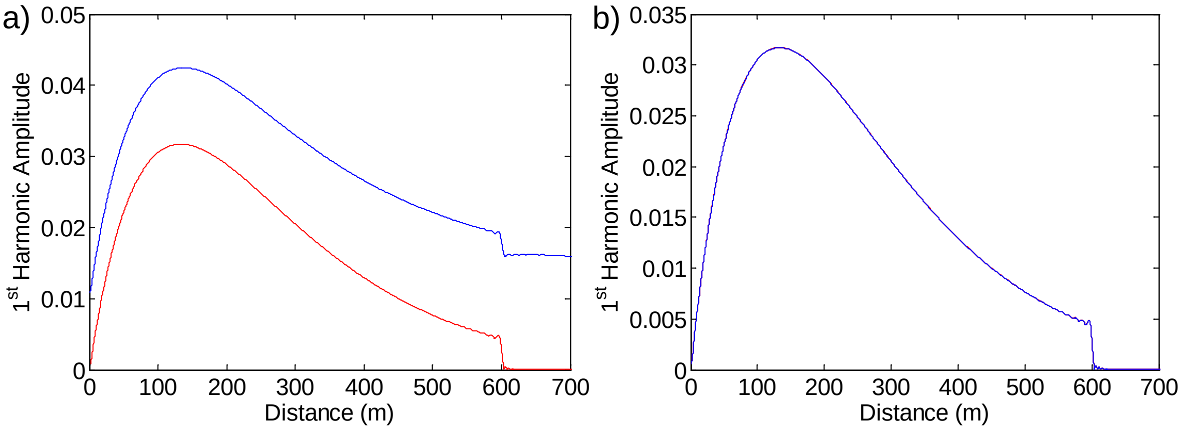

Figure 4.44. 1st harmonic retrieved data of a medium with gas for $N_p = 2\ (a)$ and $N_p = 4\ (b)$ with (blue) and without (red) distortion coming from other harmonics for a modulation index where $m = 0.1$ and at a modulation point where $\overline{\nu} = 1/\sqrt{3}$

Figure 4.44 shows that for the case of $N_p = 2$ (Fig. 4.44.a), similar behavior to that obtained for $m = 2$ is present (blue line), but for the case of $N_p = 4$ (Fig. 4.44.b) the retrieved gas-medium data is practically equal to that of the ideal case. This demonstrates that while the 1st and 2nd harmonic responses are greater for higher values of m, distortion coming from higher-order harmonics is also greater. Therefore a compromise must be reached when choosing m values, as even very small levels of distortion can affect the final result.

Table 4.5 gives the maximum absolute values of amplitude around the absorption line for the different harmonics for the values of m given in its first row . Note that while for $m = 0.1$ the maximum value of each harmonic is divided by a factor of approximately 20 with respect to the previous one, for $m = 2$ this value is only divided by a factor 2. This explains the different behavior obtained for the cases of higher and lower m values. From here on the value m, $N_p = 8$ will be considered a reasonable value to perform the calculation, even for high values of m. Other values may prove optimal for different cases.

Table 4.5. The evolution of the harmonic maximum amplitude around the absorption line with respect to the modulation index m

Harmonic MAX	m = 0.1	m = 0.5	m = 1	m = 2
1st Harmonic	$3.5\cdot10^{-2}$	0.18	0.3	0.45
2nd Harmonic	$2\cdot10^{-3}$	$4\cdot10^{-2}$	0.13	0.25
3rd Harmonic	$6\cdot10^{-5}$	$6\cdot10^{-3}$	$3\cdot10^{-2}$	0.1
4th Harmonic	$3\cdot10^{-6}$	$1.5\cdot10^{-3}$	$1.4\cdot10^{-2}$	$6\cdot10^{-2}$
5th Harmonic	$1\cdot10^{-7}$	$2.5\cdot10^{-4}$	$4\cdot10^{-3}$	$3\cdot10^{-2}$
6th Harmonic	$5\cdot10^{-9}$	$6\cdot10^{-5}$	$2\cdot10^{-3}$	$2\cdot10^{-2}$

Some incomplete examples have been chosen to illustrate different cases found when the modulation point $\bar{\nu}$ and the modulation index m. are changed. Figure 4.45, which corresponds to figures 4.42(d) and 4.43(d), represents the response of the 1st (a) and 2nd (b) harmonic for the case of $m = 2$ and $\bar{\nu} = 1/\sqrt{3}$. Figure 4.46, also gives the $|r_{21}|$ ratio for this case.

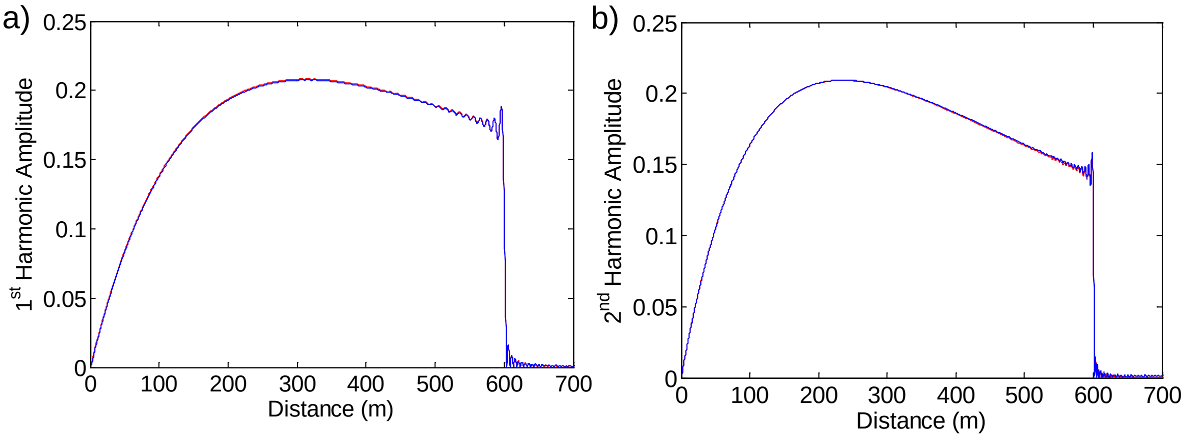

Figure 4.45. 1st (a) and 2nd (b) harmonics retrieved data of a medium with gas with (blue) and without (red) distortion coming from other harmonics for $N_p = 8$ for a modulation index where $m = 2$ and at a modulation point of $\bar{\nu} = 1/\sqrt{3}$

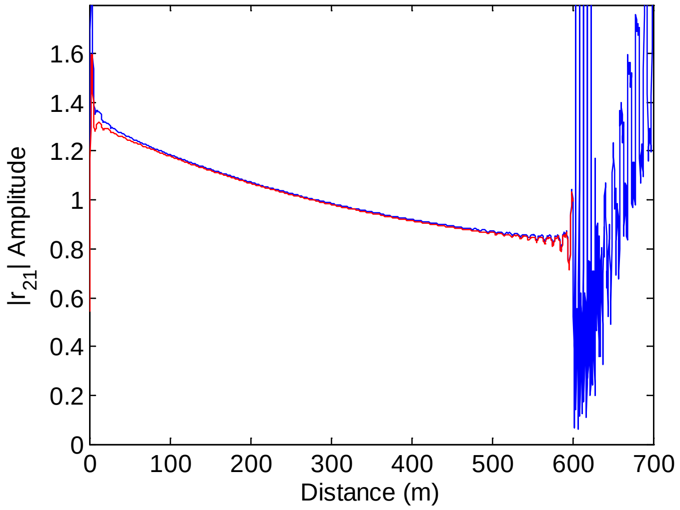

Figure 4.46. $|r_{21}|$ ratio of a medium with gas with (blue) and without (red) distortion coming from other harmonics for $N_p = 8$ for a modulation index where $m = 2$ and at a modulation point of $\overline{\nu} = 1/\sqrt{3}$

Figure 4.47 gives the response of the 1st (a) and 2nd (b) harmonic for the case of $m = 0.1$ and $\overline{\nu} = 1/\sqrt{3}$. Figure 4.48 also gives the $|r_{21}|$ ratio for this case.

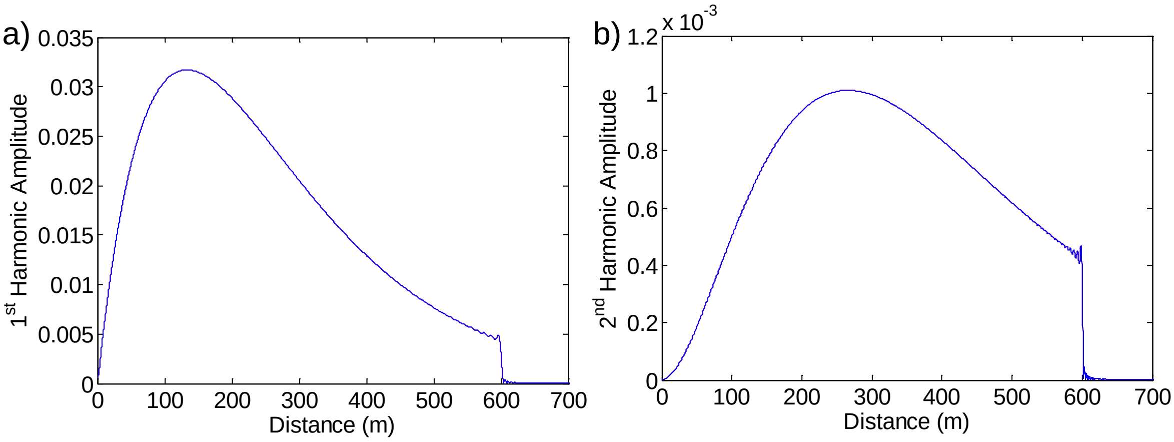

Figure 4.47. 1st (a) and 2nd (b) harmonics retrieved data of a medium with gas with (blue) and without (red) distortion coming from other harmonics for $N_p = 8$ for a modulation index $m = 0.1$ and at a modulation point $\overline{\nu} = 1/\sqrt{3}$

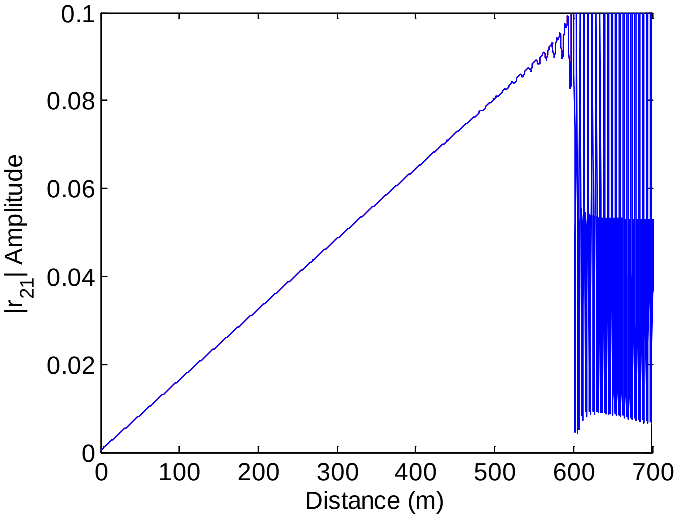

Figure 4.48. $|r_{21}|$ ratio of a medium with gas with (blue) and without (red) distortion coming from other harmonics for $N_p = 8$ for a modulation index $m = 0.1$ and at a modulation point $\bar{\nu} = 1/\sqrt{3}$

Figure 4.49 gives the response of 1st (a) and 2nd (b) harmonics for the case of $m = 2$ and $\bar{\nu} = 2$. Figure 4.50 also gives the $|r_{21}|$ ratio for this case. In this case, the zero-crossing of the 2nd harmonic at around 470 meters invalidates the method beyond this distance because of the problem of ambiguity.

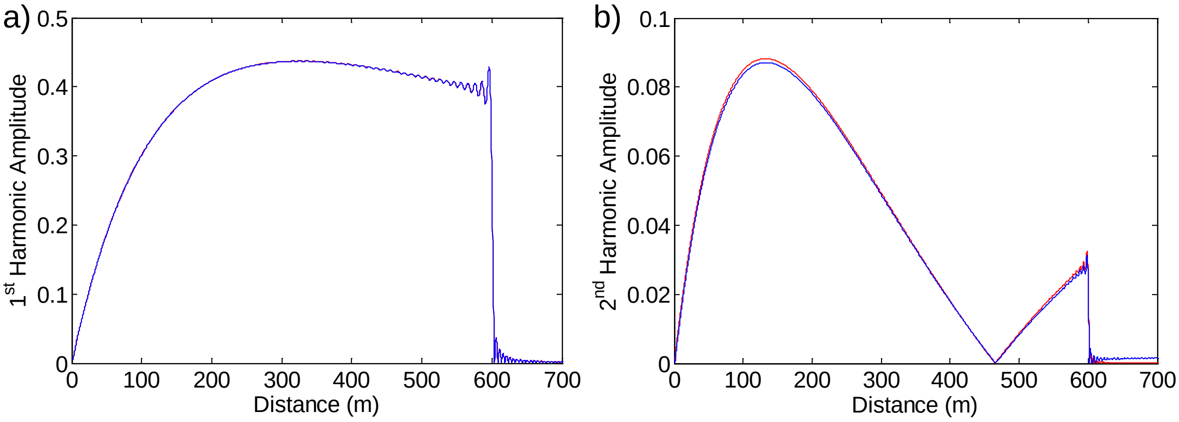

Figure 4.49. Absolute value of 1st (a) and 2nd (b) harmonics retrieved data of a medium with gas with (blue) and without (red) distortion coming from other harmonics for $N_p = 8$ for a modulation index where $m = 2$ and at a modulation point of $\bar{\nu} = 2$

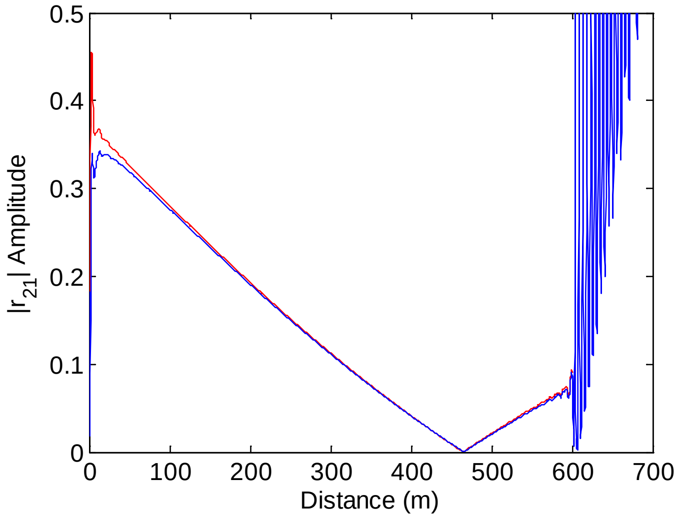

Figure 4.50. The $|r_{21}|$ ratio of a medium with gas with (blue) and without (red) distortion coming from other harmonics for $N_p = 8$ for a modulation index where $m = 2$ and at a modulation point of $\overline{\nu} = 2$

4.4.4.2 The application of the phase-hop method to a realistic medium of constant backscatter coefficient and constant gas concentration

After testing the phase-hop method applied to gases by means of simulations, it is necessary to perform a complete simulation of a system probing a typical lidar-backscattering medium with both a constant backscatter coefficient and a constant gas concentration. The characteristics of the medium are represented in figure 4.51 and the chosen phase-hop level is $N_p = 8$. The modulation point is $\overline{\nu} = 1/\sqrt{3}$ and the modulation index $m = 0.5$.

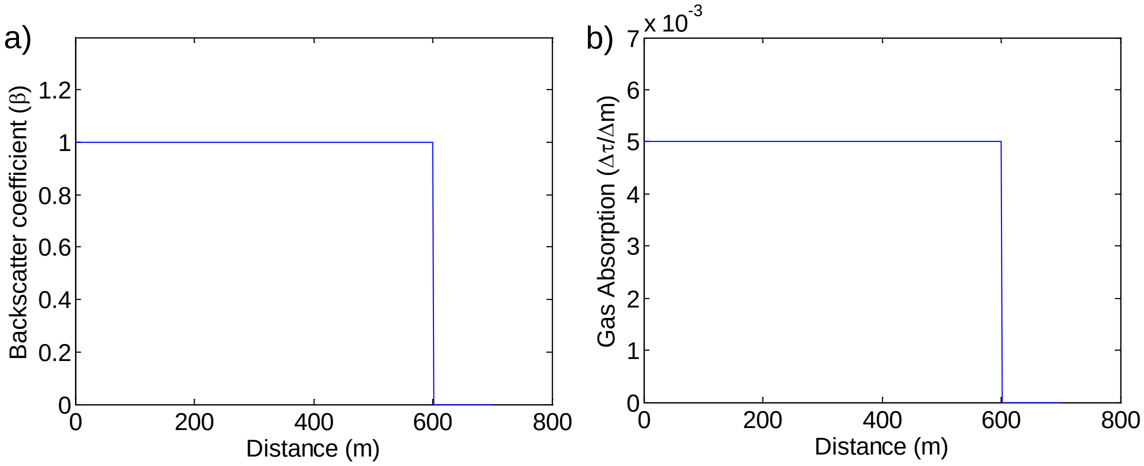

Figure 4.51. Ideal distributed-medium characteristics of aerosol backscattering (a) and gas absorption (b) along distance for a normalized constant-backscatter-coefficient medium.

Figure 4.52 shows the responses for the 1st (a) and 2nd (b) harmonics. The shapes of the curves are quite similar but, as shown in figure 4.53, when the ratio between 2nd and 1st harmonic is performed some differences arise.

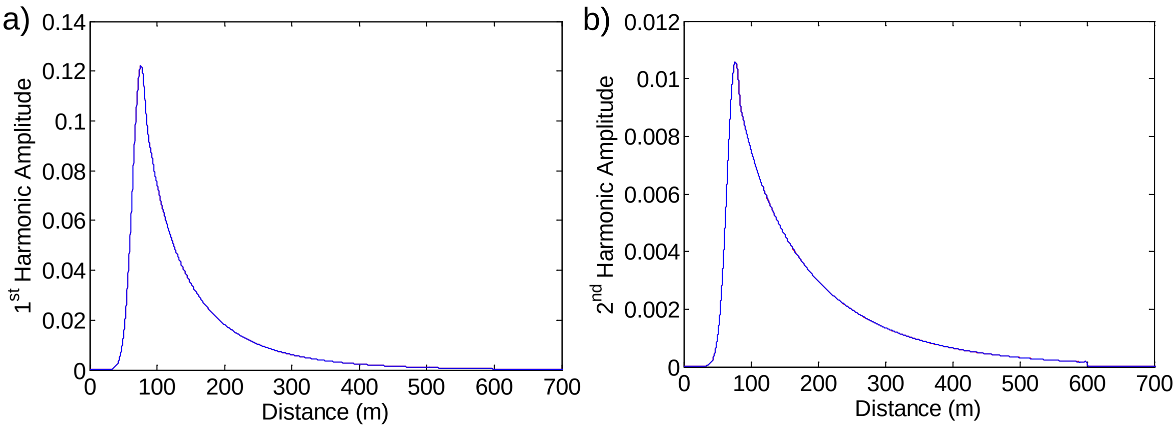

Figure 4.52. 1st (a) and 2nd (b) harmonics retrieved data in a constant-backscatter-coefficient medium with gas with (blue) and without (red) distortion coming from other harmonics for $N_p = 8$ for a modulation index where $m = 0.5$ and at a modulation point of $\overline{\nu} = 1/\sqrt{3}$. The red and blue curves almost coincide.

In Figure 4.53 it is possible to observe the chaotic behavior that occurs before 30 meters and after 600 meters, with very small values for both 1st and 2nd harmonic responses. In the central zone, the response obtained compares well to that of the ideal response (red). But this only provides us with information about the $|r_{21}|$ ratio and we need to know what value of τ_g will give us the gas absorption and consequently the gas concentration.

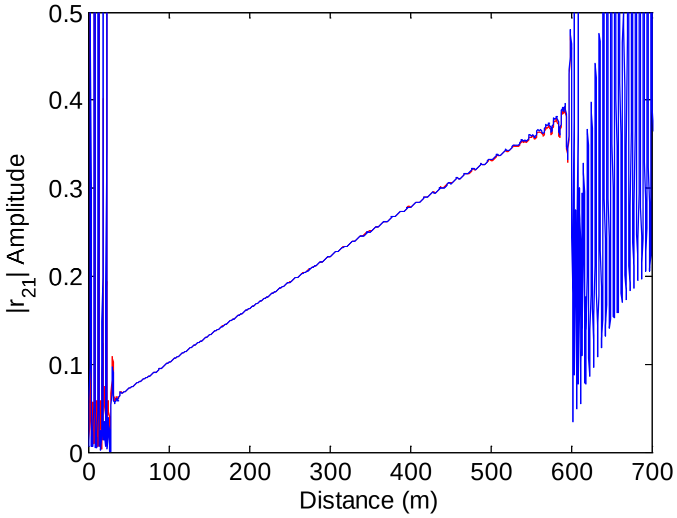

Figure 4.53. The $|r_{21}|$ ratio in a lidar-like medium with gas with (blue) and without (red) distortion coming from other harmonics for $N_p = 8$ for a modulation index where $m = 0.5$ and at a modulation point of $\overline{\nu} = 1/\sqrt{3}$

Gas absorption information must be obtained by inverting the function of τ_g from the 2nd to 1st harmonic ratio. Figure 4.54(a) illustrates the simulation of this function, Fig. 4.54(b) gives some inverted values of τ_g (red crosses) to which a 6-order polynomial has been fitted.

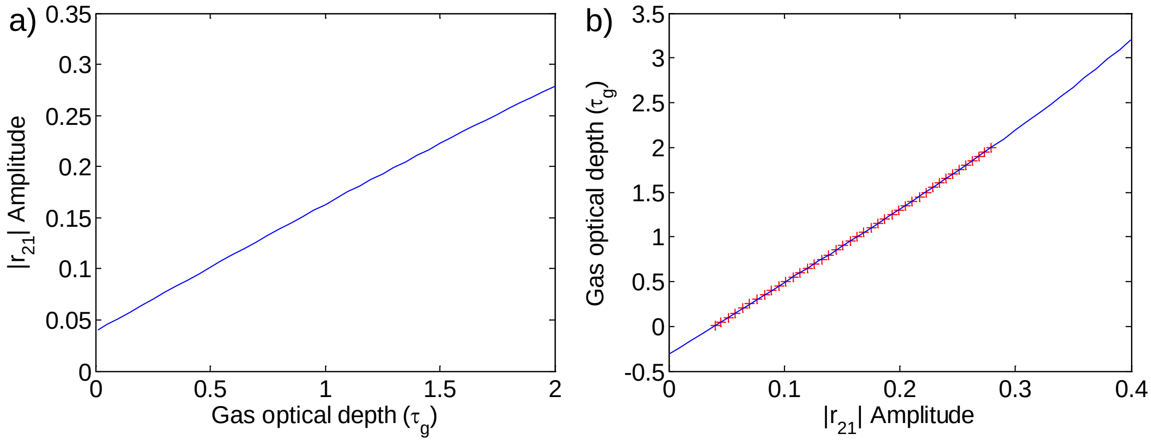

Figure 4.54. The $|r_{21}|$ ratio with respect to τ_g function (a) and its inverted function (b) graphically obtained from (a), interpolating a number of points (red crosses) for a modulation index $m = 0.5$ and at a modulation point $\overline{\nu} = 1/\sqrt{3}$

With the help of this inverted function we are able to obtain the τ_g-parameter function from the 2nd to 1st harmonic ratio function. This result is represented by the blue line in figure 4.55 with the theoretical value superposed in red.

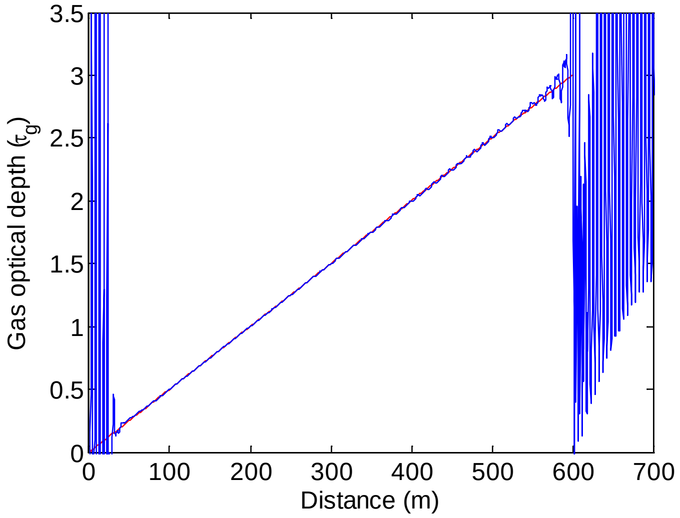

Figure 4.55. τ_g -parameter with respect to distance in a constant-backscatter-coefficient medium with gas with (blue) and without (red) distortion coming from other harmonics for $N_p = 8$ for a modulation index where $m = 0.5$ and at a modulation point of $\overline{\nu} = 1/\sqrt{3}$

Finally, by differentiating τ_g with respect to the distance we are able obtain the value of the differential absorption $\Delta\tau_g$ for all ranges up to 600 meters (Fig. 4.56). These final results demonstrate a large ringing effect due to the fact that the scenario has been limited to 600 meters, as after this point the lidar-like aerosol backscattering function falls directly to zero.

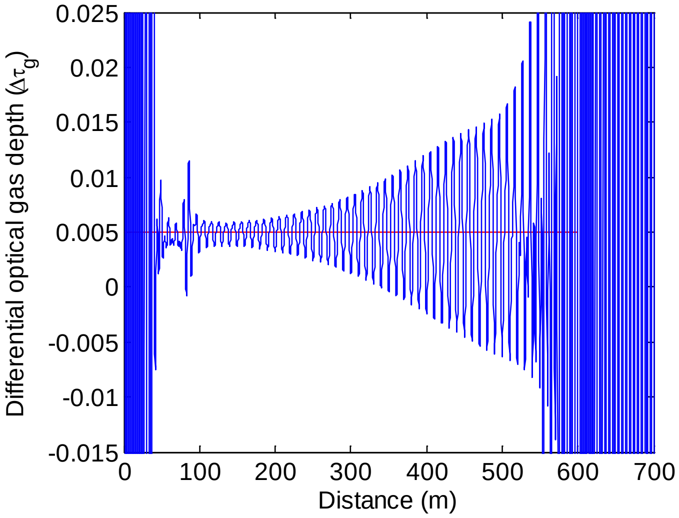

Figure 4.56. $\Delta\tau_g$ -parameter with respect to distance in a constant-backscatter-coefficient medium with gas for $N_p = 8$ for a modulation index $m = 0.5$ and at a modulation point $\overline{\nu} = 1/\sqrt{3}$ with the expected value (red)

To overcome this problem, a moving average of 10 meters has been applied to the data, giving the improved results seen in figure 4.57. Even after smoothing out this ringing effect, there is still a distortion beyond 400 meters.

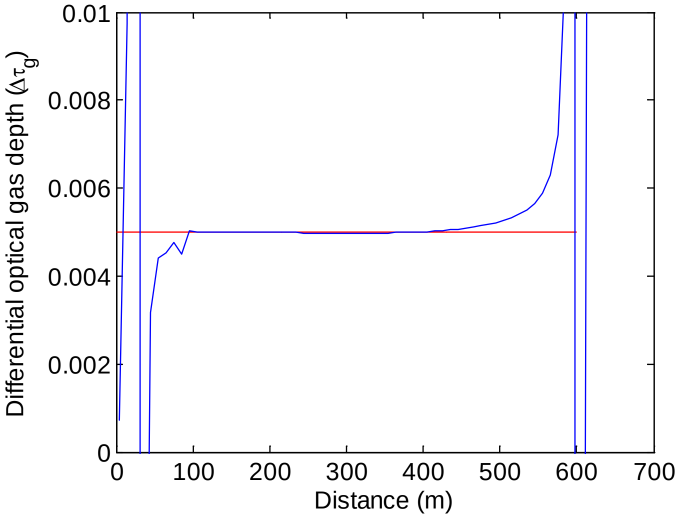

Figure 4.57. $\Delta\tau_g$ -parameter with respect to distance in a constant-backscatter-coefficient medium with gas for $N_p = 8$ for a modulation index where $m = 0.5$ and at a modulation point of $\overline{\nu} = 1/\sqrt{3}$ with the expected value (red). Averaged case

One more simulation was performed (Fig. 4.58) with the same characteristics as the previous one but with a higher phase-hop level $\left(N_p = 16\right)$. The results show that this distortion has been partially reduced on the right side which seems to indicate that the main cause could be the sudden decrease in the backscatter coefficient of the medium at 600 meters. This suggests that in a real case, where such a sharp decrease is unlikely to happen, such distortion effects would be less pronounced.

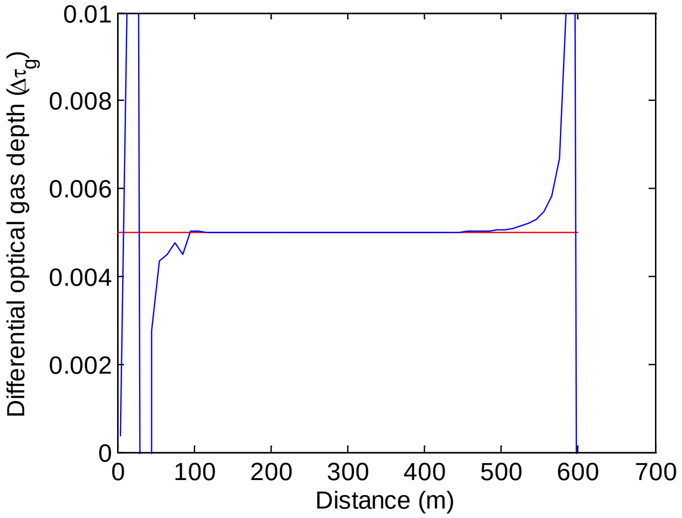

Figure 4.58. $\Delta\tau_g$ -parameter with respect to distance in a constant-backscatter-coefficient medium with gas for $N_p = 16$ for a modulation index where $m = 0.5$ and at a modulation point of $\overline{\nu} = 1/\sqrt{3}$ with the expected value shown in red. Averaged case.

4.5 Chapter conclusions

The analysis of the FMCW technique for distributed media has been performed in this section. It has been shown that if the modulating signal has a bandpass nature a harmful bandpass filtering effect occurs in the signal processing that precludes recovering the information on the spatial 0-frequency of the probed gas distribution. To overcome this difficulty, a novel phase-hop method is proposed which includes the baseband shift of the modulating signal and the introduction of a changing phase in this modulating signal to filter out the interfering sum-frequency components. The analytical calculation of the signal-to-noise ratio for an aerosol-detection FMCW system has also been developed, with the conclusion that it is possible to cover ranges of several kilometers provided that system components are correctly selected and integration times are sufficiently long.

Moreover, the FMCW technique has been analyzed in its application to gas detection. First, the case with the use of a topographical target to provide backscattering has been studied, then the analysis has been extended to the more general (and interesting, as it allows range resolution) case of using aerosols (distributed medium) as backscattering medium. These cases have been analytically developed and a number of simulations have been performed to confirm the analytical results. A sensitivity analysis formulation for the case of using aerosols as backscattering medium has been carried out. The results obtained identify the critical parameters and point out how they must be improved to design practical systems. Finally, an extension of the phase-hop method for the case of gas detection has been proposed that would overcome the problems of interference produced by higher order harmonics on the detected signal, allowing the FMCW lidar technique to be applied to the detection of gases.

List of variables of chapter 4	
A_R	Telescope area
c	Speed of light
R	Range
$\alpha(R)$	Extinction coefficient
$\beta(R)$	Backscatter coefficient
τ	Pulse duration
S_0	Radar emitted amplitude
f_0	Initial RF frequency
K	Rate of change in frequency
A_t	Radar backscatter factor
φ_0	Radar phase
i_0	DC bias current
Δi	Current modulation amplitude
P_0	Mean emitted power
γ_{IP}	Laser slope efficiency
i_{th}	Threshold current
m_{AC}	Intensity modulation index
$u(t)$	Field amplitude
ν_{LAS}	Laser central wavelength
δ_ν	Wavelength-current ratio
σ_0	Radar cross section
r(R)	Medium impulse response
T	Period duration
ϕ_1	Phase term 1
ϕ_2	Phase term 2
N	Number of points in a period
F_s	Sampling frequency
f_c	Central frequency
$f_{\min}$	Chirp min frequency
$f_{\max}$	Chirp max frequency
ϕ_0	Chirp initial phase
$\phi_{FM}(t)$	Internal phase-hop phase
θ_-	Phase-hop difference phase
θ_+	Phase-hop addition phase
E_{Period}	Period energy
η_n	Electrical-noise-power spectral density
$\Re$	Optoelectronic conv. Factor [V/W]
P_{Rec}	Received power from distance R

ΔR	Resolution distance
ξ	Receiving optical-system transmittance
T_0	Medium transmittance
E	Background spectral irradiance
$\Delta\lambda_{filter}$	Optical filter bandwidth
P_N	Total optical noise equivalent power
$\pi\theta^2$	Vision solid angle
Δf_D	Detector electrical bandwidth
NEP	Amplifier noise equivalent power
P_q	Quantum noise power
h	Planck constant
η	Quantum efficiency
F	Excess noise factor
M	Averaged periods
$\varphi(t)$	Random phase term
$\alpha_a(R,\nu)$	Aerosol-induced extinction
$\alpha_g(R,\nu)$	Gas-induced extinction
$N(x)$	Gas concentration
σ	Peak gas-absorption cross section
$g(\nu)$	normalized absorption-line shape
ρ_{top}	Target surface reflectivity
ν	Optical signal wavelength
$\tau_a(R)$	Aerosol-produced optical thickness
$T_a(R)$	Round-trip aerosol transmittance
$\tau_g(R)$	Gas optical depth
$\Delta\nu_{\max}$	Maximum optical frequency deviation
$T_{g,n}\left(\tau_g,\nu\right)$	Gas-interaction-produced-harmonics amplitudes
P_0''	Gas-independent constant terms
f_R	Range frequency
$r_{21}(R)$	Second-to-first harmonic ratio
m	Relative level of modulation
$\bar{\nu}$	Relative point of modulation
$\Im(x)$	Gas optical depth to r_{21} ratio function
$n(t)$, $n_1(t)$ and $n_2(t)$	Additive white Gaussian noises
C_1	Gas-independent power factor
N_p	Number of phase-shifted single periods
ϕ_p	Gas-phase-hop emitted-signal phase

5 Experimental FMCW

Chapter 4 focuses on studying the lidar FMCW technique for both aerosol and gas detection. This chapter describes a number of experiments which were performed as an initial test of the analytical developments explained in chapter 4, and is divided into three sections.

Section 1 is devoted to the design and development of a baseband chirp generator which will provide the signal to apply the phase-hop method. This generator was designed by modifying a chirp generator previously intended for synthetic aperture radar (SAR) applications.

Section 2 describes the initial test of the FMCW-lidar signal analysis for a bandpass and for a baseband input modulation scheme. By comparing the results of the simulation with those of the experiment it is possible to demonstrate the bandpass filtering effect found in the analysis of the FMCW-lidar signal in section 4.4.3. In the case of baseband input modulation, the bandpass filtering effect disappears demonstrating the feasibility of using baseband chirp modulation for distributed media.

The final section 3 is devoted to applying FMCW lidar to gas detection. Section 5.3.1 develops the WMS technique in an experiment using high frequencies (a few MHz), demonstrating several characteristics that differ from a typical low-frequency case. These characteristics are significant for the second section which is concerned with integrated-concentration gas detection (as in the WMS case) using FMCW lidar. As with the WMS technique, gas detection is performed by obtaining the first-harmonic graphic by analyzing the detected power as shown in 5.3.2.

5.1 Baseband Chirp Generator

When applied to distributed media the lidar FMCW technique test requires the use of a baseband chirp-waveform generator as a modulator for the laser source in order to emit a light signal of the correct baseband amplitude modulation. The design and implementation of the generator carried out for the research is explained in this section.

The generator was designed to emit a baseband chirp signal traveling from 30 MHz down to 0 and back up to 30 MHz to obtain a resolution of 5 meters in about 1 millisecond. This signal requires several specific phase conditions in order to simulate a signal that travels ideally from -30 MHz to 30 MHz, as explained below.

Other elements can be added to the generator to achieve a compact system for both modulating the emission source and acquiring and mixing the received and original signals. To this end, the introduction of an analog-digital converter and a digital mixer would significantly simplify the design of the system and improve the results of a future FMCW-lidar project.

5.1.1 The Characteristics of the initial system

The initial circuit used as the starting point for the design and development of the baseband chirp generator is a subsystem used in the generation of in-phase and quadrature signals for a SAR radar system. This circuit is composed of two direct digital synthesizers (DDS) controlled by an FPGA and each generating a baseband chirp signal, one in phase and the other in quadrature, which are then used to generate the SAR signal to be emitted. In the original design the output signal of each DDS goes through a transformer, preventing grounding problems which could damage the circuit (Fig. 5.1). However, the lowpass filtering effect of the transformer also has a significant influence, distorting the lowpass part of the signal, resulting in problems for our application.

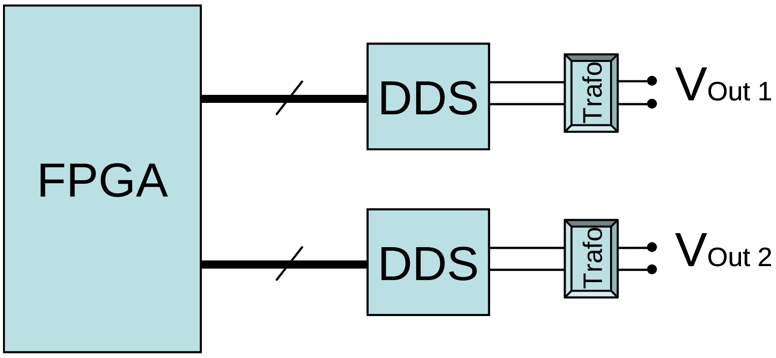

Figure 5.1. Initial circuit scheme for baseband chirp generation

The DDS generates a digital signal with a frequency of 400 MHz that is analog-converted at the output. This signal starts with a given initial frequency which increases in regular steps until reaching its final frequency. The step period is constant with a value of 10 ns (4 times slower than the sampling frequency) and the other variables such as the initial frequency, the frequency step and the final frequency are provided before the system can start working. Moreover, the initial phase was selected to ensure that each of the signals are pure in-phase and quadrature signals. All these values are loaded into the FPGA which controls the DDS chips.

Table 5.1. Main-components list of the Baseband Chirp Generator

Component	Description
Xilinx Spartan – 3E300	Field Programmable Gate Array (FPGA)
AD9954	Direct Digital Synthesizer (DDS)
AC8009	Operational Amplifier (OA)
2N2222	Bipolar Junction Transistor (BJT)

5.1.2 New lidar-system design

It was necessary to remove the transformer from the system to eliminate the lowpass filtering effects generated. The system described above was modified to obtain a current source with baseband amplitude modulation as circuit output. To achieve this, the transformer was substituted for an operational amplifier plus a BJT transistor acting as a current source, as shown in figure 5.2.

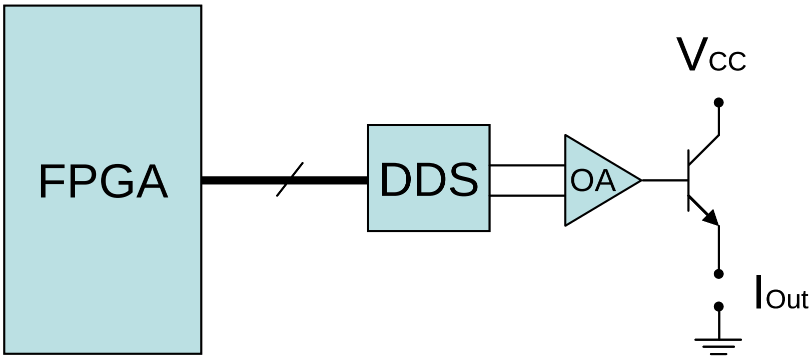

Figure 5.2. Modified circuit scheme for baseband chirp generation

In the new circuit, the amplifier plus the BJT transistor act as a barrier to grounding effects for the DDS. Moreover, these components allow the signal to be amplified and conditioned as a current source to be inserted in the laser diode with a bias-T as a modulating signal.

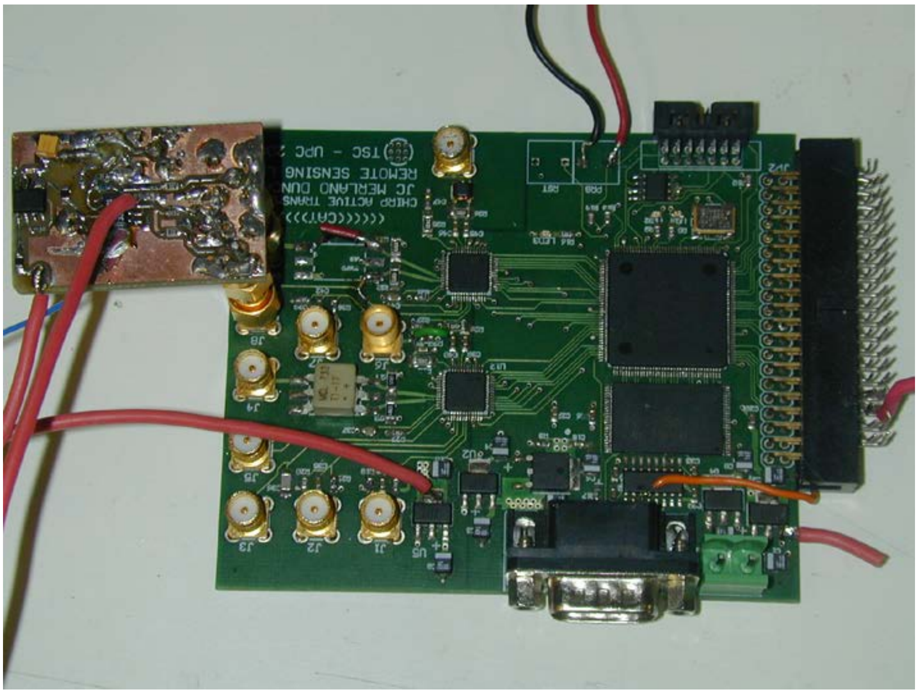

Figure 5.3. Photo of the baseband FMCW generator developed for the study

Table 5. 2. shows changes to time, frequency and phase constants to produce a bandwidth of 30 MHz and a duration of 1 millisecond. Moreover, in-phase and quadrature signals have been time-multiplexed in a unique DDS for their use in the phase-hop technique, to allow for eliminating the sum-frequency harmonics in the resulting signal. Using in-phase and quadrature signals simulates a phase jump of $\pi/2$ between both signals, corresponding to the definition of the phase-hop signal in section 5.3. In table 5.2, the initial phase values of the in-phase and quadrature signals have been selected in order to obtain phase values of 0 and pi halves radians respectively on approaching the point of zero-frequency.

Table 5.2. Variable values in the chirp generator for a 30 MHz baseband chirp

Characteristic	Digital Value	Corresponding real value
Clock frequency	100000000 Hex	400 MHz
Initial frequency	13324424 Hex	~30 MHz
Frequency step	192A Hex	~600 Hz
Frequency-step period	40000000 Hex	100 MHz
Half period time	49994	~500 ms
Reference phase	4000 Hex	360º
Initial phase (in-phase)	1E70 Hex	171.21º
Initial phase (quadrature)	2E70 Hex	261.21º

5.1.3 Testing the system. Data acquisition and processing

Preliminary testing of the system was carried out by acquiring two different signals, an in-phase signal and a quadrature signal, given in figure 5.4. The results show the signal at the output of the waveform generator, indicating that while some residual noise is maintained, the lowpass filtering problem of the output transformer has been solved.

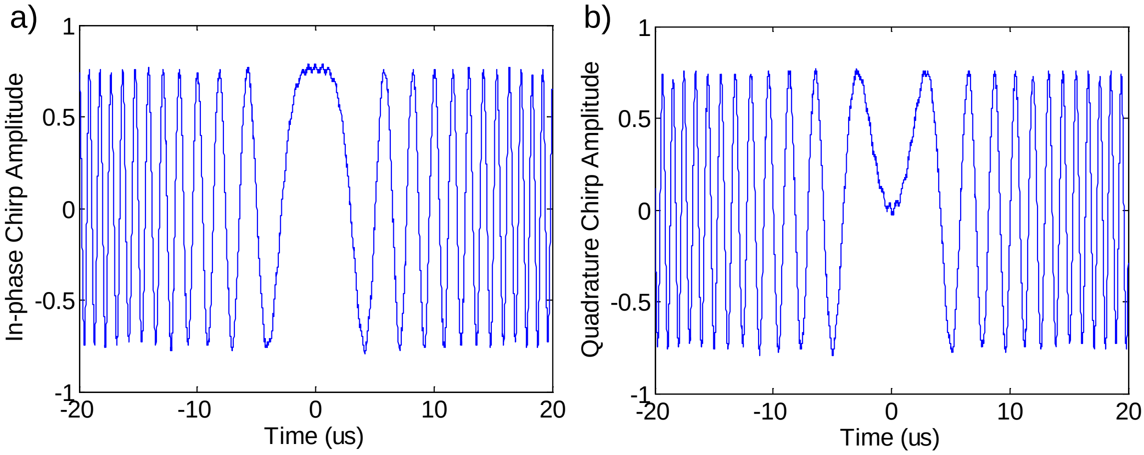

Figure 5.4. Detail of the in-phase (a) and quadrature (b) chirped signals used for the modulation of the FMCW lidar system when applying the phase-hop method.

The results of mixing the signal with itself for both acquired signals are given in figure 5.5. The presence of a clear *sinc* shape in both cases confirms the quality of the signal provided by the waveform generator.

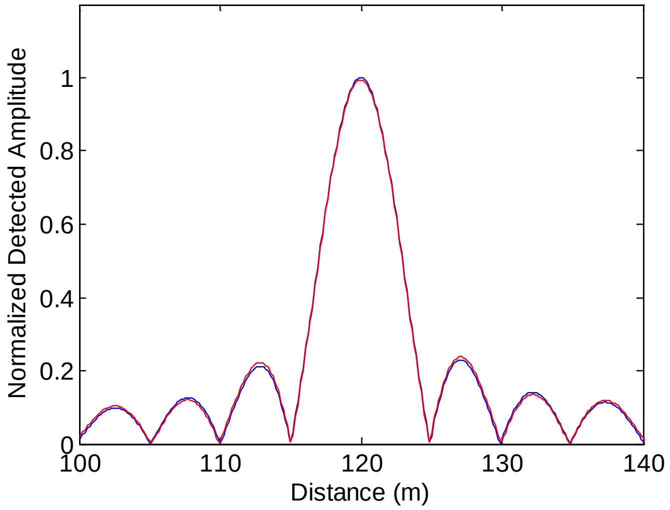

Figure 5.5. Detail of the Fourier transform of the in-phase (blue) and quadrature (red) signals mixed with a delayed version of themselves simulating an hypothetical detected target at 120 m of the system

5.2 Unresolved multiple-target detection

At the start of this research project, a series of simulations were performed to see how an FMCW lidar system works in a distributed medium, as can be seen at the beginning of section 5.3. Poor results were obtained from these simulations and it was decided to analyze the behavior of the system with two targets as the simplest distributed medium.

This section attempts to demonstrate the behavior of a two-target medium sounded by bandpass (initial configuration) and baseband (evolved configuration) emitting signals as the first important experimental test for theory developed here. The baseband chirp–waveform generator described in the previous section is also tested.

5.2.1 Bandpass and baseband two-target interference simulations

A series of simulations were performed to validate the theory outlined in section 5.3 and to analyze the interaction of two targets with both a bandpass and a baseband emitting signal. Two targets are considered: the first is fixed at a certain distance while the other is located at progressively distant points from the first. A 60 MHz sweep signal with 2.5 meters of range resolution was used as modulation for sounding this medium. For the baseband signal, the modulation starts at 30 MHz, decreases to DC and then back up to 30 MHz. For the bandpass signal, the modulation starts at 20 MHz and reaches 80 MHz.

Figure 5.6 shows a simulation of the detected peak amplitude and the distance error of the closest target for the case of the bandpass emitting signal. The corresponding parameters for the distant target are comparable: an equal value for the peak amplitude and an opposite sign for the distance error. The amplitude of this target decreases rapidly until there is a distance of approximately one meter between targets, then it bounces back and oscillates around the original value of 1. The error distance is positive and is located on a straight line with a slope equal to 1 corresponding to a position where both targets merge up to 3 meters, except for a zone at approximately 1.5 meters where both targets appear to be separate. After a distance of 3 meters, targets show clear separate positions and the distance error oscillates around the balance position of error equal to 0.

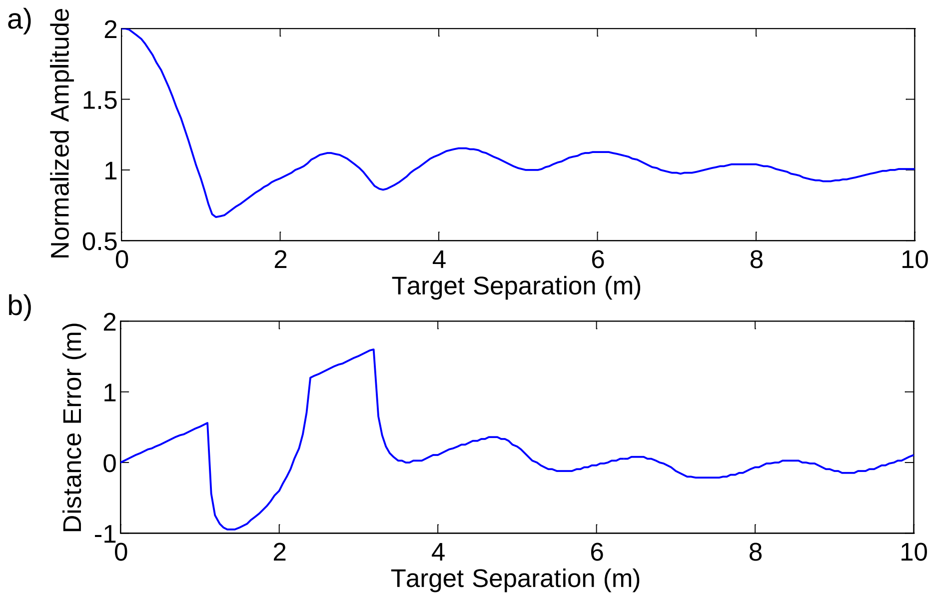

Figure 5.6. Simulation of the evolution of the echo-signal peak amplitude of the first target (a) and the distance error in the first target position (b) in a 2-target detection for a bandpass emitted signal between 20 and 80 MHz

In contrast with Fig. 5.6, for Fig. 5.7 the same simulation was performed for the case of a baseband emitting signal. The amplitude of the first target decreases slowly until the distance between targets is approximately three meters then it starts oscillating around the original normalized value of 1. The error distance is positive and is located on a straight line with a slope equal to 1 corresponding to a position around 3 meters where both targets merge. Beyond 3 meters, targets are detected as being clearly separated and the distance error slowly oscillates around the balance position of error equal to 0.

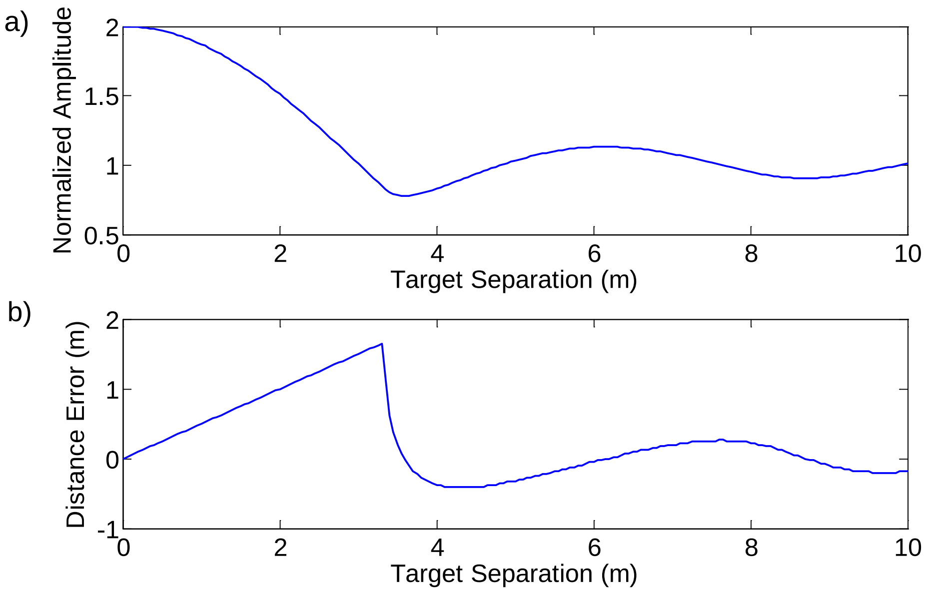

Figure 5.7. Simulation of the evolution of the echo-signal peak amplitude of the first target (a) and the distance error in the first target position (b) in a 2-target detection for a baseband emitted signal with 30 MHz bandwidth

5.2.2 Experimental Setup

The system used to test the FMCW technique in a two-target media is composed of a NEL DFB laser *NLK1556STG* at 1504 nm, an ILX-Lightwave laser driver *LDC 3724-B*, an Agilent waveform generator *38250A*, a tailored waveform generator (described in the previous section), a 50-meter coaxial cable (used for signal delay), a glass wedge (used as the 1st target), a metallic reflector (used as the 2nd target), a 200-MHz-bandwidth OEC detector and a computer with a Gage Cobra Compuscope CS22G8 acquisition card used to detect the signal.

The signal is emitted by the laser and then partially backscattered by the glass wedge located in the center of the setup (Fig. 5.8) which sends the signal back to the receiver. The part of the signal that crosses the wedge is then reflected by the metallic reflector and directed towards the receiver where the joint signal is detected and transmitted to the computer. The modulation signal coming from the waveform generator and the signal coming from the receiver are mixed and Fourier transformed by the software. The result is depicted graphically and the targets appear in a position proportional to their distance to the emitter and with an amplitude proportional to their cross section.

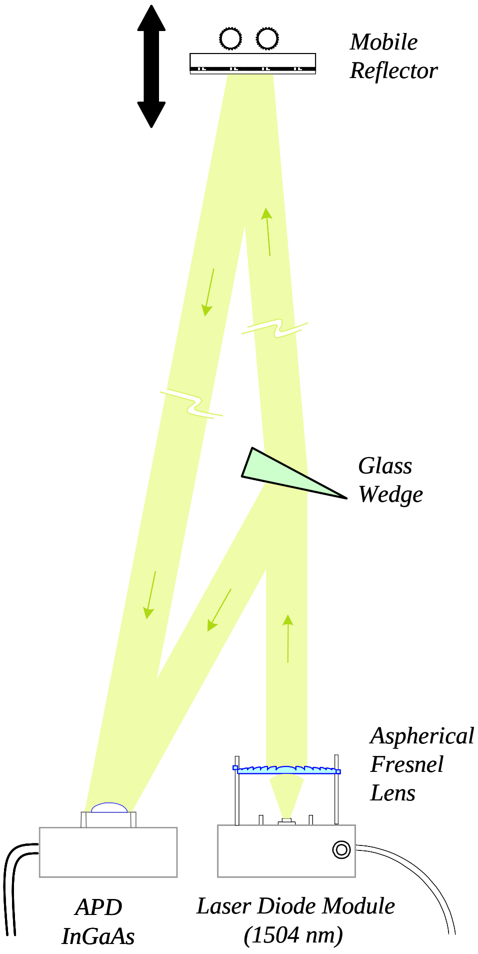

Figure 5.8. Experimental Setup

5.2.3 Data and discussion

A series of experiments were carried out to test the validity of the previously simulated data. The system just described was used to measure the response of a two-target system in two different configurations, namely, with a bandpass input modulation and with baseband one, showing a good correspondence with the simulation shown in section 4.

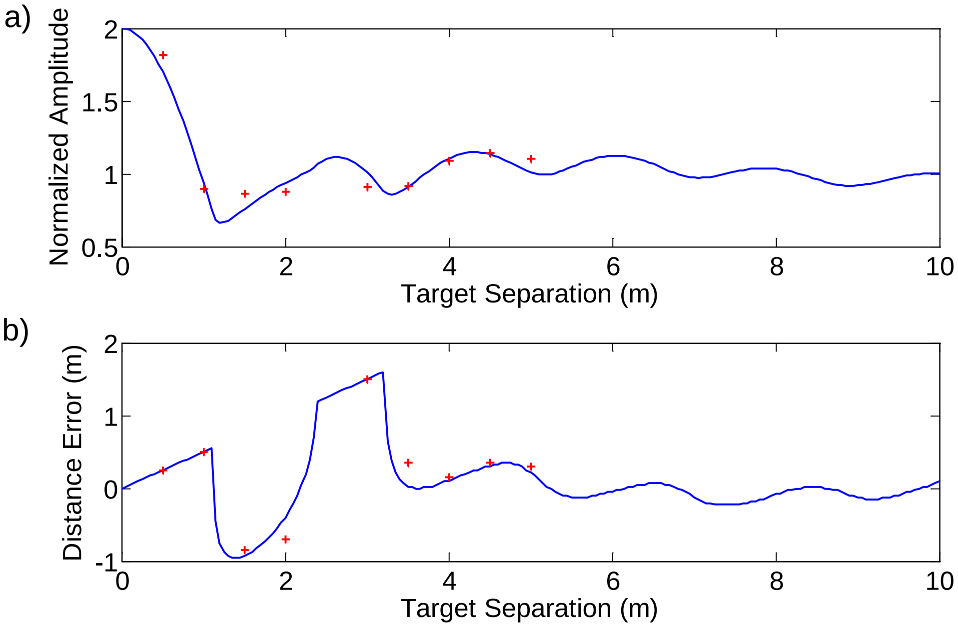

Figure 5.9. Experimental data (crosses) of the evolution of peak amplitude (a) and distance error of the nearby target with respect to the distance to the far-off one (b) in a 2-target detection for a bandpass emitted signal between 20 and 80 MHz

Figure 5.9 gives the same simulation data as that shown in figure 5.6 with the experimental data superimposed in the form of crosses. They correspond quite well and this corroborates the bandpass nature of the detected signal when the input signal is bandpass modulated.

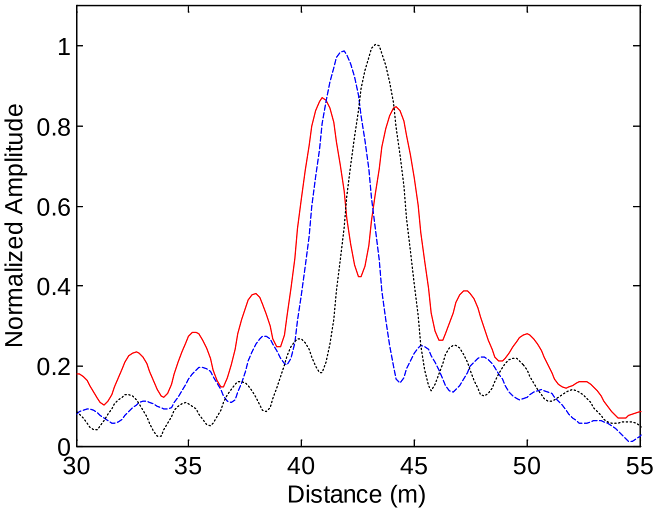

Figure 5.10. Interaction of two targets (whose separate echoes are the dashed and the dotted lines) for a bandpass emitted signal between 20 and 80 MHz. The recovered signal (solid line) as a result of the mixing of the two targets shows a change in position and amplitude of both of them.

Figure 5.10 gives the response with targets separated by 1.5 meters. In this case, the two targets remain separated with a distance error of 1 meter with respect to their real position and with 80% of their original amplitude.

A problem arose when attempting to perform the measurement of the two-target medium for the case of baseband modulation. The frequency response of the laser between 20 MHz and 80 MHz is approximately constant which makes the post-processing of the signal quite straightforward. However, the frequency response of the laser between DC and 30 MHz is highly variable (Fig. 5.11, left) resulting in the need to equalize the response of the system (Fig. 5.11, right) in order to obtain a much better result when analyzing the targets under study.

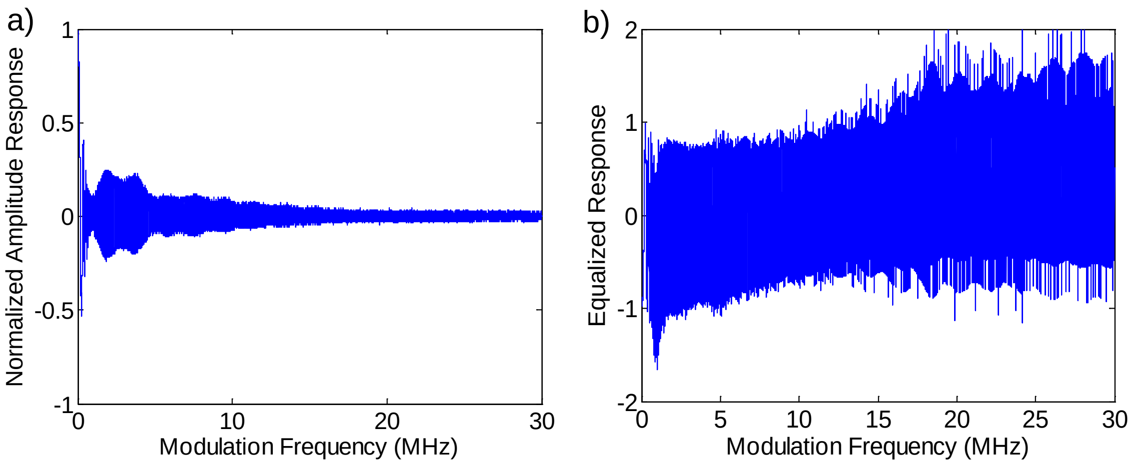

Figure 5.11. Modulation amplitude response (a) and its software equalization (b) for a emitting DFB laser at 1504 nm.

Figure 5.12 gives the same simulation as figure 5.7, with the experimental data superimposed (crosses).

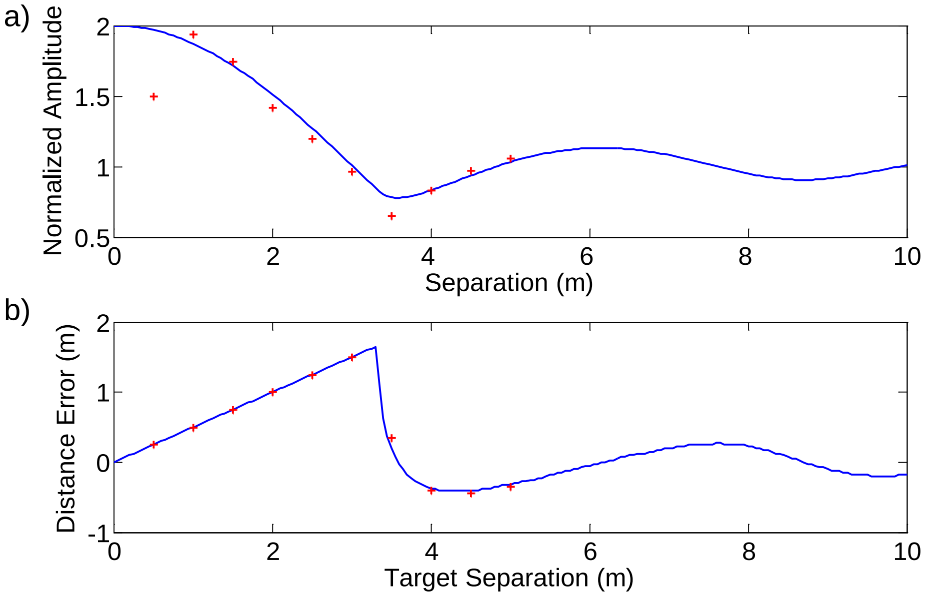

Figure 5.12. Experimental data (crosses) of the evolution of peak amplitude (a) and distance error of the nearby target with respect to the distance to the furthest (b) in a 2-target detection for a baseband emitted signal with 30 MHz bandwidth

The correspondence between them is quite good and it shows that with a baseband emitted signal, the detected signal is a baseband signal as well, but there are two points showing some disagreement. Firstly, in the 0.5-meter measurement, the experimental data shows an abnormally low value that could be produced by a coherence effect between the backscattered signals corresponding to both targets. Moreover, in the 3.5-meter measurement, a very low value of amplitude comes from an effect of the bad modulation frequency response of the laser as shown above.

Finally, figure 5.13 shows the interaction of two targets at 1.5 meters for the baseband configuration. In this case, the two targets remain merged and located in a position between their original positions and with an amplitude of some 80% greater than the one-target amplitude. It is important to note the secondary lobe to the left of the main lobe, in all likelihood the result of the bad frequency modulation response of the laser, which caused poor experimental results at 3.5 meters.

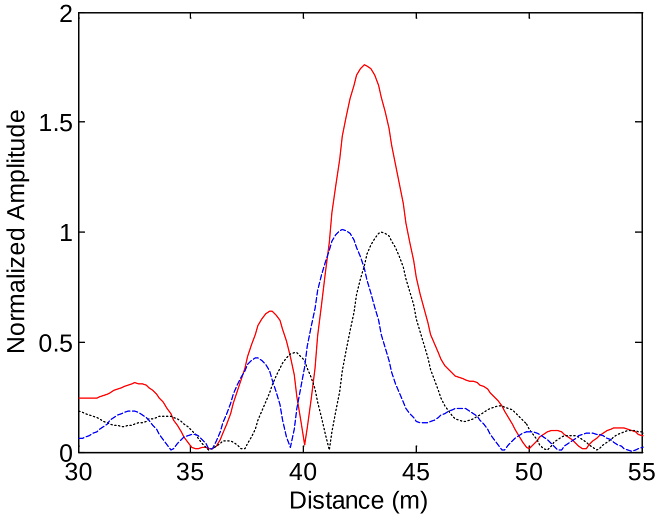

Figure 5.13. Interaction of two targets (dashed and dotted lines) for a baseband emitted signal with 30 MHz bandwidth. The recovered signal (solid line) as a result of the mixing of the two targets shows the targets merged in an intermediate position.

5.3 Gas detection with FMCW (Solid Target)

The main goal behind developing the FMCM-lidar technique is gas detection with range resolution. This section details an initial experiment which explores the capabilities and drawbacks of this technique for gas detection. The first section describes an experiment with a high-frequency version of WMS (some MHz) to determine which characteristics of the wavelength laser modulation affect the application of the FMCW lidar to gas detection. The second section describes an experiment in which gas detection is performed using FMCW lidar technique.

The gas concentration is determined by means of a wavelength sweep around the absorption line, generated by an input current sweep. While for the WMS this sweep was performed dynamically, this was not possible for the FMCW-lidar technique, the sweep for which had to be performed step by step. For each step, a number of chirped periods are emitted and detected, obtaining a peak in a frequency proportional to the distance of the system to the topographic target when applying a Fourier transform to the mixed signal. The modulus and phase of this topographic target is the information needed to display the 1st harmonic curve mentioned previously. As seen in section 5.4.1, when a gas is present in the environment, a double component of amplitude modulation is detected in reception because of the initial amplitude modulation and the interaction of the light signal with the gas. As in the WMS case, these components are separated in order to obtain the desired first-harmonic curve.

5.3.1 Gas detection with High-Frequency WMS

WMS with high-frequency current modulations show similar characteristics to the low-frequency version described in Chapters 2 and 3. The principal difference which needs to be tackled when using high-frequency WMS is the low level of wavelength modulation present at these frequencies, as reflected in figure 3.1, Chapter 3 (figure of laser-diode wavelength modulation). This means that, for the same level of input current modulation, the output light will show similar amplitude modulation to that for low-frequency WMS, but a much lower level of wavelength modulation.

As a result it is necessary to use much higher levels of current modulation in the laser, resulting in higher levels of distortion during measurement, including higher levels of residual amplitude modulation (RAM) effects which will definitely reduce the SNR ratio. Moreover, the use of higher levels of modulating power results in the reduction of linearity and the possible appearance of saturation effects in the laser source. The wavelength modulation phase with respect to the amplitude modulation is also affected. This aspect needs to be taken into account when applying FMCW to the WMS technique due to its change along the modulation frequency.

Different measurements were performed at 20, 30 and 40 MHz input current modulation and an external Lock-In Amplifier (Stanford Instruments) was used to improve the signal to noise ratio. Figure 5.14 shows a representation of 1st and 2nd harmonics where higher modulation levels are present compared to the WMS component with respect to the low-frequency case (chapter 3) are evident.

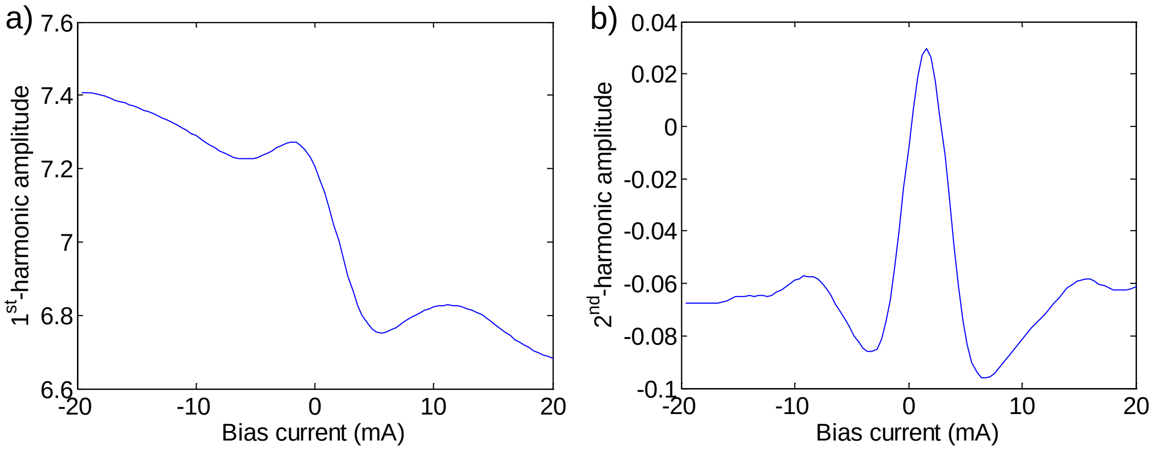

Figure 5.14. Evolution of 1st harmonic (a) and 2nd harmonic (b) functions along current at 4 V and 20 MHz of input modulation

In figure 5.14m which shows the 1st harmonic graphic, the first peak of the WMS component is smaller in magnitude than the second peak, even though this component should be antisymmetric with respect to its central point. This effect is clearer in figure 5.15 for a case with a higher level of modulation. This high degree of asymmetry is caused by the presence of a more intense RAM effect due to the reduction of wavelength modulation because of the higher modulation frequency. This increased RAM effect also appears in the second harmonic representation where one of the negative peaks is bigger than the other and the difference becomes even greater as the level of the input modulation signal increases, as demonstrated by the 1st harmonic case.

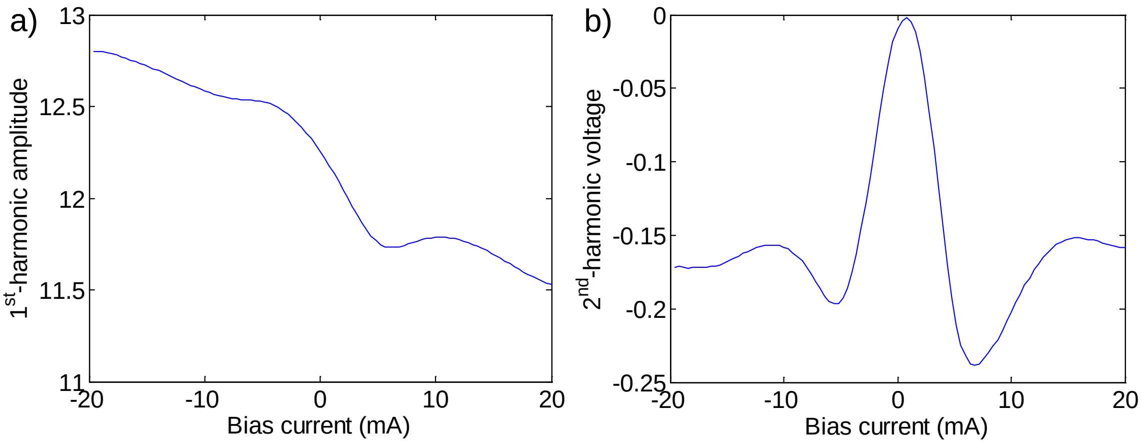

Figure 5.15. Evolution of 1st harmonic (a) and 2nd harmonic (b) functions along current at 7 V and 20 MHz of input modulation

It may prove possible to improve the shape of these functions as well as the concentration measurements by applying a correction to the estimated background that takes this RAM effect into account. With this objective in mind an initial evaluation of the linewidth and the absorption is performed to estimate the RAM effect contribution to the background and then this is applied to recalculate the linewidth and absorption values with a recursive technique. The results after two iterations can be seen in figures 5.16 and 5.17 for the previous two cases of input modulation

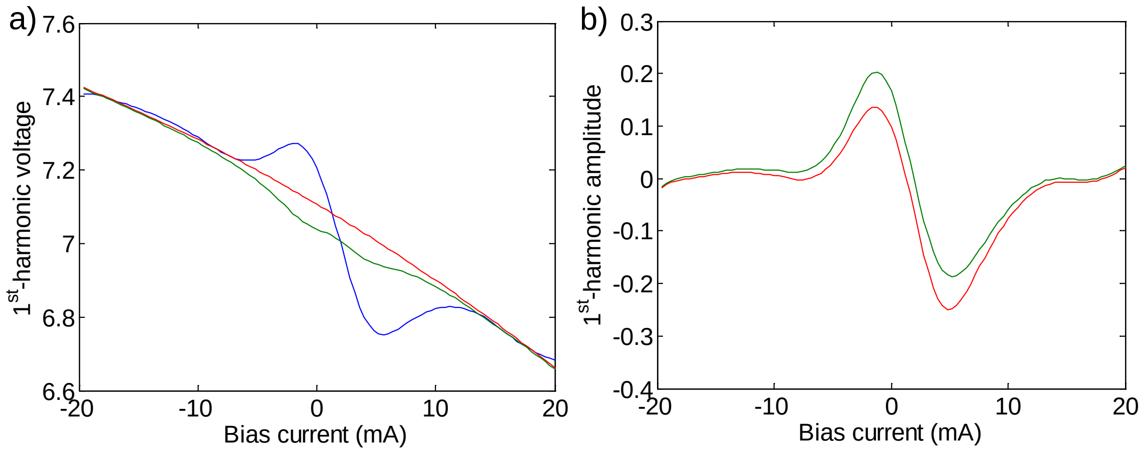

Figure 5.16. Evolution of (a) 1st harmonic function (blue) along current as well as estimated background (red) and RAM-corrected background (green), and (b) 1st harmonic function after subtracting background (red) and after subtracting the corrected background (green) at 4 V and 20 MHz of input modulation.

The results of this processing can be seen in figure 5.16.b and 5.17.b where the red line represents the 1st harmonic data without the background component and the green line, this same 1st harmonic but in this case without the RAM-corrected background component. The latter showing greater similarity to the expected WMS shapes.

It is evident that this data processing improves the received data and consequently should improve the concentration results obtained. However, the purpose here is not to produce precise calculations, but rather to show the signal distortions present in the data obtained. When performing calculations of the peak-to-peak values of the 1st harmonic and the peak values of the 2nd harmonic prior to correcting for any variables, the difference between the values obtained for corrected and uncorrected calculations differ to a degree of between 2% and 4%. Consequently, it was decided to perform the measurements in this simpler uncorrected manner in order to obtain reasonable values without complicating the process.

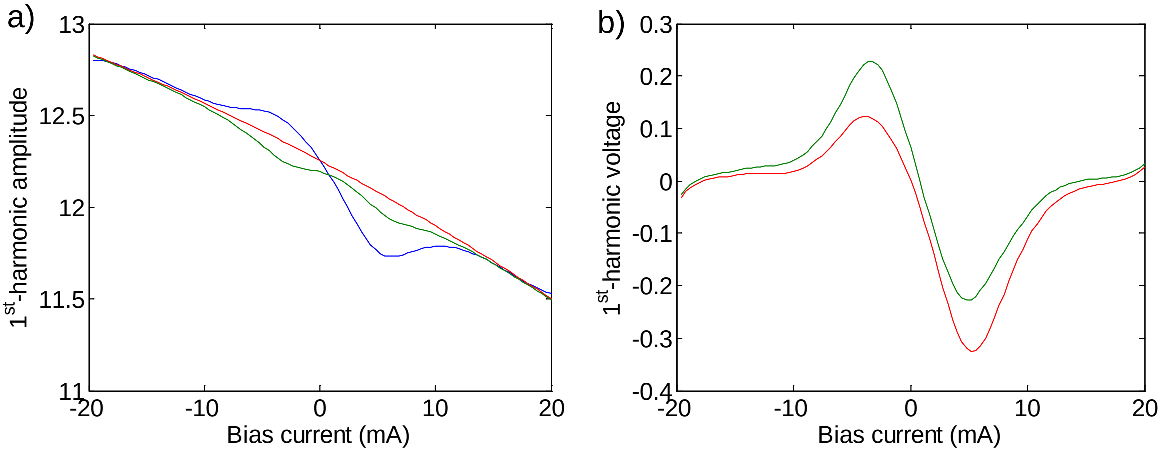

Figure 5.17. Evolution of (a) 1st harmonic function (blue) along current as well as estimated background (red) and RAM-corrected background (green), and (b) 1st harmonic function without background (red) and without corrected background (green) at 7 V and 20 MHz of input modulation.

Figures 5.18 and 5.19 give the graphic results for the cases of 20 MHz and 30 MHz input modulation. Despite the difficulties that occurred during the process, a high degree of correlation is found between the experimental data and that obtained from the simulation. The graphic results were obtained while minimizing the minimum square error as in the case of low-frequency WMS in chapter 3.

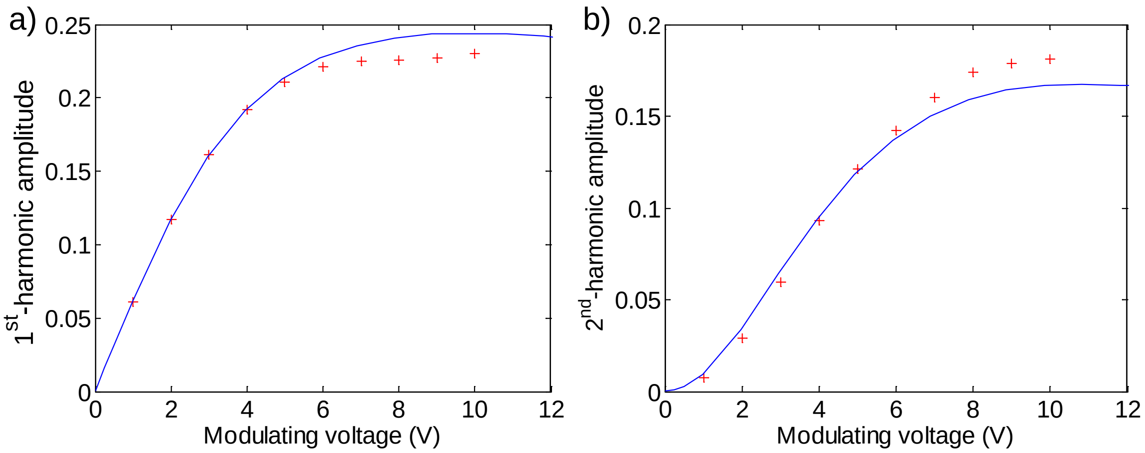

Figure 5.18. Evolution of peak value for 1st harmonic (a) and 2nd harmonic (b) functions along current (red points) and the corresponding estimation (blue) at 20 MHz of input modulation.

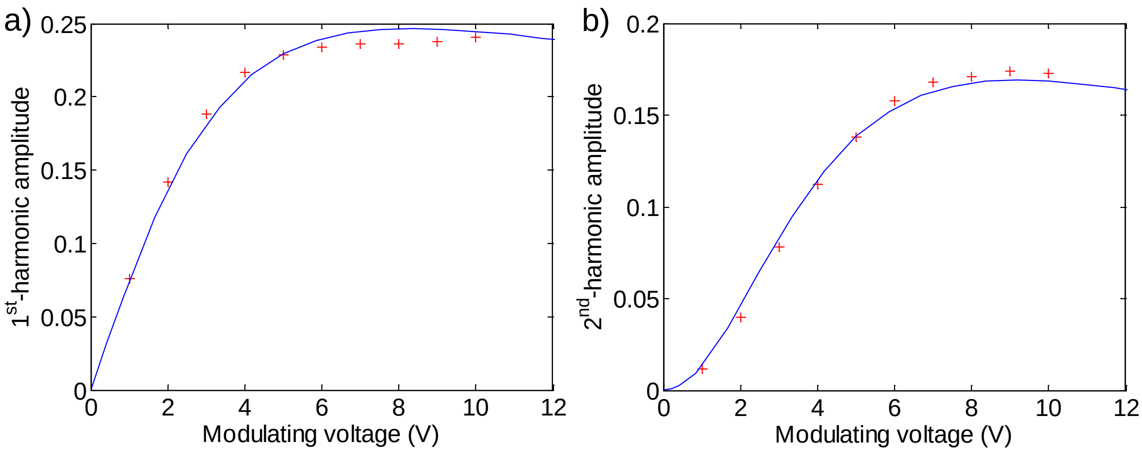

Figure 5.19. Evolution of peak value for 1st harmonic (a) and 2nd harmonic (b) functions along current (red points) and the corresponding estimation (blue) at 30 MHz of input modulation.

Table 5.3 presents the results of the measurements carried out for the three cases of 20, 30 and 40 MHz of input modulation frequency. It is evident that the levels of amplitude and width are similar to those obtained in Chapter 3 for the water-vapor concentration in the atmosphere (in this case, with a slightly higher level of concentration). Additional data, contained in the last column has been added showing the level of wavelength modulation present in the laser output signal with respect to amplitude modulation. This can be called “wavelength modulation performance” and consists of the level of wavelength modulation for a certain frequency with respect to the wavelength shift in DC.

Comparing these wavelength modulation performance values with their respective values for the low-frequency WMS case (10 kHz) of ~42%, a large decrease in wavelength modulation is evident. This effect is the cause of the higher levels of RAM and distortion previously mentioned in this section and it has the effect of severely impairing the measured data in the FMCW gas experiments described in the next section, as demonstrated below.

Table 5.3. Final data obtained from high-frequency WMS for water-vapor detection

Modulation frequency	Amplitude	Width(cm^{-1})	Concentration (% in volume)	Wavelength modulation performance
20 MHz	0.0232	0.108 cm^{-1}	1.94 %	12.2 %
30 MHz	0.0235	0.106 cm^{-1}	1.96 %	14.4 %
40 MHz	0.0224	0.099 cm^{-1}	1.87 %	13.4 %

5.3.2 Application of gas detection with FMCW

As demonstrated in section 4.4, the FMCW technique can be also used to detect gas in the atmosphere. As outlined in section 5.2, when a laser diode emits a signal modulated in amplitude, a wavelength modulation also occurs. If the wavelength of the emitted signal is tuned in the vicinity of the absorption line of the gas under analysis, this modulation can be used for gas detection. This section outlines the use of this technique with the addition of signal processing, to obtain curves similar to those obtained in the

WMS-HF case. This will demonstrate the system's capability to perform an integrated measurement of gas concentration (section 5.4.1).

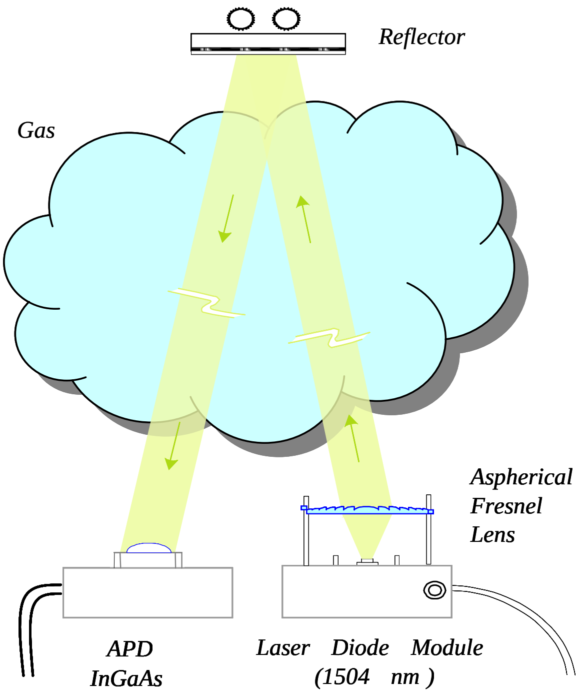

Figure 5.20. Experimental FMCW setup for gas-measurement.

The method consists of fixing a bias current for the laser and then applying a high-frequency chirped current modulation to the laser source. This signal is backscattered by a solid target and returns to the system, as shown in figure 5.20, where it is detected and mixed with the modulating signal. The result is a superposition of the amplitude modulation directly emitted by the laser itself and the amplitude modulation resulting from the interaction of the wavelength modulation with the absorption line of the gas under study (section 5.4.1).

Finally, this signal is Fourier transformed and the resulting amplitude-modulated signal coming from the reflector and after crossing the gas is concentrated in a frequency proportional to the target distance.

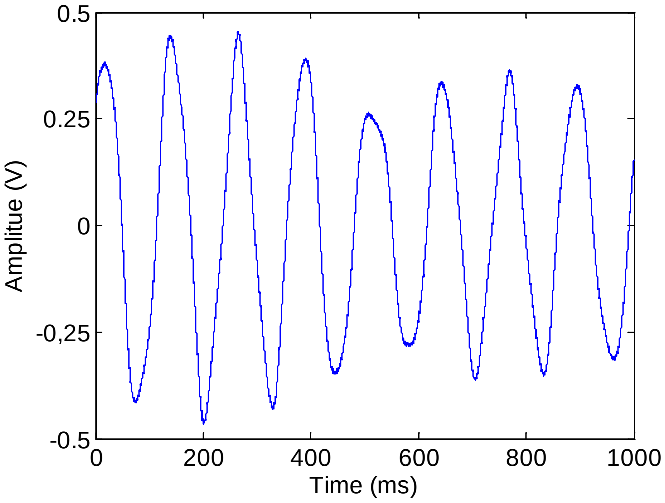

Figure 5.21. Detected signal with bias current at the center of the line for the case of a 3-volt modulation.

Figure 5.21 gives us the detected signal with the bias current fixed at the center of the absorption line, and figure 5.22 the Fourier-transform amplitude and the phase of this detected signal.

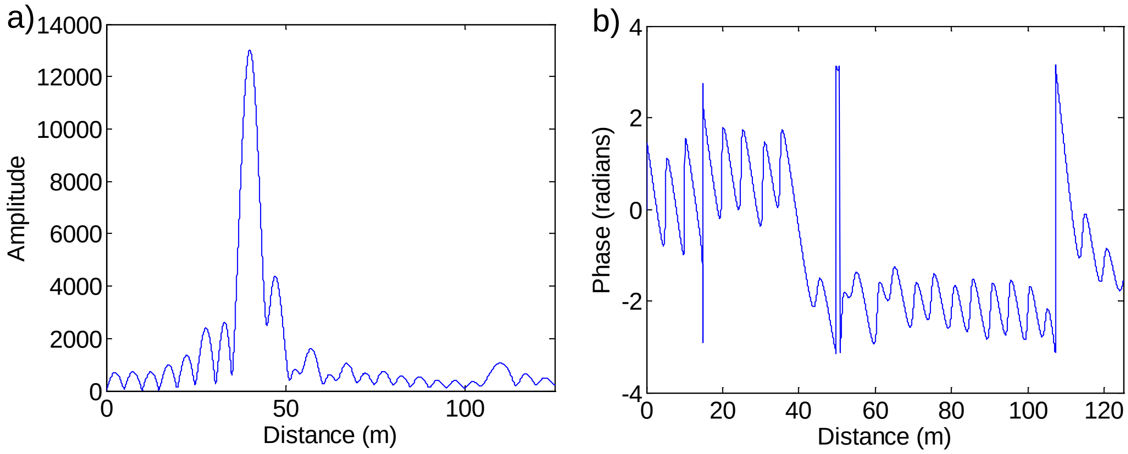

Figure 5.22. Amplitude (a) and phase (b) of the detected signal with bias current at the center of the line for the case of a 3-volt modulation.

By changing the bias current which fixes the central wavelength of the emitted signal a sweep of the zone around the wavelength absorption line can be performed and a function similar to the WMS-HF case (Fig. 5.14.a) can be obtained. If this bias current sweep is performed point by point around the absorption line, the amplitude and phase curves shown in figure 5.23 are obtained. Figure 5.23 demonstrates how the amplitude and phase of the received signal evolve along the bias current and we can also see the effect of the absorption line (around 115 mA) for both variables.

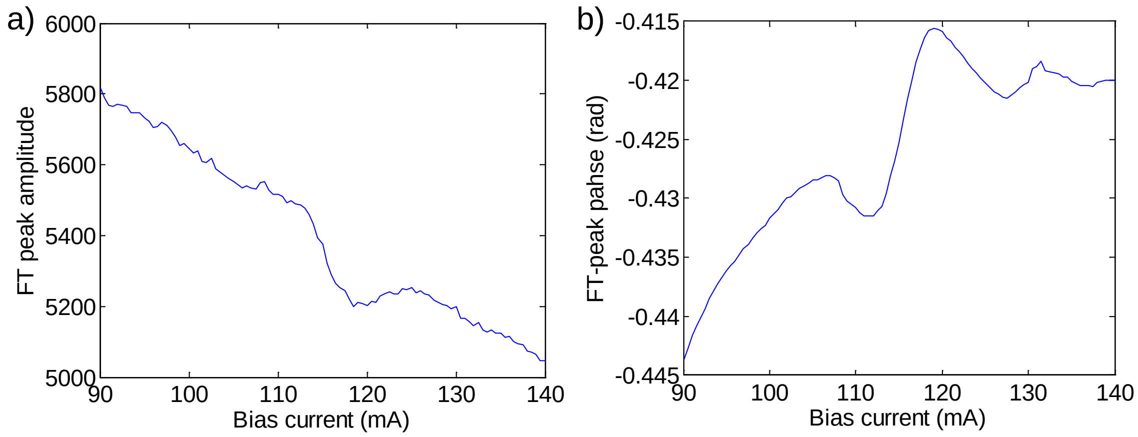

Figure 5.23. Evolution of Fourier-transform peak amplitude (a) and phase (b) along the bias current for the case of a 3-volt modulation.

After obtaining the previous results, all that remains is to find the in-phase and quadrature components by using the data in figure 5.23. Figure 5.24 gives us the result where both of the components present a certain degree of gas-interaction-generated component. Here, the background produced by the laser direct amplitude modulation has been suppressed by applying a 2^nd^-order polynomial approximation to both extremes of the in-phase and quadrature components.

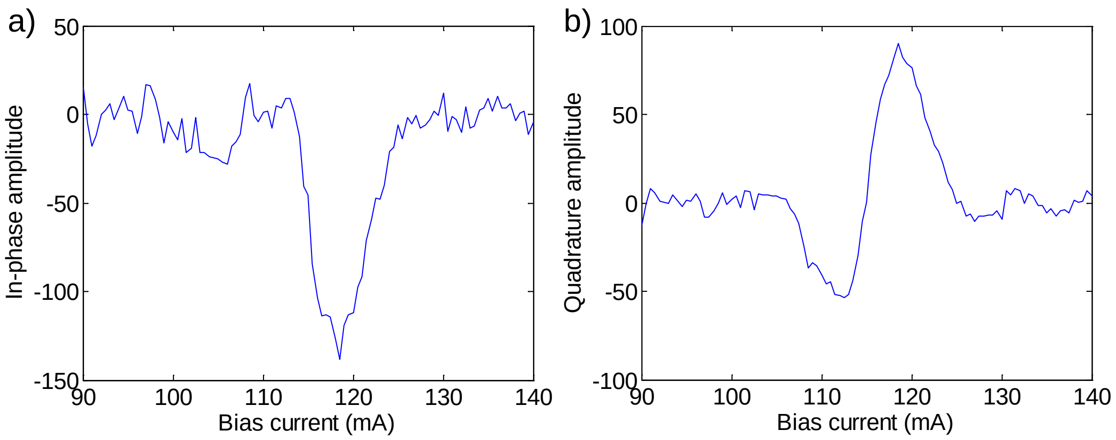

Figure 5.24. In-phase (a) and quadrature (b) components of the Fourier-transform results along the bias current for the case of a 3-volt modulation.

At this point, the effect of the interaction between the light signal and the gas is separated between the in-phase and the quadrature component. In order to simplify the calculation of the component produced by gas-interaction, it is much simpler to use a phase shift to calculate the in-phase and quadrature components. In this way it is possible to concentrate the gas-produced amplitude modulation for the component we are interested in, whilst practically eliminating it from the other component. The result for two different cases are given in figures 5.25 and 5.26 where the in-phase component concentrates the entire gas-interaction produced modulation.

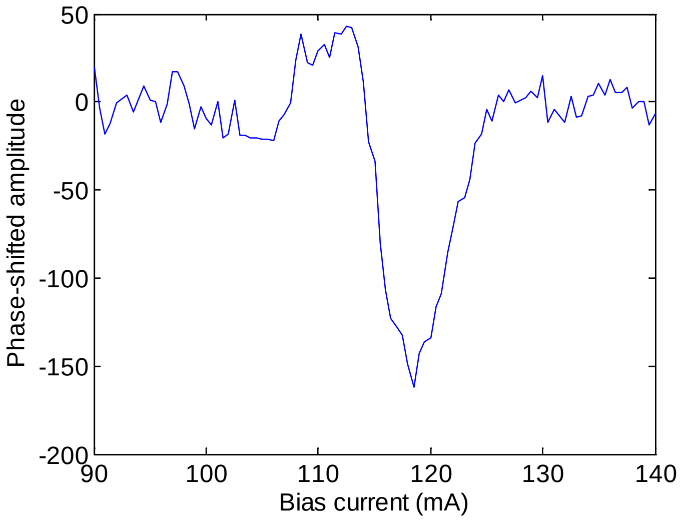

Figure 5.25. Phase-shifted in-phase component of the Fourier-transform results along the bias current for the cases of a 3-volt modulation.

At this point, it is evident that the graphs obtained are similar to those of the WMS-HF case despite the presence of greater distortion. The causes of this distortion will be discussed at the end of the section. The analysis to be performed is parallel to those ones performed for the WMS-HF case. From these graphics we can see the impact of the RAM effect in the results as was also the case for the WMS-HF case. An analysis could be performed in order to obtain better shapes for the results but as seen in the previous section, the peak-to-peak value of the 1st-harmonic component does not change significantly after the correction.

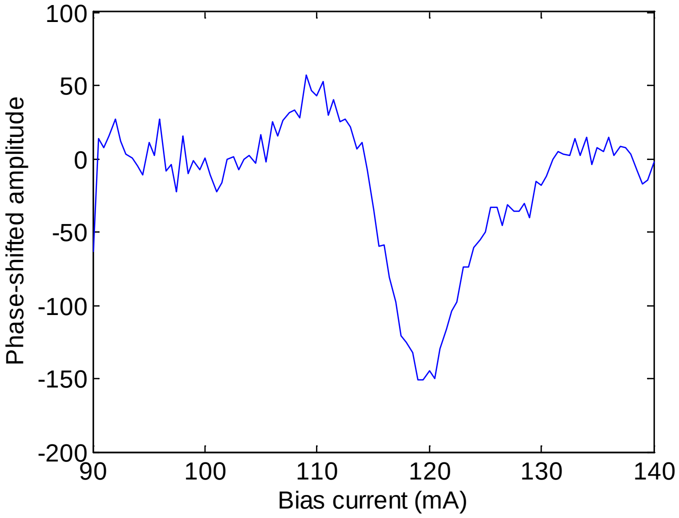

Figure 5.26. Phase-shifted in-phase component of the Fourier-transform results along the bias current for the cases of a 7-volt modulation

Figure 5.27 gives us the peak-to-peak values of the 1st harmonic component for different values of input modulation. Analysis of this shows reasonable agreement between the graphs of experimental and theoretical data. As in the case of low-frequency WMS in chapter 3, the graphic results were obtained while minimizing the square error. However, in this case, the last point of the curve was not taken into account because it clearly shows a high level of distortion.

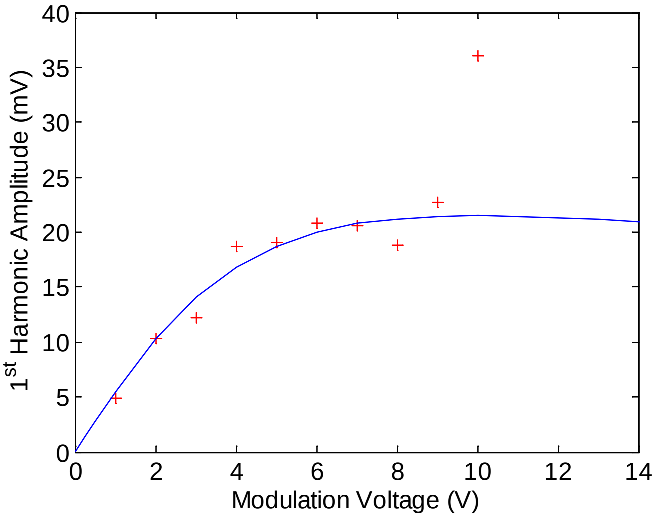

Figure 5.27. Evolution of peak value for 1st harmonic function along current (red points) and the corresponding estimation (blue) for a modulation between 20 and 50 MHz

The results of the measurements are presented in table 5.4. The amplitude and width levels found are comparable to those obtained in the previous section.

Table 5.4. Final data obtained from Gas-FMCW for water-vapor detection

Modulation frequency	Amplitude	Width(cm^{-1})	Concentration (% in volume)	Wavelength modulation performance
20-50 MHz	0.0204	0.107 cm^{-1}	1.71 %	12 %

After performing all of these experiments, the results and conditions required to obtain them warrant discussion. It is evident from figures 5.25 and 5.26, that despite remaining coherent with the previous WMS-HF case even when performed on different days, the results obtained were poorer.

The main cause of this deterioration in the results is the fact that they were obtained using different processes. In the first case, as in the case of the classic low-frequency WMS method, a slow sweep of approximately 10 Hz around the absorption line was performed while modulating with a high frequency signal of a few MHz. The second case employed the FMCW technique, which works by emitting chirped periods that need to be long enough to obtain a good SNR ratio. These periods were emitted for duration of about 1 second which does not permit the use of a constant sweep around the absorption line. To do this, in the FMCW case, the sweep was performed manually point by point, allowing the presence of a high level of background noise coming from the laser; the results can be seen in figure 5.23.

Additional minor problems, not present with WMS-HF, occur with the Gas-FMCW technique. In the WMS-HF case, a lock-in amplifier was used to extract the 1st harmonic modulation. A lock-in amplifier cannot be used with Gas-FMCW due to the continuous change of frequency (chirped signal), and so a simple mixer was used for this purpose. Another problem that occurs with the use of Gas-FMCW is the dependence on the modulation frequency of the wavelength modulation performance parameter described above, causing a level of distortion. Another distortion effect might result from a change in the phase between the amplitude modulation and the wavelength modulation leaving the laser, which can appear as the modulation frequency increases.

It is clear that all of these effects, especially those resulting from the different sweep method, cause a high level of distortion in the output signal. The results given in figure 5.18 indicate that gas-provoked amplitude modulation is present in the data obtained; this therefore can be seen as an initial test for developing a distributed-medium FMCW system for gas detection.

6 Optical Amplification

Optical amplifiers have evolved over the last few years to improve optical fiber communication around the world. Recently, major optical networks have changed from using electro-optical amplifiers requiring optical-electrical conversion of the signal to be amplified and re-conversion to an optical signal, to using optical amplifiers that perform the regeneration of the signal solely in the optical domain. This change improved communications to a level creating the most recent technology bubble, as the previous method produced a bottleneck within world communication networks. This investment in communication technology has resulted in an improvement in optics engineering that can be exploited by other fields of technology, such as, optical spectroscopy.

Low Signal-to-Noise ratios (SNR) have been obtained as a result of the development of a Frequency-Modulation Continuous-Wave lidar system. In order to obtain better signal-to-noise ratios, long-time averaging is required. By analyzing the terms of this SNR it is possible to identify the output power of the system as one of components that can boost this ratio. In fact, a factor 10 increase in the output power of the system has the same effect as a factor 100 increase in the average time. So the growth of the output power represents an important step forward for the development of a prototype of a functional FMCW lidar.

The study and development of an optical amplifier was carried out at The National Center for Atmospheric Research (NCAR) in Boulder, USA, where the EOL-APOL group is devoted, among other topics, to the study of in-situ gas detection and concentration measurement [42 - 44]. This group has performed many international gas measurement campaigns to further our understanding of the mechanisms of atmospheric chemistry. The group operates one of the most advanced systems in the world for gas detection, using a difference-frequency generation (DFG) system for measurement at mid-infrared wavelengths, and the WMS method is used for gas detection, with the probing signal generated using DFG. This technique consists of mixing two different optical signals by means of a non-linear crystal in order to obtain a resulting signal with a frequency equal to the difference of the input signals frequency.

The research project consists of the design and implementation of an optical amplifier around 1550 nm, and the subsequent analysis of the erbium-doped optical-fiber temperature and pressure dependence in the detection of gases using a WMS system. This optical amplifier has been integrated into the DFG complete system for gas detection.

6.1 Erbium-doped fiber amplifiers

Optical Amplifiers can be divided into two types [45]. The first type consists of semiconductor optical amplifiers (SOA). An SOA is an electronic device similar to a laser diode that has some special features, such as the lack of a feedback mechanism, that prevent it generating a coherent optical output. It is composed of an active medium powered by electrical current. This current supplies electrons with energy, raising them to higher levels and helping to produce a population inversion. Then the signal photons that travel through the medium trigger the excited electrons drop by means of stimulated emission, thereby producing an amplified signal at the output.

The second type are active-fiber or doped-fiber amplifiers (DFA are the alternative to SOA, and those most frequently used are the Erbium-Doped fiber amplifiers. The amplification process of these devices consists of the transference of power from one light wave to another by means of interaction with the fiber material. The material interacts with the shortest-wavelength wave (some 976 nm) by absorbing it and reemits it in the longest-wavelength wave (some 1550 nm) thanks to stimulated absorption and emission effects. This means that no electronic device needs to be present, simplifying the process and reducing the costs for the case of an autonomous device. In order to amplify the wave, a backwards or forwards pump wave must be introduced into the fiber. The process consists of the excitation of certain levels of the Erbium atoms with the pump wave, a non-radiative fall of the electrons to an intermediate metastable state and the final emission of signal photons by effects of stimulated emission. Although EDFA are the most commonly used amplifiers in optical communications in the third window, other materials are being used such as ytterbium or thulium for access to longer wavelengths in infrared.

The structure of erbium atoms shows different levels of energy. Those used in this application are ${}^4I_{11/2}$, ${}^4I_{13/2}$ and ${}^4I_{15/2}$ (figure 6.1). The 976-nm photons interacting with these atoms are mainly absorbed, promoting the electrons from level ${}^4I_{15/2}$ to level ${}^4I_{11/2}$. The excited electrons undergo a non-radiative decay to the ${}^4I_{13/2}$ layer. The width of this layer allows the emission of photons from some 1530 nm to 1610 nm. So, it is the interaction of the signal wave (at some 1550 nm) with the medium that produces the final decay of the electrons to ${}^4I_{15/2}$ layer and the subsequent emission of photons that contribute to the amplification of this signal. An alternative pumping wavelength for erbium-doped fibers is 1480 nm, which excites the electrons to the highest energies part of ${}^4I_{13/2}$ layer where they decay to the emission levels.

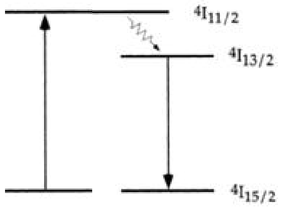

Figure 6.1. Diagram of energy levels in erbium atoms.

The fibers used for light amplification are standard silica fibers that have undergone a process of doping with rare-earth atoms, in this case erbium, in order not only to guide the wave but also to cause the interaction with the light itself. The fibers are doped to levels of some 1000 parts per million in weight in order to obtain peak absorptions (at around 1530 nm) up to some 120 dB/m.

The maximum output power that can be extracted from an EDFA can be described as:

$$P_{s,out} \leq P_{s,in} + \frac{\lambda_p}{\lambda_s} P_{p,in} \tag{6.1}$$

where $P_{s,in}$ is the input signal power, $P_{p,in}$ is the input pump power, $P_{s,out}$ is the output signal power, λ_s is the signal wavelength and λ_p corresponds to the pump wavelength. From equation (6.1) it is evident that a loss of theoretical efficiency is produced that depends on the wavelengths of the input waves. The cause of this loss is the quantum defect that can be defined as the part of the energy which is lost in the process of conversion from one wavelength to another. Due to the quantization of energy, for every pump photon absorbed only one signal photon can be emitted. This implies a reduction of energy equal to $h(\omega_a - \omega_e)$ for every transferred photon that is converted in heat (where ω_a and ω_e are the absorption and emission angular frequency of the photons respectively). This assumes a maximum theoretical efficiency in the case of 976-nm pumping and 1550-nm signal of some 63%. The inequality reflects the losses due to spontaneous emission, interactions with impurities or other effects.

From equation (6.1), we can also obtain an expression for amplifier gain G_f without taking into account other effects:

$$G_f = \frac{P_{s,out}}{P_{s,in}} \leq 1 + \frac{\lambda_p}{\lambda_s}\frac{P_{p,in}}{P_{s,in}} \tag{6.2}$$

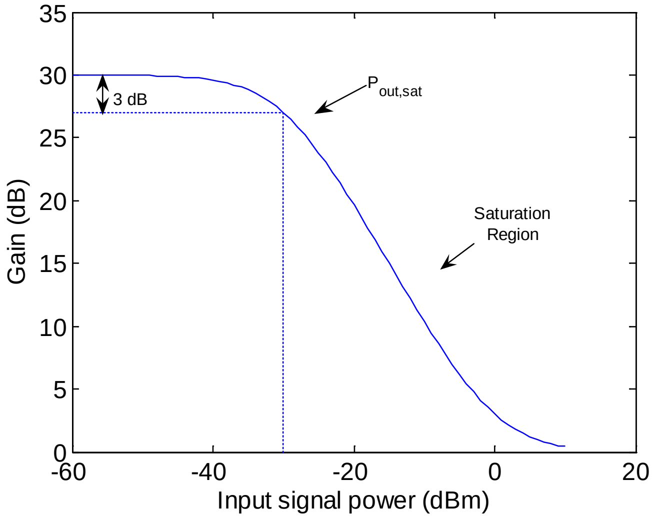

Figure 6.2. Typical dependence of the single-pass gain on optical input power for a small-signal gain of $G_f = 30dB$ (a gain of 1000)

The other main factor that limits gain in an optical amplifier is the length of the erbium-doped fiber [46]:

$$G_f \leq \exp(\rho\sigma_e L) \tag{6.3}$$

where ρ is the dopant concentration, σ_e is the signal-emission cross section and L corresponds to the length of the fiber. The gain increases exponentially with this length and the dopant concentration. Combining both inequalities, we obtain a more complex expression that establishes the limits of amplification:

$$G_{f,\max} \le \left\{ \exp\left(\rho\sigma_e L\right); 1 + \frac{\lambda_p}{\lambda_s}\frac{P_{p,in}}{P_{s,in}} \right\} \tag{6.4}$$

This expression shows saturation behavior when working with long lengths or small input pump power with respect to input signal power. Figure 6.2 gives an example showing the gain evolution with respect to the input power. The higher the input power, the smaller the input pump-signal power ratio and the gain to be obtained. The output saturation power is the point at which the gain is reduced by 3 dB, in this case, at an input power of -30 dB.

Different zones can be distinguished when gain is analyzed with respect to fiber length. Firstly, an initial linear zone is present when population inversion is sufficiently high. In this zone, pump power is sufficient to feed the emission band and medium absorption coefficients are sufficiently high. Secondly, there is an intermediate zone where the fiber does not provide sufficient energy for the signal wave and saturation is produced. Finally, if the fiber is too long, the signal wave itself is reabsorbed by the fiber resulting in a reduction of output power.

When working with different wavelengths, each wavelength can be amplified in a different zone due to the changing characteristics of the fiber along wavelength. Therefore, the choice of the best zone to work in becomes the design objective when building an optical amplifier. For this study the saturation zone was selected in order to obtain maximum output signal energy.

Temperature also needs to be taken into account. Figure 6.3 shows the absorption spectrum in the 976-nm zone and the emission spectrum at 1550 nm for a given erbium-doped fiber, demonstrating certain temperature dependence in both spectra. Since this can cause signal distortion in the system output, they will be studied for our application in section 6.3 in order to establish the advisability of temperature controlling the fiber.

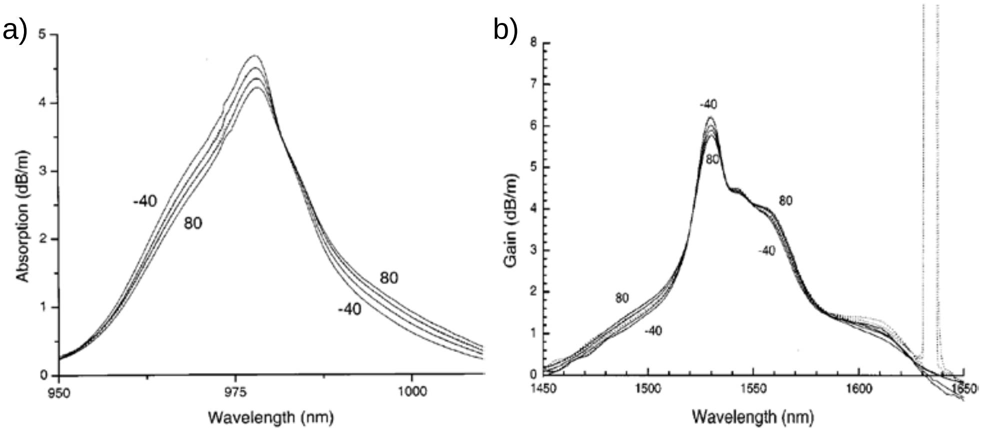

Figure 6.3. Temperature influence upon absorption (a) and emission (b) spectra for an erbium-doped fiber [47]

Noise is another important factor to be taken into account. The dominant noise generated in optical amplifiers is known as Amplified Spontaneous-Emission noise (ASE). The spontaneous recombination of electrons produces a broad spectrum noise tenths of nanometers in width. By looking closely at the power received by a detector and the current generated it is possible to analyze these noise components more specifically. Incident power has the form:

$$P_0 = G_f P_{s,in} + S_{ASE} \Delta \nu_{opt} \tag{6.5}$$

where $S_{ASE} = h\nu N_{sp}\left(G_f - 1\right)$, $N_{sp} = N_2 / \left(N_2 - N_1\right)$ is the population-inversion factor and $\Delta \nu_{opt}$ corresponds to the optical-filter bandwidth. There are different types of noise such as thermal noise, shot noise from both contributions and the crossed products of these contributions:

$$\left\langle i_{total} \right\rangle^2 = \sigma_T^2 + \sigma_{shot-S}^2 + \sigma_{S-ASE}^2 + \sigma_{shot-ASE}^2 + \sigma_{ASE-ASE}^2 \tag{6.6}$$

where σ_T is the thermal noise, σ_{shot-S} is the signal shot noise, σ_{S-ASE} is the signal-ASE crossed product, $\sigma_{shot-ASE}$ is the ASE shot noise and $\sigma_{ASE-ASE}$ is the ASE-ASE crossed product. Thermal noise is normally low and the magnitude of last four noises is similar when the entire optical bandwidth is considered. Usually, an optical filter of approximately 1 nm bandwidth is located before detection, greatly reducing the last two terms, which are linearly proportional to the optical bandwidth. So the expression can be approximated to [48]:

$$\left\langle i_{total} \right\rangle^2 \approx \sigma_{shot-S}^2 + \sigma_{S-ASE}^2 = 2qRG_f P_{s,in} B + 4\left(RG_f P_{s,in}\right)\left(RS_{ASE} B\right) \tag{6.7}$$

where $R = \eta q / \left(h\nu\right)$ corresponds to the receiver responsivity. We obtain an expression for signal-to-noise ratio [46] of:

$$\left.\frac{S}{N}\right|_{out} = \frac{i_{ph}^2}{\sigma_{total}^2} = \frac{R^2 G_f^2 P_{s,in}^2}{\sigma_{total}^2} = \frac{RP_{s,in}}{2qB} \frac{G_f}{1 + 2\eta N_{sp}\left(G_f - 1\right)} \tag{6.8}$$

where i_{ph}^2 is the mean-square input photocurrent. If we take into account the expression of the input SNR:

$$\left.\frac{S}{N}\right|_{in} = \frac{RP_{s,in}}{2qB} \tag{6.9}$$

we have a noise figure F of:

$$F = \frac{\left(S/N\right)_{in}}{\left(S/N\right)_{out}} = \frac{1 + 2\eta N_{sp}\left(G_f - 1\right)}{G_f} \tag{6.10}$$

This means that for the case of a large gain, the noise figure is equal to $2\eta N_{sp}$. And with a typical N_{sp} of 2, assuming $\eta = 1$, the input SNR is reduced by a factor of 4.

6.2 EDFA Design and Development

Several steps need to be followed to develop EDFA. First, an analysis of the different designs that can be used to build the device. Second, a series of simulations to validate the models and adjust the main parameters. Third, components need to be selected taking into account the limiting factors of the design and trying to respect them as much as possible. Finally, the construction and subsequent test of the device which allows for evaluating design quality and characteristics.

6.2.1 Model and Simulations

Figure 6.4 shows the basic model for an EDFA. We can see the signal and the pump waves combine in a wavelength division multiplexor. These combined waves are then sent down an erbium-doped fiber which will amplify the signal wave by absorbing the pump power, that is, it transfers the energy from one wave to the other. This results in an amplified signal wave with an SNR slightly degraded by the effect of ASE.

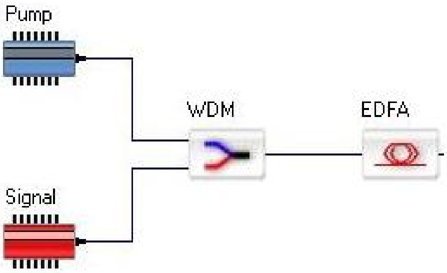

Figure 6.4. Basic Liekki-model simulator of an erbium-doped fiber amplifier

To build a more realistic model it is necessary to incorporate elements that will help to isolate the system from signal returns that would reduce its efficiency, in addition to check points to control the behavior of the amplifier and the splice points. This is shown in figure 6.5 where some 99/1 couplers were added to improve signal monitoring.

Once the real model was built, a series of simulations were performed to establish the amplifier’s optimal performance. The simulation tool was LIEKKI^{TM} Application Designer v4.0. The basic parameters such as power and signal and pump wavelength are usually previously established, so those main parameters remaining to be selected are the type and length of erbium-doped fiber.

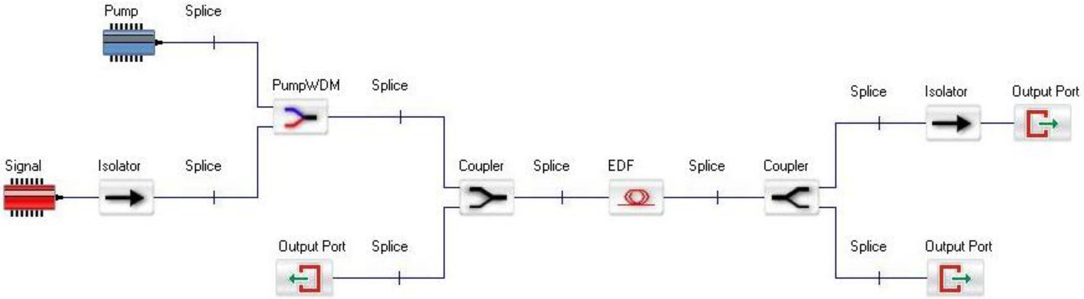

Figure 6.5. Realistic Liekki-model simulator of an erbium-doped fiber amplifier

A standard DFB laser was selected for the signal and pump supply; this was a single-mode pump laser with the current maximum available power of 976 nm, approximately 750 mW. A series of simulations were performed under these conditions with the main results shown in figure 6.6. A Liekki erbium-doped fiber with peak core absorption of 16 dB/m at 1530 nm and a length of 5 meters was chosen.

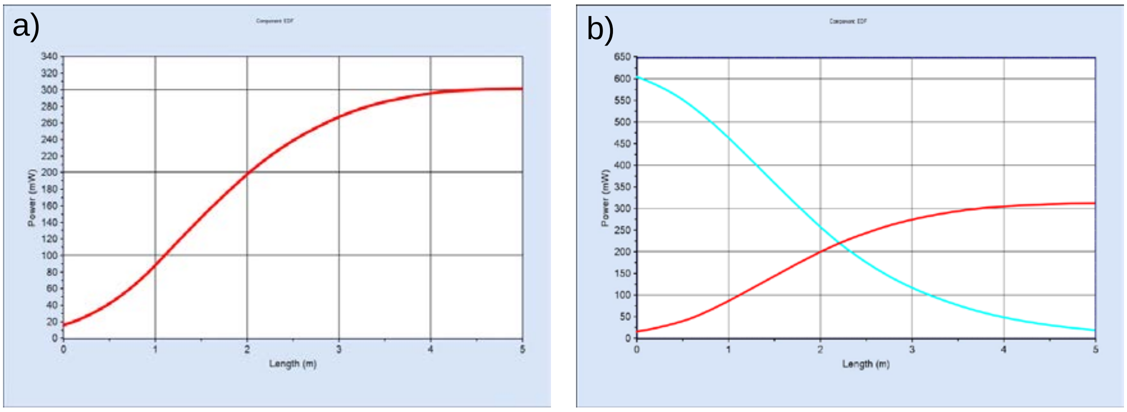

Figure 6.6. Signal (a) and pump (b) power evolution along the erbium-doped fiber length

Figure 6.6 shows an initial exponential evolution of signal power that tends to stabilize at 300 mW. Graphic b) shows both pump and signal and the transference of power from one wave to the other along the fiber, giving very low residual values of pump power. The noise is also analyzed for this configuration.

Figure 6.7 gives the evolution of ASE noise power along the fiber. The first graphic corresponds to the evolution of the noise for different wavelengths. Starting from 1500 nm, as wavelength increases a peak appears at around 2 meters, with a maximum at a wavelength of 1530 nm, where the peak of absorbance is located. This peak then starts to decrease while shifting to higher wavelengths until a value of some 1550 or 1560 nm is obtained and the maximum value of ASE at the output of the fiber appears. At that point the values start decreasing. In the second graphic only the value of ASE at 1550 nm is shown, this is the only one that remains after applying an optical filtering to the output of the fiber. It presents similar behavior to that of the signal power evolution, with power values 55 dB smaller.

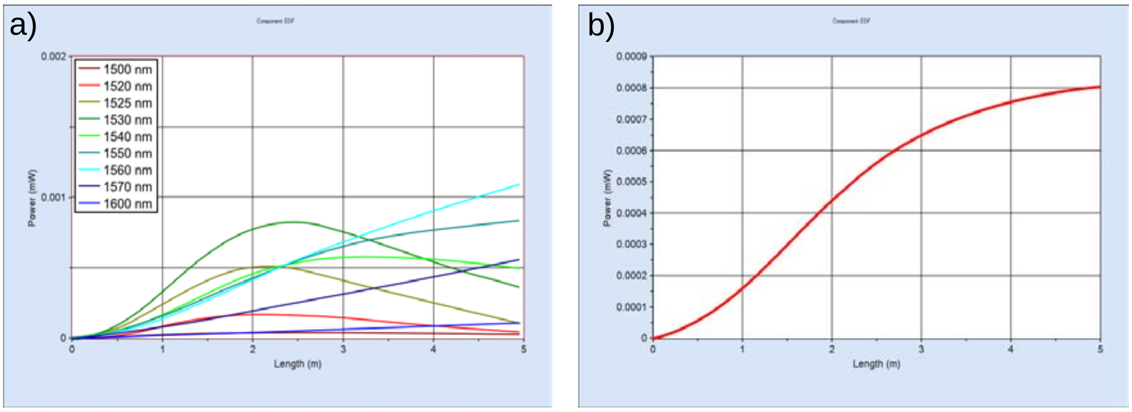

Figure 6.7. ASE noise evolution along fiber length for different wavelengths (a) and for the case of 1550 nm (b)

More simulations of the wavelength behavior of the system were performed to illustrate the system's viability and to test the possibility of using it for the amplification of other wavelengths around 1550 nm. As the fiber amplifier was clearly designed for a central wavelength of 1550 nm, the output for other wavelengths is not optimal with respect to fiber length. A 5-meter fiber length was used as a trade-off to obtain good results for these wavelengths.

Figure 6.8 gives the signal output power with respect to wavelength. A smaller output value is visible for lower wavelengths which reach their peak values for a smaller fiber length. After the peak at 1560 nm it decreases again for the opposite reason, that is, the peak output value for longer wavelengths is found in longer fiber lengths.

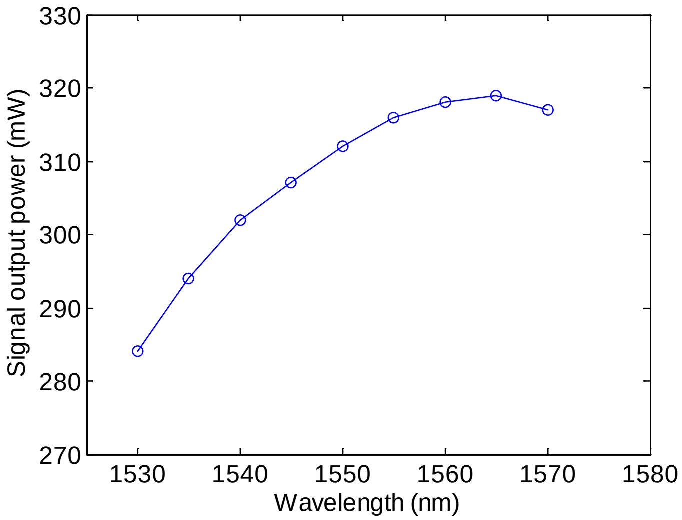

Figure 6.8. Erbium-doped fiber output power vs. wavelength for a fiber length of 5 meters

In order to increase the output power of the system, a new model of double, back-and-forth pumping was proposed. This model uses two pump diodes for the injection of energy to the erbium-doped fiber from both sides. Figure 6.9 shows a setup of the double-pump model where the backwards pump diode has been inserted with the help of a wavelength-dependent combiner.

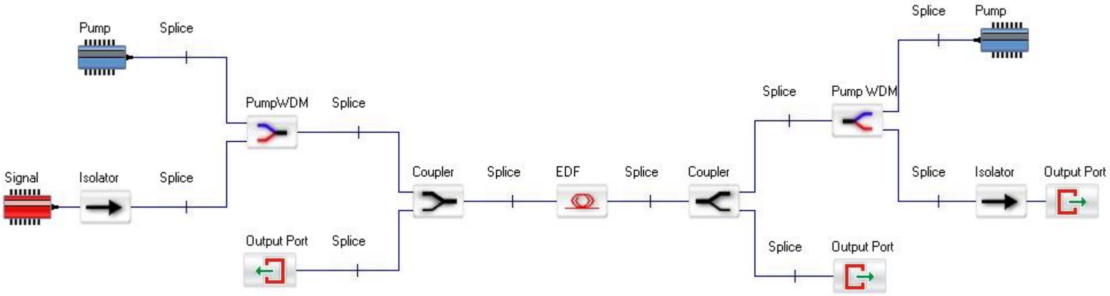

Figure 6.9. Erbium-doped fiber-amplifier double-pumping setup

A series of simulations were performed to validate this model. Due to the variability of the results with respect to the fiber length, the optimum length cannot be determined for simulations using a very long fiber, but these simulations must be performed systematically with respect to the fiber length. This effect is produced by the fact that the backwards pump signal enters the fiber at a different length for each iteration.

In order to compare this result with the previous one obtained from single-sided pumping, a total input value of some 750 mW of pump power (450-mW forward pumping and 300-mW backward pumping) was assumed. Under these conditions, the best result was obtained for the case of a 5.5 meter-long fiber. Figure 6.10 shows the evolution of signal power along the fiber, obtaining an output signal value similar to the case of a single-sided model.

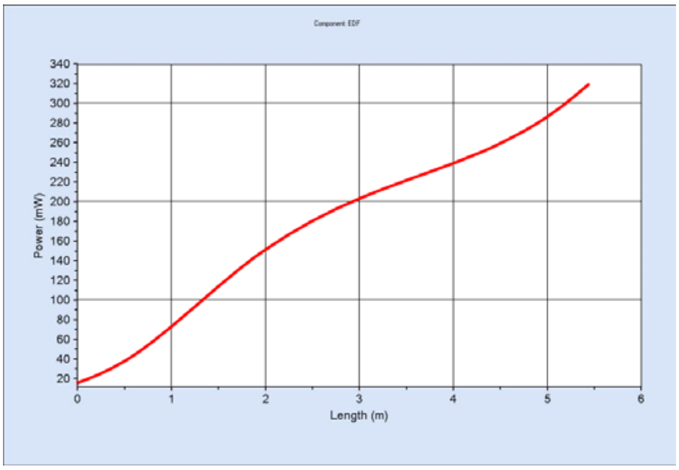

Figure 6.10. Signal power evolution with respect to erbium-doped fiber length in double-pumping configuration.

6.2.2 Development and Testing

Once the basic design was completed, the assembly of the various parts began with assembling the pump lasers subsystem. The final design allowed for control of the laser diodes and dissipation of the heat produced when being operated.

Pump lasers were tested for different input currents while maintaining a stable temperature of 25 C. The result is an almost linear response to the input stimulus, as seen in figure 6.11. The maximum input current is approximately 800 mA with a corresponding output power approaching 470 mW.

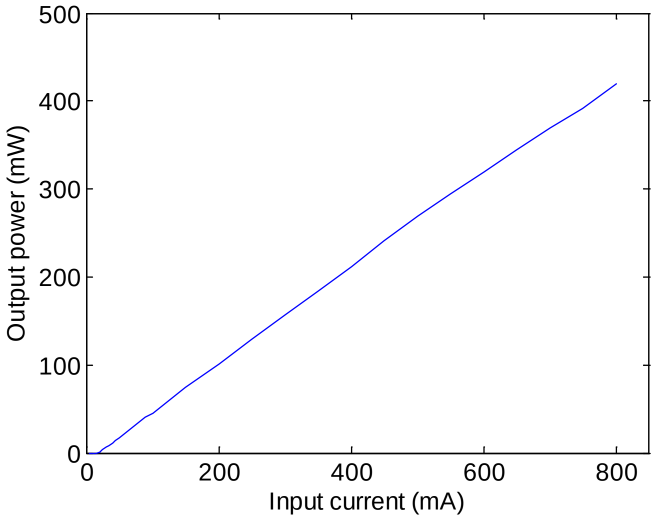

Figure 6.11. 450mW Pump-laser Output Power with respect to input current

Both sources were then combined with a wavelength-dependent multiplexor and introduced into the erbium-doped fiber. Figure 6.12 plots the output signal power vs. the input pump power.

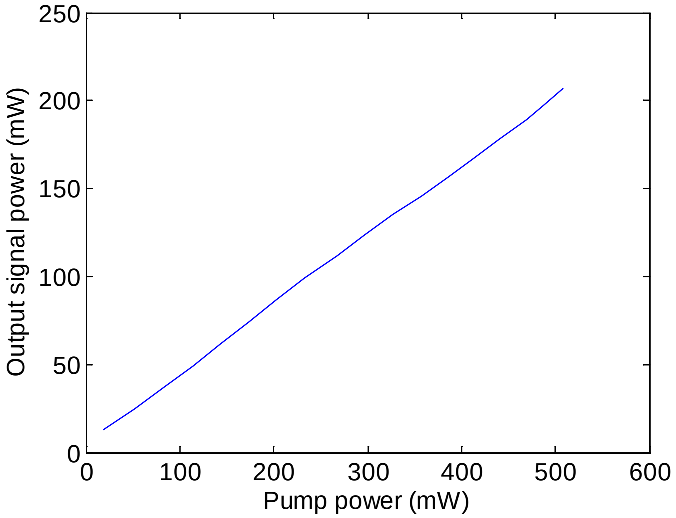

Figure 6.12. Fiber Output Power vs. LD Output Power

Further tests to validate the output power stability were carried out. Figure 6.12 shows the drift of output power along time. A value of approximately 0.7% drift can be inferred by analyzing the data in the graphic.

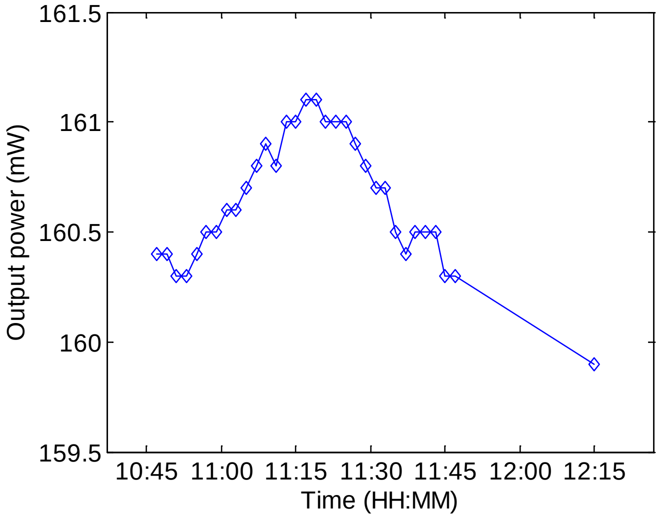

Figure 6.13. 450mW Pump Laser Output Power Stability with time

A wavelength dependence analysis of the output was performed with the help of an external cavity diode laser (ECDL) with tuning capability for sweeping along the zone of interest (Fig. 6.14).

The output power values are similar to those obtained in the theoretical simulation (Fig. 6.8), however they deviate slightly from the simulation for the longest wavelengths where the power falls much more rapidly in the lab tests.

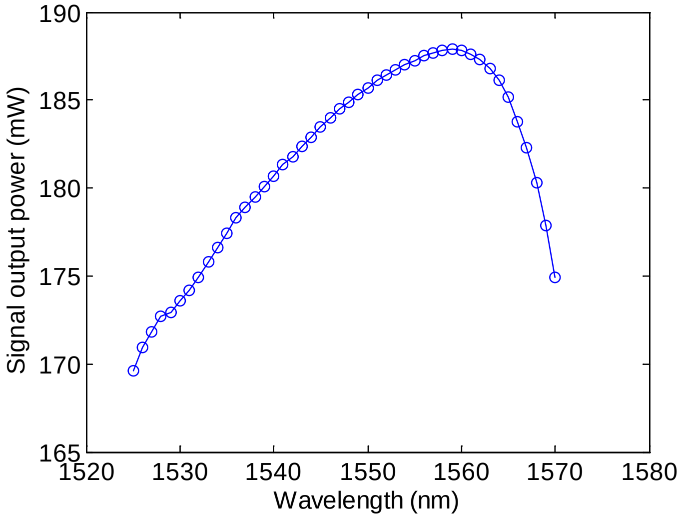

Figure 6.14. Experimental fiber output power respect to wavelength

The validation of the output power value with respect to noise was performed by spectra analysis. Figure 6.15 gives the spectrum for the case of a signal of 1530-nm. The levels of signal are approximately 60 dB higher than those for ASE noise. Moreover, the ASE spectrum is quite smooth around the signal peak. The wider spectrum graphic (Fig. 6.15.b) shows a certain increase in the ASE value along wavelength with an increase of about 10 dB of the relative value. This is in perfect agreement with the evolution of ASE noise power shown in figure 6.7, where the maximum ASE output power coincided with the wavelength of 1560 nm.

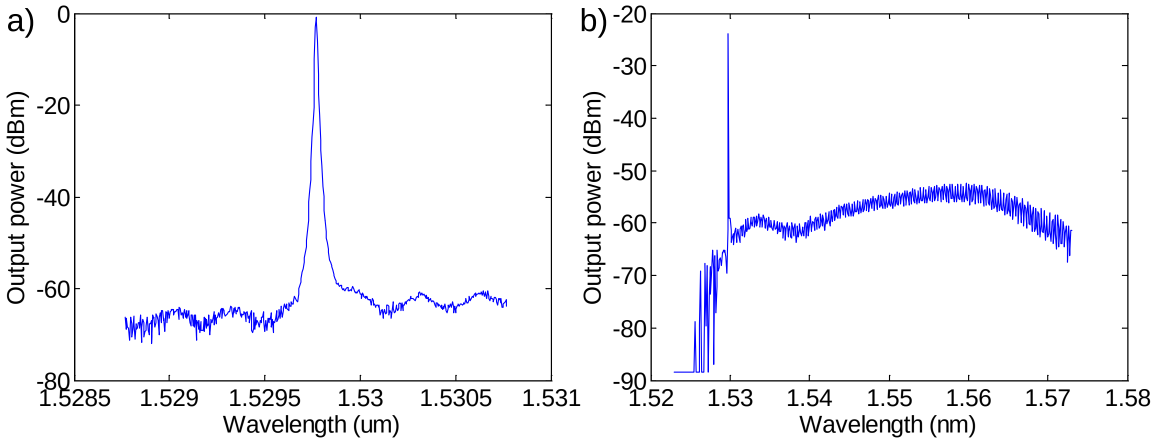

Figure 6.15. Signal Output Spectrum for an input wavelength of 1530 nm with different spans of 2 nm (a) and 50 nm (b)

Once the simple model was tested the extension of the model to a double-pump setup was analyzed. However, a feedback problem appeared between the pump diodes which did not allow the system to operate correctly.

Figure 6.16 gives the readings of output power along time in both pump lasers. The nominal output-power values of both lasers are 450 mW and 280 mW respectively, clearly indicating the presence of a feedback effect in this setup. Moreover, a clear correlation between both signals can be observed, confirming this feedback effect.

Two solutions were proposed for this problem but they were not implemented due to lack of time. The first solution proposed was to substitute all the fibers by polarized ones which would allow the pump laser waves to be orthogonally polarized. The second solution was to install isolators at the output of the pump lasers to prevent the energy coming from one from distorting the other.

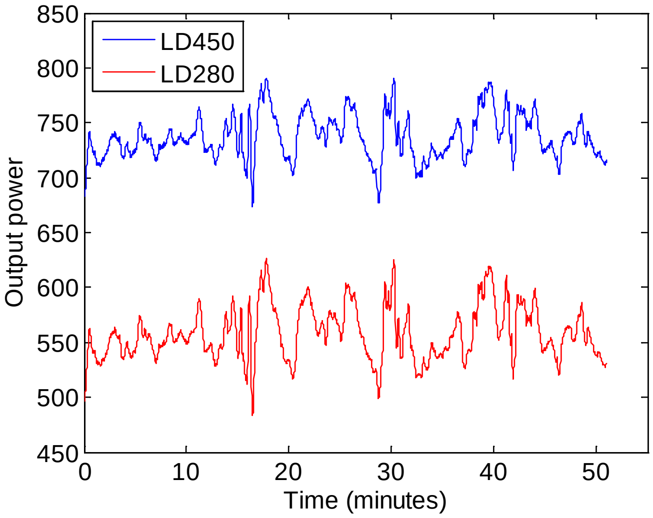

Figure 6.16. Evolution of Output Power of Pump Lasers with time

After all the different tests a final setup was determined to perform modulation tests and validate the EDFA for a gas-detection system. Figure 6.17 shows the final component setup which includes additional elements such as an adaptor for the insertion of both pump and signal to the erbium-doped fiber and a 99/1 coupler at the last stage to perform the modulation tests.

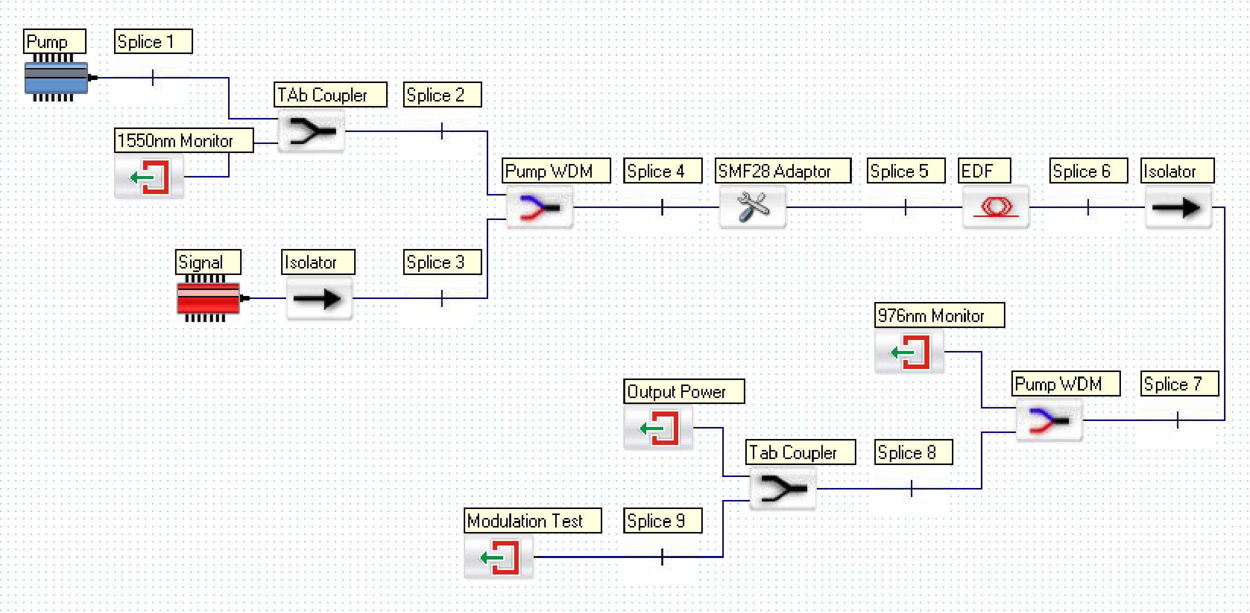

Figure 6.17. Final EDFA setup for the performance of the modulation tests

The components selected and their characteristics can be seen in Appendix F as well as the splicing table with the characteristics of the splices performed.

6.2.3 Modulation Tests

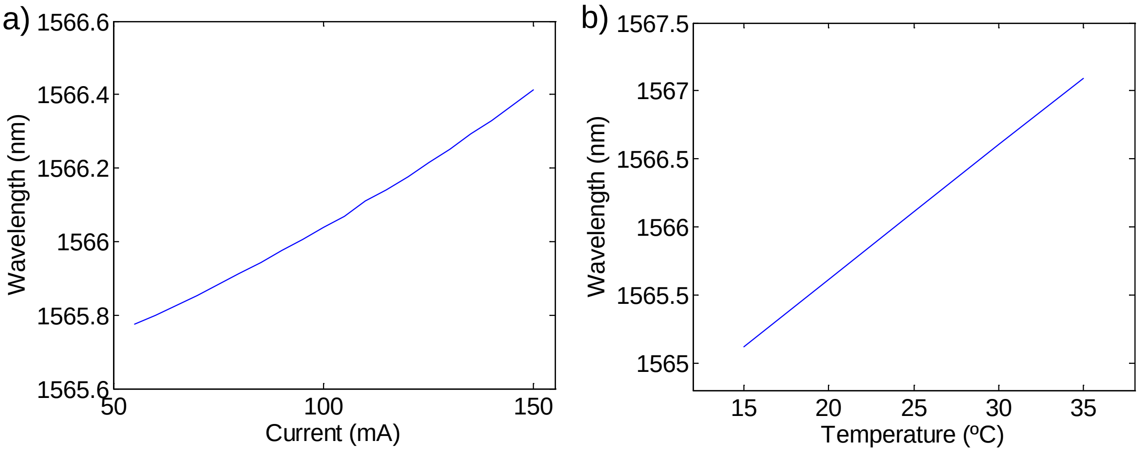

Figure 6.18. Signal laser wavelength dependence with input current and temperature

Once the amplifier setup was developed and the basic tests performed, it was extended to perform modulation tests to validate the amplifier for its final application - gas detection. A signal laser diode was used with wavelength characteristics given in figure 6.18.

A lens positioned at the end of the fiber collimates the outgoing light wave so it can be directed through the gas cell to a detector. There, light is transformed into a voltage signal that is acquired by a PC where a concentration value is obtained by means of data processing, as shown in figure 6.19. An extra element was introduced in order to fix the signal wavelength. A beam splitter was located at the output of the optical fiber that sends the light wave through another cell with the same gas being measured and with the help of another detector. This signal is acquired and used for wavelength locking the signal source with the help of a PLL design.

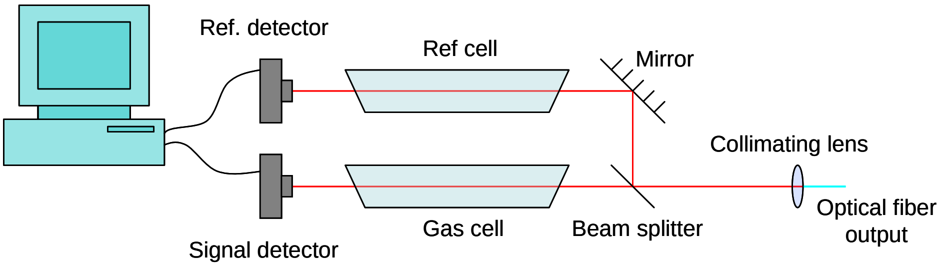

Figure 6.19. Experimental setup for the modulation tests

The signal modulation applied to the source is the classic combination of a low-frequency high-amplitude ramp that sweeps the zone where the absorption line lies and a mid-frequency sinusoid to avoid the low-frequency noise in detection. The frequencies of the ramp and the sinusoid are 25 Hz and 50 kHz respectively. The system allows the concentration measurement to be performed with a period of 1 second. Figure 6.20 gives the result of a 1-second gas measurement of the reference gas cell (a), equivalent to a formaldehyde concentration of 300 parts per billion in volume (ppbv), and a background measurement (b).

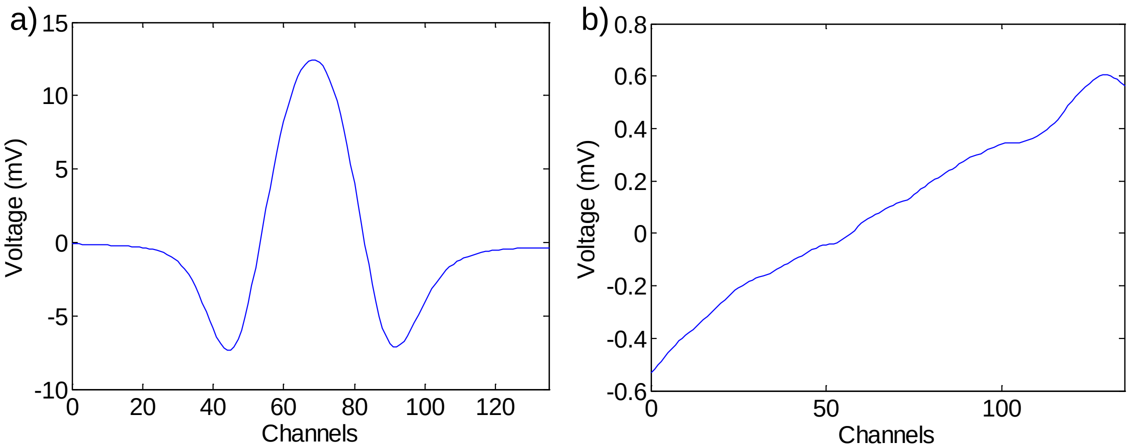

Figure 6.20. Calibration signal corresponding to a concentration of 300 ppbv of formaldehyde (a) and example of background measurement during the modulation tests.

The measurement test consists of performing a measurement of gas concentration with the background acquired signal having as a reference the gas cell concentration measurement. The levels of noise and stability of the background signal will allow for evaluating the optimal averaging time and its minimum detection limit via Allan-variance calculations [19].

Figure 6.21 presents different Allan-variance graphics (explanations are provided in the appendices). The Allan variance is observed with the detector covered (a), with the detector uncovered but without signal (b), with the signal but without pump power (c) and with signal and pump power entering the fiber (d).

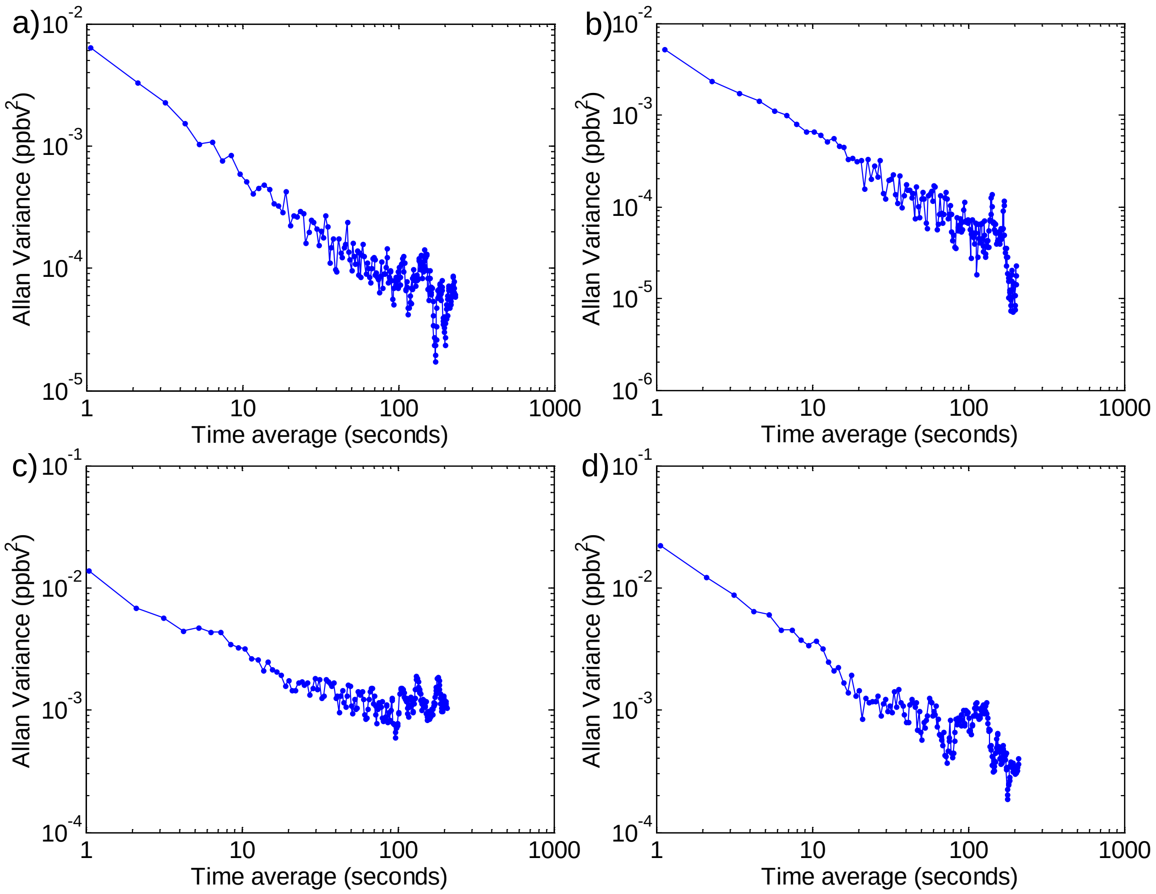

Figure 6.21. Allan Variance of the calculated concentration values for different cases: (a) detector covered, (b) detector uncovered but fiber output covered (c) fiber output uncovered with only signal power entering the fiber and (d) both signal and pump power entering the fiber.

The system was adjusted to recreate a formaldehyde measuring system with a measurement cavity of some 100-meters-long optical path. The measured values of Allan Variance are given in ppbv^2 (American billions). An increase can be observed in the initial level of noise by a factor of around 2 when the input is turned on. Looking at the last two graphics, a detection level of at least some 30 parts per trillion in volume (pptv) could be achieved by this system with an averaging time of around 1 minute.

6.3 Temperature and Pressure Testing

After designing and developing the optical amplifier, the next main objective was testing its temperature and pressure. This device was designed for the detection of gases under harsh atmospheric conditions because it works onboard an aircraft, which means rapid temperature and pressure changes during the measurement campaigns, so a complete analysis under these conditions must be completed in order to validate the system.

The possibility of temperature and pressure isolating this system is a potential solution if temperature and pressure tests give poor results. The design for a device to control the fiber temperature, which was used to test the performance of the system under changing fiber temperatures, is set out in the following section including an analysis of the temperature tests and data. Finally, a series of pressure tests were conducted with the corresponding results shown in the last section.

6.3.1 Temperature Control Device Design

The fiber temperature test was performed using a device specially designed for this purpose which heats the fiber up to 40 ºC and cools it down to room temperature. This device was designed with *SolidWorks* and consists of an empty cylinder with a covered bottom and a spiral groove in the external wall (Fig. 6.22) to coil the fiber around. This cylinder was made of a conductor material such as copper to allow rapid heating and cooling and was designed for the fiber to be in maximum contact with metal in order to obtain as homogeneous a temperature as possible in the fiber.

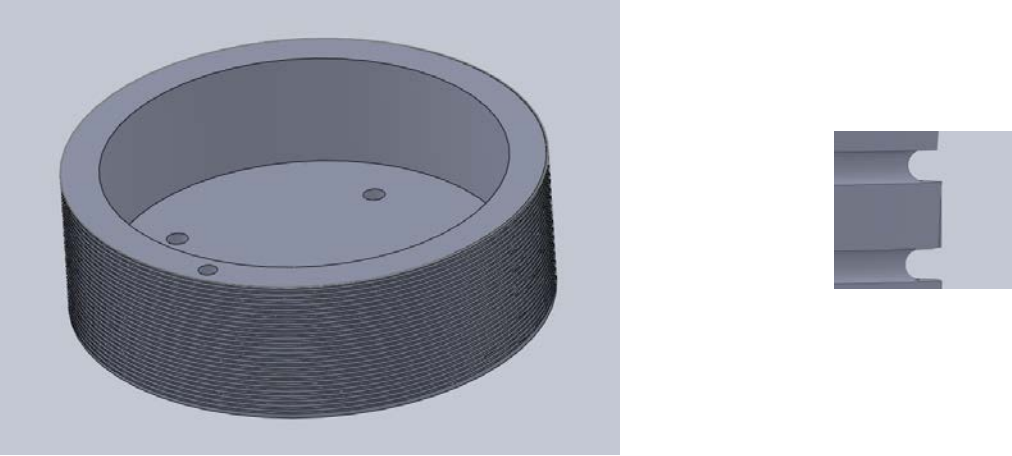

Figure 6.22. Fiber temperature testing device and detail of the groove.

The setup is completed with a TEC device for the change of temperature, and an aluminum plate as a heat sink. The complete setup can be seen in figure 6.23 with all its components correctly located.

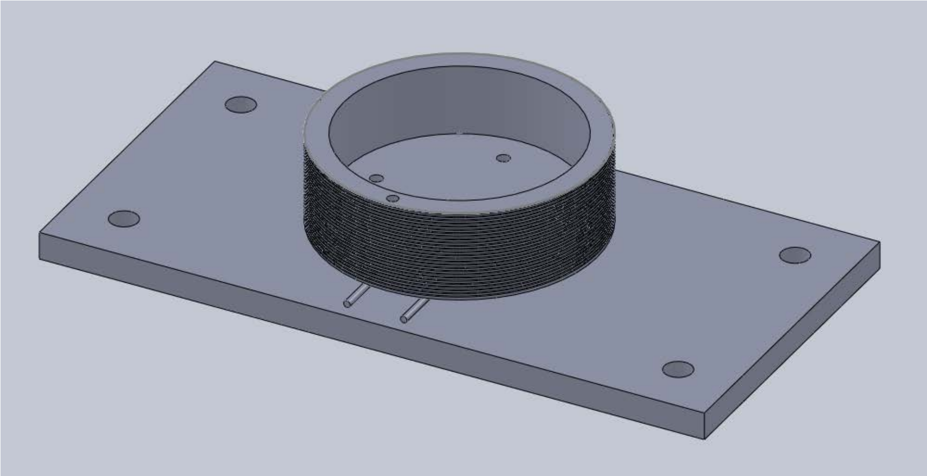

Figure 6.23. Complete setup of the fiber temperature testing device.

The TEC power is 6 watts and the spool is about 104 J for the theoretically-calculated heat to increase 1 Celsius degree. Taking into account these numbers, the theoretical time to heat the device from 20 C to 40 C is 5.8 min. The experimental time (including losses) for heating from 20 C to 40 C was 7.7 min.

6.3.2 Temperature testing

After validating the modulation scheme and with the help of the temperature device previously described, many tests were performed to investigate the effects of changing the fiber temperature. The results of a long-duration test giving the main effects of fiber temperature change are presented.

Figure 6.24 gives the results of the test with the evolution of temperature and of gas concentration superimposed. At first glance it allows us to see some effects of concentration change despite the fact that the concentration measurement is quite noisy.

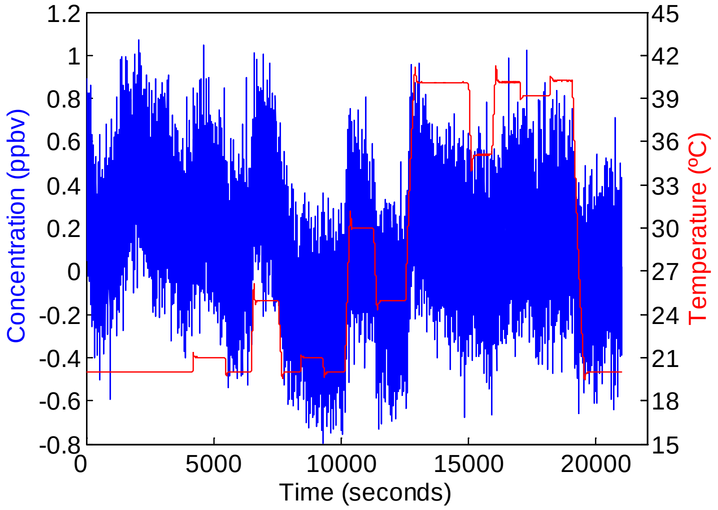

Figure 6.24. Long-duration test concentration (blue) and temperature (red) evolution.

The measurement was performed for a period of 40 minutes. During this time, as indicated by the red line in figure 6.24, the temperature was constantly increased and decreased. The spectra obtained during this test were saved in order to calculate the concentration value and the spectrum peak-to-peak value evolution over time, and these effects are analyzed in section 6.2.3. Figure 6.25 shows concentration with respect to temperature. No underlying relationship can be inferred from this graphic.

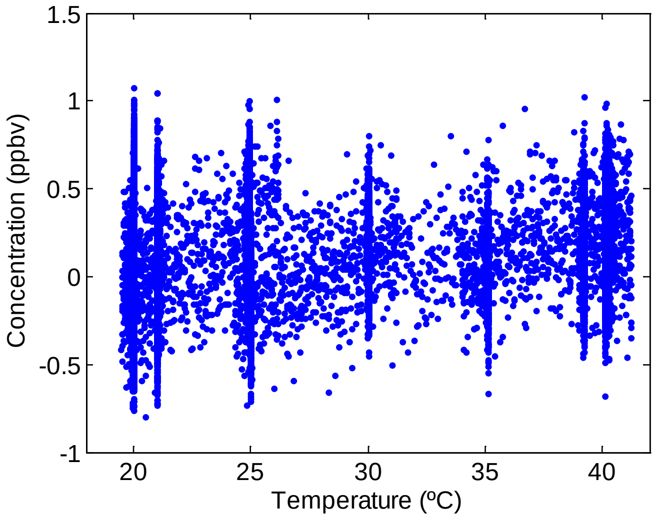

Figure 6.25. Evolution of concentration with respect to temperature.

One more step in the visualization of these effects was performed. In figure 6.26.a, a moving average of 20 samples was applied both to concentration and temperature measurements with a detail of this shown in figure 6.26.b. The result is the clarification of the temperature effects on the concentration measurement which was possible to deduce from the previous graphic.

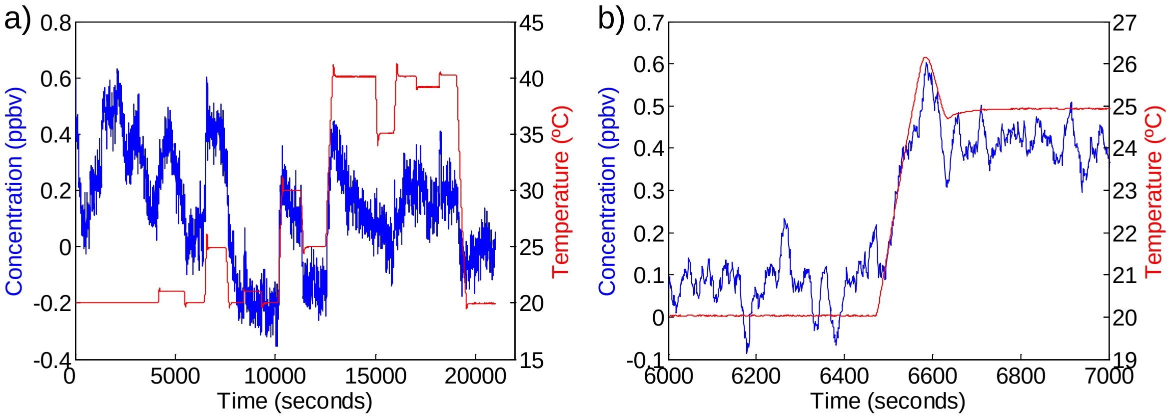

Figure 6.26. Long-duration test concentration and temperature evolution with a 20-sample average (a) and detail of this test (b).

Another way to validate this temperature effect is to study the background graphic behavior. Figure 6.27 gives the background spectra before and after temperature change for the case shown in figure 6.26.b. A major change of these spectra in correlation with the temperature change is evident.

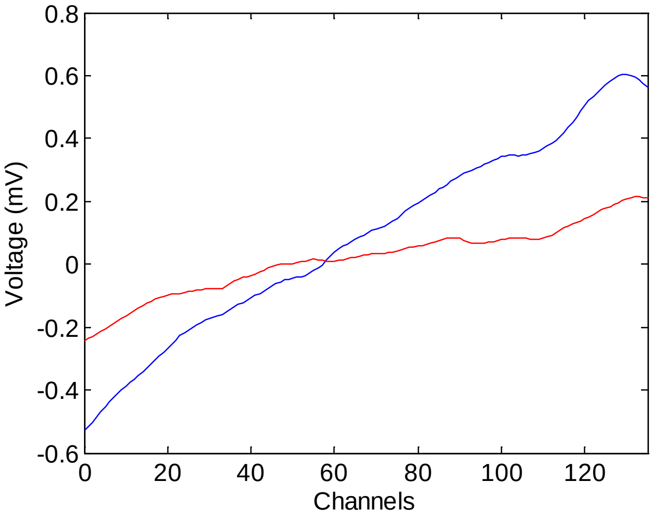

Figure 6.27. Backgrounds before and after the temperature change.

Figure 6.28 gives both peak-to-peak amplitude and temperature along time. Rapid changes of peak-to-peak value can be seen in background spectra with temperature changes. These amplitude changes are much clearer than those in concentration measurements and the relation is much more direct as shown in figure 6.29.a, which shows a graphic of peak-to-peak amplitude with respect to temperature. For example, one can see from looking at this graphic that the stability of peak-to-peak value lies between 35 and 40 C,.

In figure 6.29.b, the same graphic has been plotted but, in this case, a 30-sample average in both temperature and concentration measurements was applied. The results show smoother paths along which peak-to-peak amplitudes vary with respect to temperature.

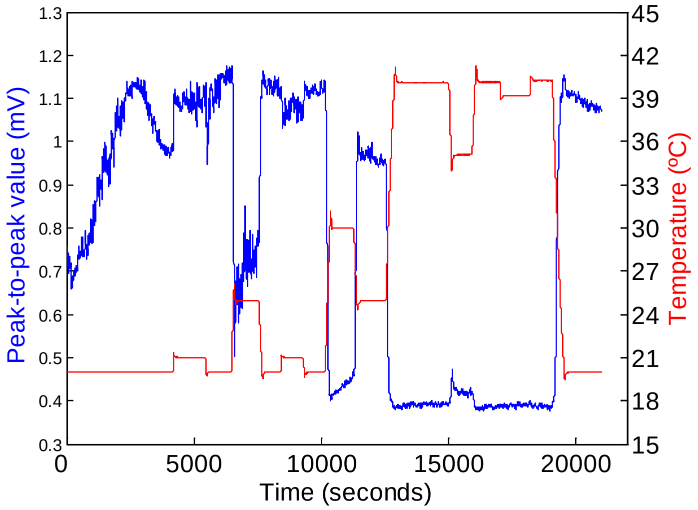

Figure 6.28. Evolution of background profiles with respect to temperature. Average of 30 samples.

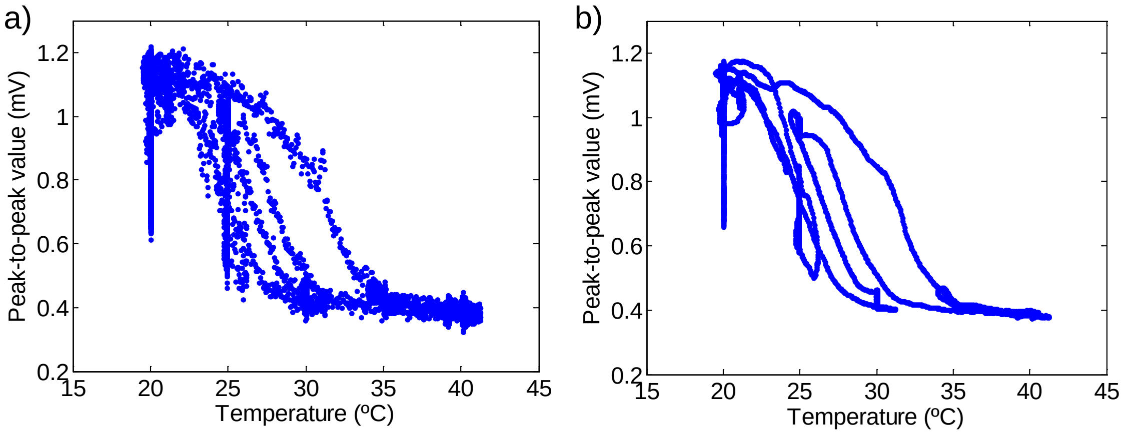

Figure 6.29. Evolution of background profiles with respect to temperature (a) and average of 30 samples of this evolution (b).

Finally, the data was processed to show a 75-second period sequence. In this sequence the first 15 seconds are dedicated to background measurement and the next 60 seconds to signal measurement. The final concentration value is obtained by averaging both signal and background measurements and then subtracting the average of previous and following background measurement from the signal measurement. This is given in figure 6.30.a and it is evident that the effect of temperature is well compensated for. In figure 6.30.b, only post background was extracted and, in this case, the effects are a little more evident.

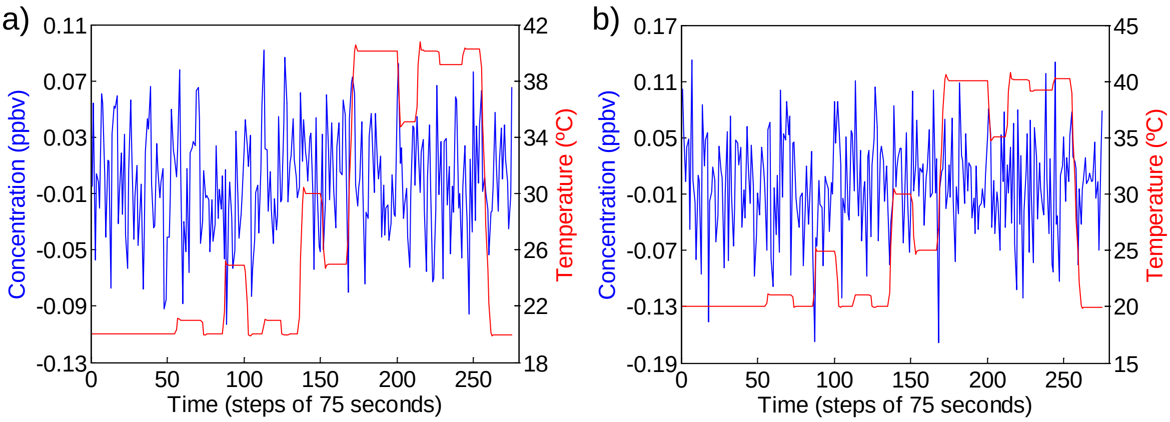

Figure 6.30. Concentration with pre- and post-background extraction (a) and with only post-background extraction (b), and temperature evolution.

The objective of the measurements was to test if a system with a smaller frequency of background extraction is feasible under these conditions. In figure 6.31, the background is extracted every ten signal measurements (10-minute cycles). Temperature effects are clearly visible when the measurement is performed in this way.

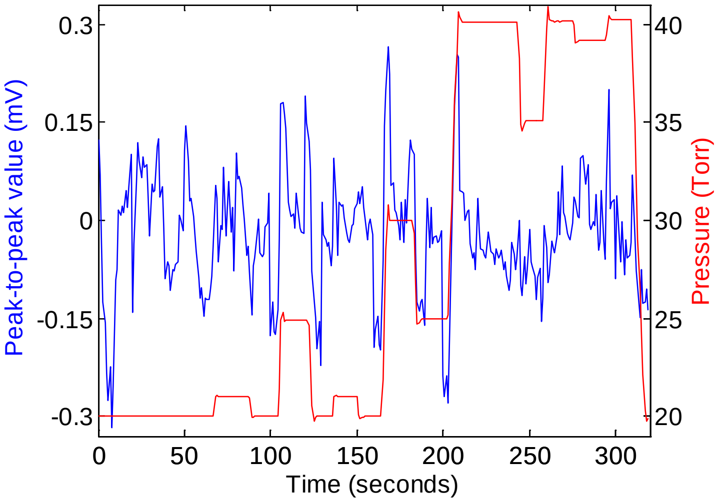

Figure 6.31. Concentration with background compensation every 10 minute cycles.

6.3.3 Pressure Testing

More tests were performed to check the dependence of the erbium-doped fiber performance with respect to pressure, taking advantage of a predesigned pressurizing device with an introduced erbium-doped fiber. The results obtained indicate that strong pressure changes have no major effect on the output signal.

Figure 6.32 shows a case where a pressure change from 400 Torr to 635 Torr (environmental pressure) is applied to the fiber and the concentration is not seen to show any relevant change during this test. The same test is given in figure 6.32.b where a 20-second moving average was applied to the concentration measurement. This confirms that the inherent drift and noise of the system are much greater than the effect of the pressure change.

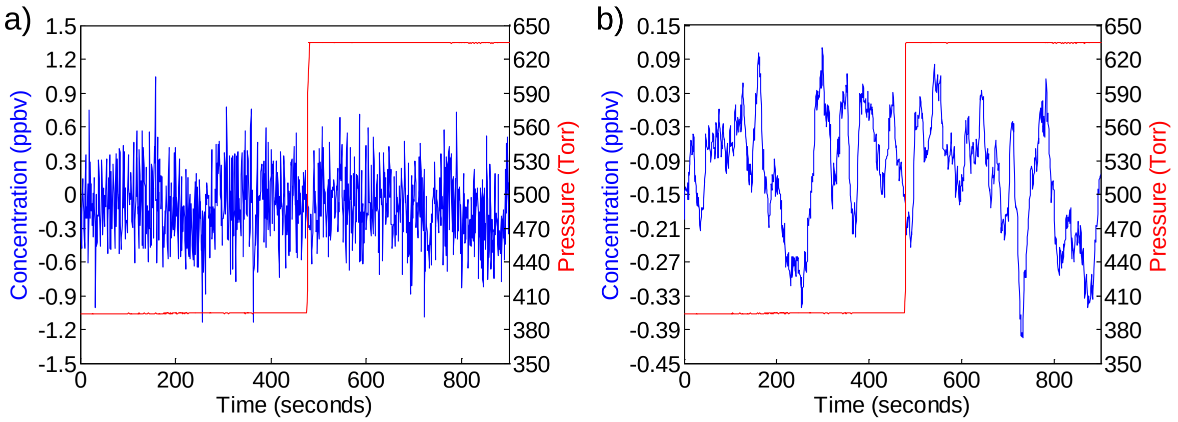

Figure 6.32. Evolution of concentration measurement with a strong pressure change (a) and the same measurement applying a 20-sample moving average (b)

Another test was performed with even a bigger pressure change from 100 Torr to 635 Torr (environmental pressure).

Figure 6.33 shows the behavior of the concentration during this pressure test and figure 6.34 shows the behavior of the peak-to-peak value. No significant changes are observed in any of the measurements performed.

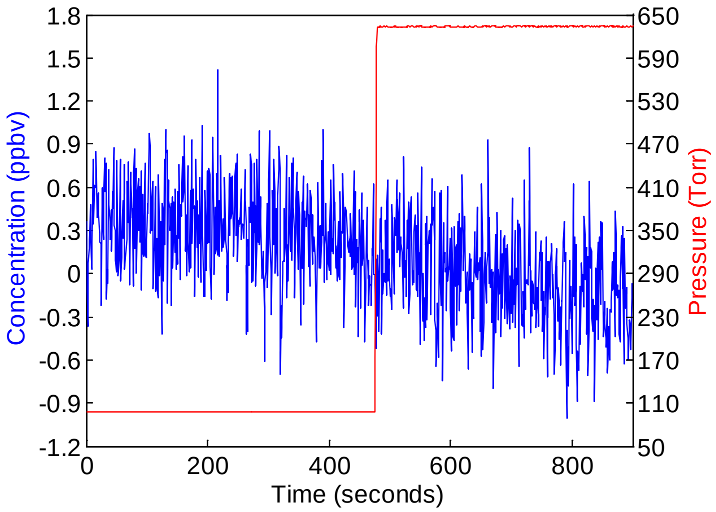

Figure 6.33. Evolution of concentration measurement with a strong pressure change

Therefore it can be concluded that with the data obtained in our tests, pressure change does not have a great influence on the concentration measurements. However, for a more precise assessment of the effect it is necessary to carry out more tests on more sensitive systems.

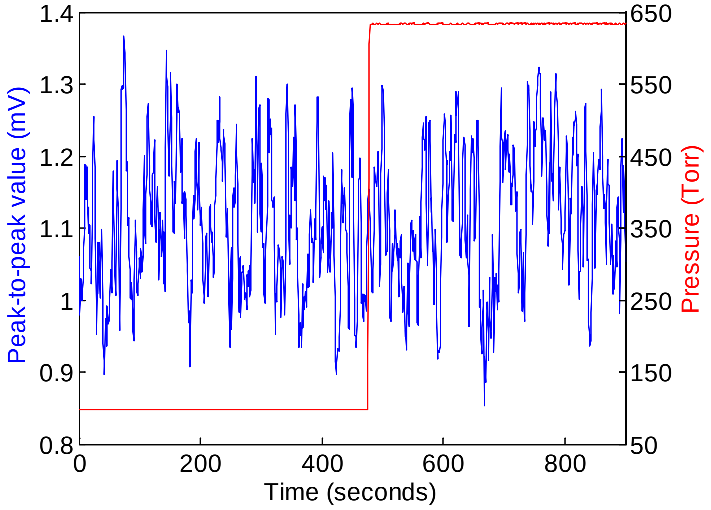

Figure 6.34. Evolution of peak-to-peak value with a strong pressure change

6.4 Chapter conclusions

This chapter has outlined the different steps required in the design of an optical fiber amplifier. First, a theoretical analysis of the erbium-doped fiber mechanism of amplification of the optical signal traveling through the fiber was performed. This is followed by a number of simulations performed to assess the theoretical results. A design was proposed and developed, testing all the separate elements during the assembly of the system. A signal diode laser was located at the input to generate the wavelength-modulated signal responsible for the gas-concentration test. A setup was designed to test the concentration of a gas cell while fixing at the same time the signal wavelength with the help of another reference gas cell in similar conditions of gas concentration (low pressures). Different tests were performed to obtain a sufficiently low noise level which would be useful in performing the temperature and pressure test (Fig 6.21).

Finally, a number of temperature and pressure tests of the erbium-doped fiber were carried out to test the behavior of the fiber under changing temperature and pressure conditions. Significant changes in the background, produced by temperature variations seem to be responsible for dramatic changes of concentration. This aspect should be taken into account in the future use of these devices. Further tests with pressure changes in the fiber were performed, but no significant change was observed either in the background or in the concentration obtained.

7 Conclusions and future lines of research

The work presented in this study leads to the conclusions discussed below and points towards lines of research that merit further development. The most significant conclusions are as follows:

- In order to acquire expertise, the WMS technique was analyzed and a WMS system constructed and tested on different gas cells and in open-path media, giving reasonable results for concentration measurements. Some discrepancies between the measurement and the manufacturers' specifications were found in the concentration of the gas cells. Although there is internal consistence in the measurements of the gas cells using two different techniques, which gives some degree of confidence in our measurements, determining in a certain way the cause of the discrepancy between these measurements and the manufacturer's specification would require an independent measurement method.

- An analysis of the FMCW technique for distributed media was performed and during the processing stage of this technique an inherent difficulty was found: a harmful bandpass filtering effect, produced by the bandpass nature of the modulating signal, was identified. This has led to an experimental verification of these problems and to the proposal of an original technique to overcome them.

- An experimental test of the interaction between the signals backscattered by nearby-targets using a FMCW lidar system was carried out. The results obtained confirmed the presence of the bandpass filtering effect identified in the previous analytical developments.

- A novel phase-hop method was proposed to overcome the difficulties encountered. This new method consists of substituting a baseband signal, with some phase characteristics allowing for the retrieval of the low spatial-frequency content of the medium profile for the classical modulating signal. This opens the possibility of performing measurements of distributed-media backscatter, including the spatial 0-frequency component.

- The analytical calculation of the signal-to-noise ratio for a FMCW system for aerosol detection was developed. It is possible to cover ranges of several kilometers with this system provided that components are correctly selected and integration times are sufficiently long.

- An analysis of the FMCW technique applied to gas detection was also performed. Two different scenarios were studied, with the use of either topographical targets or aerosols (distributed media) as backscattering medium. Both cases were analyzed and a basic gas-detection experiment using a topographical target was carried out that confirmed the analytical results.

- A sensitivity analysis for a gas-detection FMCW system using aerosols as backscattering medium was developed. This allowed the identification of critical parameters that must be taken into account in the design of practical systems.

- An extension of the phase-hop method for a gas-detection distributed-media FMCW-lidar system was proposed to overcome interference produced by the higher order harmonics on the detected signal. A series of simulations to corroborate the effectiveness of this technique were performed. This opens the way to the implementation of FMCW systems able to measure spatial distributions of gas concentrations including the 0-frequency spatial component.

- An optical fiber amplifier was studied, simulated, designed and developed for a difference-frequency generation (DFG) system for gas detection. The fiber amplifier was tested under conditions of temperature and pressure change, giving significant results in the first case. An amplifier of this type could be used in an FMCW-lidar system to extend its range.

Proposals of future research in this field are as follows:

- The design and construction of a FMCW aerosol lidar in all the relevant aspects such as hardware, signal acquisition software and signal processing.

- Further parametric analysis of optimal gas detection in a distributed-media FMCW-lidar system.

- The assessment of a gas-detection FMCW-lidar system, using either a topographical target or distributed media as backscattering medium, with external wavelength modulation or with an optical amplifier (smoothing out the emitted amplitude modulation).

- The investigation of wavelength-modulation efficiency in laser-diodes as a function of the modulation frequency both in terms of signal amplitude and phase.

- Market research into laser diodes to obtain higher wavelength deviation ratios with respect to the input current.

List of publications

1. O. Batet, F. Dios and A. Comeron, “FMCW lidar for a multiple-target sounding,” Proc. SPIE vol. 7813, pp. 7813-0H (2010)

2. O. Batet, F. Dios, A. Comeron, & R. Agishev, “Intensity-modulated linear-frequency-modulated continuous-wave lidar for distributed media: fundamentals of technique” *Appl. Opt., OSA,* **2010**, *49*, 3369-3379

3. M. Sicard, F. Rocadenbosch, M. N. M. Reba, A. Comerón, S. Tomás, D. García-Vízcaino, O. Batet, R. Barrios, D. Kumar, J. M. Baldasano, “ Seasonal variability of aerosol optical properties observed by means of a Raman lidar at an EARLINET site over Northeastern Spain,” Atmos. Chem. Phys., 11, 175-190 (2011)

4. M. Sicard, M. N. M. Reba, F. Rocadenbosch, A. Comerón, S. Tomás, D. García-Vízcaino, O. Batet, R. Barrios and D. Kumar, “ Seasonal variability of aerosol optical properties observed by means of an elastic-Raman lidar over Northeastern Spain,” Atmos. Chem. Phys. Discuss., 10, 14053 – 14094, doi:10.5194/acpd-10-14053-2010 (2010)

5. M. Sicard, M. Nadzri Reba, S. Tomás, A. Comerón, O. Batet, C. Muñoz, A. Rodríguez, F. Rocadenbosch, C. Muñoz, J. Fuensalida. “Site-testing results by means of an aerosol, backscatter lidar at the Roque de los Muchachos Observatory”. Monthly Notices of the Royal Astronomy Society.

6. D. Richter, P. Weibring, A. Fried, L. Rippe, M. Lewander, O. Batet, J. Walega, S. Spuler. “Tunable Difference Frequency Generation Laser Spectrometer: Successes, Challenges and Opportunities”. Invited paper at Laser Applications to Chemical, Security and Environmental Analysis, LACSEA 2010

7. M. Sicard, S. Tomas, M. N. M. Reba, A. Comeron, O. Batet, C. Munoz-Porcar, A. Rodriguez, F. Rocadenbosch, C. Munoz-Tunon and J. J. Fuensalida, "Aerosol stratification characterization of an astronomical site by means of a backscatter lidar at the Roque de los Muchachos observatory," Proc. SPIE vol. 7475, pp. 74750P, 2009

8. F. Dios, J. Recolons, A. Rodríguez, O. Batet. “Temporal analysis of laser beam propagation in the atmosphere using computer generated long phase screens”. A: Optics Express, Vol. 16, Issue 3, pp. 2206-2220, 2008

9. M. Sicard, S. Tomás, A. Comerón, F. Rocadenbosch, A. Rodríguez, C. Muñoz, O. Batet. “Planetary boundary layer height and wind field characterization by means of a lidar at the Teide observatory in the Canary islands”. A: *Proceedings IEEE International Geoscience & Remote Sensing Symposium 2008*. IEEE, p. 915-918, 2008

10. C. Muñoz, A. Rodríguez, A. Comerón, O. Batet, D. García, F. Rocadenbosch, M. Sicard.. “Speed measurements with a continuous wave Lidar prototype”. A: *Proceedings of IEEE International Geoscience and Remote Sensing Symposium (IGARSS-07)*. IEEE, p. 2775-2778., 2007

Appendices

Appendix A

The responses of two targets located at a certain range will interact when the difference of the distance from these targets to the source is small in terms of the resolution of the system, that is, the response of a target located at a distance R will almost not interact with the response of a target located at a distance R+5ΔR, ΔR being the resolution in range of the system. Then we can analyze this τ^2 term (Eq. (5.26)) for the case of two targets located at R_1 and R_2 range respectively in order to determine its importance in the equation.

Taking into account Eq. (5.24), we can write the next expression for one point response:

$$G_{p1p}\left(f\right)=\frac{T}{2}\sin c\left[T\left(f-K\tau\right)\right]\exp\left\{+j2\pi\left[\left(f_0+K\frac{T}{2}\right)\tau-\left(\frac{K}{2}\tau^2+f\frac{T}{2}\right)\right]\right\}. \tag{A.1}$$

Then we can calculate the values of the signal phase for both targets at the position of the first one. We can assume the delays of their signals as τ_1 and τ_2 so the frequency position of the first target will be $f=K\tau_1$ and $\tau_1-\tau_2=1/\Delta f$, where $\Delta f=f_{\max}-f_{\min}$. And finally calculate the difference between both of them.

If we observe the difference of phase for both targets (table 1) and we take into account the fact that $\Delta f=KT$, we have that the impact in the total phase of the last term is approximately $2\pi\tau_1/T$ so it's completely negligible because $T \gg \tau_1$.

Table A.1. Interference between two nearby targets

	Target *1* position (f = Kτ₁)
Target 1	$2\pi\left(f_0\tau_1-\frac{K}{2}\tau_1^2\right)$
Target 2	$2\pi\left(f_0\tau_2+\frac{KT}{2}\left(\tau_2-\tau_1\right)-\frac{K}{2}\tau_2^2\right)$
Difference	$2\pi\left(-\frac{f_0}{\Delta f}-\frac{KT}{2\Delta f}+\frac{K\left(\tau_2+\tau_1\right)}{2\Delta f}\right)$

Appendix B

Starting from Eq. (5.27) and taking into account that the function $r(\tau)$ is zero outside the integration limits, we can consider this formula to be a Fourier transform of two functions depending on τ in the frequency point: $\nu = -f_c$. Then, the function to be transformed would be the product of r by the sinc function so we have:

$$G_p\left(f;\nu\right)=\frac{P_0\delta}{4}\int_{-\infty}^{+\infty} r\left(\tau\right)\operatorname{sinc}\left[T\left(f-K\tau\right)\right]\exp\left(-j2\pi\nu\tau\right)d\tau\,. \tag{B.1}$$

Once here, we can apply the properties of the Fourier transform in order to obtain another representation of this expression, so we have:

$$G_p\left(f;\nu\right)=\frac{P_0\delta}{4KT}R\left(\nu\right)*\left[\Pi\left(\frac{\nu}{KT}\right)\exp\left(-j2\pi\nu\frac{f}{K}\right)\right], \tag{B.2}$$

R being the Fourier transform of the responsivity function. Basically, we obtain the convolution product of the Fourier transform of r, and a pulse function shifted in frequency. If we expand this convolution product, we have:

$$G_p\left(f;\nu\right)=\frac{P_0\delta}{4KT}\int_{-\infty}^{+\infty} R\left(\nu-\nu'\right)\Pi\left(\frac{\nu'}{KT}\right)\exp\left(-j2\pi\nu'\frac{f}{K}\right)d\nu'\,. \tag{B.3}$$

We observe that there is a phenomenon of windowing of R around the point ν and with a width of KT. If we perform the substitution of the variable ν, we can see that it is equivalent to a bandpass filtering around the point: $\nu = -f_c$ giving the result shown in Eq. (5.28).

Appendix C

Starting from Eq. (5.32) and developing the Fourier transform, we have:

$$G_{Sum\_F}\left(f\right)=\int_{-\infty}^{+\infty}\int_{0}^{\tau_{MAX}} r\left(\tau\right)\cos\left(2\pi\left\{f_0\left(2t-\tau\right)+\frac{K}{2}\left[t^2+\left(t-\tau\right)^2\right]\right\}\right)d\tau\exp\left(-j2\pi ft\right)dt\,. \tag{C.1}$$

From here on, we only take into account the positive exponential term of the cosine. The negative exponential term is very similar to the positive one. So we have:

$$G_{Sum\_F+}\left(f\right)=\frac{1}{2}\int_{-\infty}^{+\infty}\int_{0}^{\tau_{MAX}} r\left(\tau\right)\exp\left(j2\pi\left\{f_0\left(2t-\tau\right)+\frac{K}{2}\left[t^2+\left(t-\tau\right)^2\right]\right\}\right)d\tau\exp\left(-j2\pi ft\right)dt\,. \tag{C.2}$$

Reorganizing the terms:

$$\begin{aligned}G_{Sum\_F+}\left(f\right)=\frac{1}{2}\int_{-\infty}^{+\infty}\int_{0}^{\tau_{MAX}} r\left(\tau\right)\exp\left(j2\pi\left\{K\left[t+\left(\frac{f_0-f/2}{K}-\frac{\tau}{2}\right)\right]^2\right\}\right)\times\\ \times\exp\left\{j2\pi\left[\frac{K}{4}\cdot\left(\tau-\frac{f}{K}\right)^2\right]\right\}d\tau dt\exp\left\{-j2\pi\left[\frac{\left(f-f_0\right)^2+f_0^2}{2K}\right]\right\}.\end{aligned} \tag{C.3}$$

In Eq. (C.3), we have three different exponential terms. The first one is a Gaussian term that can be integrated, giving a constant. The third one is a term independent of τ, so it can be taken off the integral giving the result shown in Eq. (5.33).

For the case of the negative exponential term the result is similar having the form:

$$G_{Sum\_F-}\left(f\right)=\frac{C_2}{2}\exp\left[j2\pi\frac{\left(f+f_0\right)^2+f_0^2}{2K}\right]\int_{0}^{\tau_{MAX}} r\left(\tau\right)\exp\left[-j2\pi\frac{K}{4}\left(\tau+\frac{f}{K}\right)^2\right]d\tau\,. \tag{C.4}$$

Appendix D

To calculate the value of $\mathrm{E}\left[\left|\frac{N_1(f+\Delta f)-N_1(f)}{\Delta f}\right|^2\right]$, we have:

$$
\begin{aligned}
&\mathrm{E}\left[\left|\frac{N_1(f+\Delta f)-N_1(f)}{\Delta f}\right|^2\right]=\frac{1}{\Delta f^2}\mathrm{E}\left[\int_0^T\int_0^T n_1(t)\left(\exp(-j2\pi\Delta ft)-1\right)n_1(t')\times\right.\\
&\left.\left(\exp(j2\pi\Delta ft')-1\right)\exp\left(-j2\pi f(t-t')\right)dtdt'\right]=\frac{1}{\Delta f^2}\int_0^T\int_0^T \mathrm{E}\left[n(t)n(t')\right]\times \qquad \text{(D.1)}\\
&\cos\left[2\pi\left(f_0t+Kt^2/2\right)\right]\left(\exp(-j2\pi\Delta ft)-1\right)\cos\left[2\pi\left(f_0t'+Kt'^2/2\right)\right]\times\\
&\left(\exp(j2\pi\Delta ft')-1\right)\exp\left(-j2\pi f(t-t')\right)dtdt'
\end{aligned}
$$

If we suppose the noise to be AWGN, that is, $E\left[n(t)n(t')\right]=\eta_n\delta(t-t')$ we have:

$$
\begin{aligned}
&\mathrm{E}\left[\left|\frac{N_1(f+\Delta f)-N_1(f)}{\Delta f}\right|^2\right]=\frac{1}{\Delta f^2}\int_0^T\int_0^T \eta_n\delta(t-t')\cos\left[2\pi\left(f_0t+Kt^2/2\right)\right]\times\\
&\left(\exp(-j2\pi\Delta ft)-1\right)\cos\left[2\pi\left(f_0t'+Kt'^2/2\right)\right]\left(\exp(j2\pi\Delta ft')-1\right)\times\\
&\exp\left(-j2\pi f(t-t')\right)dtdt'=\frac{\eta_n}{\Delta f^2}\int_0^T\int_0^T\left(\exp(-j2\pi\Delta ft)-1\right)\left(\exp(j2\pi\Delta ft)-1\right)\times \qquad \text{(D.2)}\\
&\cos^2\left[2\pi\left(f_0t+Kt^2/2\right)\right]dt=\frac{4\eta_n}{\Delta f^2}\int_0^T\sin^2(\pi\Delta ft)\cos^2\left[2\pi\left(f_0t+Kt^2/2\right)\right]dt=\\
&=\frac{2\eta_n}{\Delta f^2}\left(\int_0^T\sin^2(\pi\Delta ft)\,dt+\int_0^T\sin^2(\pi\Delta ft)\cos\left[4\pi\left(f_0t+Kt^2/2\right)\right]dt\right)
\end{aligned}
$$

The first integral is straightforward with the result:

$$
\int_0^T\sin^2(\pi\Delta ft)\,dt=\frac{T}{2}\left(1-\frac{\sin(2\pi\Delta fT)}{2\pi\Delta fT}\right) \qquad \text{(D.3)}
$$

To solve the second integral in Eq. (D.2), we can apply that:

$$
\int_0^T\frac{\sin^2(\pi\Delta ft)}{\Delta f^2}\cos\left[4\pi\left(f_0t+Kt^2/2\right)\right]dt<\pi^2\int_0^T t^2\cos\left[4\pi\left(f_0t+Kt^2/2\right)\right]dt \qquad \text{(D.4)}
$$

Then taking into account that $f_0=-\frac{KT}{2}$ (due to the baseband characteristic of the signal) and applying a variable change with $l=t-T/2$, we have:

$$\int_0^T t^2\cos\left[4\pi\left(-\frac{KT}{2}t+Kt^2/2\right)\right]dt$$
$$=\int_0^T t^2\cos\left[2\pi K\left(t-\frac{T}{2}\right)^2-\pi K\frac{T^2}{2}\right]dt\;\square\int_{-T/2}^{T/2}\left(l+\frac{T}{2}\right)^2\cos\left(2\pi Kl^2-\pi K\frac{T^2}{2}\right)dl \tag{D.5}$$
$$=\frac{1}{2}\int_{-T/2}^{T/2}\left(l+\frac{T}{2}\right)^2\left[\exp\left(j\left(2\pi Kl^2-\pi K\frac{T^2}{2}\right)\right)+\exp\left(-j\left(2\pi Kl^2-\pi K\frac{T^2}{2}\right)\right)\right]dl$$

Then, if we suppose that, from $l=T/2$, the contribution to the integral is approximately zero due to the fast oscillation of the exponential, we can approximate the limits of the integral to vary from –∞ to ∞, obtaining:

$$\frac{1}{2}\int_{-T/2}^{T/2}\left(l+\frac{T}{2}\right)^2\exp\left(j\left(2\pi Kl^2-\pi K\frac{T^2}{2}\right)\right)dl\approx\frac{1}{2}\int_{-\infty}^{\infty}\left(l+\frac{T}{2}\right)^2\exp\left(j\left(2\pi Kl^2-\pi K\frac{T^2}{2}\right)\right)dl$$
$$=\frac{1}{2}\exp\left(-j\pi K\frac{T^2}{2}\right)\int_{-\infty}^{\infty}\left(l+\frac{T}{2}\right)^2\exp\left(j2\pi Kl^2\right)dl \tag{D.6}$$
$$=\exp\left(-j\pi K\frac{T^2}{2}\right)\int_0^{\infty}\left(l^2+\frac{T^2}{4}\right)\exp\left(j2\pi Kl^2\right)dl$$

where in the last step, the linear term of $\left(l+\frac{T}{2}\right)^2$ vanishes because of its oddness. Then applying known results of integral evaluations:

$$\int_0^{\infty}\exp\left(jax^2\right)dx=\frac{1}{2}\sqrt{\frac{j\pi}{a}} \tag{D.7}$$

$$\int_0^{\infty}x^2\exp\left(jax^2\right)dx=\frac{\sqrt{\pi}}{2}\left(\frac{j}{a}\right)^{3/2} \tag{D.8}$$

we have:

$$\frac{1}{2}\int_{-T/2}^{T/2}\left(l+\frac{T}{2}\right)^2\exp\left(j\left(2\pi Kl^2-\pi K\frac{T^2}{2}\right)\right)dl\approx\exp\left(-j\pi K\frac{T^2}{2}\right)\sqrt{\frac{j}{2K}}\left(\frac{j}{4\pi K}+\frac{T^2}{8}\right), \tag{D.9}$$

so

$$\int_0^T t^2\cos\left[4\pi\left(-\frac{KT}{2}t+Kt^2/2\right)\right]dt=2\,\mathrm{Re}\left[\exp\left(-j\pi K\frac{T^2}{2}\right)\sqrt{\frac{j}{2K}}\left(\frac{j}{4\pi K}+\frac{T^2}{8}\right)\right] \tag{D.10}$$

and:

$$\mathrm{E}\left[\left|\frac{N_1(f+\Delta f)-N_1(f)}{\Delta f}\right|^2\right]=\frac{2\eta_n}{\Delta f^2}\left\{\frac{T}{2}\left(1-\frac{\sin(2\pi\Delta fT)}{2\pi\Delta fT}\right)+\right.$$
$$\left.2\pi^2\Delta f^2\,\mathrm{Re}\left[\exp\left(-j\pi K\frac{T^2}{2}\right)\sqrt{\frac{j}{2K}}\left(\frac{j}{4\pi K}+\frac{T^2}{8}\right)\right]\right\}\approx\frac{\eta_n T}{\Delta f^2}\left(1-\frac{\sin(2\pi\Delta fT)}{2\pi\Delta fT}\right) \qquad \text{(D.11)}$$

where the last approximation has been obtained taking into account that $T \square \left(T\Delta f\right)^2/\sqrt{K}$ or $\Delta f_D = KT \square \left(T\Delta f\right)^4/T$ for $T\Delta f < 5$. In figure D.1 we can see the evolution of $\frac{1}{2\eta T^3}\mathrm{E}\left[\left|\frac{N_1(f+\Delta f)-N_1(f)}{\Delta f}\right|^2\right]$ with respect to the factor ΔfT where it is clearly shown the fall of the function as the factor ΔfT increases.

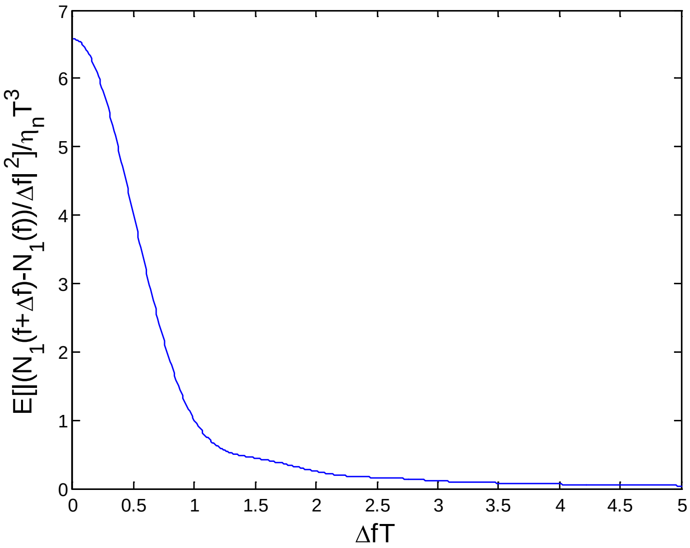

Figure D.1. Evolution of the normalized frequency difference equation with respect to the parameter ΔfT

For the case of $\mathrm{E}\left[\left|\frac{N_2(2f+2\Delta f)-N_2(2f)}{\Delta f}\right|^2\right]$, we have as in Eq. (D.1) that:

$$\mathrm{E}\left[\left|\frac{N_2(2f+2\Delta f)-N_2(2f)}{\Delta f}\right|^2\right]=\frac{1}{4\Delta f^2}\mathrm{E}\left[\int_0^T\!\!\int_0^T n_2\left(\frac{t}{2}\right)\left(\exp(-j2\pi\Delta ft)-1\right)n_2\left(\frac{t'}{2}\right)\times\right.$$
$$\left.\left(\exp(j2\pi\Delta ft')-1\right)\exp\left(-j2\pi f(t-t')\right)dtdt'\right]=\frac{1}{4\Delta f^2}\int_0^T\!\!\int_0^T \mathrm{E}\left[n\left(\frac{t}{2}\right)n\left(\frac{t'}{2}\right)\right]\times \qquad \text{(D.12)}$$
$$\cos\left[4\pi\left(f_0t+Kt^2/2\right)\right]\left(\exp(-j2\pi\Delta ft)-1\right)\cos\left[4\pi\left(f_0t'+Kt'^2/2\right)\right]\times$$
$$\left(\exp(j2\pi\Delta ft')-1\right)\exp\left(-j2\pi f(t-t')\right)dtdt'$$

Then if we suppose the noise to be AWGN, that is, $E\left[n(t)n(t')\right]=\eta_n\delta(t-t')$ we have:

$$\begin{aligned}
&\mathrm{E}\left[\left|\frac{N_2(2f+2\Delta f)-N_2(2f)}{\Delta f}\right|^2\right]=\frac{1}{4\Delta f^2}\int_0^T\int_0^T\eta_n\delta\left(\frac{t-t'}{2}\right)\cos\left[4\pi\left(f_0t+Kt^2/2\right)\right]\times\\
&\left(\exp(-j2\pi\Delta ft)-1\right)\cos\left[4\pi\left(f_0t'+Kt'^2/2\right)\right]\left(\exp(j2\pi\Delta ft')-1\right)\times\\
&\exp\left(-j2\pi f\left(t-t'\right)\right)dtdt'=\frac{\eta_n}{2\Delta f^2}\int_0^T\int_0^T\left(\exp(-j2\pi\Delta ft)-1\right)\left(\exp(j2\pi\Delta ft)-1\right)\times\\
&\cos^2\left[4\pi\left(f_0t+Kt^2/2\right)\right]dt=\frac{2\eta_n}{\Delta f^2}\int_0^T\sin^2(\pi\Delta ft)\cos^2\left[4\pi\left(f_0t+Kt^2/2\right)\right]dt=\\
&=\frac{\eta_n}{\Delta f^2}\left(\int_0^T\sin^2(\pi\Delta ft)\,dt+\int_0^T\sin^2(\pi\Delta ft)\cos\left[8\pi\left(f_0t+Kt^2/2\right)\right]dt\right)
\end{aligned}\tag{D.13}$$

Comparing Eq. (D.13) with Eq. (D.2) and taking into account the result in Eq. (D.11), we have that:

$$\mathrm{E}\left[\left|\frac{N_2(2f+2\Delta f)-N_2(2f)}{\Delta f}\right|^2\right]=\frac{\eta_nT}{2\Delta f^2}\left(1-\frac{\sin(2\pi\Delta fT)}{2\pi\Delta fT}\right)\tag{D.14}$$

Appendix E

To calculate the value of $\mathrm{E}\left[\left(\frac{N_1(f+\Delta f)-N_1(f)}{\Delta f}\right)\left(\frac{N_2(2f+2\Delta f)-N_2(2f)}{\Delta f}\right)^*\right]$, we have:

$$\mathrm{E}\left[\left(\frac{N_1(f+\Delta f)-N_1(f)}{\Delta f}\right)\left(\frac{N_2(2f+2\Delta f)-N_2(2f)}{\Delta f}\right)^*\right]=\frac{1}{2\Delta f^2}\mathrm{E}\left[\int_0^T\int_0^T n_1(t)\times\right.$$
$$\left.\left(\exp(-j2\pi\Delta ft)-1\right)n_2\left(\frac{t'}{2}\right)\left(\exp(j2\pi\Delta ft')-1\right)\exp\left(-j2\pi f\left(t-t'\right)\right)dtdt'\right]=$$
$$\frac{1}{2\Delta f^2}\int_0^T\int_0^T\mathrm{E}\left[n(t)n\left(\frac{t'}{2}\right)\right]\cos\left[2\pi\left(f_0t+Kt^2/2\right)\right]\left(\exp(-j2\pi\Delta ft)-1\right)$$
$$\cos\left[4\pi\left(f_0\frac{t'}{2}+K\frac{t'^2}{8}\right)\right]\left(\exp(j2\pi\Delta ft')-1\right)\exp\left(-j2\pi f\left(t-t'\right)\right)dtdt' \tag{E.1}$$

Then applying the variable change $t''=t'/2$ and assuming AWGN noise, we have:

$$\mathrm{E}\left[\left(\frac{N_1(f+\Delta f)-N_1(f)}{\Delta f}\right)\left(\frac{N_2(2f+2\Delta f)-N_2(2f)}{\Delta f}\right)^*\right]=$$
$$\frac{1}{\Delta f^2}\int_0^T\int_0^{T/2}\mathrm{E}\left[n(t)n(t'')\right]\cos\left[2\pi(f_0t+Kt^2/2)\right]\left(\exp(-j2\pi\Delta ft)-1\right)$$
$$\cos\left[4\pi\left(f_0t''+Kt''^2/2\right)\right]\left(\exp(j4\pi\Delta ft'')-1\right)\exp\left(-j2\pi f\left(t-2t''\right)\right)dtdt''=$$
$$\frac{\eta}{\Delta f^2}\int_0^{T/2}\cos\left[2\pi(f_0t+Kt^2/2)\right]\left(\exp(-j2\pi\Delta ft)-1\right)\cos\left[4\pi\left(f_0t+Kt^2/2\right)\right]\times$$
$$\left(\exp(j4\pi\Delta ft)-1\right)\exp(j2\pi ft)dt=\frac{4\eta}{\Delta f^2}\int_0^{T/2}\exp(j\pi\Delta ft)\sin\left(2\pi\frac{\Delta f}{2}t\right)\sin(2\pi\Delta ft)\times$$
$$\cos\left[2\pi(f_0t+Kt^2/2)\right]\cos\left[4\pi\left(f_0t+Kt^2/2\right)\right]\exp(j2\pi ft)dt=$$
$$\frac{2\eta}{\Delta f^2}\int_0^{T/2}\exp(j\pi\Delta ft)\sin\left(2\pi\frac{\Delta f}{2}t\right)\sin(2\pi\Delta ft)\left\{\cos\left[2\pi(f_0t+Kt^2/2)\right]+\right.$$
$$\left.\cos\left[6\pi\left(f_0t+Kt^2/2\right)\right]\right\}\exp(j2\pi ft)dt \tag{E.2}$$

We can now apply that the cosine functions evolve much faster than the initial exponential term and the sine terms. So we can assume that in the range where the cosine functions present a contribution to the integral, that is, for very low values of t:

$$\frac{1}{\Delta f^2}\exp(j\pi\Delta ft)\sin\left(2\pi\frac{\Delta f}{2}t\right)\sin(2\pi\Delta ft)\approx 2\pi^2t^2 \tag{E.3}$$

Then, we can analyze the first term $\cos\left[2\pi(f_0 t + Kt^2/2)\right]$ and extrapolate the results to the second one $\cos\left[6\pi(f_0 t + Kt^2/2)\right]$. Taking into account that $f_0 = -\frac{KT}{2}$ (due to the baseband characteristic of the signal) and applying a variable change with $l = t - \frac{T}{2} + \frac{f}{K}$, we have:

$$\begin{aligned}
&\int_0^{T/2} t^2 \cos\left[2\pi\left(-\frac{KT}{2}t + Kt^2/2\right)\right]\exp\left(j2\pi ft\right)dt \\
&= \frac{1}{2}\int_0^{T/2} t^2 \left[\exp\left(j2\pi\left(\left(-\frac{KT}{2} + f\right)t + Kt^2/2\right)\right) + \exp\left(-j2\pi\left(\left(-\frac{KT}{2} - f\right)t + Kt^2/2\right)\right)\right]dt \\
&\square \frac{1}{2}\int_{-\frac{T}{4}+\frac{f}{K}}^{\frac{T}{4}+\frac{f}{K}} \left(l + \frac{T}{2} - \frac{f}{K}\right)^2 \left[\exp\left(j2\pi\frac{K}{2}\left(l^2 - \left(\frac{T}{2} - \frac{f}{K}\right)^2\right)\right) + \exp\left(-j2\pi\frac{K}{2}\left(l^2 - \left(\frac{T}{2} + \frac{f}{K}\right)^2\right)\right)\right]dt
\end{aligned} \qquad \text{(E.4)}$$

From here on, we will concentrate on the zone where $|f| \square KT/2$ which includes the zone where the signal we want to detect is located. Then, if we suppose that, from $l \approx T/4$, the contribution to the integral is approximately zero due to the fast oscillation of the exponential, we can approximate the limits of the integral to vary from –∞ to ∞, obtaining:

$$\begin{aligned}
&\int_{-\frac{T}{4}+\frac{f}{K}}^{\frac{T}{4}+\frac{f}{K}} \left(l + \frac{T}{2} - \frac{f}{K}\right)^2 \exp\left(j2\pi\frac{K}{2}\left(l^2 - \left(\frac{T}{2} - \frac{f}{K}\right)^2\right)\right)dt \\
&\approx \int_{-\infty}^{\infty} \left(l + \frac{T}{2} - \frac{f}{K}\right)^2 \exp\left(j2\pi\frac{K}{2}\left(l^2 - \left(\frac{T}{2} - \frac{f}{K}\right)^2\right)\right)dl \\
&\approx \exp\left(-j2\pi\frac{K}{2}\left(\frac{T}{2} - \frac{f}{K}\right)^2\right)\int_{-\infty}^{\infty}\left(l^2 + \left(\frac{T}{2} - \frac{f}{K}\right)^2\right)\exp\left(j2\pi\frac{K}{2}l^2\right)dl
\end{aligned} \qquad \text{(E.5)}$$

where in the last step we take into account that the linear term of $\left(l + \frac{T}{2} - \frac{f}{2}\right)^2$ vanishes because of its oddness. Then parallel to Eq. (D.5), we could evaluate the integral using expressions (D.7) and (D.8), to obtain a similar value in amplitude. Comparing this result with the ones obtained in appendix 1, we can say that for low values of $T\Delta f$:

$$\begin{aligned}
&\mathrm{E}\left[\left(\frac{N_1(f+\Delta f) - N_1(f)}{\Delta f}\right)\left(\frac{N_2(2f+2\Delta f) - N_2(2f)}{\Delta f}\right)^*\right] \square \\
&\mathrm{E}\left[\left|\left(\frac{N_1(f+\Delta f) - N_1(f)}{\Delta f}\right)\right|^2\right], \mathrm{E}\left[\left|\left(\frac{N_2(2f+2\Delta f) - N_2(2f)}{\Delta f}\right)\right|^2\right]
\end{aligned} \qquad \text{(E.6)}$$

Appendix F. Component selection, characteristics and splicing table of the optical amplifier development

Table F.1. Selected components for the development of the EDFA

Component	Selected Model
Signal laser	NEL1550nmDFB_20mW
Pump lasers	JDSU_980pump_450mW & JDSU_980pump_450mW
Pump lasers' drivers	Wavelength_LDTC2/2
Tab Couplers	Sifam (GH) fused Coupler C band
WDM Couplers	SifamWDM 976_1570
Erbium-doped fiber	Liekki_ Er16-8/125
Isolator	AdValue_Photonics_Isolator

Table F.2. Output-power value with respect to input wavelength and pump laser temperature

Output Power (mW)	T = 20C	T = 25C	T = 30C
λ = 1525 nm	162.4	159.3	156.3
λ = 1545 nm	173.2	170	166.8
λ = 1565 nm	176.8	173.5	170.5

Table F.3. Output-power value with respect to input wavelength and pump-laser output power

Output Power (mW)	λ = 1525 nm	λ = 1545 nm	λ = 1565 nm
P.Power = 50 (I=100mA)	7.93	10.97	13.26
P.Power = 100 (I=180mA)	24.3	28.3	30.9
P.Power = 200 (I=350mA)	58	64	67.3
P.Power = 350 (I=600mA)	108.4	116.6	120.2
P.Power = 500 (I=900mA)	159.4	170	173.7

Table F.4. Splicing table

Splice Number	Splicer	Program	Theoretical Losses	Experimental Losses
Splice 1	Ericsson FSU925	12 (SMF28 – SMF28)	*1st 1550nm: 0.08 dB 2nd 1550nm: 0.02 dB	*1st 1550nm: 0.05 dB 2nd 1550nm: 0.04 dB
Splice 2	Ericsson FSU925	14 (HI1060 – HI1060)	1550nm: 0.05 dB	1550nm: 0.03 dB
Splice 3	Ericsson FSU925	18 (HI1060 – SMF28)	980nm: 0.02 dB	980nm: 0.19 dB
Splice 4	Ericsson FSU925	18 (HI1060 – SMF28) Modified	980nm: 0.31 dB 1550nm: 0.01 dB	980nm: 0.03 dB 1550nm: 0.00 dB
Splice 5	Ericsson FSU995PM	11 (Liekki erbium Fiber)	980nm: 0.18 dB 1550nm: 0.19 dB	980nm: 0.04 dB 1550nm: 0.10 dB
Splice 6	Ericsson FSU995PM	11 (Liekki erbium Fiber)	1550nm: 0.28 dB	1550nm: 0.04 dB
Splice 7	Ericsson FSU925	18 (HI1060 – SMF28)	1550nm: 0.08 dB	1550nm: 0.01 dB
Splice 8	Ericsson FSU925	18 (HI1060 – SMF28)	1550nm: 0.05 dB	1550nm: 0.1 dB
Splice 9	Ericsson FSU925	12 (SMF28 – SMF28)	1550nm: 0.03 dB	1550nm: 0.02 dB

(*) First splice for initial analysis, second splice for modulation analysis

References

1. R.R. Agishev, and R.K. Sagdiev, “Theoretical description of LD-WM-CW ladar,” Atmos. Ocean. Opt. **13,** 959-961 (2000).

2. R. Agishev, B. Gross, F. Moshary, A. Gilerson, and S. Ahmed, “Atmospheric CW-FM-LD-RR ladar for trace-constituent detection: a concept development,” Appl. Phys. B **81,** 695-703 (2005).

3. D. A. McQuarrie and J. D. Simon, *Physical Chemistry: A Molecular Approach* (University Science Books, 1997).

4. J. M. Brown, *Molecular Spectroscopy* (Oxford University, 1998).

5. http://webbook.nist.gov/chemistry/form-ser.html

6. W. Demtröder, *Laser Spectroscopy* (Springer, 2002)

7. J. M. Hollas, *Modern Spectroscopy, 3rd ed.* (John Wiley & Sons, 1996)

8. J. M. Hollas, *High Resolution Spectroscopy, 2nd ed.* (Butterworths, 1998)

9. J. Humlicek, “Optimized computation of the Voigt and complex probability functions,” J. Quant. Spectrosc. Radiat. Transfer **27,** 437–444 (1982).

10. B. H. Armstrong, “Spectrum line profiles: The Voigt function,” J. Quant. Spectrosc. Radiat. Transfer **7,** 61–88 (1967).

11. L. S. Rothman et al., “The HITRAN Molecular Spectroscopic Database and Hawks (HITRAN Atmospheric Workstation): 1996 EDITION,” J. Quant. Spectrosc. Radiat. Transfer **60,** 665–710 (1998).

12. L. S. Rothman et al., “The HITRAN 2004 Molecular Spectroscopy Database,” J. Quant. Spectrosc. Radiat. Transfer **96,** 139–204 (2005).

13. R. Arndt, “Analytical line shapes for Lorentzian signals broadened by modulation,” J. Appl. Phys. **36,** 2522-2524 (1965).

14. G. C. Bjorklund, “Frequency-modulation spectroscopy: a new method for measuring weak absorptions and dispersions,” Opt. Lett. **5,** 15-17 (1980).

15. G. R. Janik, C. B. Carlisle & T. F. Gallagher, “Two-tone frequency-modulation spectroscopy,” J. Opt. Soc. Am. B **3,** 1070-1074 (1986).

16. J. Reid & D. Labrie, “Second-harmonic detection with tunable diode lasers – Comparison of experiment and theory,” Appl. Phys. B **26,** 203-210 (1981).

17. J. M. Supplee, E. A. Whittaker & W. Lenth, “Theoretical description of frequency modulation and wavelength modulation spectroscopy,” Appl. Opt. **33,** 6294-6302 (1994).

18. H. Wahlquist, “Modulation Broadening of Unsaturated Lorentzian Lines,” The J. Chem. Phys. **35,** 1708-1710 (1961).

19. P. Werle, R. Mücke & F. Slemr, “The limits of signal averaging in atmospheric trace-gas monitoring by tunable diode-laser absorption spectroscopy (TDLAS),” Appl. Phys. B **57,** 131-139 (1993).

20. R. M. Measures, *Laser Remote Sensing: Fundamentals and Applications* (Krieger, 1992).

21. C. Weitkamp, *Lidar: range-resolved optical remote sensing of the atmosphere* (Springer, 2005).

22. E. D. Hinkley, *Laser monitoring of the atmosphere* (Springer-Verlag, 1976).

23. http://lidar.tropos.de/en/research/raman.html

24. N. Takeuchi, N. Sugimoto, H. Baba, and K. Sakurai, “Random modulation cw lidar,” Appl. Opt. **22**, 1382-1386 (1983).

25. N. Takeuchi, H. Baba, K. Sakurai, and T. Ueno, “Diode-laser random-modulation cw lidar,” Appl. Opt. **25**, 63-67 (1986).

26. R. Matthey, and V. Mitev, “Pseudo-random noise-continuous-wave laser radar for surface and cloud measurements,” Opt. Lasers Eng. **43**, 557-571 (2005).

27. G. M. Brooker, “Understanding Millimetre Wave FMCW Radars,” in *Proceedings of 1st International Conference on Sensing Technology*, G. Sen Gupta, S. C. Mukhopadhyay and C. H. Messom, ed. (2005), pp. 152–157.

28. A. Meta, and P. Hoogeboom, “Development of Signal Processing Algorithms for High Resolution Airborne Millimeter Wave FMCW SAR,” in *Proceedings of IEEE International Radar Conference* (IEEE, 2005), pp. 326–331.

29. T. Takano, Y. Suga, K. Takei, Y. Kawamura, K. Sakai, H. Kumagai, T. Takamura, Y. Nakanishi, and T. Nakajima, “Development of a cloud profiling FM-CW radar at 95 GHz and its preliminary results,” Proc. SPIE **4894**, 132-139 (2003).

30. T. Takano, Y. Suga, K. Akita, Y. Kawamura, H. Kumagai, T. Takamura, Y. Nakanishi, and T. Nakajima, “First observational results with the newly developed cloud profiling FM-CW radar at 95 GHz,” Proc. SPIE **5235**, 517-524 (2004).

31. T. Takano, K. Akita, H. Kubo, Y. Kawamura, H. Kumagai, T. Takamura, Y. Nakanishi, and T. Nakajima, “Observation of clouds with the newly developed cloud profiling FM-CW radar at 95 GHz,” Proc. SPIE **5979**, 597907 (2005).

32. T. Ince, S. J. Frasier, A. Muschinski, and A. L. Pazmany, “An S-band frequency-modulated continuous-wave boundary layer profiler: Description and initial results,” Radio Sci. **38**, 1072 (2003).

33. M. U. Piracha, D. Nguyen, D. Mandridis, T. Yilmaz, I. Ozdur, S. Ozharar, and P. J. Delfyett, “Range resolved lidar for long distance ranging with sub-millimeter resolution,” Opt. Express **18**, 7184-7189 (2010).

34. C. J. Karlsson, F. A. A. Olsson, D. Letalick, and M. Harris, “All-fiber multifunction continuous-wave coherent laser radar at 1.55µm for range, speed, vibration, and wind measurements,” Appl. Opt. **39**, 3716–3726 (2000).

35. R. Schneider, P. Thurmel, and M. Stockmann, “Distance measurement of moving objects by frequency modulated laser radar,” Opt. Eng. **40**, 33–37 (2001).

36. B. L. Stann, W. C. Ruff, and Z. G. Sztankay, “Intensity-modulated diode laser radar using frequency-modulation/continuous-wave ranging techniques,” Opt. Eng. **35**, 3270-3278 (1996).

37. B. C. Redman, W. Ruff, and M. Giza, “Photon Counting Chirped AM Ladar: Concept, Simulation, and Initial Experimental Results,” Proc. SPIE **6214**, 62140p (2006).

38. B. C. Redman, B. Stann, W. Lawler, M. Giza, and W. Ruff, “Chirped AM Ladar for 3-D Imaging and Range-Doppler Tracking at 1550 nm Wavelength," in *Conference on Lasers and Electro-Optics/Quantum Electronics and Laser Science and Photonic Applications, Systems and Technologies*, Technical Digest (CD) (Optical Society of America, 2005), paper PThA4.

39. N. Levanon, *Radar Principles* (John Wiley & Sons Inc., 1988).

40. R. Agishev, B. Gross, F. Moshary, S. Ahmed & A. Gilerson, “Development of a SNR parameterization scheme for general lidar assessment,” Appl. Phys. B **80,** 765-776 (2005).

41. W. L. Wolfe & G. J. Zissis, *The Infrared* Handbook (Office of Naval Research, Department of the Navy, 1985).

42. D. Richter, B. P. Wert, A. Fried, P. Weibring, J. G. Walega, J. W. C. White, B. H. Vaughn & F. K. Tittel, “High-precision CO_2 isotopologue spectrometer with a difference-frequency-generation laser source,” Opt. Lett. **34,** 172-174 (2009).

43. D. Richter, A. Fried & P. Weibring, “Difference frequency generation laser based spectrometers,” Laser Photon. Rev. **3,** 343-354 (2009).

44. D. Richter P. Weibring, A. Fried, L. Rippe, M. Lewander, O. Batet, J. G. Walega & S. Spuler, “Tunable Difference Frequency Generation Laser Spectrometers: Successes, Challenges, and Opportunities,” in *Laser Applications to Chemical,*

Security and Environmental Analysis, *Laser Applications to Chemical*, *Security and Environmental Analysis*, *Optical Society of America*, **2010**, LMA4.

45. A. Ghatak and K. Thyagarajan, *An Introduction to Fiber Optics* (Cambridge University Press, 1998).

46. G. Keiser, “Optical Amplifiers,” in *Optical Fiber Communications. Third Edition* (McGraw–Hill, 2000), pp. 423–456.

47. M. Bolshtyansky et al., “Model of Temperature Dependence for Gain Shape of Erbium-Doped Fiber Amplifier,” J. Lightwave Tech. **18,** 1533–1540 (2000).

48. E. Desurvire, *Erbium-Doped Fiber Amplifiers* (John Wiley & Sons, 1994).

Further references

49. R. K. Hanson, M. E. Webber & J. M. Seitzmann, *ME 264: Introduction to Spectroscopic Diagnostics for Gases* (Stanford University course materials, 2001).

50. G. V. H. Wilson, “Modulation Broadening of NMR and ESR Line Shapes,” J. Appl. Phys. **34,** 3276–3285 (1963).

51. V. G. Avetisov & P. Kauranen, “Two-tone frequency-modulation spectroscopy for quantitative measurements of gaseous species: theoretical, numerical, and experimental investigation of line shapes,” Appl. Opt. **35,** 4705–4723 (1996).

52. D. E. Cooper & R. E. Warren, “Frequency modulation spectroscopy with lead-salt diode lasers: a comparison of single-tone and two-tone techniques,” Appl. Opt. **26,** 3726-3732 (1987).

53. W. Lenth, “High frequency heterodyne spectroscopy with current-modulated diode lasers,” J. Quant. Electron. **20,** 1045 – 1050 (1984).

54. J. A. Silver, “Frequency-modulation spectroscopy for trace species detection: theory and comparison among experimental methods,” Appl. Opt. **31,** 707–717 (1992).

55. T. Iseki, H. Tai & K. Kimura “A portable remote methane sensor using a tunable diode laser,” Meas. Sci. Tecnol. **11,** 594 (2000).

56. T. M. Taczak & D. K. Killinger, “Development of a Tunable, Narrow-Linewidth, CW 2.066-um Ho:YLF Laser for Remote Sensing of Atmospheric CO_2 and H_2O,” Appl. Opt. **37,** 8460–8476 (1998).

57. G. Morthier & P. Vankwikelberge, *Handbook of Distributed Feedback Laser Diodes* (Artech House, Inc., 1997).

58. L. A. Coldren, and S. W. Corzine, *Diode Lasers and Photonic Integrated Circuits* (John Wiley & Sons, 1995).

59. Y. B. Kumar, “Portable lidar system for atmospheric boundary layer measurements,” Opt. Eng. **45,** 076201 (2006).

60. G. J. Koch, “Automatic laser frequency locking to gas absorption lines,” Opt. Eng. **42,** 1690-1693 (2003).

61. G. J. Koch, A. N. Dharamsi, C. M. Fitzgerald & J. C. McCarthy, “Frequency Stabilization of a Ho:Tm:YLF Laser to Absorption Lines of Carbon Dioxide,” Appl. Opt. **39,** 3664–3669 (2000).

62. T. Ahola, J. Hu & E. Ikonen, “A digital control system for the iodine stabilized He-Ne laser,” Rev. Sci. Inst. **69,** 1934–1937 (1998).

63. J. E. Bjorkholm & H. G. Danielmeyer, “Frequency control of a pulsed optical parametric oscillator by radiation injection,” Appl. Phys. Lett. **15,** 171–173 (1969).

64. T. Yanagawa, S. Saito & Y. Yamamoto, “Frequency stabilization of 1.5-um InGaAsP distributed feedback laser to NH3 absorption lines,” Appl. Phys. Lett. **45,** 826 -828 (1984).

65. R. S. Eng, A. W. Mantz & T. R. Todd, “Low-frequency noise characteristics of Pb-salt semiconductor lasers,” Appl. Opt. **18,** 1088-1091 (1979).

66. K. Uehara, “Dependence of harmonic signals on sample-gas parameters in wavelength-modulation spectroscopy for precise absorption measurements,” Appl. Phys. B **67,** 517-523 (1998).

67. W. Jin, Y. Z. Xu, M. S. Demokan & G. Stewart, “Investigation of interferometric noise in fiber-optic gas sensors with use of wavelength modulation spectroscopy,” Appl. Opt. **36,** 7239–7246 (1997).

68. P. Werle, “Laser excess noise and interferometric effects in frequency-modulated diode-laser spectrometers,” Appl Phys. B **60,** 499–506 (1995).

69. P. Werle, F. Slemr, M. Gehrtz & C. Bräuchle, “Wideband noise characteristics of a lead-salt diode laser: possibility of quantum noise limited TDLAS performance,” Appl. Opt. **28,** 1638–1642 (1989).

70. S. Lee, J. McNeil, T. Zenker & T. Chyba, “Methane concentration measurements with a mid-infrared optical parametric oscillator-based differential absorption lidar system,” *Lasers and Electro-Optics, 1999. CLEO/Pacific Rim '99. The Pacific Rim Conference on*, **1999**, *2*, 272 -273 vol.2.

71. F. Yang, Y. He, J. Shang, and W. Chen, “Experimental study on the 1550nm all fiber heterodyne laser range finder,” Appl. Opt. **48**, 6575-6582 (2009).

72. R. R. Agishev, “Analytic comparison of some features of pulse-lidar and CW-FM-ladar remote sensing,” Proc. SPIE **5086**, 305-316 (2003).

73. R. R. Agishev, A. Comeron, L. Duch, R. K. Sagdiev, V. F. Dios, J. C. Cifuentes, and M. A. Lopez, "Development features of atmospheric LD ladar based on the CW-FM-range-finding principles," Proc. SPIE **5235**, 549-558 (2004).

74. R. Agishev, B. Gross, F. Moshary, A. Gilerson, and S. Ahmed, “Range-resolved pulsed and CWFM lidars: potential capabilities comparison,” Appl. Phys. B **85**, 149-162 (2006).

75. M. L. Simpson, M. Cheng, T. Q. Dam, K. E. Lenox, J. R. Price, J. M. Storey, E. A. Wachter, and W. G. Fisher, “Intensity-modulated, stepped frequency cw lidar for distributed aerosol and hard target measurements," Appl. Opt. **44**, 7210-7217 (2005).

76. J. M. Senior, “Optical amplification and integrated optics” in *Optical Fiber Communications: Principles and Practice. Second Edition* (Prentice Hall, 1992), pp. 512–550.

77. J. Hecht, “Amplification, Regeneration and Wavelength Conversion” in *Understanding Fiber Optics. Fifth Edition* (Prentice Hall, 2006), pp. 275–306.

78. L. Goldberg et al., *High-power side-pumped fiber amplifiers and lasers* (OSA course).

79. R. Paschotta, *Modeling of Fiber Amplifiers and Fiber Lasers* (OSA course).

80. Q. Luo, H. Xu, S. Hosseini, J.-F. Daigle, F. Théberge, M. Sharifi & S. Chin, “Remote sensing of pollutants using femtosecond laser pulse fluorescence spectroscopy,” Appl. Phys. B **82,** 105–109 (2006).